

LUIS GUILHERME ARNEIRO MENDES

POSITRON EMISSION TOMOGRAPHY:
IMAGE RECONSTRUCTION BASED ON MULTISCALE AND
RESOLUTION METHODS



UNIVERSITY OF COIMBRA

2012

LUÍS GUILHERME ARNEIRO MENDES

Positron Emission Tomography: Image reconstruction
based on multiscale and resolution methods

*Dissertação apresentada à
Faculdade de Medicina da Universidade de Coimbra para a prestação de
provas de Doutoramento em Ciências da Saúde- Ramo de Ciências
Biomédicas*

Orientadores:

Prof. Doutor Nuno Ferreira e Doutor Claude Comtat



UNIVERSITY OF COIMBRA

2012

This PhD work was supported by Fundação para a Ciência e Tecnologia, under the Grant SFRH/BD/ 38137 / 2007.

TABLE OF CONTENTS

Agradecimientos/Acknowledgments	i
Resumo.....	iii
Abstract.....	v
Abbreviations.....	vii
Introduction.....	1
1 Introduction to Positron Emission Tomography.....	3
1.1 Positron Emission Tomography.....	3
1.2 Stages of a PET Exam.....	5
1.3 Positron Emission and Annihilation	7
1.4 Data Acquisition	9
1.4.1 Photon Detection.....	9
1.4.2 Detected Events in Positron Emission Tomography.....	11
1.4.3 Acquisition Modes	13
1.4.4 LOR Parameterization and Data Storage.....	14
1.5 Data Correction.....	15
1.5.1 Normalization Correction	15
1.5.2 Attenuation Correction.....	16
1.5.3 Scatter Correction	18
1.5.4 Correction for Random Coincidences.....	19
1.6 Characterization of PET Scanners	20
1.6.1 Spatial Resolution	20
1.6.2 Sensitivity.....	22
2 Image Reconstruction in PET	23
2.1 Analytic Methods.....	23
2.1.1 The 2D Radon Transform	23
2.1.2 2D Central-Section Theorem	25
2.1.3 2D Filtered-Backprojection.....	27
2.2 Iterative Methods	28
2.2.1 Algebraic Reconstruction Technique.....	36
2.2.2 Maximum-Likelihood Expectation-Maximization	37
2.2.3 Block Iterative Reconstruction Methods.....	41

3	Resolution Modelling in PET	45
3.1	High Resolution Research Tomograph	46
3.2	Resolution Modelling Reconstruction Techniques	47
3.2.1	Resolution Modelling in Projection Space	49
3.2.2	Resolution Modelling in Image Space	51
3.2.3	Effect of the Resolution Modelling in the Reconstructed Image	52
3.3	HRRT Sinogram Resolution Modelling	53
3.3.1	Sinogram Blurring Kernel	53
3.4	Materials and Methods	57
3.4.1	Estimating of the Sinogram Blurring Kernel	57
3.4.2	Data Reconstruction	58
3.4.3	Performance Criteria	59
3.5	Results	60
3.5.1	Estimating of the Sinogram Blurring Kernels	60
3.5.2	Image Reconstruction	61
3.6	Discussion	65
3.7	Conclusion	66
4	Multiscale Reconstruction in PET	67
4.1	Multiscale Reconstruction	67
4.2	Materials and Methods	72
4.2.1	The Multiscale Algorithm	72
4.2.2	Generation of the Simulated Raw Data	75
4.2.3	Performance Criteria	78
4.3	Results	80
4.3.1	Interpolator Operator	80
4.3.2	Performance of the Multiscale Reconstruction Algorithm	86
4.4	Discussion	89
4.5	Conclusion	91
5	The Multiscale/Multiframe Reconstruction Approach	93
5.1	Multiscale/Multiframe Reconstruction	93
5.1.1	MS/MF Applications	95
5.2	Material and Methods	96
5.2.1	Phantom n° 2 Dataset	96
5.2.2	Phantom n° 1 Datasets	97

5.2.3	Micro-Deluxe Phantom Dataset.....	99
5.2.4	Performance Criteria.....	100
5.3	Results.....	100
5.3.1	Phantom n° 2 Dataset.....	101
5.3.2	Phantom n°1 Datasets.....	104
5.3.3	Micro-Deluxe Phantom Dataset.....	110
5.4	Discussion.....	112
5.5	Conclusions.....	114
6	A Generalized Morozov Discrepancy Criterion for the MS/MF.....	117
6.1	Stopping Criteria.....	118
6.2	A Generalized Morozov Discrepancy Principle.....	121
6.2.1	Morozov Criterion.....	122
6.2.2	Weighted Discrete Fourier Morozov Criterion.....	123
6.3	Material and Methods.....	125
6.3.1	Reconstruction Using the ML-EM.....	125
6.3.2	Reconstruction Using the MS/MF.....	126
6.3.3	WDF-Morozov Criterion.....	129
6.4	Results.....	129
6.4.1	Reconstruction Using the ML-EM.....	130
6.4.2	Reconstruction Using the MS/MF.....	132
6.4.3	WDF-Morozov Criterion.....	146
6.5	Discussion.....	147
6.6	Conclusions.....	148
7	Main Conclusions and Possible Developments.....	151
	List of Figures.....	157
	List of tables.....	169
	Bibliography.....	171

Agradecimentos/Acknowledgments

Ao Professor Doutor Nuno Ferreira, meu orientador, por me ter iniciado nesta área do conhecimento e me ter dado as condições indispensáveis para a realização do trabalho de investigação.

I would like to thanks to Prof. Dr. Claude Comtat (Service Hospitalier Frédéric Joliot, Orsay, France) for the support, the suggestions and the material.

To Prof. Dr. Michel Defrise (Department of Nuclear Medicine, University Hospital UZ-VUB, Brussels, Belgium) for the care, the discussions, the dedication and the perspectives.

Ao Professor Doutor Francisco Alves, Professor Doutor Miguel Castelo Branco, Professor Doutor Rui Bernardes, Professor Doutor Francisco Caramelo e Professor Doutor Antero Abrunhosa por todo o apoio e incentivo ao longo destes anos.

Ao Professor Doutor José Bioucas (IT/IST) por me ter ajudado a dar os primeiros passos nos “*Inverse Problems*”.

A todos aqueles com quem partilhei o espaço de trabalho.

A todos os investigadores, técnicos e funcionários do ICNAS e IBILI que ao logo destes anos me apoiaram.

E por fim, mas não menos importante, à minha Família.

Resumo

O trabalho de investigação apresentado nesta tese foi dedicado ao estudo e desenvolvimento de métodos de reconstrução de imagem para Tomografia por Emissão de Positrões (PET).

Esta técnica de imagiologia não invasiva permite obter a biodistribuição de radiofármacos emissores de positrões, que após administrados, participam num determinado processo metabólico. Ao longo dos anos, vários desenvolvimentos ao nível da instrumentação e das técnicas de reconstrução e correção de dados permitiram expandir as suas aplicações. Hoje em dia, esta técnica desempenha um papel de relevo em áreas como a oncologia, a neurologia e a cardiologia.

As características das imagens finais dependem, em muito, dos métodos de reconstrução utilizados, os quais podem ser classificados como analíticos ou iterativos. Os últimos permitem modelar de forma precisa os processos físicos, bem como introduzir alguma informação *a priori* sobre a biodistribuição de radiofármacos.

Ao longo do trabalho de investigação foram explorados métodos de reconstrução iterativos baseados em modelação de resolução e em multi-escala. A modelação de resolução (RM) permite, em geral, melhorar a resolução espacial e o contraste da imagem final. Em PET, é usualmente assumido um modelo linear para relacionar os dados adquiridos com a distribuição da actividade. A matriz que permite estabelecer essa relação é denominada matriz do sistema. As técnicas de RM tentam modelar de forma realista esta matriz. Foi desenvolvido e implementado um método de modelação de resolução adaptado à geometria do tomógrafo dedicado ao estudo do cérebro *High Resolution Research Tomograph* (HRRT). Ao contrário dos tomógrafos usualmente utilizados em clínica para estudos de corpo inteiro, a geometria do HRRT não é cilíndrica. O HRRT é composto por 8 cabeças de detector organizadas em octógono. Para esta geometria, os fótons de aniquilação penetram com ângulos de incidência não normais independentemente da posição radial. Estes ângulos levam à degradação da resolução. O modelo de modelação desenvolvido e

implementado depende dos ângulos de incidência. Baseado na reconstrução de uma fonte pontual adquirida em diferentes posições, a modelação de resolução proposta permite melhorar a resolução bem como reduzir a sua variação.

Durante a exploração do conceito de multi-escala aplicado à reconstrução, foi desenvolvido um algoritmo, Multiscale/Multiframe (MS/MF), que poderá ser utilizado para gerar imagens em tempo quase real na escala mais adequada à estatística dos dados existentes. Usualmente, a reconstrução dos dados é feita sempre na mesma escala. No método MS/MF a reconstrução começa durante a aquisição e numa escala mais grosseira. Todos os eventos adquiridos até um determinado instante t_1 são processados nessa escala. O resultado dessa reconstrução, após ter sido redimensionado, é utilizado como condição inicial para o processamento numa escala mais fina, onde todos os eventos desde o início da aquisição até um dado instante t_2 , posterior a t_1 , ($t_2 > t_1$), são utilizados. Este processo é repetido até se chegar à escala mais fina de todas, escala onde a imagem é reconstruída com o tamanho de voxel usual. Este método de reconstrução, quando combinado com computação de alto desempenho, pode permitir a optimização dos parâmetros de aquisição durante a execução do exame.

O método MS/MF introduz novas variáveis na reconstrução, nomeadamente a escolha do método de interpolação, o número de iterações a realizar numa dada escala e o número de conjuntos de dados acumulados. Foram realizados vários estudos de forma a optimizar estes parâmetros. A escolha do número de conjuntos de dados acumulados deve ter em conta a especificidade do estudo e o tomógrafo utilizado. Foi testado e generalizado um método estatístico que permite seleccionar, de forma automática, o número de iterações a realizar numa dada escala.

Diversos estudos foram feitos de forma a caracterizar as imagens finais reconstruídas com o método MS/MF. Os resultados mostram que este método permite acelerar a convergência especialmente em zonas de pouca actividade.

O método proposto poderá ser utilizado na reconstrução de dados de tomógrafos com alta sensibilidade e alta resolução, em sistemas adaptativos de detecção de lesões e em radioterapia.

Abstract

Positron Emission Tomography (PET) is a nuclear medicine imaging technique that provides three-dimensional functional images of the human body. It is a quantitative technique that allows to measure the radiotracer's concentration and to estimate physiological parameters. This thesis is devoted to PET reconstruction methods that allow improving the resolution of the final images as well as exploring the concept of multiple scales in PET image reconstruction.

A resolution modelling reconstructing technique adapted to the High Resolution Research Tomograph was developed, implemented and tested. The proposed reconstruction approach allows to incorporate the effects of the inter-crystal penetration into the reconstruction process. The proposed blurring kernel model has into account the angle of incidence formed by the intersection of the line of response (LOR) with the detector head. A spatial variant asymmetric Gaussian function was used to model this blurring effect. Based on the reconstruction results of point source data acquired in multiple positions, the proposed reconstruction allows for the improvement of the resolution and also for the reduction of its variation.

During the exploration of the concept of multiple scales in PET reconstruction, a novel reconstruction algorithm, the Multiscale/Multiframe algorithm, was developed. This reconstruction algorithm introduces the concept of accumulated time frame in multiscale reconstruction. The Multiscale/Multiframe algorithm can be used to generate near real-time images in the scale that is the most suitable to the data statistics available at a given frame. Different datasets were used to characterize this reconstruction method. The use of a better initial condition for the finest scale improves the convergence speed (compared with the uniform image), in particular for regions of lower tracer uptake, allowing a reduction of the overall reconstruction time. A Morozov discrepancy principle for Poisson data was proposed to adaptively select the number of iterations to perform at a given scale.

Abbreviations

3DRP	3D Reprojection Algorithm
APD	Avalanche Photodiodes
ART	Algebraic Reconstruction Technique
CV	Cross Validation
CT	Computer Tomography
DRF	Detector Response Function
DOI	Depth Of Interaction
FBP	Filtered Backprojection
FDG	2-[18F]Fluoro-2-deoxy-D-Glucose
FFT	Fast Fourier Transform
FOV	Field Of View
FWHM	Full Width at Half Maximum
FWTM	Full Width at Ten Maximum
HPC	High Performance Computing
HRRT	High Resolution Research Tomograph
ICD	Grid Iterative Coordinate Descent
IRM	Image Resolution Modelling
ISRA	Image Space Reconstruction Algorithm
LHS	Left-Hand Side
LOR	Line Of Response
LSO	Lutetium Oxyorthosilicate
LYSO	Lutetium Yttrium Orthosilicate
MISRE	Minimum Image Space Reconstruction Error
ML-EM	Maximum-Likelihood Expectation-Maximization
MRI	Magnetic Resonance Imaging
MS	Multiscale
MS/MF	MultiScale/MultiFrame
OSEM	Order Subsets Expectation Maximum

PET	Positron Emission Tomography
PMT	Photomultiplier Tubes
PSF	Point Spread Function
PVE	Partial Volume Effect
RAMLA	Row-Action Maximum Likelihood
RHS	Right-Hand Side
RM	Resolution Modelling
SRM	Sinogram Resolution Modelling
SNR	Signal to Noise Ratio
TOF	Time-Of-Flight
WDF-Morozov	Weighted Discrete Fourier Morozov

Introduction

Positron emission tomography (PET) is a widespread imaging technique that allows to measure the distribution of the radiotracer administered to a subject. Several improvements related to the resolution and sensitivity of the scanners allowed to expand the applications of the Positron Emission Tomography. This technique plays a key role in oncology, neurology, cardiology, preclinical imaging and in drug design and development.

The characteristics of the final PET images are very dependent on the reconstruction methods used. These methods can be classified as analytic or iterative. Iterative reconstruction methods allow incorporating an accurate model of the physical processes and also *a priori* information about the activity distribution.

The main motivation of this thesis was the development of image reconstruction techniques that allow for the improvement of the resolution of the final images as well as the convergence, while reducing computation time. Resolution modelling reconstruction techniques can be used to improve the resolution of the final reconstruction image. These techniques, in general, allow for the improvement of the spatial resolution and the contrast as well for the reduction of the image noise. The concept of multiscale in PET image reconstruction was also explored in this thesis. Based on this concept a new reconstruction technique was developed and characterized.

Chapter 1 introduces some basic aspects of PET. Chapter 2 presents an overview of the different image reconstruction techniques used in PET. Chapter 3 presents the resolution modelling technique developed for the High Resolution Research Tomograph (HRRT), a dedicated human brain scanner with high resolution. Chapter 4 is devoted to the multiscale reconstruction technique. The characterization and optimization of a multiscale reconstruction algorithm was made using simulated data. Chapter 5 introduces and characterizes the Multiscale/Multiframe reconstruction approach. Chapter 6 presents the work done in the development of a statistical stopping criterion for the MS/MF reconstruction algorithm. The performance of this criterion was assessed using simulation data. This algorithm can be applied to other

fields such as microscopy or astronomy. Finally, a general conclusion are presented in Chapter 7.

Chapter 1

1 Introduction to Positron Emission Tomography

1.1 Positron Emission Tomography

Positron Emission Tomography (PET) is a nuclear medicine imaging technique that provides three-dimensional functional images of the human body. It's a quantitative technique that allows to measure the radiotracer's concentration and to estimate physiological parameters. A tracer is a molecule that carries an unstable isotope [Nuyts, 2012]. A specific tracer is chosen according to the clinical study. After being administered, this molecule will participate in a particular metabolic process. During the decay process of an unstable isotope a pair of annihilation photons is emitted in opposite directions. The amount of tracer must always be small in order to not interfere with the process being studied [Nuyts, 2012]. The most used tracer in clinical PET is Fluorodeoxyglucose (FDG), a glucose analog. In oncology this technique is used to detect tumours and metastases as well as in treatment planning and for measuring the response to therapy. In neurology, for example, it has been used in the study of dementia. In preclinical imaging it can be used in drug discovery and in the development of new tracers. Usually in clinical applications it's combined with other modalities such as Computer Tomography (CT) or Magnetic Resonance Imaging (MRI).

The first PET scanner dedicated to phantom studies was built by Ter-Pogossian in 1970s. In 1974 M. Phelps and Ed Hoffman developed a scanner, named

PET III, for human studies. The first published images of human PET reconstructed with the Filtered Backprojection algorithm (FBP) were acquired with this scanner. The ECAT II (Emission computed Axial Tomograph), developed in 1976 in collaboration with M. Phelps and Ed Hoffman, was the first commercial PET scanner.

Several advances done over the years have contributed to the widespread use of this technique, such as [Cherry, 2006] whole body acquisition, 3D mode of acquisition, iterative reconstruction, preclinical systems, Time Of Flight (TOF) and multimodality.

Nowadays the whole body PET imaging plays a key role in oncology medical imaging [Cherry, 2006]. Cancer staging and monitoring the response of the therapy are two application examples.

The 3D acquisition mode allows for the improvement of the sensitivity of the scanner [Cherry et al., 2006]. With the increase of the counts rate, the duration of the exams or the dose injected into the patient can be reduced. The main drawback of the use of this acquisition mode is the increase of the scatter fraction and the increase of the number of random coincidences. However, the development in the detectors and in the data correction techniques allow for the minimization of these effects. Nowadays, the 3D acquisition mode is the standard acquisition mode.

Dedicated small-animal PET scanners have helped position PET as a key translation tool in the field of molecular imaging [Cherry, 2006]. Preclinical advances are more likely to translate into the clinic because PET is already a clinical standard [Levin et Zaidi, 2007].

Time of flight PET scanners use the time of flight difference to improve the estimation of the annihilation position [Conti, 2009]. In the 1980s TOF PET scanners were built but their performance was poor. The crystals available with an adequate time resolution had a poor stopping power and so the sensitivity of these scanners was very low. In the last decade new crystals with higher stopping power and better time resolution have been found. Nowadays TOF PET scanners are used in clinical environment. The TOF information allows to improve the signal-to-noise ratio [Conti, 2009]. In oncology TOF PET allows improvements in lesion detection especially for lesions with low contrast [Fakhri et al., 2011].

In the past, analytical reconstruction methods were used to process the PET data. With the advances in high performance computing (HPC), the iterative

reconstruction methods began to be used in the clinical environment. These reconstruction methods allow a better modelling of the physics and of the detector characteristics. The reconstructed images exhibit improvements in the trade-off between the signal-to-noise and the spatial resolution and also a reduction of the streak artefacts that are characteristics of analytical image reconstruction methods such as FBP [Defrise et al., 2005].

In the late '90s, D. Townsend and R. Nutt proposed the combination of the PET scanner with the CT scanner in a tandem configuration. The functional information (PET image) is combined with the anatomical information (CT image) which led to a paradigm shift in the practice of clinical PET [Cherry, 2006]. It was considered by the TIME's magazine the invention of 2000. The PET/CT scanners are widely used in clinical. The CT image can also be used to correct the PET data (attenuation correction and estimation of scatter events).

Recently, a simultaneous whole body PET/MRI scanner was introduced in the market [Drzezga et al., 2011]. The PET/MRI advantages over PET/CT are related with the excellent soft-tissue contrast of MRI, reducing the overall radiation dose to the subject by replacing CT with MRI and the multifunction image options that MRI offers [Cherry, 2006] [Catana et al., 2008].

1.2 Stages of a PET Exam

PET is a multidisciplinary field in the sense that different competencies are needed at the different states of the PET exam (see Figure 1.1). The process begins with the production of the radionuclide using a cyclotron. Then, the synthesis of tracer molecules that will be administered into the patient is made. Some studies require an uptake time. Next, the data are acquired, processed and is done the analysis and the exploration of the results. The image reconstruction is done during the processing step. The projections (the raw data) are used to recover the image of the activity distribution. These images will be used in the following step (analysis and the exploration step).

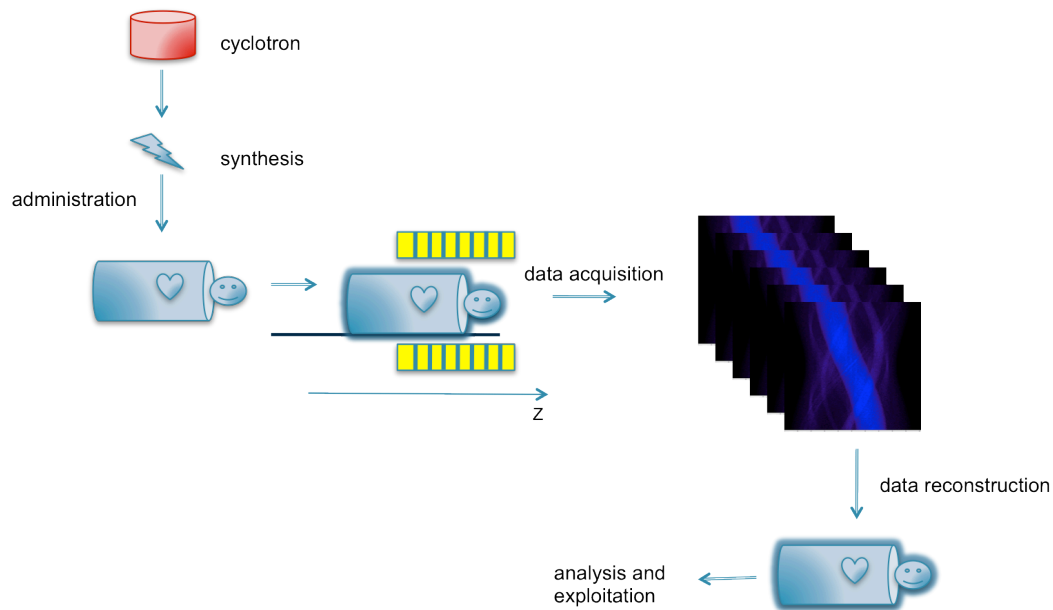


Figure 1.1- Schematic representation of the different stages of a PET exam.

Different radionuclides (unstable isotopes) can be used in PET studies. The most common radionuclides as well as its main characteristics are presented in Table 1.1. The radionuclide will be used in the synthesis of the tracer, a particular molecule carrying the radionuclides. After administration, this molecule will participate in a particular metabolic process. The Fluorodeoxyglucose (FDG), a glucose analog, is the most used tracer in clinical PET.

Table 1.1- List of radionuclides used in PET imaging. The E_{\max} corresponds to the maximum kinetic energy of the emitted positrons. Adapted from [Cherry et al., 2006].

Radionuclide	Half-life	E_{\max} (Mev)
^{11}C	20.4 min	0.96
^{13}N	9.97 min	1.20
^{15}O	122 s	1.73
^{18}F	109.8 min	0.63
^{22}Na	2.60 years	0.55

1.3 Positron Emission and Annihilation

In positron emission (β^+ decay) a proton is transformed into a neutron and a positron [Nuyts, 2012]:



where p^+ is the proton, n the neutron, ν the neutrino, E_k the kinetic energy and e^+ the positron. The kinetic energy will be shared between the daughter nucleus, the positron, and the neutrino. The positron follows a tortuous path due to multiple direction-changing interactions with the atomic electrons of the tissue. Once almost in rest, it will annihilate with an electron. The distance from the emission site to the place where the annihilation occurs is named positron range [Cherry et al., 2006]. The positron range depends on the maximum kinetic energy of the emitted positrons, i.e., depends on the radionuclide. This effect leads to errors in the determination of the line along which an emission took place (see Figure 1.2). If not corrected, this effect introduces a blurring effect in the reconstructed image.

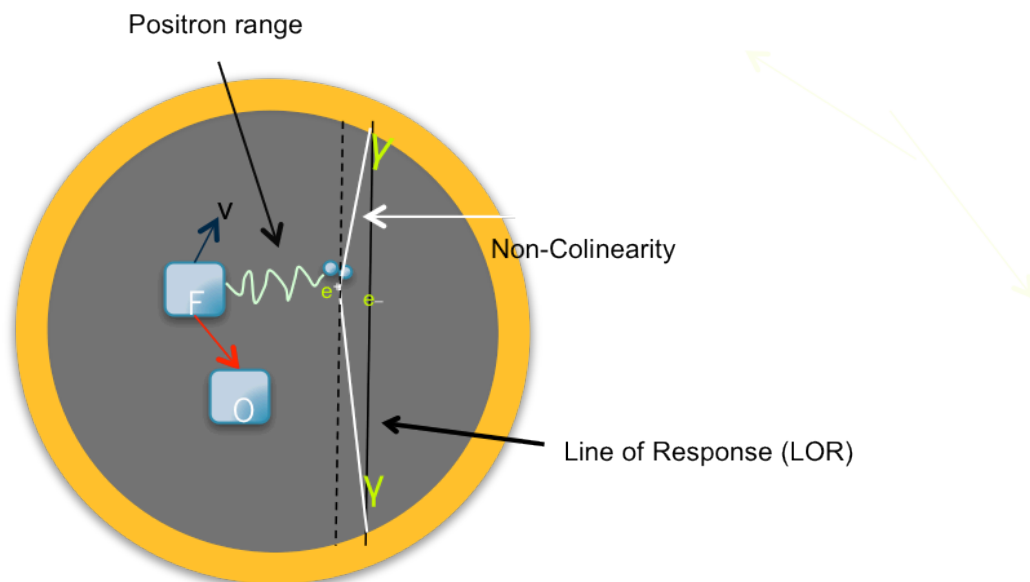


Figure 1.2- Schematic representation of the positron emission and the annihilation process. The positron range and non-collinearity effect are highly exaggerated.

The result of the annihilation process is the emission of two 511 keV photons. If the positron is at rest, due to the conservation of the linear moment and the energy, the photons are emitted 180° apart. In reality, they are emitted with a distribution of angles around $180^\circ \pm 0.5^\circ$ [Cherry et al., 2006]. This effect is known as non-collinearity and it's independent of the radionuclide. The detection of the two annihilation photons within a short timing window allows to define a line where the annihilation occurs (see Figure 1.2). The recovery of the activity distribution will be done using that information.

1.4 Data Acquisition

1.4.1 Photon Detection

A PET scanner is composed of a set of detectors that allows for the detection of the annihilation photons. The line that connects the two detectors hit by the annihilation photons is called Line of Response, LOR (see Figure 1.2).

The most common geometry for whole body scanners is the ring geometry. During the detection process, the energy of the annihilation photons is converted into an electric signal. The detection is usually done using scintillator detectors coupled to photomultiplier tubes.

The scintillator detectors, composed of scintillation crystals, convert the energy of the annihilation photon (~ 511 keV) into visible wavelength photons, producing a visible flash. The interaction of the annihilation photon with matter occurs mainly by Compton and photoelectric interactions [Cherry et al., 2006]. The number of visible photons produced is proportional to the energy deposited by the annihilation photon. The choice of the scintillator should have into account several properties, such as, [Cherry et al., 2006] [Schmitz et al., 2005]: the stopping power, the decay constant, the energy resolution and the light output. The stopping power is defined as the inverse of the mean distance travelled by the photons before depositing their energy in the crystal [Schmitz et al., 2005]. The scintillator must be dense in order to improve the interaction with the annihilation photons and thus stop a large fraction of the photons. The decay constant is defined as the average time that the electrons remain in the excited state before releasing a scintillation photon [Schmitz et al., 2005]. The decay constants should be small to allow the detection of a large number of events. Good energy resolution allows to discard annihilation photons that have been scattered before being measured. The light output, photon yield per incoming keV, should be as high as possible.

Some scintillators that can be used in PET are the Sodium iodide, the Bismuth Germanate, Lutetium Oxyorthosilicate (LSO) and the Gadolinium Oxyorthosilicate. In the Table 1.2 are presented the proprieties of these scintillators.

The photomultiplier tubes convert the scintillation light into electric current [Cherry et al., 2006]. The incident light photons are converted, by photoelectric effect,

to photo-electrons, that are accelerated and amplified. The charge amplification is done using a series of dynodes each of which is held at a greater voltage with a resistor chain [Cherry et al., 2006]. The output current is proportional to the number of light photons. High gains (amplification) lead to high signal-to-noise pulses. When compared with the scintillation decay time the response time of a PMT is very short (a few ns) [Cherry et al., 2006].

A large detector area composed of small crystals arranged in a two-dimensional matrix (block design) can be used to determinate the localization of the interaction [Nuyts, 2012]. Often, each block (typically composed of 64 crystals) is coupled to four photomultiplier tubes (see Figure 1.3). The position of interaction can be calculated by weighting the signals of the photomultipliers.

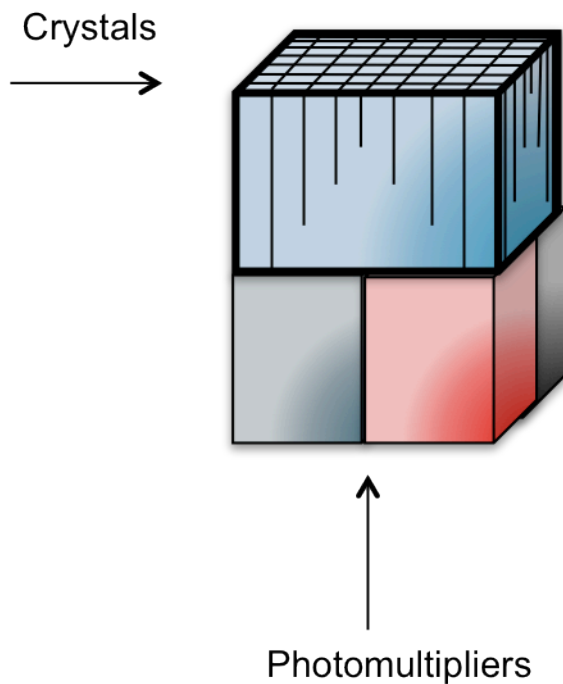


Figure 1.3- Schematic representation of a typical PET block detector.

Other type of detectors can be used to detect the annihilation photons. For example liquid xenon [Lewellen, 2008] can be used to replace the scintillator crystals or avalanche photodiodes can be used as an alternative to the photomultiplier. Due to its insensitivity to magnetic fields, avalanche photodiodes (APD) are suitable to be used in simultaneous PET/RMI scanners [Cherry et al., 2006] [Cherry, 2006] [Catana

et al., 2008]. More recently, other semi-conductor photodetector devices built around a series of APD micro-cells, the silicon photomultiplier (siPM), are under active development [Lewellen, 2008].

CdZnTe detectors [Cherry et al., 2006] or resistive plate chamber (RPC) [Couceiro et al., 2012] are examples of technologies that can replace the entire standard detection system.

Table 1.2- Properties of common scintillator materials used in PET. Adapted from [Cherry et al., 2006].

Scintillator	Density (g/cm ³)	Light output (photons per 511keV)	Decay time (ns)	Linear attenuation at 511 keV (cm ⁻¹)	Ratio between photoelectric and Compton
NaI(Tl)	3.67	19400	230	0.34	0.22
BGO	7.13	4200	300	0.96	0.78
LSO	7.40	~13000	~47	0.88	0.52
GSO	6.71	~4600	~56	0.70	0.35

1.4.2 Detected Events in Positron Emission Tomography

Under ideal conditions the detection of the two annihilation photons by the detection ring should be done roughly at the same time. The annihilation occurs somewhere in the line that connects the two photon-detection points. An event (decay) is detected using a technique referred to as coincidence detection [Cherry et al., 2006]. The two main factors that are responsible for the detection not occurring at the same time are [Cherry et al., 2006] the time resolution of the detection system and the difference in the distance of the annihilation site to each detector. The first factor depends mainly on the decay time and on the light output of the crystal. To avoid the loss of events, the detection of the two photons is assumed to be arising from the same annihilation if the time difference between the detection of the two photons is less than a defined constant.

The detected events can be classified into single, true, random, scatter and multiple [Bailey, 2005] (see Figure 1.4).

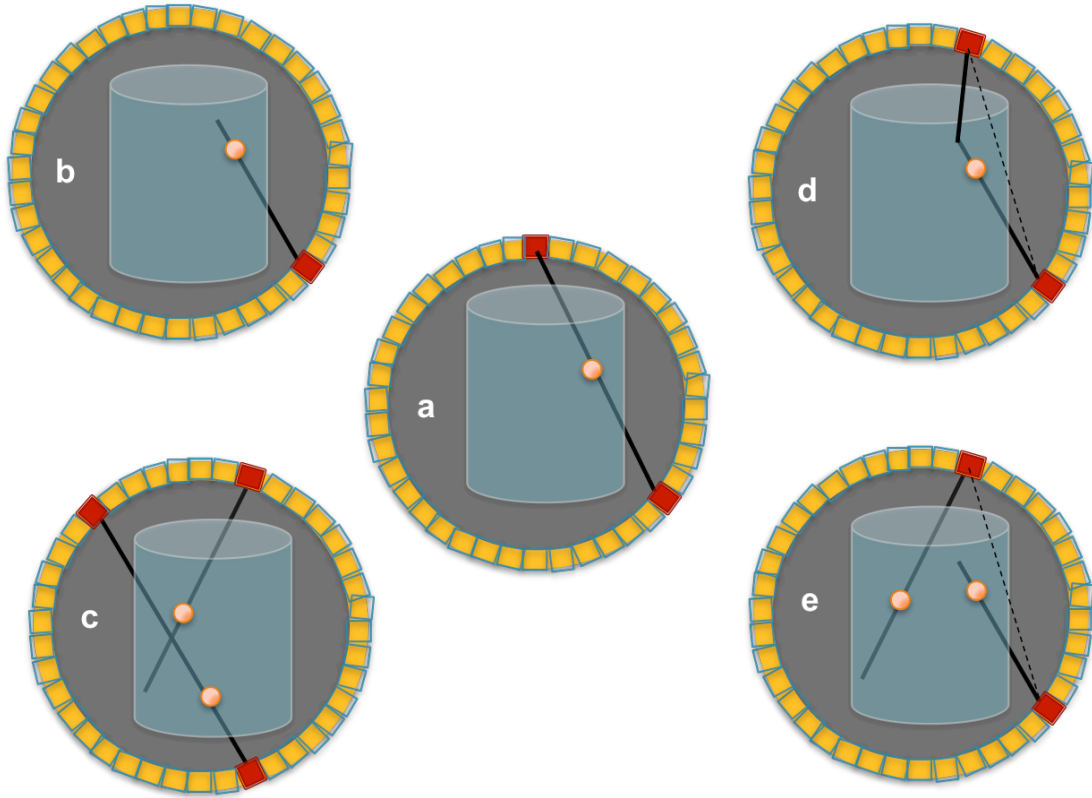


Figure 1.4- Different type of events: trues (a),singles(b),multiple (c), scatter (d) and random(e).

A single event is recorded when only one of the annihilation photon is detected. These events are not coincidences and usually correspond to more than 90% of the photons detected by the scanner [Cherry et al., 2006]. There are several causes that can lead to the not detection of the second photon, such as: attenuation, finite size of the scanner or not being registered by the detector system.

True events correspond to the (ideal) situation where the two annihilation photons are detected within the time window and without interacting significantly with the matter.

Random events are produced by the detection of two unrelated single photons within the same coincidence window. These events introduce wrong spatial information in the raw data. The random events count rate between the detector a and the detector b , R_{ab} , is given by [Bailey, 2005]:

$$R_{ab} = 2\tau N_a N_b \quad (1.2)$$

where N_a and N_b are the single event rate of the detectors a and b , respectively, and 2τ is the coincidence time window width. Assuming that both detectors have similar

single event rates, $N_a \approx N_b$, the random events rate increases approximately proportionally to the square of the single rate of the detectors.

Multiple events are produced when three (or more photons) usually from two annihilations are detected within the same coincidence time window. Usually these events are discarded.

Scatter events are coincidence events where one or both annihilation photons changed direction due to a Compton scatter interaction. The Line of Response (LOR) represented by this type of events is not correlated with the true activity. These events produce a low spatial frequency background and introduce inaccurate quantification in the final image [Cherry et al., 2006] [Bailey, 2005]. The fraction of scattered events depends on the object and on the radioactivity distribution.

1.4.3 Acquisition Modes

Some clinical PET scanners, composed of multiple rings, can operate in two acquisition modes: 2D mode or 3D mode (see Figure 1.5). In the 2D acquisition mode the rings are separated by septa and only events that occur in direct planes (ring difference is 0) or cross planes (ring difference is 1) are acquired. In fully 3D mode, the septa are retracted (or do not exist) and all the possible LORs are recorded, independently of the ring difference.

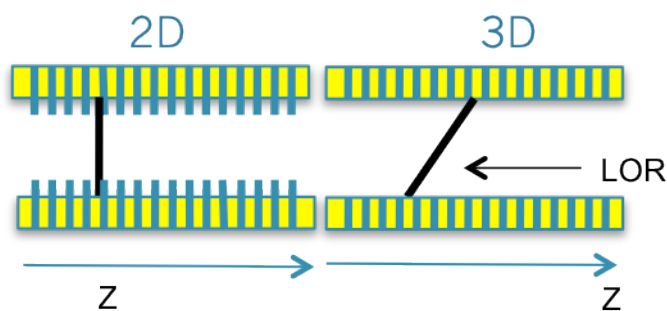


Figure 1.5- Schematic representation of the 2D (left) and the 3D (right) acquisition mode.

For a scanner with N rings operated in the 2D acquisition mode, $2N-1$ coincidence planes (N direct planes and $N-1$ cross planes) can be defined. In the case

of the 3D acquisition mode N^2 coincidence planes can be defined [Cherry et al., 2006].

The spatial resolution of the recovered image is approximately independent of the acquisition mode. The 3D acquisition mode provides a dramatic improvement in sensitivity (a factor of $5\times$ to $7\times$ when compared with 2D acquisition [Cherry et al., 2006]), allowing to reduce the injected dose or the exam duration. However the scatter and random events also increase.

1.4.4 LOR Parameterization and Data Storage

The lines of response in the projections space for cylindrical scanners can be parameterized using four variables: the radial position (s), the azimuthal angle (ϕ), the polar angle (θ) and the axial position (ζ) (see Figure 1.6). In the case of 2D acquisition mode the polar angle is ~ 0 .

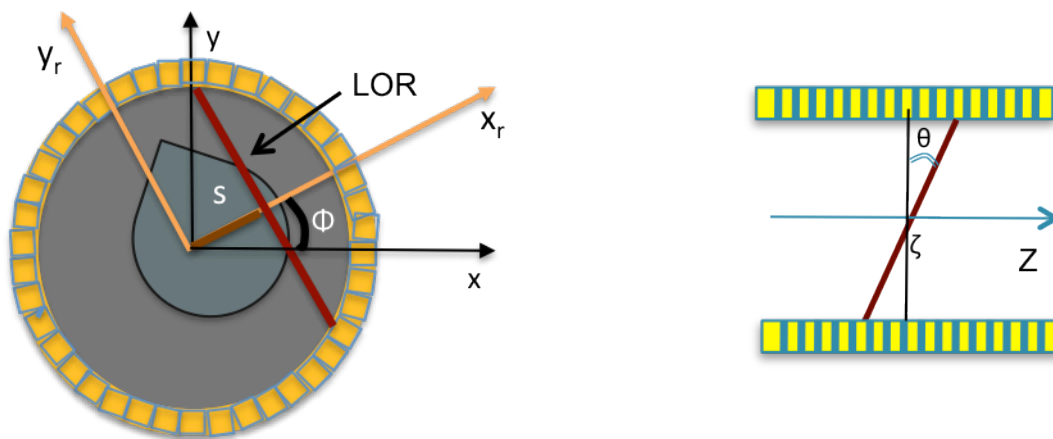


Figure 1.6- Parameterization of a line of response.

Two different methods can be used to store the PET raw data: histogram or list-mode [Defrise et Kinahan, 1998].

In the histogram format the total counts of each LOR are stored into a matrix. Data acquired in 2D mode can be stored into N matrices where the bin value (individual matrix elements) of the row i and column j corresponds to the number of

events occurred in the LOR parameterized with the azimuthal angle and radial position related to the row and column index, respectively. This matrix is known as sinogram. Usually some consideration about the discretization of the parametric variables is made before the image reconstruction, i.e. the sampling of the projection space is optimized. In the case of 3D acquisition the histogram matrices have four dimensions.

In the list-mode data format the event information is stored in a list-type format on an event-by-event basis as the events are detected [Defrise et Kinahan, 1998]. The list-mode format allows preserving the temporal information as well as other additional information, such as, the crystals index and the energy deposited in the detectors. When the ratio between the total bin counts and the number of bins in the sinogram format is less than one, the list-mode format allows to store the data more compactly. It should also be noted that it is possible to convert the data from the list-mode format to sinogram format.

1.5 Data Correction

1.5.1 Normalization Correction

Variations in the detection efficiency between different LORs introduce artefacts in the reconstructed images and do not allow the recover of quantitative information. Different factors contribute for the arise of these variations, such as, the non uniformities in individual detectors efficiencies, geometric and solid angle effects, detector electronics and the summing of adjacent data elements [Meikle et Badawi, 2005]. The normalization correction tries to compensate these variations by weighting each LOR with a multiplicative factor, the normalization coefficient. The estimation of these factors can be done using two main methods: direct measurements or component based methods.

In direct measurement methods, a planar or a rotating linear positron source is used to measure in coincidence the variations between all LORs of the system. A low activity source must be chosen in order to avoid dead time and pile-up effects [Cherry et al., 2006]. Very long scans (several hours) are required in order to obtain adequate counts per LOR.

In component-based normalization methods [Meikle et Badawi, 2005][Casey et al., 1996] [Ferreira et al., 2009][Ollinger, 1995] the coincidence detection efficiencies of a pair of detectors are modelled as a product of factors that can be measured independently. These approaches allow for the reduction of the duration of the acquisitions used for the calculation of the normalization parameters.

1.5.2 Attenuation Correction

The 511 keV annihilation photons will interact with the matter predominantly through Compton interactions [Cherry et al., 2006]. Only a part of the photons will escape from the patient body, i.e., the flux of annihilation photons is attenuated. This effect can be described using the Beer's law [Zeng, 2010]. In PET the reduction of the photon flux is independent of the localization of the annihilation along the LOR.

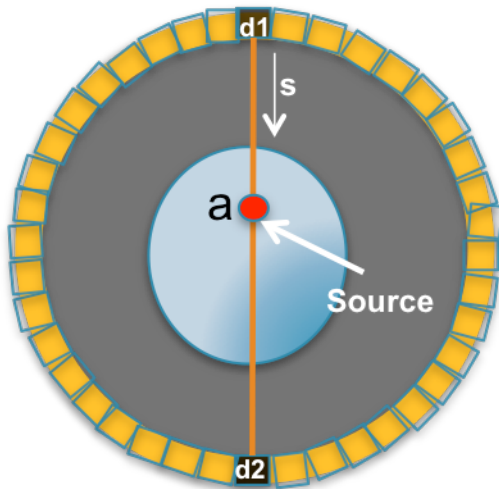


Figure 1.7- The attenuation path of two annihilation photons emitted from a point source inside the object.

The probability that both annihilation photons escape from the object is given by [Nuyts, 2012][Zeng, 2010],

$$e^{-\int_{d1}^a \mu(s)ds} e^{-\int_a^{d2} \mu(s)ds} = e^{-\int_{d1}^{d2} \mu(s)ds} \quad (1.3)$$

where $d1$ and $d2$ are the position of the two detectors hit by the pair of annihilation photons emitted along the s -axes, a the position of the source and $\mu(s)$ the

attenuation coefficient of the object at the point s (see Figure 1.7). If the attenuation coefficients at every point of the object are known, the attenuation correction factors ($a_{d1,d2}$) used to correct the raw data can be easily calculate using

$$a_{d1,d2} = e^{+\int_{d1}^{d2} \mu(s)ds}. \quad (1.4)$$

The estimation of the attenuation coefficients can be done using direct measurements (transmission scan) in coincidence mode, e.g, by placing a rotation positron-emitting source outside the object. First a *black scan* is made where transmission data are acquired without the object. Then the object is placed in the scanner and a second transmission scan is performed. The attenuation correction factors are given by the ratio between the *black scan* sinograms and the transmission scan sinograms [Cherry et al., 2006], i.e., the ratio between the number of counts measured for each LOR in the absence of attenuation and in the presence of the attenuation medium. Usually the sources are made from ^{68}Ge . Although in theory these methods allow a very accurate estimation of the attenuation correction factor, one of the main problems of these techniques is the long acquisition time needed to ensure a good statistics.

Another approach is to do direct measurements (transmission scan) in singles acquisition mode. In this case the attenuation LOR is found using the position of the source and the position of the detector hit by the photon that penetrate into the object. In this attenuation acquisition scheme a more active source can be used which allows for the improvement of the statistical of the transmission scan and/or for the reduction of the acquisition time [Cherry et al., 2006]. The main drawback of this approach is the higher scatter fraction that leads to an under estimation of the attenuation correction [Cherry et al., 2006].

Nowadays most of the clinical PET scanners are coupled with CT scanners (sharing the same patient bed). The CT images can be used to measure the attenuation coefficients. The main problem of this approach is that the CT data must be converted to an estimate of the attenuation factors at 511 keV. The x-ray photons used in clinical CT usually yield a continuous energy spectrum between 30 to 120 keV. For water and soft tissues the mass attenuation coefficient (linear attenuation coefficient divided by density) at the energies of PET and CT are similar. Based on this fact, Kinahan *et al.*

[Kinahan et al., 1998] proposed a bilinear scaling method where the attenuation coefficients are estimated by using separate scaling factors for bone and non-bone components [Townsend et Beyer, 2005]. The segmentation between bone and non-bone is done based on the CT image. When compared with the direct measures methods, attenuation correction based on CT data allows to estimate the coefficients faster and with less statistical noise. This technique has some limitations such as the truncation of the CT FOV or the effects of CT contrast agents [Townsend et Beyer, 2005].

1.5.3 Scatter Correction

Annihilation photons that undergo a Compton interaction change direction and lose part of the energy. At 511 keV, 50% of all Compton interactions produce photons with a scattering angle of 60° or less [Cherry et al., 2006]. If the detector energy resolution were excellent and all the energy of the photon is deposited in the detector, the detection of annihilation photons would be easy and energy discrimination would allow to distinguish between scattered and unscattered events. However the energy resolution of the detectors is not so good and only a part of the photon's energy is deposited in the detector. Scattered events may significantly degrade the quantitative accuracy and reduce the image contrast [Meikle et Badawi, 2005]. Three main types of approaches were proposed to perform the estimation of scattered events [Cherry et al., 2006]: analytic approach [Bowen et al., 1994][Cherry et Huan, 1995], methods based on energy windows [Ferreira et al., 2000][Adam et al., 2000][Shao et al., 1994] and simulation methods [Watson, 2000] [Levin et al., 1995].

The most accurate scatter correction methods are based on the simulation methods. The simulation of the estimated scatter can be done based on a model [Watson, 2000] or using Monte Carlo [Levin et al., 1995] [Qi et Huesman, 2002] methods. These estimation approaches require the calculation of the map of the attenuation coefficients and an initial estimate of the scatter-free radioactivity distribution.

The implementation of the scatter correction methods based on simulation can be divided into five main steps [Meikle et Badawi, 2005]:

1. Calculation of the map of linear attenuation coefficients (attenuation map). When direct measurements were used for the attenuation correction, the attenuation map is estimated using the 2D reconstructions of the blank and transmission sinograms.
2. Reconstruction of an initial estimate of the emission volume. In literature different approaches were proposed for this task [Watson, 2000] [Ollinger, 1996] [Holdsworth et al., 2001].
3. Estimation of the scatter contribution to the projections.
4. Scaling of the scatter estimate. For regions where only scatter is present, i.e., regions not occupied by the object, the scatter distribution is scaled globally to ensure a good fit between the estimated scatter and the measured data.
5. Correction of the 3D emission projections for scatter. The estimated scatter is subtracted from the measured data.

1.5.4 Correction for Random Coincidences

Due to the finite width of the coincidence time window, two non-related events may be interpreted as a coincidence event (random coincidences). The methods of correction of random events estimate the number of random events present at each LOR, which is subtracted to the prompt data (true+randoms+scatter). Two main approaches can be used to correct the random coincidences [Cherry et al., 2006].

In the first method the estimation of the random count rate is done based on equation (1.2). It has into account the singles counting rate for each detector pair and the coincidence time window width. This method tends to overestimate the amount of random coincidences and the time width must be known with good accuracy for each detector.

The second approach, the delayed coincidence window method, is the most usual method to correct the random events. In this technique an additional coincidence circuit is used with the same duration of the time window but where the events recorded by one of the detectors are delayed by a sufficiently long time in order to ensure the no detection of true or scatter events. The number of counts in the delayed window has the same expectation value as the random events recorded by the coincidence circuit with the normal window. The subtraction of the estimated random

events is done on-line. This technique allows removing the bias but the variance on the corrected data increases. The estimate of the random coincidences is noisy, leading to the increase of noise in the corrected data.

The simplest way to reduce the variance in the estimate of the random coincidences is to acquire the delayed coincidences separately and then smooth the data [Brasse et al., 2005]. Analytic [Defrise et al., 1991] and iterative techniques [Panin et al., 2007] [Byars et al., 2005] using the delays coincidence sinograms were also proposed to reduce the variance.

1.6 Characterization of PET Scanners

For comparing the performance of different clinical PET scanners, the National Electrical Manufacturers Association proposed in 1994 a set of guidelines [NEMA, 1994]. In 2001, a new standard more suitable for whole body PET imaging was published [NEMA, 2001].

In the design of PET scanners several factors should be taken into account to maximize the performance of the scanner. Two of them are the spatial resolution and the sensitivity of the system.

1.6.1 Spatial Resolution

The spatial resolution in PET depends on several factors, such as the positron range, the non-collinearity of annihilating photons, the angle of incidence of the LOR with the detector and the depth of interaction of the photon in the detector, the size and geometry of the detector, acquisition parameters and the reconstruction method.

The resolution attainable by PET is limited by the positron range. This effect depends on the radionuclide and the surround medium. Based on simulated data, Sánchez-Crespo *et al.* [Sánchez-Crespo et al., 2004] studied the positron annihilation distribution for different positrons (^{11}C , ^{13}N , ^{15}O , ^{18}F , ^{68}Ga and ^{82}Rb) in various human tissues (human compact bone, adipose tissue, soft tissue and lung tissue). They concluded that for high resolution PET (1-2 mm) the positron range will be a limiting factor in lung tissue regardless of the choice of the radionuclide. Kemerink *et al.* [Kemerink et al., 2011] investigated the effect of positron range on the visualization and quantification with different radiotracers (^{18}F , ^{68}Ga and ^{124}I) on lung-like tissue.

They concluded that lung lesions will be visualized similarly, and at least as sharp as in soft tissue [Kemerink et al., 2011]. For a complete activity recovery the ^{68}Ga and ^{124}I images need large volumes of interest. [Kemerink et al., 2011]. The positron range of radionuclides, speciality for radionuclides with high E_{max} (see Table 1.1), can be reduced by using strong magnetic fields [Wirrwar et al., 1997].

The non-collinearity between the annihilation photons (see Figure 1.2) also leads to resolution degradation. Assuming a Gaussian distribution and small angles of incidence, the blurring effect due to the non-collinearity depends linearly on the diameter of the PET scanner [Cherry et al., 2006][Rahmim et al., 2008].

$$FWHM = 0.5 \frac{\pi}{180} \frac{L}{4} = 0.0022L, \quad (1.5)$$

where L is the separation of the detectors in coincidence.

Another factor of degradation of the image is the inter-crystal scatter and penetration (see Figure 1.8).

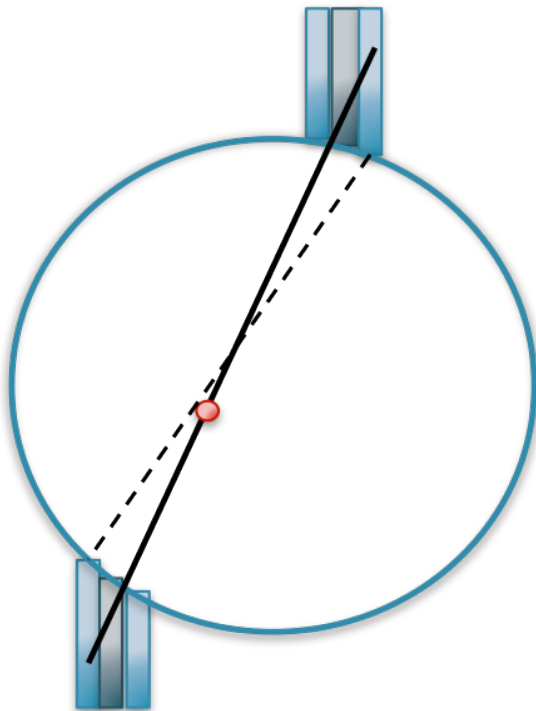


Figure 1.8- Representation of the inter-crystal penetration. The dash line represents the LOR assigned and the continuous line to the real LOR.

Due to the inter-crystal penetration for cylindrical scanners, the spatial resolution depends on the radial distance. Off-centre events can penetrate with non-normal angles of incidence and be assigned to inaccurate LORs (see Figure 1.8) [Cherry et al., 2006]. Some scanners are able to estimate the depth in which each photon interacts within the crystal, Depth of Interaction (DOI), and so they can mitigate this effect.

1.6.2 Sensitivity

The system sensitivity is defined as the number of events detected per unit of radioactive concentration in a specific phantom [Cherry et al., 2006]. The design of a PET scanner should try to maximize the sensitivity. The duration of the exam and/or the dose injected depend on this factor. High sensitivity scanners allow for the detection of more events for a fixed scan duration and for a fixed activity which lead to the improvement of the quality of the reconstructed image. The sensitivity of the system is mainly determined by the efficiency of the detector at 511keV, the scanner geometry, the localization of the source relative to the detectors, the energy window used and the detector dead time [Cherry et al., 2006][Bailey, 2005]. The 3D acquisition mode allows for the improvement of the sensibility by a factor of $5\times$ to $7\times$ when compared with 2D acquisition [Cherry et al., 2006].

Chapter 2

2 Image Reconstruction in PET

Different methods were proposed to recover the image of the distribution of the radiotracer activity from the coincidence measures. Usually they are classified as analytical or iterative. The analytic methods allow a faster reconstruction as well as an easier control of the resolution and noise correlations [Defrise et Kinahan, 1998]. The iterative methods allow for the incorporation of an accurate model of the physical processes and also *a priori* information about the activity distribution.

We begin by introducing some fundamental mathematical concepts used in tomography. We then present an overview of the most popular reconstruction algorithms.

2.1 Analytic Methods

2.1.1 The 2D Radon Transform

The Radon transform, introduced by the Johann Radon in 1917, allows to relate the object with the collection of all line-integrals parallel to a given projection direction [Bertero et al., 1998] [Zeng, 2010],

$$\mathbf{p}_\phi(s) = \int_{-\infty}^{+\infty} \mathbf{f}(s \cos\phi - l \sin\phi, s \sin\phi + l \cos\phi) dl \quad (2.1)$$

where $\mathbf{p}_\phi(s)$ is the projection of the LOR l with the azimuthal angle ϕ and the radial distance s (see Figure 2.1) and \mathbf{f} a density function in the x - y plane. The radial distance is related with x and y (see Figure 2.1) by $s = x \cos \phi + y \sin \phi$ [Bertero et al., 1998].

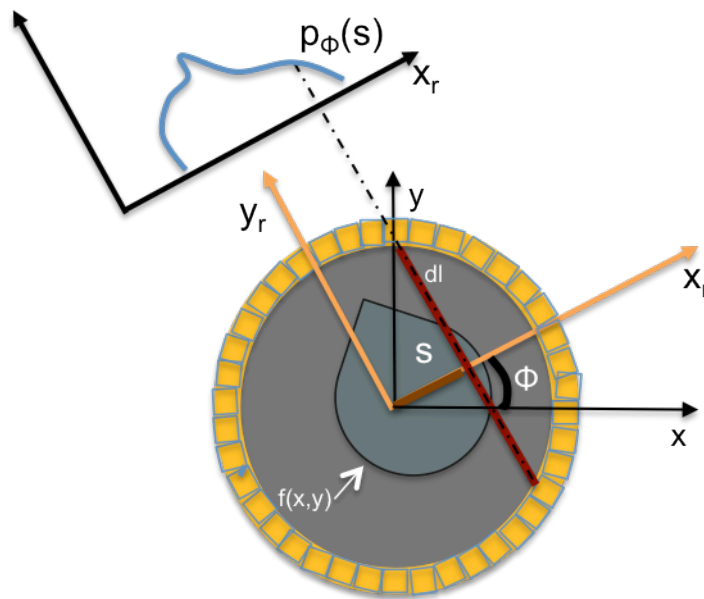


Figure 2.1- One dimensional projection of a 2D object as the collection of all parallel line-integrals for an angle ϕ relative to the scanner. The x and y are the coordinate axes related to the scanner. The y_r and x_r are the coordinate axes related to the lines of response (LOR). Adapted from [Defrise et Kinahan, 1998].

An equivalent equation is given by [Deans, 1983] [Zeng, 2010]:

$$\mathbf{p}_\phi(s) = \iint_{-\infty}^{+\infty} \mathbf{f}(x, y) \delta(x \cos\phi + y \sin\phi - s) dx dy \quad (2.2)$$

where δ is the Dirac delta function.

2.1.2 2D Central-Section Theorem

The central-section theorem allows to relate the Fourier transform of the measured projection data with the Fourier transform of the activity distribution.

Let us consider the 1D Fourier transform of $\mathbf{p}_\phi(s)$ with the direction of the radial offset, $F_1\{\mathbf{p}_\phi\}(v_{x_r})$ [Defrise et Kinahan, 1998] [Zeng, 2010]:

$$\begin{aligned} F_1\{\mathbf{p}_\phi\}(v_{x_r}) &= \int_{-\infty}^{+\infty} \mathbf{p}_\phi(s) e^{-2i\pi s v_{x_r}} ds \\ &= \iiint_{-\infty}^{+\infty} \mathbf{f}(x, y) \delta(x \cos\phi + y \sin\phi - s) e^{-2i\pi s v_{x_r}} dx dy ds \end{aligned} \quad (2.3)$$

The central section theorem can be derived by expanding the right hand side of (2.3) having into account the properties of the Dirac delta function [Defrise et Kinahan, 1998] [Zeng, 2010],

$$\begin{aligned} F_1\{\mathbf{p}_\phi\}(v_{x_r}) &= \int_{-\infty}^{+\infty} \mathbf{p}_\phi(s) e^{-2i\pi s v_{x_r}} ds \\ &= \int_{-\infty}^{+\infty} \int_{-\infty}^{+\infty} \mathbf{f}(x, y) e^{-2i\pi(x \cos\phi + y \sin\phi)v_{x_r}} dx dy \\ &= F_2\{\mathbf{f}\}(v_{x_r} \cos\phi, v_{x_r} \sin\phi) \\ &= F_2\{\mathbf{f}\}(v_x, v_y) \end{aligned} \quad (2.4)$$

where $F_2\{\mathbf{f}\}$ is the 2D Fourier transform of \mathbf{f} with respect to the two variable, $v_x = v_{x_r} \cos\phi$ and $v_y = v_{y_r} \sin\phi$.

Equation (2.4) states that the 1D Fourier transform of a projection at an angle ϕ is equivalent to the values along a line through the origin (for the same angle) of the 2D Fourier transform of the activity distribution (see Figure 2.2).

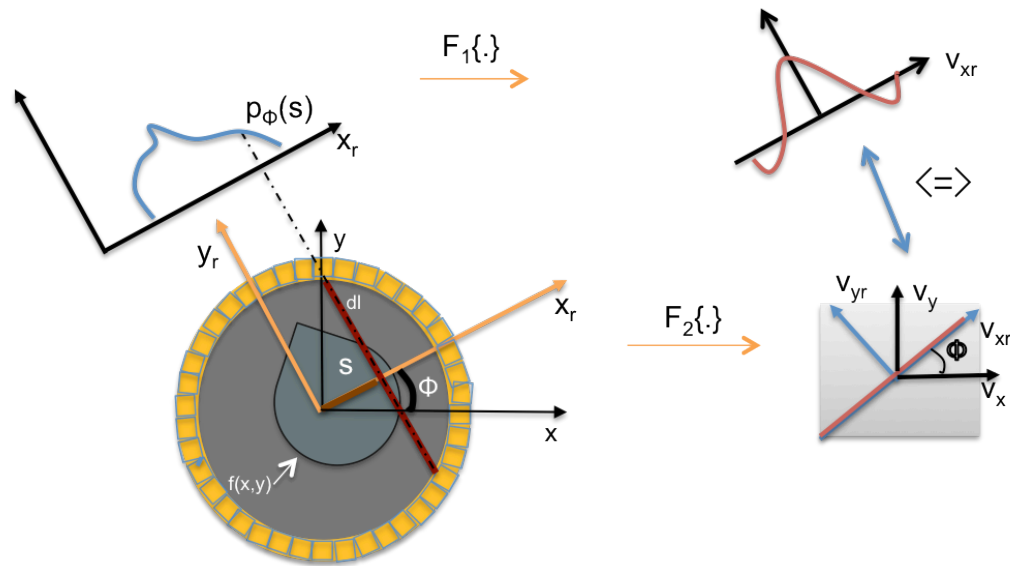


Figure 2.2- Illustration of the 2D central-section theorem. Adapted from [Defrise et Kinahan, 1998].

This theorem establishes that if $p_\phi(s)$ is known for all the $|s| \leq R$ and all the $\phi: 0 \leq \phi < \pi$ the density function, $f(x,y)$, can be recovered. One possible reconstruction algorithm is to calculate the $F_1\{p_\phi\}(v_{x_r})$ for all $\phi: 0 \leq \phi < \pi$, organize these profiles as a 2D array representing the $F_2\{f\}$ and then the estimated $f(x,y)$ is calculated by taking the inverse 2D Fourier transform,

$$f(x, y) = \int_{-\infty}^{+\infty} \int_{-\infty}^{+\infty} F_2\{f\}(v_x, v_y) e^{i2\pi(v_x x + v_y y)} dv_x dv_y . \quad (2.5)$$

A practical problem arises from the use of the central theorem to perform the reconstruction. Most of the implementations of discrete Fourier transform are based on Fast Fourier Transform (FFT) algorithms that assume that the data are represented in the Cartesian coordinate system. On the other hand, the Fourier transform of the data, $F_1\{p_\phi\}(v_{x_r})$, is sampled along radial lines in polar coordinates, and so it must be interpolated to a regular grid, prior to the inverse 2D Fourier transform. Interpolation accuracy is very important to guarantee good reconstruction results [Matej et Bajla, 1990] [Choi, 1998].

As can be seen in Figure 2.3, the sampling of the Fourier space is not uniform. The over-weighting of the low frequency components blurs the image. This non-uniformity on the sampling of the Fourier space is proportional to the $\frac{1}{\sqrt{v_x^2 + v_y^2}}$ [Defrise

et Kinahan, 1998][Zeng, 2010].

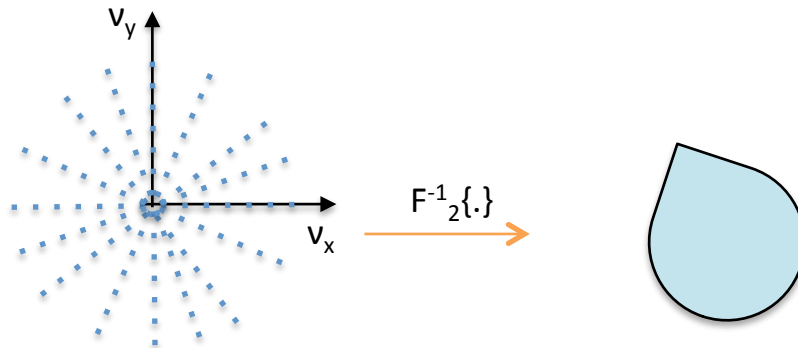


Figure 2.3- 2D image reconstruction based on the central slice theorem.

2.1.3 2D Filtered-Backprojection

The Filtered Backprojection (FBP) is a fast reconstruction algorithm that compensates the non uniformity of the sampling in the Fourier space (see Figure 2.3) by multiplying the 1D Fourier transform of the data, $F_1\{\mathbf{p}_\phi\}(v_{x_r})$, by a ramp-filter.

The backprojection operator, the adjoint operator of the forward projection, can be described by [Defrise et Kinahan, 1998]:

$$\mathbf{b}(x, y) = \int_0^\pi \mathbf{p}_\phi d\phi . \quad (2.6)$$

For 2D PET, the backprojection operation can be considered the output of a linear shift-invariant imaging process [Defrise et Kinahan, 1998],

$$\mathbf{b}(x, y) = \mathbf{f}(x, y) ** \mathbf{h}(x, y) \quad (2.7)$$

where $\mathbf{h}(x, y)$ is the 2D shift-invariant point spread function (PSF) and $**$ denotes the 2D convolution operator.

The 2D Fourier transform of $\mathbf{b}(x, y)$ is equal to the weighted version of the 2D Fourier transform of the $\mathbf{f}(x, y)$ as expressed by [Defrise et Kinahan, 1998]:

$$\mathbf{B}(x, y) = F_2\{\mathbf{b}(x, y)\} = F_2\{\mathbf{f}(x, y)\} \frac{1}{\|\mathbf{v}\|}$$

$$\text{with } \|v\| = \sqrt{v_x^2 + v_y^2}. \quad (2.8)$$

The backprojection image corresponds to a blurred version of $f(x,y)$.

The FBP algorithm can be written as [Defrise et Kinahan, 1998]:

$$\int_0^{2\pi} \left[\int_{-\infty}^{+\infty} |v_{x_r}| F_1\{\mathbf{p}_\phi\}(v_{x_r}) e^{i2\pi v_{x_r} s} dv_{x_r} d\phi \right]. \quad (2.9)$$

The ramp filter, $|v_{x_r}|$, gives more weight to the high-spatial frequencies than the low frequencies, reversing the effects of the blurring. In the presence of noise, i.e. in practice, an apodizing filter is used to remove any contributions from frequencies above a pre-determined cut-off frequency. Some of the most common filters are the Hann, Shepp–Logan and Hamming filters [Cherry et al., 2006].

The implementation of the FBP algorithm can be given using the following steps [Defrise et Kinahan, 1998]:

1. Fourier transform of the projection $\mathbf{P}_\phi(v_{x_r}) = F_1\{\mathbf{p}_\phi\}(v_{x_r})$ for a given ϕ .
2. Filter the projection in frequency space $\mathbf{P}_\phi^{Filter}(v_{x_r}) = |v_{x_r}| \mathbf{P}_\phi(v_{x_r})$.
3. Inverse Fourier transform of the filtered projection $\mathbf{p}_\phi^{Filter}(v_{x_r}) = F_1^{-1}\{\mathbf{P}_\phi^{Filter}(v_{x_r})\}$.
4. Backproject the filtered projection $\mathbf{B}\{\mathbf{p}_\phi^{Filter}(v_{x_r})\}$.
5. Repeat steps 1-4 for each $\phi: 0 < \phi < \pi$

2.2 Iterative Methods

The image of the distribution of the radiotracer activity can be recover from the coincidence measures using iterative methods. These reconstruction methods allow incorporating a more accurate modelling of the physical processes and also *a priori* information about the activity distribution. A simplified flowchart of an iterative reconstruction is presented in Figure 2.4. First, the estimated image is mapped to the projection space. Then the estimated projection is compared with the acquired projection having into account a given criterion. If the criterion is satisfied,

the reconstruction stops. If the criterion is not satisfied, the estimated image is updated and the process is repeated.

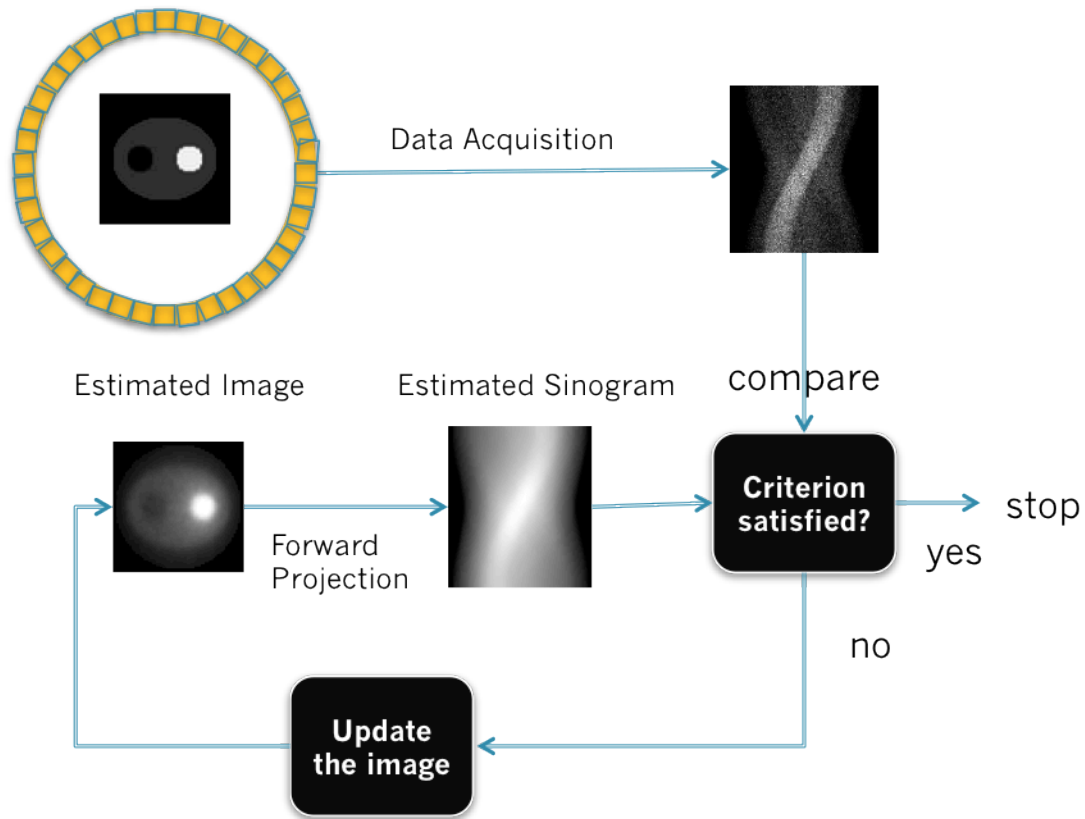


Figure 2.4- A simplified flowchart of an iterative reconstruction. Adapted from [Cherry et al., 2006].

The data acquisition process can be naturally described as a discrete-continuous problem that relates the discrete data acquired by the tomograph and the continuous function that represents the spatial distribution of activity [Lewitt et Matej, 2003]. In terms of the formulation of the reconstruction problem, this model has some attractive theoretical properties since it's not necessary to introduce any discretization or approximation. However it's not very used, mainly because it needs to construct and solve large and non-sparse linear systems [Lewitt et Matej, 2003].

The most usual model used in iterative methods is the discrete-discrete (D-D) model where the activity function is represented by a linear combination of a finite number of basis functions [Lewitt et Matej, 2003] [Fessler, 2004]. Under this model, the reconstruction process has five general components [Lewitt et Matej, 2003]: the object parameterization, the system physical model, the statistical model, the cost function and the algorithm.

Object Parameterization

The basis functions can be classified as localized basis functions (such as voxels or Kaiser-Bessel window functions (blobs)) or global basis functions (such as Fourier series) [Fessler, 2004].

The most used basis function is the voxel. This basis is orthogonal and each elementary function corresponds to a parallelepiped. The elementary function has unit value inside the voxel and zero value outside the voxel. The choice of the proper voxel size has to be done carefully. For unregularized reconstruction methods, voxels that are too small can lead to over-parameterization whereas if they are too big they can produce model mismatch and image features can be lost [Fessler, 1994]. The orthogonality of the basis function is not an essential propriety. The use of non-overlapping uniform voxels to model the image can introduce too many artificial high-frequency components into the image due to the discontinuities contained in the model [Zeng, 2010]. A more realistic band-limited image model can be achieved by the use of radial functions with overlapping, blobs. The main problem of the use of blobs is the computational complexity.

System Physical Model

Under the D-D model, the data acquisition can be related to the activity as a linear relation:

$$\mathbf{y}_i \approx \sum_{j=1}^m \mathbf{H}(i, j) \lambda_j \quad (2.10)$$

with m being the number of voxels and $\mathbf{H}(i, j)$ expressing the probability that an annihilation in the j th voxel, λ_j , is detected by the i th detector pair \mathbf{y}_i .

The probability expressed by the matrix H must have into account different factors such as the geometric sensitivity, photon pair non-collinearity, attenuation, intrinsic detector sensitivity and positron range.

The matrix \mathbf{H} can be factorized into several sub-matrixes [Qi et al., 1998][Mumcuoglu et al., 1996],

$$\mathbf{H} \approx \mathbf{S}_N \mathbf{S}_{det.blur} \mathbf{S}_A \mathbf{S}_{geom} \mathbf{S}_{positron} \quad (2.11)$$

with \mathbf{S}_N the diagonal matrix containing the detection efficiency of each detector pair, $\mathbf{S}_{det.blur}$ the matrix that models the blurring effects introduced by the detectors and \mathbf{S}_A a diagonal matrix containing the attenuation factors. The \mathbf{S}_{geom} is the geometric projection matrix with each element (i, j) equal to the probability that a photon pair produced in voxel j reaches the front faces of the detector pair i in the absence of attenuation and assuming perfect photon-pair collinearity. The $\mathbf{S}_{positron}$ is a matrix that includes the effects of the positron range.

The geometric relations between the projection space and the image space can be established using three types of projectors: the ray-driven projectors, the pixel-driven projectors and the distance driven projectors. Due to the memory limitations, usually these relations are calculated on the fly.

In the ray-driven projectors, a ray connecting each detector bin pair is drawn and the contribution of each voxel is calculated in accordance with its overlapping with the ray. Siddon [Siddon, 1985] proposed one of the most used ray-driven projectors. This method reduces the complexity of the computation by having into consideration that the voxels consist of the intersection of orthogonal sets of equally spaced parallel planes (see Figure 2.5).

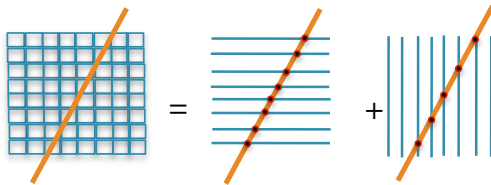


Figure 2.5- Siddon algorithm concept. The reduction of the complexity of the computation is done having into consideration that the voxels consist of the intersection of orthogonal sets of equally spaced parallel planes.

Another popular ray tracing method was proposed by Joseph [Joseph, 1982]. It begins by determining the ray direction that lies closer to the x,y or z axis. Then, for each intersection of the LOR with the planes of the grid orthogonal to this direction, it is assigned a value obtained by bilinear interpolation with the four closest voxels.

In the case of a pixel driven projector using a bilinear projection, the centre of every voxel is projected onto the projection plane, and bilinear interpolation between the nearest four projections elements determines their respective weights [Egger et al., 1996][Cho et al., 1990]. This technique is a common way to perform backprojection

when the data are stored as sinograms [Cherry et al., 2006].

In the 2D distance-driven projector, the detector array boundaries and the pixel boundaries are mapped onto a common axis, and then a one-dimensional kernel operation to map the data from one set of boundaries to another is applied [DeMan et Basu, 2004].

The geometric part of the system matrix is very sparse and usually is also very symmetric, i.e., many LOR are linked by geometrical symmetries. The symmetries can be used to reduce the size of the system matrix [Qi et al., 1998].

A Model of the Measurement Uncertainty

The model of the measurement uncertainty expresses the probability distribution of the data around their expected value. Depending on the noise model assumed, different reconstruction algorithms can be derived. In some reconstruction methods no model is assumed for the noise.

In PET, the detection of each decay event by the system can be modelled as a Bernoulli process, i.e, the sinogram data are a collection of independent Poisson random variables [Qi et Leahy, 2006]. Under this model for the noise, the corresponding reconstruction method is the Maximum Likelihood-Expectation Maximization (ML-EM) reconstruction algorithm.

The justification for using non-Poisson models such as the Gaussian model arises from the fact that if data corrections are applied prior to the reconstruction, the data no longer follow a Poisson model [Lewitt et Matej, 2003].

Objective Function

This function gives a measure of how well the estimated image fits the data and how well this image matches any prescribed a priori image properties such as positivity and smoothness [Lewitt et Matej, 2003][Defrise et al., 2005].

In the case of non-statistical reconstruction algorithms, the cost function is usually the minimization of the square of the Euclidian distance between the estimated projections and the acquired projections.

For statistical reconstruction methods, the cost function is usually the Poisson likelihood or the Gaussian likelihood. Please note that only when data have

redundancies the noise model has effect on the solution [Zeng, 2010]. For 3D PET this is true, i.e., the number of projections is higher than the number of voxels.

The Bayes' rule adapted to the PET reconstruction problem can be written as [Nuyts, 2012],

$$Prob(\boldsymbol{\lambda}|\mathbf{y}) = \frac{Prob(\mathbf{y}|\boldsymbol{\lambda})Prob(\boldsymbol{\lambda})}{Prob(\mathbf{y})}, \quad (2.12)$$

where $Prob(\boldsymbol{\lambda})$ is called the prior and is the likelihood of the distributions of the activity without having into account the data. The function $Prob(\mathbf{y}|\boldsymbol{\lambda})$ gives the probability of obtaining the measurements \mathbf{y} assuming that the true distributions of the activity is $\boldsymbol{\lambda}$.

This term is called the likelihood. The value of $Prob(\mathbf{y})$ is constant since the data have been already measurement. The function $Prob(\boldsymbol{\lambda}|\mathbf{y})$ is called the posterior.

Under this statistics framework we want to find the $\boldsymbol{\lambda}$ that maximizes the posterior function. Assuming that $Prob(\boldsymbol{\lambda})$ is constant, i.e., all the solutions have the same probability of occurring, the value of $\boldsymbol{\lambda}$ that maximize the likelihood will also maximize the posterior function. Since likelihood function is easier to calculate, the solution to the reconstruction problem is found by maximize the likelihood function.

The maximum-likelihood estimators have attractive properties such as asymptotic unbiasedness and efficiency [Qi et Leahy,2006].

Poisson likelihood

Assuming a Poisson model for the measurement of uncertainty, the probability of obtaining the measurement \mathbf{y}_i assuming that the true activity distribution is given by $\boldsymbol{\lambda}$ can be expressed by [Nuyts, 2012][Hunter et Lange, 2004][Dempster et al., 1977]:

$$Prob(\mathbf{y}_i|\boldsymbol{\lambda}) = \frac{e^{-\sum_{j=1}^m \mathbf{H}(i,j)\lambda_j} (\sum_{j=1}^m \mathbf{H}(i,j)\lambda_j)^{y_i}}{\mathbf{y}_i!} \quad (2.13)$$

where $\mathbf{H}(i,j)$ express the probability that a photon emitted from the voxel j will be detected by the pair of detectors i , \mathbf{y}_i is a sample from a Poisson distribution with the expected value equal to $\sum_{j=1}^m \mathbf{H}(i,j)\lambda_j$, i.e., is a random variable describing the number of photons detected by the pair of detectors i and λ_j the number of the

photons emitted from the voxel j .

When all projections are statistically independent, the likelihood function is the joint probability density function by considering all projections together,

$$Prob(\mathbf{y}|\boldsymbol{\lambda}) = \prod_{i=1}^n \frac{e^{-\sum_{j=1}^m \mathbf{H}(i,j)\lambda_j} (\sum_{j=1}^m \mathbf{H}(i,j)\lambda_j)^{y_i}}{y_i!}. \quad (2.14)$$

And the log-likelihood is given by:

$$\ln(Prob(\mathbf{y}|\boldsymbol{\lambda})) = \sum_{i=1}^n \left(-\sum_{j=1}^m \mathbf{H}(i,j)\lambda_j + y_i \ln \left(\sum_{j=1}^m \mathbf{H}(i,j)\lambda_j \right) + const \right) \quad (2.15)$$

with *const* equal to a term that not depend on λ_j .

Gaussian likelihood

Assuming a Gaussian model for the measurement of uncertainty, the i th projection measurement, y_i , is a random variable with mean equal to $\sum_{j=1}^m \mathbf{H}(i,j)\lambda_j$ and variance $(\sigma_i)^2$. The correspondent Gaussian distribution density function is given by [Zeng, 2010]:

$$Prob(y_i|\boldsymbol{\lambda}) = \frac{1}{\sqrt{2\pi\sigma_i}} e^{-\frac{([\mathbf{H}\boldsymbol{\lambda}]_i - y_i)^2}{(2\sigma_i)^2}} \quad (2.16)$$

When all projections are statistically independent, the likelihood function is given by,

$$Prob(\mathbf{y}|\boldsymbol{\lambda}) = \prod_{i=1}^n \frac{1}{\sqrt{2\pi\sigma_i}} e^{-\frac{([\mathbf{H}\boldsymbol{\lambda}]_i - y_i)^2}{(2\sigma_i)^2}} \quad (2.17)$$

and the log-likelihood is given by,

$$Prob(\mathbf{y}|\boldsymbol{\lambda}) = -\frac{1}{2} \sum_{i=1}^n \frac{([\mathbf{H}\boldsymbol{\lambda}]_i - y_i)^2}{\sigma_i^2} + const. \quad (2.18)$$

Numerical Algorithm

The objective of the numerical algorithm is to find the coefficients values of the basis function that allow to maximize (or minimize) the objective function. Iterative algorithms produce a sequence of estimates of the image which, in principle, converge to the solution [Defrise et Kinahan, 1998]. The final solution should be independent of the choice of the numerical algorithm. For convex problems and if the optimization algorithms are appropriate to the problem, it is expected that they converge to the same solution. In practice it is common to stop an iterative algorithm before reaching the maximum (minimum) of the objective function. Different algorithms generate different estimated images sequences and so different final images can be obtained.

The most popular iterative algorithm for PET data reconstruction is the Expectation maximization algorithm [Dempster et al., 1977]. This algorithm can be viewed as a special case of a more general class of optimization algorithms called MM [Hunter et Lange, 2004] (in minimization MM stands for majorize/minimize, and in maximization stands for minorize/maximize). An MM algorithm operates by creating a surrogate function that minimizes or maximizes the objective function. When the surrogate function is optimized, the objective function is driven uphill or downhill as needed [Hunter et Lange, 2004].

2.2.1 Algebraic Reconstruction Technique

The Algebraic Reconstruction Technique (ART) [Gordon, 1974] is a non-statistical algorithm that was developed by Kaczmarz [Censor et al., 1983] to solve systems of linear equations.

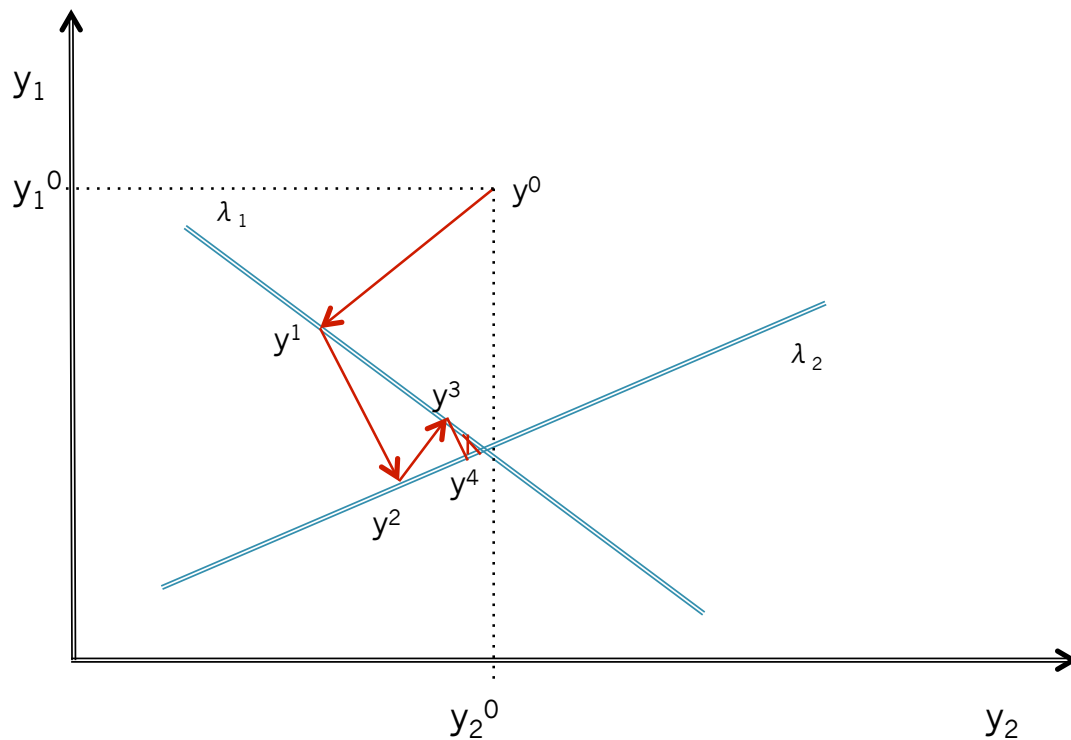


Figure 2.6- ART algorithm. Estimated solution sequence (y^j) for a toy problem with two LORs (λ_1, λ_2) and two pixels (y_1, y_2). The initial pixels values were equal to y^0 .

The ART algorithm generates the sequence of estimated images satisfying one equation at a time, as illustrated in Figure 2.6. In this toy problem, two LORs (that represent two equations) and two pixels were used. In the absence of noise, the solution is the intersection of the two LORs. The initial solution, y^0 , is projected perpendicularly (minimal distance) to λ_1 , obtaining the first estimated of the solution, y^1 . Then the y^1 is projected perpendicularly to λ_2 . This procedure will be repeated to all projections. In the presence of noise the equations are not consistent and the algorithm does not converge to a unique solution. The iterative form of this row-action algorithm can be as expressed by [Herman, 1980]:

$$\lambda_j^k = \lambda_j^{k-1} + \frac{\mathbf{y}_i - \sum_j^m \mathbf{H}(i,j)\lambda_j^{k-1}}{\sum_j^m \mathbf{H}(i,j)^2} \mathbf{H}(i,j), \quad (2.19)$$

with m being the number of voxels and $\mathbf{H}(i,j)$ expressing the probability that an annihilation in the j th voxel, λ_j , is detected by the i th detector pair \mathbf{y}_i . The λ_j^k is the estimated value for the j th voxel of the activity distribution image at the iteration k .

This algorithm considers one projection \mathbf{y}_i at a time. The convergence speed depends on the order in which the projections are process. To force the convergence in the presence of noise a relaxation parameter is introduced [Censor et al., 1983] [Herman, 1980]:

$$\lambda_j^k = \lambda_j^{k-1} + r \frac{\mathbf{y}_i - \sum_j^m \mathbf{H}(i,j)\lambda_j^{k-1}}{\sum_j^m \mathbf{H}(i,j)^2} \mathbf{H}(i,j) \quad (2.20)$$

where r is the relaxation parameter with values between 0 and 1. This parameter will reduce the update weight and force the convergence to a point somewhere in the middle of the partial solutions.

2.2.2 Maximum-Likelihood Expectation-Maximization

Currently, the most popular iterative methods for PET image reconstruction are based on the Maximum-Likelihood Expectation-Maximization [Shepp et Vardi, 1982]. The Expectation-Maximization was proposed by Dempster [Dempster et al., 1977] as a general approach to iterative computation of the maximum-likelihood estimates when the observations can be viewed as incomplete data. Assuming a Poisson model for the noise, the log-likelihood function \mathbf{H} is given by,

$$\mathbf{L}_y = \ln(\text{Prob}(\mathbf{y}|\boldsymbol{\lambda})) = \sum_{i=1}^n \left(- \sum_{j=1}^m \mathbf{H}(i,j)\lambda_j + \mathbf{y}_i \ln \left(\sum_{j=1}^m \mathbf{H}(i,j)\lambda_j \right) + \text{const} \right)$$

where $\mathbf{H}(i,j)$ express the probability that a photon emitted from the voxel j will be detected by the pair of detectors bins i , \mathbf{y}_i is a sample from a Poisson distribution

with the expected value equal to $\sum_{j=1}^m \mathbf{H}(i, j)\lambda_j$, i.e., is a random variable describing the number of photons detected by the pair of detectors i and λ_j the number of the photons emitted from the voxel j .

The objective of the EM algorithm is to find the image that maximizes the log-likelihood function,

$$\lambda_{ML} = \arg \max_{\lambda} \left(\sum_{i=1}^n \left(- \sum_{j=1}^m \mathbf{H}(i, j)\lambda_j + y_i \ln \left(\sum_{j=1}^m \mathbf{H}(i, j)\lambda_j \right) \right) \right) \quad (2.21)$$

For solving this optimization problem the EM algorithm introduces a new Poisson random variable, \mathbf{X} , to the problem. This variable is called complete data and $\mathbf{X}(i, j)$ is the number of photons actually emitted from the pixel j and recorded by the pair of detectors i . The expectation value of this variable, given λ , is

$$E(\mathbf{X}(i, j)|\lambda) = \mathbf{H}(i, j)\lambda_j. \quad (2.22)$$

From the complete data, \mathbf{X} , computation of the acquired (incomplete) data is straightforward attending to $y_i = \sum_j \mathbf{X}(i, j)$. Instead of trying to maximize (2.21), the EM approach maximize the log-likelihood for the complete data. The corresponding log-likelihood function of all Poisson distributed random variables \mathbf{X} is given by [Nuyts, 2012][Lange et Carson, 1984] :

$$L_{\mathbf{X}}(\mathbf{X}, \lambda) = \sum_i^n \sum_j^m (\mathbf{X}(i, j) \ln(\mathbf{H}(i, j)\lambda_j) - \mathbf{H}(i, j)\lambda_j) \quad (2.23)$$

This method has two steps, the E (expectation) step and the M (maximization) step. In the E step are estimated the conditional expected values of the complete data, \mathbf{X} , and in the M-step the new estimate for λ is calculated by maximization of the function derived in the E-step.

E step

Since \mathbf{X} is unknown, it is not possible to calculate $L_{\mathbf{X}}$. The value of $\mathbf{X}(i, j)$ is replaced in (2.24) by its expected value using the measurement y_i and the current

estimate of λ_j at the iteration k , λ_j^k , that can be written as, [Nuyts, 2012][Lange et Carson, 1984]

$$E(\mathbf{X}(i, j) | \mathbf{y}_i, \lambda^k) = \frac{H(i, j) \lambda_j^k}{\sum_p H(i, p) \lambda_p^k} \mathbf{y}_i . \quad (2.24)$$

Doing that the conditional expected values of the complete data with respect to \mathbf{y} and the λ_j^k are obtained,

$$E(L_X(\mathbf{X}, \lambda) | \mathbf{y}, \lambda^k) = \sum_{i, j} \left(\frac{H(i, j) \lambda_j^k}{\sum_p H(i, p) \lambda_p^k} \mathbf{y}_i \ln(H(i, j) \lambda_j) - H(i, j) \lambda_j \right). \quad (2.25)$$

M step

In the M step a new estimated λ^{k+1} is calculated that maximizes the function computed in the E-step with respect to λ_j by setting the partial derivative to zero:

$$\frac{\partial E(L_X(\mathbf{X}, \lambda) | \mathbf{y}, \lambda^k)}{\partial \lambda_j} = \sum_i \left(\frac{H(i, j) \lambda_j^k}{\sum_p H(i, p) \lambda_p^k} \mathbf{y}_i \frac{H(i, j)}{H(i, j) \lambda_j} - H(i, j) \right) = 0 . \quad (2.26)$$

Solving for λ_j we find the usual (multiplicative) iterative form of the ML-EM algorithm,

$$\lambda_j^{k+1} = \frac{\lambda_j^k}{\sum_i H(i, j)} \sum_i H(i, j) \frac{\mathbf{y}_i}{\sum_p H(i, p) \lambda_p^k} . \quad (2.27)$$

The term of comparison used by this algorithm is the ratio between the measured data and the forward projection of the current estimates. This ratio determines a modification factor to update the current estimate of the image. Richardson [Richardson, 1972] and Lucy [Lucy, 1974] proposed a similar iterative algorithm for restoration of astronomy images. The ML-EM algorithm can also be written in an additive form so that it appears like a gradient descent algorithm as in [Fessler, 2004]:

$$\lambda^{k+1} = \lambda^k + \frac{\lambda^k}{\mathbf{H}^T \mathbf{1}_y} \left[\mathbf{H}^T \frac{\mathbf{y}}{H \lambda^k} - \mathbf{H}^T \mathbf{1}_y \right]. \quad (2.28)$$

De Pierro [DePierro, 1993] used an elegant approach to derive the ML-EM algorithm without using the concept of complete data. In his derivation he only used the convexity of the log-likelihood objective function and the Jensen's inequality. One possible way to incorporate the correction of data into the iterative form of the ML-EM is to use the Ordinary Poisson ML-EM [Comtat et al., 2004],

$$\lambda^{k+1} = \frac{\lambda^k}{\mathbf{S}_{geom}^T \mathbf{A} \mathbf{N} \mathbf{1}_p} \mathbf{S}_{geom}^T \frac{\mathbf{p}}{\mathbf{S}_{geom} \lambda + \mathbf{A}^{-1} (\mathbf{N}^{-1} \mathbf{d} + \mathbf{s})}, \quad (2.29)$$

where \mathbf{p} are the prompt coincidences, \mathbf{d} the delayed coincidences and \mathbf{s} the scattered coincidences. \mathbf{N} and \mathbf{A} are the inverse of the normalization and attenuation correction factors, respectively. The λ^k is the estimated activity image at the iteration k and $\mathbf{1}_p$ a vector of ones with the same size as \mathbf{p} .

In the ML-EM derivation it was assumed that the model for the noise was Poissonian. The Image Space Reconstruction Algorithm (ISRA) [DePierro, 1993] is the corresponding reconstruction algorithm when the model for the noise is assumed to be Gaussian. The iterative form of ISRA algorithm is given by [DePierro, 1993],

$$\lambda_j^{k+1} = \lambda_j^k \frac{\sum_{i=1}^n \mathbf{H}(i, j) y_i}{\sum_{i=1}^n \mathbf{H}(i, j) (\sum_{l=1}^m \mathbf{H}(i, l) \lambda_l)} \quad (2.30)$$

Properties of the ML-EM Iteration

- The cost function, the log-likelihood function, increases monotonically at each iteration [Qi et Leahy, 2006]. Assuming that this function is a concave function (the number of projections is greater or equal than the number of voxels and the system matrix has full rank), all the maxima of this function are

global maxima and so the ML-EM iteration gives the sequence of images that converge to the global maximum likelihood estimator. In practice, the reconstruction is stopped at a given iteration. With the increase of the number of iterations the estimated image becomes too noisy (see section 6.1).

- In contrast with the Filtered BackProjection (FBP), the ML-EM algorithm is non-linear [Defrise et al., 2005]. In general, the sum of the final reconstructed volumes of the raw data of individual objects is not equal to the reconstruction result of the raw data of the sum of the objects. The estimated activity distribution of a point source in a uniform background, using a small number of iterations, broadens when the strength of the background is increased [Defrise et al., 2005]. The final reconstructed volumes also depend on the position of the objects. The non-linearity also explains the slower convergence for regions of low tracer uptake than for regions of high tracer uptake. When compared with the FBP, quantitative results show that the ML-EM reconstruction allows a better SNR in regions of low tracer uptake, resulting in a better visibility of the contours of the body [Defrise et al., 2005].
- If the system matrix is normalized the total counts of the sinogram will be preserved.
- If the initial image is positive, then, all the estimated images will be positive. The estimated image is calculated by multiplying the previous estimated image with a multiplicative factor.

2.2.3 Block Iterative Reconstruction Methods

One of the main problems for the use of ML-EM in clinical applications was the long reconstruction time. In each iteration one projection and one backprojection must be done. Due to its slow convergence several iterations must be performed. In the case of FBP only a single backprojection is needed. Block iterative reconstruction methods allow reducing the reconstruction time by processing the data in blocks (subsets) within each iteration. Two of the most popular block iterative methods are the Ordered Subsets Expectation Maximum (OSEM) and Row-Action Maximum Likelihood Algorithm (RAMLA).

Order Subset Expectation Maximization

In 1994 Hudson *et al.* [Hudson et Larkin, 1994] proposed a block iterative reconstruction method called Order Subset Expectation Maximization algorithm. This approach is similar in concept to block-Kaczmarz methods introduced by Eggermont *et al.* [Censor et al., 1983][Eggermont et al., 1981] for iterative reconstruction.

In OSEM the data is divided in to N_s disjoint balanced subsets, S , in which the ML-EM is applied. By balanced it is meant that the $\sum_{i \in S_q} \mathbf{H}(i, j)$ is independent on each subset q , where $\mathbf{H}(i, j)$ expressing the probability that an annihilation in the j th voxel, λ_j , is detected by the i th detector pair \mathbf{y}_i . The update equation of the OSEM is given by equation [Qi et Leahy, 2006],

$$\lambda_j^{(k,q)} = \frac{\lambda_j^{(k,q-1)}}{\sum_{i \in S_q} \mathbf{H}(i, l)} \sum_{i \in S_q} \mathbf{H}(i, j) \frac{\mathbf{y}_i}{\sum_p \mathbf{H}(i, p) \lambda_p^{(k,q-1)}}, \quad (2.31)$$

for $j=1, \dots, n$ and $q=1, \dots, N_s$

with

$$\begin{aligned} \lambda_j^{(k, N_s)} &= \lambda_j^{(k)} \\ \lambda_j^{(k, 0)} &= \lambda_j^{(k-1)} \end{aligned} \quad (2.32)$$

Although this technique improves the convergence speed by a factor proportional to the number of subsets [Hudson et Larkin, 1994], the convergence of the algorithm is not guaranteed [Qi et Leahy, 2006] [Byrne, 1998].

In practice, since the reconstruction problem is ill conditioned, the ML-EM algorithm is stopped before the maximum of the objective function is reached, avoiding noise amplification (see section 6.1).

Row-Action Maximum-Likelihood

Another popular reconstruction algorithm in the clinical context is the row-action maximum-likelihood algorithm (RAMLA). Inspired in the row-action ART

algorithm, Browne and De Pierro [Browne et DePierro, 1996] developed the RAMLA algorithm that allows to maximize the Poisson likelihood function with a reduced computational effort when compared with the ML-EM algorithm. The iterative form of the algorithm is given by [Qi et Leahy, 2006]:

$$\lambda_j^{(k,q)} = \lambda_j^{(k,q-1)} + \eta_k \lambda_j^{(k,q-1)} \sum_{i \in S_q} \left(\frac{\mathbf{H}(i,j) \mathbf{y}_i}{\sum_p \mathbf{H}(i,p) \lambda_p^{(k,q-1)}} - 1 \right), \quad (2.33)$$

for $j=1, \dots, n$ and $q=1, \dots, N_s$

where η_k is a sequence of positive relaxation parameters such that,

$$\lim_{k \rightarrow \infty} \eta_k = 0 \quad \sum_{k=0}^{\infty} \eta_k = +\infty \quad (2.34)$$

The image is updated for each projection view (row of the system matrix). In [Browne et DePierro, 1996] the selection of the appropriate relaxation parameters for a specific task was made using a training process. An incorrect choice of the relaxation parameters can greatly reduce the performance of the method.

In their experiments, the iterations 1, 2, 3, and 4 of RAMLA reach comparable log-likelihood values as the iterations 45, 60, 70, and 80, respectively, of ML-EM.

For cost function strictly concave, it was showed that RAMLA converges to the maximum of the cost function (assuming a correct choice of the relaxation parameters).

In 2001 De Pierro et Yamagishi [DePierro et Yamagishi, 2001] presented an extension of RAMLA for maximum a posteriori reconstruction and in 2003 [DePierro, 2003] extended the concept to transmission tomography. Note that the ML-EM algorithm does not yield a closed-form solution when used to maximize the Poisson likelihood in transmission CT [DePierro, 2003].

Chapter 3

3 Resolution Modelling in PET

Resolution modelling techniques (RM) aim to improve the resolution and the quantification of the reconstructed image by better modelling the system matrix. Different approaches were proposed to estimate the system matrix, such as Monte Carlo techniques, analytic models, direct measures or a combination of the previous approaches.

A method to perform the estimation of the sinogram blurring kernel adapted to the High Resolution Research Tomograph (HRRT) scanner was developed and tested. The proposed method permits the incorporation of the effects of the inter-crystal penetration into the reconstruction process. A spatial variant asymmetric Gaussian function was used to model this blurring effect in the radial and axial direction.

We begin by presenting the main characteristics of the HRRT, and then we do an overview of the resolution modelling techniques. After that, we will present the proposed method to estimate the sinogram blurring kernel. This kernel was used in the reconstruction of a point source data acquired at different radial distances. The resulting images were compared with images obtained by reconstructing the datasets without resolution modelling and with resolution modelling in the image space.

3.1 High Resolution Research Tomograph

The High Resolution Research Tomograph is a specialized scanner that provides high resolution PET images of the human brain. Due to its high resolution and sensitivity this scanner can be also used in pre-clinical [Jan et al., 2004]. It's composed of 8 heads arranged in an octagon configuration. Each head is constituted of 9 block detectors in the transverse direction and 13 in the axial direction [Eriksson et al., 2002] and each detector is composed of two scintillator layers constituted of LSO and Lutetium Yttrium Orthosilicate (LYSO). The difference in decay times between the two crystals (40 ns for the LSO and 53 ns for the LYSO) allows for the retrieval of DOI information.

The coincidences events are stored in a list with 64 bits. Usually, the list-mode data are binned into 256 radial bins, 288 angles and 2209 planes (that correspond to span 9) [Jong et al., 2007].

The attenuation coefficients are estimated by transmission measurements using a 2D fan-collimated ^{137}Cs moving point source. First is done an acquisition without the object and then is done the acquisition with the object. After that, the attenuation data are reconstructed (usually using regularized reconstruction techniques [Nuyts et al., 2001]) and the result is re-mapped (scaled) by a factor to express the attenuation values at 511 keV. Finally the attenuation image is projected into the projection space [Knoß, 2004].

Scatter correction is done using an adapted version of the single scatter simulation method [Watson, 2000] (see section 1.5.3). The correction is based on the pre-corrected emission sinogram (corrected for attenuation, detector gaps and normalization) and on the attenuation map of the object [Knoß, 2004].

The standard normalization correction uses the direct method [Knoß, 2004]. A ^{68}Ge line source with a length of 250mm, rotating in a 165 mm radius orbit, is acquired using the same energy window as the one used in the clinical protocol. The main problem of this approach is the long acquisition time (several dozens of hours) required to obtain normalization coefficients with low noise.

Random events are estimated using a delayed window technique [Knoß, 2004] (see section 1.5.4).

Different reconstruction algorithms are available, such as, 2D FPB, 2D OSEM and 3D OSEM. For the 2D reconstruction the data rebinning is done using Fourier rebinning [Defrise et al., 1997]. In the clinical environment one of the most common method used is the OP-OSEM [Comtat et al., 2004] (see (2.29)). Usually the images were reconstructed on a $256 \times 256 \times 207$ pixels (x, y, z directions, respectively) grid of voxels with the dimensions $1.218 \times 1.218 \times 1.218$ mm \times mm \times mm in the x, y, z direction, respectively.

3.2 Resolution Modelling Reconstruction Techniques

A realistic modelling of the system matrix is needed to ensure the good quality of the reconstructed images. Different methods were proposed to improve the estimation of the system matrix.

Monte Carlo methods can be used to directly calculate the system matrix. Several research groups have proposed this approach for modelling the system matrix of small animal scanners [Rafecas et al., 2002][Gimenez et al., 2006][Ortuno et al., 2010]. The main problems of Monte Carlo methods are related with the computational resources required to simulate and store the system matrix. It is also difficult to correctly describe the effects of light collection and the electronics.

A different approach is to experimentally measure the system matrix. Panin *et al.* [Panin et al., 2006a][Panin et al., 2006b] derived the system matrix for the Siemens Biograph HiRez scanner from point source measurements acquired at different positions in the FOV. The point sources were positioned using a robot. For a direct measure of this matrix, measurements should be done for each point in the FOV. The number of acquisitions was reduced by taking into consideration the symmetries of the system and by using a parameterized model. Even so a total of 1599 acquisitions (5-minute each) was necessary.

In order to reduce the required storage and optimize the performance of the reconstruction, the system matrix can be decomposed into sub-matrices (see (2.11)),

$$\mathbf{H} \approx \mathbf{S}_N \mathbf{S}_{\text{det.blur}} \mathbf{S}_A \mathbf{S}_{\text{geom}} \mathbf{S}_{\text{positron}}$$

with \mathbf{S}_N the diagonal matrix containing the detection efficiency of each detector pair, $\mathbf{S}_{\text{det.blur}}$ the matrix that models the blurring effects introduced by the detectors and \mathbf{S}_A a diagonal matrix containing the attenuation factors. The \mathbf{S}_{geom} is the geometric projection matrix with each element (i, j) equal to the probability that a photon pair produced in voxel j reaches the front faces of the detector pair i in the absence of attenuation and assuming perfect photon-pair collinearity. The $\mathbf{S}_{\text{positron}}$ is a matrix that includes the effects of the positron range.

This representation allows an independent description of the different effects that contribute to the degradation of the image quality, such as positron range, non-collinearity, inter-crystal scatter and penetration. In most of the resolution modelling algorithms based on the factorization of the system matrix, all the non-geometric effects are combined into a single sub-matrix that is defined in the projection space (\mathbf{S}_{prm}) or in the image space (\mathbf{S}_{psf}).

If these blurring effects are modelled in the projection space, \mathbf{S}_{prm} , the factorization of the system matrix is given by:

$$\mathbf{H} = \mathbf{S}_N \mathbf{S}_{\text{det.blur}} \mathbf{S}_A \mathbf{S}_{\text{prm}} \mathbf{S}_{\text{geom}} . \quad (3.1)$$

Effects like non-collinearity, inter crystal scatter and penetration are best described in the projection space. Formally, the blurring induced by the non-collinearity depends on the point of the annihilation along the LOR and cannot be accurately described in the projection space. This effect should be modelled in the geometric matrix, \mathbf{S}_{geom} . However, to simplify the system matrix computation, one can assume that photon non-collinearity is depth independent and so can be modelled in the projection space [Rahmim et al., 2008] .

When the blurring effects are modelled in the image space, \mathbf{S}_{psf} , the factorization of the system matrix can be expressed by:

$$\mathbf{H} = \mathbf{S}_N \mathbf{S}_{\text{det.blur}} \mathbf{S}_A \mathbf{S}_{\text{srm}} \mathbf{S}_{\text{geom}} \mathbf{S}_{\text{psf}} . \quad (3.2)$$

The blurring effects of the positron range are best described in image space. Only when the condition,

$$\text{Range}\{\mathbf{S}_{\text{prm}}\mathbf{S}_{\text{geom}}\} \subseteq \text{Range}\{\mathbf{S}_{\text{geom}}\} \quad (3.3)$$

is satisfied, where $\text{Range}\{\mathbf{M}\}$ is the set of all possible linear combinations of the column vectors of the matrix \mathbf{M} , then is possible exactly describe the blurring effects in the image space [Cloquet et al., 2010]. In general this condition cannot be satisfied because the dimensions of the projection space are much higher than the dimensions of the image space.

Due to the factorization of the system matrix, the blurring kernel can be easily incorporated into the iterative form of the maximum-likelihood expectation maximization reconstruction algorithm (ML-EM). The Ordinary Poisson ML-EM reconstruction algorithm (see (2.29)) can be rewritten as:

$$\lambda^{k+1} = \frac{\lambda^k}{\mathbf{S}^T \mathbf{A} \mathbf{N} \mathbf{1}_p} \mathbf{S}^T \frac{\mathbf{p}}{\mathbf{S} \lambda + \mathbf{A}^{-1} (\mathbf{N}^{-1} \mathbf{d} + \mathbf{s})} \quad (3.4)$$

where \mathbf{p} are the prompt coincidences, \mathbf{d} the delayed coincidences and \mathbf{s} the scattered coincidences. \mathbf{N} and \mathbf{A} are the inverse of the normalization and attenuation correction factors, respectively. The λ^k is the estimated activity image at the iteration k and $\mathbf{1}_p$ a vector of ones with the same size as \mathbf{p} .

When $\mathbf{S} = \mathbf{S}_{\text{geom}}$, the reconstruction don't have into account the blurring effects introduced by the detector (noRM-EM). If $\mathbf{S} = \mathbf{S}_{\text{geom}}\mathbf{S}_{\text{psf}}$, the effects that lead to the degradation of the image quality are modelled in the image space (IRM-EM). In the case of $\mathbf{S} = \mathbf{S}_{\text{prm}}\mathbf{S}_{\text{geom}}$ these effects are modelled in the projection space.

3.2.1 Resolution Modelling in Projection Space

Different methods were proposed for the estimation of the \mathbf{S}_{prm} sub-matrix.

Qi *et al.* [Qi et al., 1998] used resolution modelling in the sinogram space to reconstruct data acquired with the microPET system [Cherry et al., 1997]. A Monte Carlo simulation was used to estimate the blurring effects of the photon pair non-collinearity and inter-crystal penetration. The blurring model was confined to the

radial and azimuthal directions. Monte Carlo simulation was also used by Alessio *et al.* [Alessio et al., 2006] to find the system model for a whole-body PET system. Besides the detector blurring effects and the non-collinearity they also took into account the influence of the Fourier rebinning. The blurring kernel was modelled as a three-dimensional function that blurs in the radial and axial directions and is spatially variant in the radial location. A different kernel model was proposed by Stute *et al.* [Stute et al., 2011]. They proposed a 4-dimensional kernel that has into account the inter-crystal scattering and penetration and the intra-crystal count distribution.

Analytic models can also be used to model the inter-crystal scatter and penetration and the photons non-collinearity. Lecomte *et al.* [Lecomte et al., 1984] [Schmitt et al., 1988] proposed an analytical model for the inter-crystal penetration which depends on the linear attenuation model and the angle of incidence. For the modelling of the non-collinearity, Rahmim *et al.* [Rahmim et al., 2008] used an angular-dependent Gaussian blurring kernel along the radial and axial directions.

Another approach to estimate the blurring kernels is based on direct measurements. Qi [Qi, 2006] proposed a maximum likelihood (ML) approach to estimate 2D sinogram blurring kernels (radial and angular directions) from experimental measurements of non-collimated point sources. These blurring kernels have into account not only the inter-crystal scatter and penetration but also other blurring effects in the photon detection process. It is assumed that the data acquired correspond to the convolution of the sinogram blurring kernels with the geometric projection of the object. The iterative form of the proposed method is given by,

$$b_{ij}^{k+1} = \frac{b_{ij}^k}{n_i \sum_{jm} g_{jm}} \sum_{m=1}^M \frac{y_{i,m} g_{j,m}}{\sum_{j=1}^N b_{i,j}^k g_{j,m}} \quad (3.5)$$

where b_{ij} is the element i,j of the sinogram blurring matrix, \mathbf{B} , and expresses the blurring contribution from detector pair j to detector pair i . $y_{i,m}$ and $g_{i,m}$ are the measured projection and calculated geometric projection, respectively, of the m point source detected by detector pair i . The n_i is the sensitivity factor for detector pair i . M is the number of point source positions, N is the number of sinogram elements and k the iteration number. This iterative form is very similar to the iterative form of the

ML-EM reconstruction algorithm. The proposed algorithm monotonically converges to an ML estimate of the blurring matrix [Tohme et Qi, 2009]. Tohme et Qi [Tohme et Qi, 2009] adapted the proposed method to the microPET II scanner [Tai et al., 2003]. The new formulation of the algorithm has into account the effect of the block detector in the rotational symmetry of the scanner geometry.

3.2.2 Resolution Modelling in Image Space

The \mathbf{S}_{psf} sub-matrix is constructed based on the results obtained by reconstructing point source or line source data. Usually, to avoid the introduction of noise in the image space blurring kernel, the reconstructed data are parameterized using a smooth functional model. The main differences between the different methods proposed in literature are related with the PSF model adopted.

Reader *et al.* [Reader et al., 2002][Reader et al., 2003] tested a 3D Gaussian PSF model (shift-invariant and isotropic). The proposed model was used to perform the reconstruction of simulated list-mode data and also to reconstruct data acquired with a GE Advance PET scanner. Sureau *et al.* [Sureau et al., 2008] used a shift-invariant PSF model in the reconstruction of (dynamic) data acquired with the HRRT. They tested two PSF models to fit the point source data: an exponential model with an offset model and a 2-weighted exponential model.

A space-variant and anisotropic PSF model was used by Rahmim *et al.* [Rahmim et al., 2008] to reconstruct list-mode data acquired in the HRRT. An exponential model and an inverse-Gaussian model were tested. Four ^{11}C line sources, oriented axially, at different radial distances were simultaneously acquired. These datasets were reconstructed using different space-invariant and isotropic Gaussian kernels. The best reconstruction result of each line source was used to parameterize the spatially-variant and anisotropic PSF model. Cloquet *et al.* [Cloquet et al., 2010] compared the performance of different asymmetric and space variant PSF models in the reconstruction of data acquired with the Philips Gemini 16 Power PET scanner [Surti et Karp, 2004]. The shift variant Gaussian model, the shift variant and asymmetrical Gaussian model and the asymmetric modified Pearson model were the PSF models tested. They have done 42 different acquisitions of a point source along the central coronal plane.

3.2.3 Effect of the Resolution Modelling in the Reconstructed Image

In general the use of resolution modelling reconstruction methods has several advantages [Sureau et al., 2008][Tong et Alessio, 2010][Rapisarda et Bettinardi, 2010][Tohme et Qi, 2009], such as improving the spatial resolution, improving the contrast recovery and reducing image noise. One consequence of these improvements is the reduction of the Partial Volume Effect (PVE). PVE is caused by the finite spatial resolution of the imaging system and by the image sampling [Soret et al., 2007]. Motion also introduces additional PVE.

The finite spatial resolution introduces blurring in the reconstructed image. It depends on the detector design and on the reconstruction method. The signal (counts) of the structures smaller than the system resolution will be spread over the neighbour voxels [Soret et al., 2007]. Even for larger structures the borders will be blurred. This “spill-out” effect results in an “apparent” reduction of the activity inside a structure.

The image sampling is the cause of the “spill-in” effect. Since the contours of the voxels usually do not match with the shape of the structure, some voxels represent different types of tissues, i.e., different structures can contribute for the measured activity at some voxels.

The PVE introduces a bias in quantification, especially for small structures with many borders. It also affects the tumour apparent size. For tumours with partially necrotic centres “spill in” will be responsibly of an “apparent” increase of activity in the centre [Soret et al., 2007].

The drawback of using resolution modelling algorithms is the introduction of some edge artefacts (Gibbs effects) in the reconstructed image [Qi et al., 1998][Reader et al., 2003]. Two main reasons are given as the cause of these effects [Snyder et al., 1987][Politte et Snyder, 1988]. The first cause is the error on the estimation of the blurring kernel. The second is related with the system matrix being ill-conditioned [Qi et al., 1998]. These effects can be reduced by the use of regularization techniques, post-smoothing the final image, or using a smaller PSF kernel. All these potential solutions will degrade the resolution of the final image.

The use of blurring kernels into the reconstruction also reduces the initial convergence speed. For the ML-EM algorithm, the estimated images in the early iterations are smoother than those reconstructed without resolution modelling.

3.3 HRRT Sinogram Resolution Modelling

The proposed sinogram blurring kernel attempts to improve the resolution and to reduce its variation. This blurring kernel was parameterized using a smooth functional model and the radial parameters were estimated based on a line source measurement.

3.3.1 Sinogram Blurring Kernel

The proposed blurring kernel model has into account the angles of incidence, α angles, formed by the intersection of each LOR, represented by each sinogram element, with the detector heads (see Figure 3.1).

For scanner with cylindrical geometry the radial profile of the detector response function becomes asymmetrical and broader with increasing the radial offsets [Cherry et al., 2006]. Off-centre events penetrate with non-normal angles of incidence that lead to the degradation of the resolution. Both angles of incidence formed by the intersection of each Line Of Response (LOR) with the detectors are identical and the radial profile depends on the radial coordinate. On the contrary, for the octagonal geometry of the HRRT, annihilation photons penetrate with oblique angles of incidence independently of the radial position.

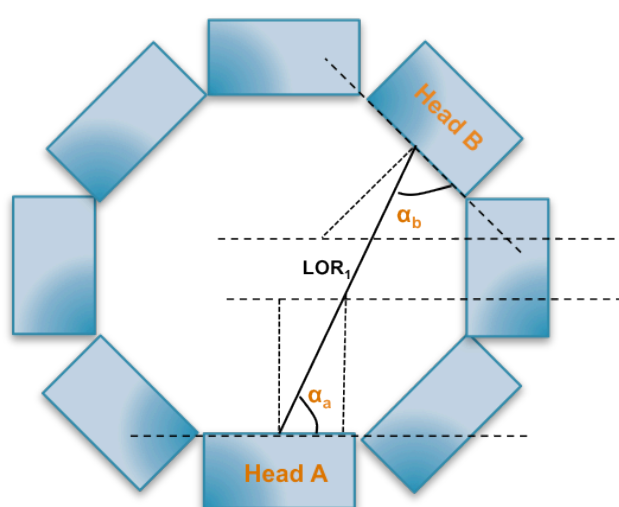


Figure 3.1- Schematic representation of the angles of incidence (α_a and α_b angles) formed by the intersection of a LOR with the detector heads.

The α angles were organized into a sinogram format, i.e., each value of the sinogram bin corresponds to the α angle in degrees. Two α sinograms were constructed (see Figure 3.2) corresponding to the angles of incidence with the detector heads (represented in Figure 3.1 by α_a and α_b).

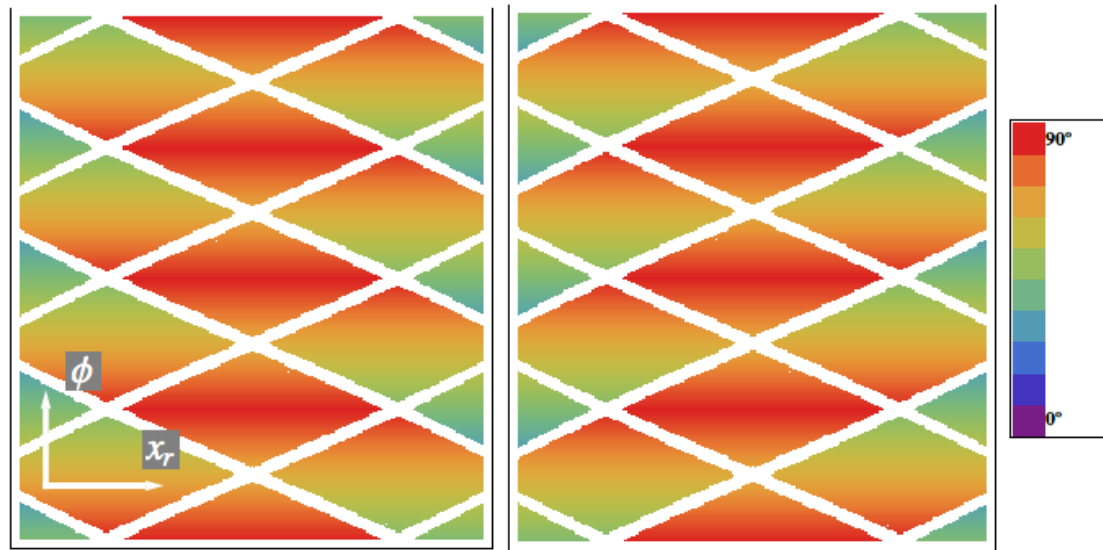


Figure 3.2- Sinograms of the α angles calculated for the intersection of the LORs with the A head (left) and B head (right) represented in Figure 3.1 by α_a and α_b , respectively.

When the two α sinograms are summed, three distinct regions can be defined. The α sinogram can be divided into these three regions, as showed in Figure 3.3.

In the Region 1 the α angles formed with the detector heads are equal. In the Region 2 and Region 3 the A head α angle and the B head α angle are related by a constant (see Figure 3.3),

$$\alpha_a + \alpha_b = \text{const} , \quad (3.6)$$

where α_a and α_b are the angles formed by the intersection of one LOR with the A and B detector heads, respectively. For the Region 2 the constant is equal to 135° and for the Region 3 is equal to 90° . The range of α_a and α_b angles is the same for a given region. For the Region 2 and 3, when α_a has the maximum value the correspondent α_b has the minimum value (see (3.4)).

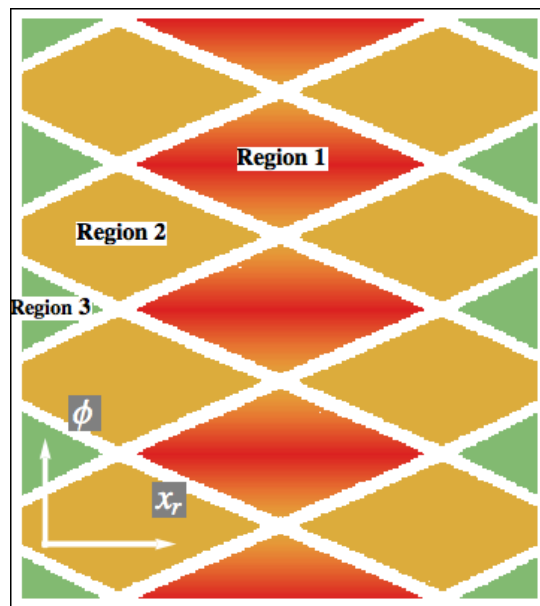


Figure 3.3- Representation of the sum of two α sinograms ($\alpha_a + \alpha_b$).

The value of the constants is related with angle formed by the perpendiculars to the detector heads in coincidence (see Figure 3.4). In Region 1 the events are detected by the pairs of detector heads that are face to face. For the Region 2 the angle between the perpendiculars to the A and B heads is 135° and in Region 3 this angle is 90° .

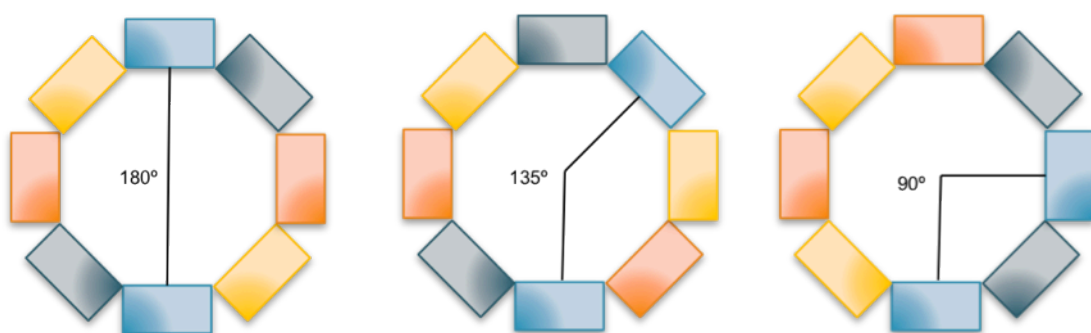


Figure 3.4- Relation between the α sinogram regions with the angles between the detector heads in coincidence. In Region 1 the events are detected by the pairs of heads that are face to face. For the events detected in Region 2 the angle between the A head and the B head is 135° and in Region 3 this angle is 90° .

Figure 3.5 presents the relations between the coincidences detected by the different pairs of detector heads and their localization in the sinogram.

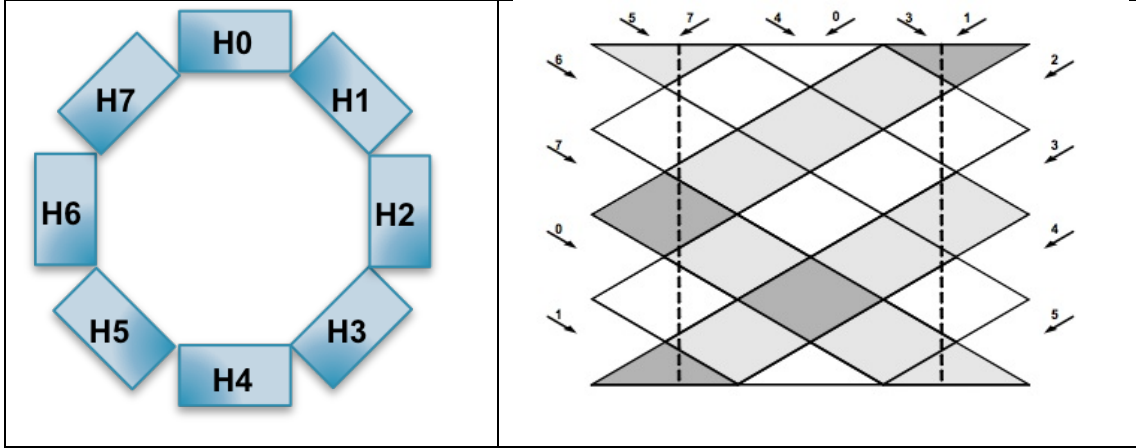


Figure 3.5- Relations between the coincidences detected in the different pairs of detector heads and the corresponding localizations in the sinogram. The numbers in the figure on the right correspond to the head number defined in the figure on the left. Only the sinogram part between the two dashed lines will be used. Adapted from [Knoß, 2004].

The radial component of the proposed blurring kernel model depends on the α Region. An asymmetric space-variant Gaussian model was used to model the blurring kernel in this direction:

$$SRM_{Radial}(\alpha R, x_r) = \begin{cases} a_r(\alpha R) e^{-\frac{(x_r - x_{r0}(\alpha R))^2}{2\sigma_{left}^2(\alpha R)}} \widehat{x}_r & , x_r < x_{r0}(\alpha R) \\ a_r(\alpha R) e^{-\frac{(x_r - x_{r0}(\alpha R))^2}{2\sigma_{right}^2(\alpha R)}} \widehat{x}_r & , x_r \geq x_{r0}(\alpha R) \end{cases} \quad (3.7)$$

$$x_r \in \alpha R$$

where αR is the α Region, x_r the radial coordinate and x_{r0} is the radial localization of the peak and a_r the radial amplitude. The σ_{left} and σ_{right} are the left and right standard deviations related to the localization of the radial peak, respectively.

For the axial direction a Gaussian model was used to fit the axial profile, as express by:

$$SRM_{Axial}(z) = a_z e^{-\frac{(z - z_0)^2}{2\sigma_a^2}} \widehat{z} \quad (3.8)$$

where a_z is the axial amplitude, z the axial coordinate and z_0 the axial localization of the peak. The σ_a is the standard deviation related to the localization of the axial peak.

3.4 Materials and Methods

3.4.1 Estimating of the Sinogram Blurring Kernel

The parameters of the proposed sinogram resolution model were found using measured data. The acquired data of a line source (see Figure 3.6) with a length of approximated 5 cm were used to fit the asymmetric radial function. The line source was positioned with a radial offset of ~ 13 cm from the centre of the scanner. First, the raw data were binned into 2209 sinograms (207 axial slices and 15 polar subsets), each with dimensions of 256 by 288 along the radial and azimuthal directions, respectively. Then, the binned data were corrected and the central slices of the segment zero (between the slices n° 102 and n° 107) were selected and sum. After that, the result was decomposed having into account the different regions (see Figure 3.7). Each subset of the data was centre and used to generate a radial profile. The profile of the α Regions 1, 2 and 3 had approximately 150 000, 600 000 and 60 000 corrected counts, respectively. Finally the Levenberg-Marquardt [Levenberg, 1944] optimization algorithm was used to estimate the radial model parameters.

A similar procedure was used for the axial component of the blurring model. In this case the profile generated from pseudo - point source was used to find the parameters of the model. The estimated value for the σ_a was equal to 1.2 mm.

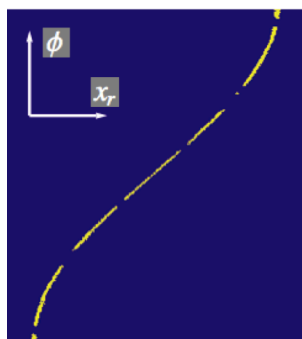


Figure 3.6- Representation of the sinogram n° 104 of segment zero (direct planes) of the raw data used to estimate the blurring model parameters.

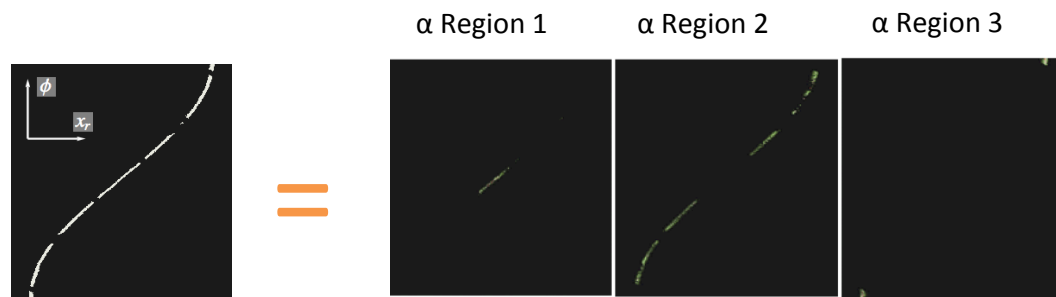


Figure 3.7- Representation of a sinogram decomposition having into account the α Regions 1 (left), the α Regions 2 (centre) and the α Regions 3 (right). The line source was positioned with a radial offset of ~ 13 cm from the centre of the scanner.

3.4.2 Data Reconstruction

A sinogram resolution modelling reconstruction (SRM-EM) was implemented (see (3.4)) and used to test the performance of the estimated blurring kernel. Point source data measured at different radial distances ($\sim 1, 5, 10$ cm) was used in this evaluation. The same datasets were reconstructed using the noRM-EM and the IRM-EM and the resulting images were compared.

Only the segment zero was reconstructed and the voxel size was equal to $0.24 \times 0.24 \times 1.22$ mm³. The total number of prompt coincidences in each dataset was $\sim 800\,000$. A block iterative reconstruction approach with 16 disjoint balanced subsets was used. For the noRM-EM the reconstruction was stopped at the iteration 5 and for the IRM-EM [Comtat et al., 2008] and SRM-EM at the iteration 10. The geometric projector utilized was based on the Joseph algorithm with bilinear interpolations [Joseph, 1982].

The estimation of the position of the point sources was made based on the centre of the mass of the reconstructed image. In Table 3.1 is presented the estimated positions (related to the centre of the scanner).

In IRM- EM a mixture of two Gaussian functions was used to model the PSF function [Comtat et al., 2008]. The first Gaussian had a FWHM equal to 2.11 mm and the second had a FWHM equal 5.9 mm. The amplitude ratio between the two was 0.05.

Table 3.1- Estimated position of the point sources for each acquisition, relatively to the centre of the scanner.

	Point Source 1cm (cm)	Point Source 5cm (cm)	Point Source 10cm (cm)
Radial	1.07	4.80	9.71
Tangential	-0.01	-0.18	-0.25
Axial	-0.15	0.23	-0.21

The sinogram n° 104 of the direct planes for the different datasets is shown in Figure 3.8.

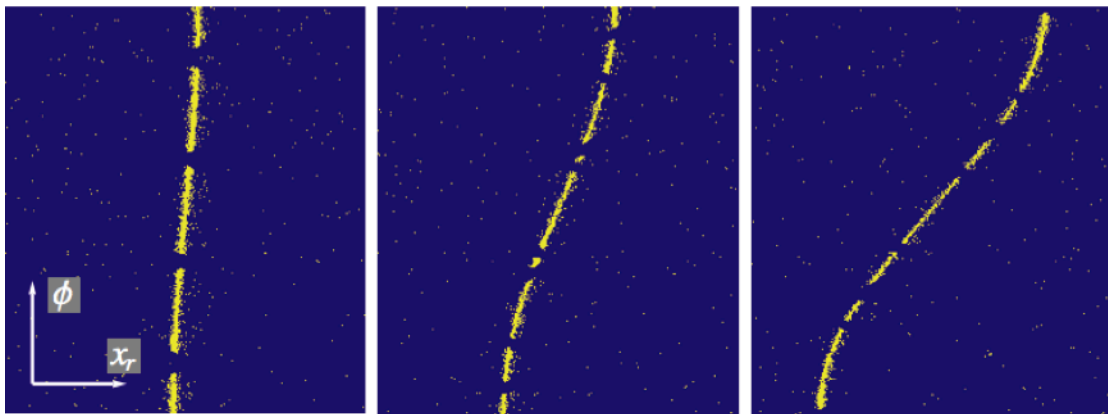


Figure 3.8- Sinogram n° 104 of the direct planes for the point sources acquired at different radial positions. Left: source position approximately at 1 cm from the centre (dataset 1). Centre: point source at 5 cm from the centre (dataset 2). Right: point source at 10 cm from the centre (dataset 3).

3.4.3 Performance Criteria

The results of the point source reconstruction using the different reconstruction techniques were compared by measuring the full width at half maximum (FWHM) of the reconstructed radial and tangential profiles. Two methods were used to measuring the FWHM.

In the first method the FWHM value was calculated following the NEMA NU 2- 2001 guidelines for spatial resolution measurements ($FWHM_{nema}$). We started by finding the maximum value of the profile by doing a parabolic fit using the peak point and its two nearest neighbouring. Then we estimated the $FWHM_{nema}$ by a linear interpolation between adjacent pixels at half the maximum value.

In the second method an asymmetric Gaussian model was used to fit the profiles. The estimated parameter values were used to calculate the correspondent FWHM for the left side ($FWHM\sigma_{left}$) and right side ($FWHM\sigma_{right}$) using

$$FWHM = 2\sqrt{2\ln 2} \sigma. \quad (3.9)$$

3.5 Results

The proposed method for the estimation of the radial sinogram blurring kernel was tested using line source data acquired in the HRRT. The decomposition of the acquired data has into account the three α Regions.

The performance of the SRM-EM using the estimated kernels was evaluated and compared with the noRM-EM and the IRM-EM.

3.5.1 Estimating of the Sinogram Blurring Kernels

Figure 3.9 presents the measured radial profiles as well as the correspondent fitted functions used in the estimation of the radial kernel for the different α Regions.

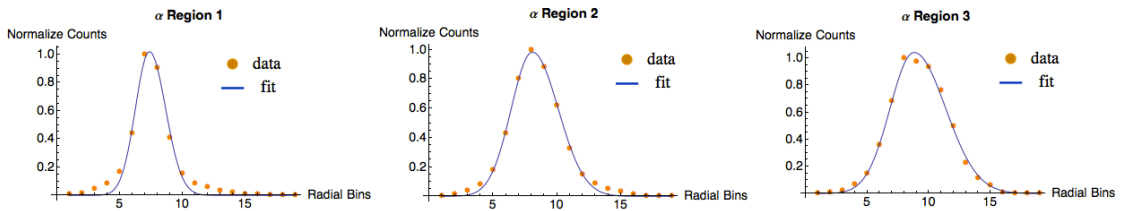


Figure 3.9- Measured radial profiles (orange points) used in the estimation of the sinogram resolution kernel parameters for the different α Regions. The blue line corresponds to the fitted curve [Levenberg, 1944]. The central slices of the segment zero of a line source acquisition were used to generate these profiles.

In Table 3.2 is presented the estimated values for the radial component σ_{left} and σ_{right} as well as the correspondent range of the α angles.

Table 3.2- Estimated values for the radial component parameters σ_{left} and σ_{right} when the decomposition of the acquired sinogram data have into account the α Regions. The corresponding range of α angles is also presented.

SRM _{radial}	Asymmetric Gaussian parameters		α angle range (degrees)	
	σ_{left} (mm)	σ_{right} (mm)	α_b range	α_a range
α Region 1	1.10	1.28	[68,90]	[68,90]
α Region 2	1.65	2.02	[45,90]	[45,90]
α Region 3	1.88	2.59	[30,60]	[30,60]

For the axial direction, the estimated value for the σ_a was equal to 1.2 mm.

3.5.2 Image Reconstruction

Figure 3.10 presents the reconstruction results using the different reconstruction algorithms for the different point source datasets. For each dataset a ROI of the transaxial slice with the maximum counts is shown.

Figure 3.11 shows the radial FWHM_{nema} as a function of the radial offset obtained using the different reconstruction algorithms. Similarly, Figure 3.12 presents the estimated tangential FWHM_{nema} as a function of the radial offset.

The variation of the radial asymmetric FWHM_{left} and FWHM_{right} as a function of the radial offset obtained using the different reconstruction algorithms is presented, respectively, in Figure 3.13 and Figure 3.14. Similarly, Figure 3.15 and Figure 3.16 shows the variation of the of the tangential asymmetric FWHM_{left} and FWHM_{right}, respectively.

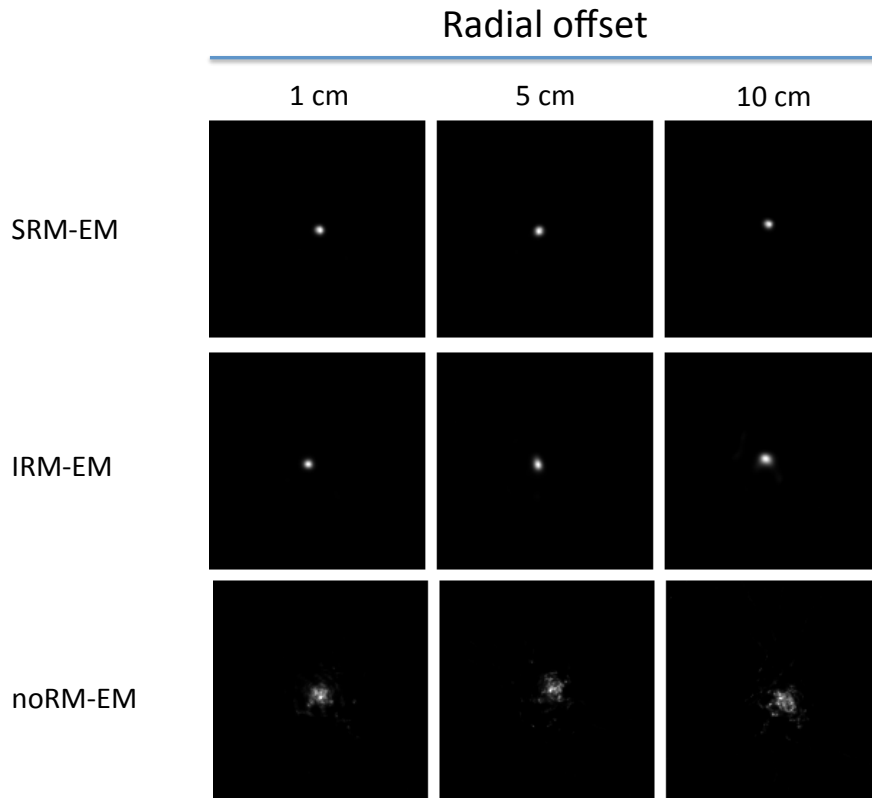


Figure 3.10- From the left to the right column: reconstruction results of a pseudo point source positioned with a radial offset of ~ 1 cm, ~ 5 cm and ~ 10 cm from the scanner centre, respectively. A block iterative reconstruction approach with 16 disjoint balanced subsets was used. For each dataset a ROI of the transaxial slice with the maximum counts is presented. Only data from the segment zero was processed. From the top to the bottom row: reconstruction results achieved by the SRM-EM (10 iterations), IRM-EM [Comtat et al., 2008] (10 iterations) and noRM-EM (5 iterations), respectively. The voxel size was equal to $0.24 \times 0.24 \times 1.22 \text{ mm}^3$.

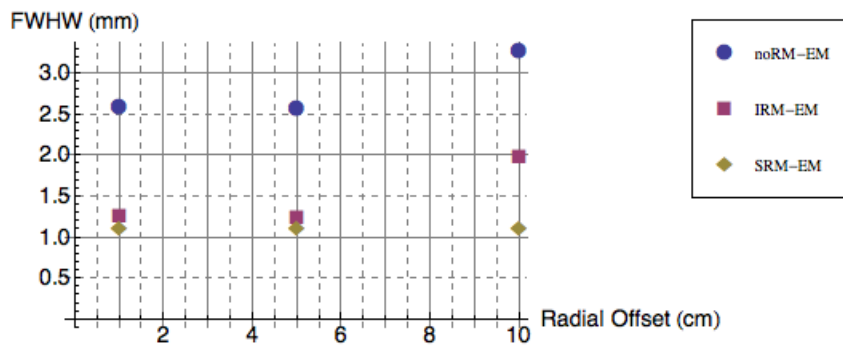


Figure 3.11- Radial $\text{FWHM}_{\text{nema}}$ as a function of the radial offset. The blue, red and yellow points correspond to the results obtained using the noRM-EM, the IRM-EM and the SRM-EM, respectively. The FWHM was calculated following the NEMA NU 2- 2001 guidelines for spatial resolution measurements.

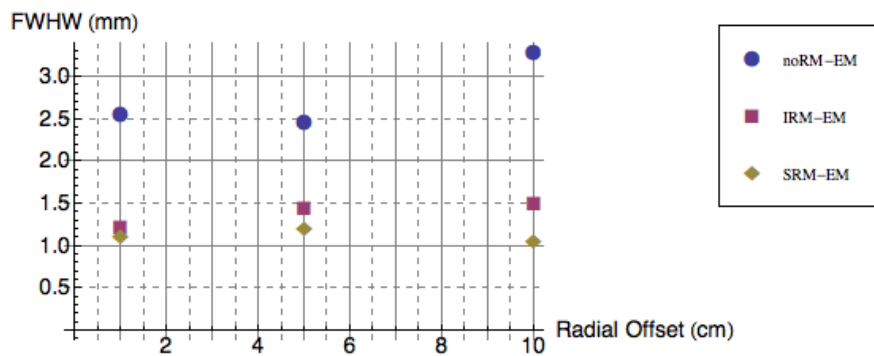


Figure 3.12 Tangential $FWHM_{nema}$ as a function of the radial offset. The blue, red and yellow points correspond to the results obtained using the noRM-EM, the IRM-EM and the SRM-EM, respectively. The FWHW was calculated following the NEMA NU 2- 2001 guidelines for spatial resolution measurements.

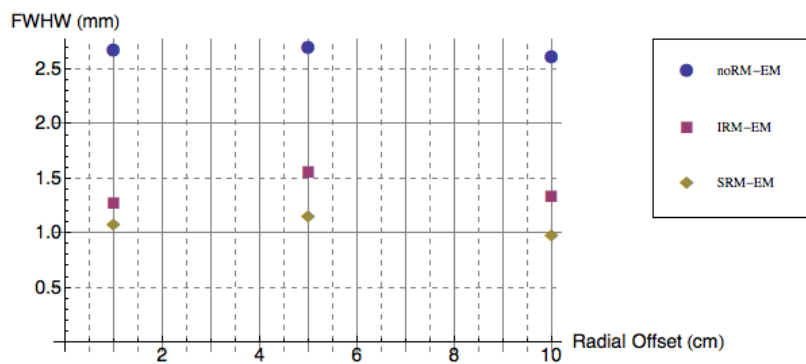


Figure 3.13- Radial asymmetric $FWHM_{left}$ as a function of the radial offset. The blue, red and yellow points correspond to the results obtained using the noRM-EM, the IRM-EM and the SRM-EM, respectively.

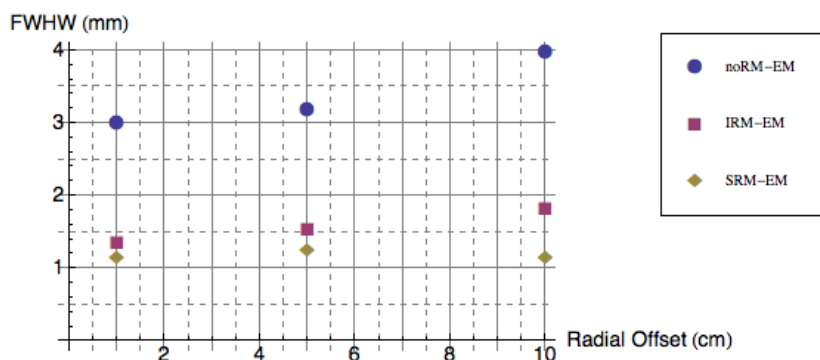


Figure 3.14- Radial asymmetric $FWHM_{right}$ as a function of the radial offset. The blue, red and yellow points correspond to the results obtained using the noRM-EM, the IRM-EM and the SRM-EM, respectively.

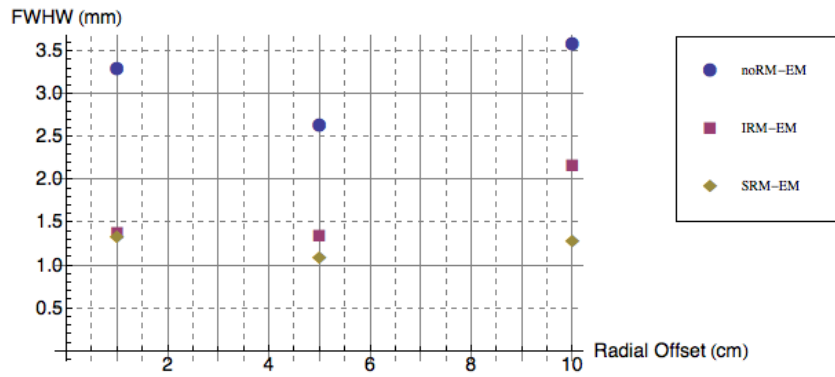


Figure 3.15- Tangential asymmetric $FWHM_{left}$ as a function of the radial offset. The blue, red and yellow points correspond to the results obtained using the noRM-EM, the IRM-EM and the SRM-EM, respectively.

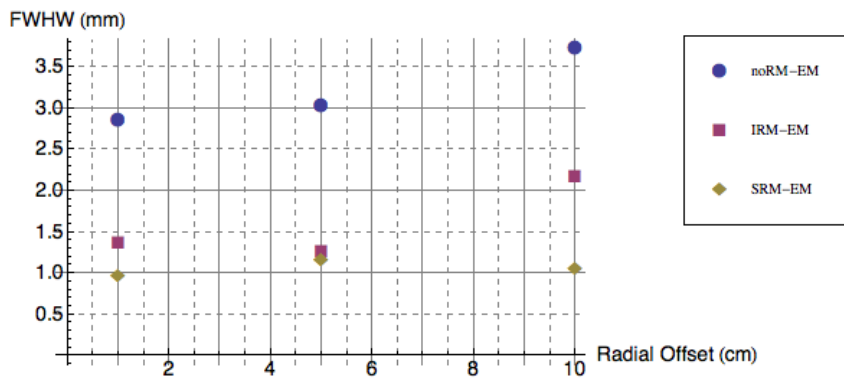


Figure 3.16- Tangential asymmetric $FWHM_{right}$ as a function of the radial offset. The blue, red and yellow points correspond to the results obtained using the noRM-EM, the IRM-EM and the SRM-EM, respectively.

3.6 Discussion

Several effects contribute to the degradation of the resolution of the reconstructed image, such as the inter-crystal penetration and non-collinearity.

A method for estimation of the sinogram blurring kernel optimized for the geometry of the HRRT was developed. Due to the geometry of the HRRT there are three different possible relations between the α angles, and thereby the sinogram can be decomposed into 3 distinct regions (α Regions). The proposed asymmetric and space-varying kernel model depends on these regions.

An acquisition of a linear source was used to measure the radial profiles of the three α Regions. The width of the α Region 1 radial profile was smaller than the profile widths of the other two regions (see Figure 3.9). This behaviour was expected because this region has the range of α values close to the 90° (normal). In opposition, for α Region 3 the maximum α value is about 60° and so the width of the profile was the highest. The values of the fitted parameters σ_{left} and σ_{right} also demonstrate this behaviour (see Table 3.2).

Point source data acquired at different radial positions were used to test the performance of the SRM-EM reconstruction algorithm (see Figure 3.10). When data were processed with the noRM-EM reconstruction algorithm the radial FWHM increase when the point source was positioned at 10 cm from the centre. At that position, the radial $\text{FWHM}_{\text{nema}}$ was 3.3 mm and when positioned at 1cm was 2.6 mm (see Figure 3.11). These results are in agreement with the resolution measurement results reported by Jong *et al.* [Jong et al., 2007].

The proposed method allows for the improvement of the resolution for the different radial positions tested (see Figure 3.11 and Figure 3.12). When compared with the IMR-EM, the SRM-EM permits the reduction of the variation of the radial and tangential $\text{FWHM}_{\text{nema}}$.

An asymmetric Gaussian model was also used to fit the radial and tangential profiles of the reconstructed point sources. Since the geometric projectors used in this study are based on the Joseph algorithm with bilinear interpolations, the reconstructed point source profiles should be Gaussian. Globally, the profiles of the point source

reconstructed with RM methods were more symmetric (see Figure 3.13 to Figure 3.16).

3.7 Conclusion

A resolution modelling in the sinogram space was developed and tested for a non cylindrical PET scanner geometry.

The proposed method for estimation of the sinogram blurring kernel has into account the angle of incidence (α angle) i.e., the angle defined by the intersection of a given LOR with a detection head. The parameters of the model radial component are found using only one measurement.

The estimated blurring kernels were used in the reconstruction of point source data acquired at different radial distances. When compared with the noRM-EM and IMR-EM, the SRM-EM allowed for the improvement of the resolution of the reconstructed point sources as well as for the reduction of the variation of the radial and tangential FWHM over the different radial positions tested.

Chapter 4

4 Multiscale Reconstruction in PET

The multiscale reconstruction (MS) algorithms were proposed to improve the convergence rate and reduce the reconstruction computation time. When compared with the usual single grid reconstruction approach, the MS introduces new variables in the reconstruction algorithm such as the interpolator operator, the number of iterations to do in a given scale and the number of scales.

The main motivations of the work presented in this chapter were to study the impact of the use of different scales in convergence speed and choose the most suitable interpolator operator.

First we present the state-of-the-art of the multiscale reconstruction for emission reconstruction. We then discuss the results that lead to the choice of the Gaussian kernel as the most suited interpolator to be used in the MS reconstruction. Finally, we compare the performance of the MS reconstruction approach with the performance of the ML-EM reconstruction algorithm.

4.1 Multiscale Reconstruction

Instead of improving the convergence of the reconstruction algorithm by using data subsets, the multiscale techniques attempt to reduce the computational effort and improve the convergence by processing the data at different scales.

In 1988 Ranganath *et al.* [Rangana et al., 1988] proposed the multigrid expectation maximization algorithm (MGEM) which explore the concept of multiscale applied to

the ML-EM for Positron Emission Tomography (PET). In this algorithm the multiscale is only applied to the image space. It was tested with simulated and with real data acquired in the TOFPET-I [142]. They claim that this algorithm allows for the decreasing of reconstruction time by a factor of 10. The number of iterations performed in each scale was chosen based on the log-likelihood function variation [Rangana et al., 1988]. In 1999 Rahej *et al.* [Raheja et al., 1999] proposed an extension of the MGEM, the Multiresolution Expectation Maximization algorithm (MREM). In this method the dimensions of the projection space also change during the reconstruction.

Figure 4.1 presents a schematic representation of a MS reconstruction.

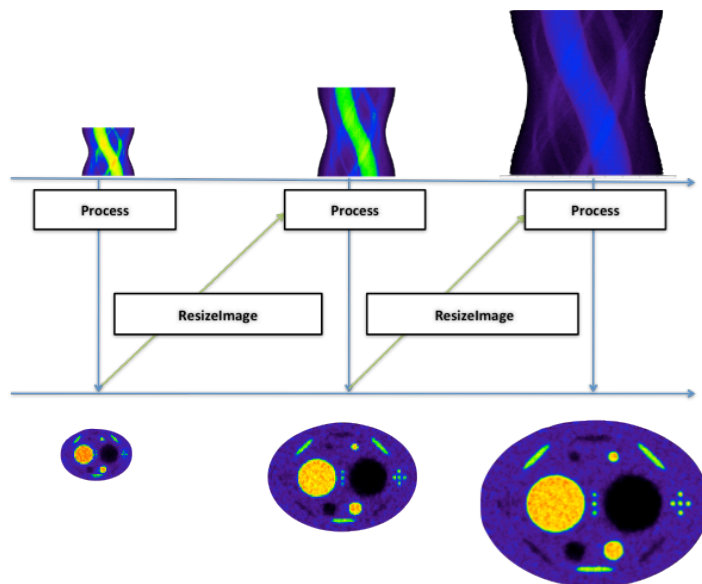


Figure 4.1- Schematic representation of the multiscale reconstruction.

In general, multiscale algorithms begin the reconstruction at coarsest image scale using data that have been binned at coarsest detector level. After a few iterations in a particular scale, the image scale and the projection binning scale switch until the finest binning projection is reached. At coarse scales the low frequency components of the image can be reconstructed with low computational effort. For dyadic scales, the maximum frequency that can be recovered on the coarse scale corresponds to approximately one-half of the maximum frequency that can be recovered on the next scale.

Using simulated data, the reconstruction root mean square error (RMSE) of the final image achieved by the MREM was lower when compared with the ML-EM [Raheja et al., 1999]. The ML-EM was allowed to iterate for an equal amount of CPU time as the MREM algorithm. The MREM stopping criterion was based on the variation of the energy of the high-high wavelet band of the reconstructed image (see section 6.1). With real data the authors of [Raheja et al., 1999] claim that MREM performs well, produces better images and also point out that this algorithm introduces some regularization in the reconstruction. In clinical protocols this kind of regularization is achieved by post-filtering of the final image. Please note that when the fine scale system matrix is not singular the ML estimate is unique and in this case the MREM algorithm should converge to the same image. However as the reconstruction is usually stopped before the maximum of the objective function has been reached, the solutions given by the two algorithms can be different.

Pan et Yagle [Pan et Yagle, 1991] made a numerical characterization of the multiscale concept versus single scale applied to different algorithms such as Landweber [Bertero et al., 1998], Algebraic Reconstruction Algorithm (ART) and ML-EM. The reconstructions were made using noise free 2D tomographic data. Three different system matrices were used in the comparative study: a small (195 projections by 144 pixels) and not singular matrix, a small (84 projections by 144 pixels) and singular matrix and a system matrix with a bigger size (4160 projections by 3228 pixel). For the multiscale reconstruction a coarse scale matrix was generated for each system matrix. Four main conclusions can be highlighted from this study.

First, Pan *et al.* underline the capabilities of the multiscale methods to recover high-frequency components in the case of the values of neighbouring fine-grid pixels to be grouped as a coarse-grid pixel have similar values [Pan et Yagle, 1991]. Second, they also found that since the fine grid iteration is able to recover the low-frequency components, the advantage of using multiscale for certain image reconstruction methods can disappear after a certain number of fine-grid iterations. Third, the authors show that for some specific cases when the system matrices are singular, the use of coarse system matrices allows for the recovery of elements in the null space of the fine-grid system matrix. Frequencies that cannot be recovered with the finest grid reconstruction with a uniform initial condition are recovered with the multiscale

initial condition. Fourth, they also presented cases where the coarse-grid iteration is unable to recover high frequencies or introduces incorrect high-frequencies.

In literature it can also be found multiscale reconstruction techniques based on wavelets [Bhatia et al., 1996][Delaney et Bresler, 1994][Delaney et Bresler, 1994][Turkheimer et al., 1999][Alpert et al., 2006][Reader et al., 2006][Verhaeghe et al., 2008]. Nowak and Kolaczyk [Nowak et Kolaczyk, 2000] proposed a statistical multiscale framework for Poisson inverse problems. They show that Harr multiscale analysis [Daubechies, 1992] is especially appropriated to Poisson data. This framework admits a simple EM algorithm for computing the Maximum a *Posteriori* reconstructions [Nowak et Kolaczyk, 2000]. Raheja *et al.* [Raheja et Dhawan, 2000] transform the MGEM algorithm to a wavelet-based Multiresolution EM (WMGEM). Instead of virtually grouping the detectors, the multi-resolution data space is generated by performing a 2D wavelet transform in the sinogram space. The High-High frequency band is discarded (in order to reduce the noise) and the Low-High and the High-Low bands are subjected to thresholding or DC shifting [Raheja et Dhawan, 2000] in order to remove the negative values. For each band the corresponding images are estimated using the ML-EM algorithm. Then, the inverse wavelet transform of the three estimated images (the High-High frequency band has the value zero) is done. The synthesized image is used as initial condition to the Low-Low band of next scale. For the other two bands the initial image is a uniform image. They tested this algorithm with simulated and real data. The authors claim that WMREM provides better quality images for PET image reconstruction when compared to MGEM and single grid EM methods. However, since the High-High band is discarded, the data is no longer Poisson distributed and the use of the ML-EM for Poisson noise is no longer justified.

Multigrid algorithms [Briggs, 2000] are very popular for solving differential equations. Under this context, these algorithms allow a systematic projection of the data from the coarse scale to the fine scale as well as from the fine scale to the coarse. Based on the previous work done on optical diffusion [Oh et al., 2005][Oh et al., 2003a][Oh et al., 2003b][Ye et al., 1999] Oh *et al.* proposed [Oh et al., 2006] a multigrid bayesian reconstruction for transmission or emission tomography. This method was tested using a three level multigrid-V recursion configuration [Briggs, 2000]. A fixed-grid Iterative Coordinate Descent (ICD) algorithm [Bouman et al.,

1996] with random-order pixel updates was used in each grid. They concluded that the multigrid approach allows for the improvement of the convergence speed.

In clinical reconstruction for emission tomography the use of ICD is not common. Recently Van Slambrouck and Nuyts [Van Slambrouck et Nuyts, 2010], [Van Slambrouck et Nuyts, 2011] proposed to divide the image in a matrix of equally sized cuboids and update them separately as groups of pixels using a grouped coordinate ascent algorithm [Fessler et al., 1997]. They reported improvements in convergence speed when applied to transmission or emission tomography. Using equally sized cuboids, they reported an improved convergence degree proportional to the square root of the number of patches. However, this method leads to differences in convergence rates between the different patches that can result in visible edges between them.

References to reconstruction algorithms where the proposed grid is not uniform (see Figure 4.2) can be found in the literature, such as reconstructions using mesh grids [Brankov et al., 2004], point cloud image representations [Sitek et al., 2006] and adaptive multi-level refinement [Schumacher et al., 2008].

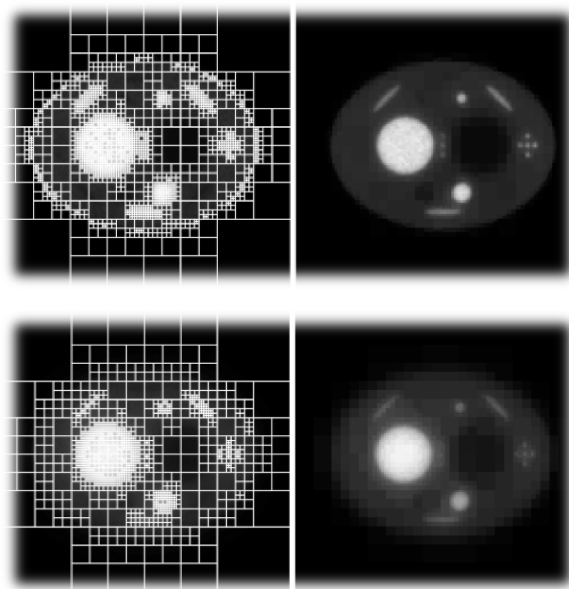


Figure 4.2- Example of the representation of an image using a non-uniform grid. Left: image using a non-uniform grid with the border pixels highlighted. Right: the same image without highlighting the borders of the pixels. The top line represents a case where the non-uniform grid allows to obtain an image with better quality than the image at the bottom, where the non-uniform representation adds artefacts.

4.2 Materials and Methods

4.2.1 The Multiscale Algorithm

In general, the MS algorithms such as MREM can be expressed as:

$$\lambda_s^{k+1} = \frac{\lambda_s^k}{\mathbf{H}_s^T \mathbf{1}_{y_s}} \mathbf{H}_s^T \frac{y_s}{\mathbf{H}_s \lambda_s^k} \quad (4.1)$$

where s represents a generic scale (the fine scale corresponds to $s=1$), \mathbf{H}_s is the system matrix at the scale s and λ_s^k the estimate image at the scale s and in the iteration k . The y_s is the set of data binned onto the projection matrix at the scale s and the $\mathbf{1}_{y_s}$ is a vector of ones with the same size as y_s . The initial condition, λ_s^0 , used in the scale s is given by:

$$\lambda_s^0 = \begin{cases} \mathbf{1}_{s_{max}}, & s = s_{max} \\ \mathbf{I}_s \lambda_s^{K_{s+1}}, & s \neq s_{max} \end{cases} \quad (4.2)$$

where K_{s+1} is the number of ML-EM iterations made in the previous scale ($s+1$), \mathbf{I} is the interpolation operator that maps the previous scale image to the next scale image and $\mathbf{1}_{s_{max}}$ is a constant image of ones with the same dimensions of the coarsest scale s_{max} , image used.

Interpolator Operator

Different resampling kernels can be used to map the reconstructed image of the previous scale to the next scale. In this study we tested four different kernels: the nearest neighbour, the cubic, the Lanczos and the Gaussian.

In the nearest neighbour interpolation the interpolated value is equal to the nearest available value. The corresponding two-dimensional kernel is given by:

$$\mathbf{w}_{nearest}(x, y) = \begin{cases} 1 & \text{if } -0.5 \leq x, y < 0.5 \\ 0 & \text{if } \textit{otherwise} \end{cases} \quad (4.3)$$

with x and y the arbitrary continuous positions in the horizontal and vertical directions, respectively.

The one dimension cubic kernel (see Figure 4.3) is defined as a piecewise cubic polynomial given by [Burger et al., 2009]

$$\mathbf{w}_{cubic}(x) = \begin{cases} |x|^3 - 2|x|^2 + 1 & \text{if } 0 \leq |x| < 1 \\ -|x|^3 + 5|x|^2 - 8|x| + 4 & \text{if } 1 \leq |x| < 2. \\ 0 & \text{if } |x| \geq 2 \end{cases} \quad (4.4)$$

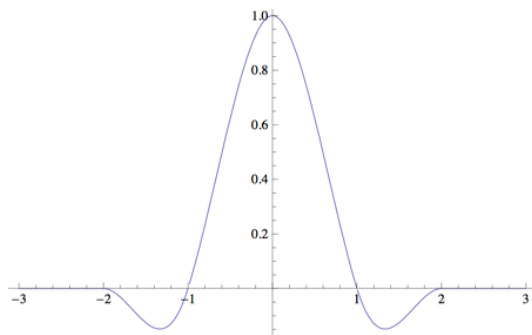


Figure 4.3- Representation of the one-dimensional cubic kernel.

The one dimensional kernel used for the Gaussian interpolation (see Figure 4.4) is given by [Burger et al., 2009] ,

$$\mathbf{w}_{gaussian}(x) = \begin{cases} e^{-\frac{x^2}{2 \cdot 0.5^2}} & \text{if } |x| < 3 \\ \frac{1}{\sqrt{2\pi} \cdot 0.5} & \text{if } |x| \geq 3 \end{cases} \quad (4.5)$$

and the one-dimensional Lanczos kernel (see Figure 4.5) is given by [Burger et al., 2009] ,

$$\mathbf{w}_{lanczos}(x) = \begin{cases} 1 & \text{if } |x| = 0 \\ 3 \frac{\sin(\pi \frac{x}{3}) \sin(\pi x)}{\pi^2 x^2} & \text{if } 0 < |x| < 3 \\ 0 & \text{if } |x| \geq 3 \end{cases} \quad (4.6)$$

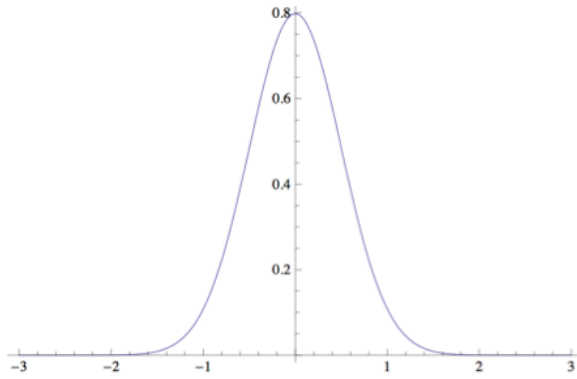


Figure 4.4- Representation of the one-dimensional Gaussian kernel.

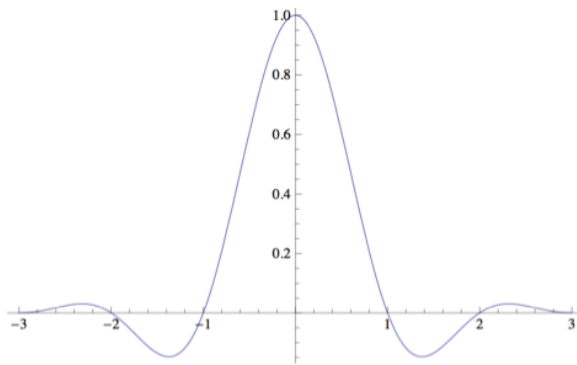


Figure 4.5- Representation of the one-dimensional Lanczos kernel.

The corresponding two dimensional kernels can be calculated using,

$$\mathbf{W}_m(x, y) = \mathbf{w}_m(x)\mathbf{w}_m(y) \quad (4.7)$$

with, $m = \{Lanczos, Gaussian, cubic, nearest\}$.

In the case of the cubic interpolation the interpolated values are calculated using [Burger et al., 2009]

$$\lambda(x, y) = \left[\sum_{v=[x_0]-1}^{|y_0|+2} \left[\sum_{u=[x_0]-1}^{|x_0|+2} \lambda(u, v) \mathbf{W}_{cubic}(x - u, y - v) \right] \right]_0. \quad (4.8)$$

This interpolation have in account the values of the 16 neighbour pixels.

The interpolated values using the Gaussian and Lanczos 2D kernels are found using [Burger et al., 2009]

$$\lambda(x, y) = \left[\sum_{v=\lfloor x_0 \rfloor - 2}^{\lfloor y_0 \rfloor + 3} \left[\sum_{u=\lfloor x_0 \rfloor - 2}^{\lfloor x_0 \rfloor + 3} \lambda(u, v) \mathbf{W}_{\{gaussian, lanczos\}}(x - u, y - v) \right] \right]_0. \quad (4.9)$$

These interpolations take into account the 36 nearest neighbor pixels. The interpolation results are projected to the \mathbb{R}_0^+ space in order to remove negative values, which do not have any physical meaning.

4.2.2 Generation of the Simulated Raw Data

We made analytic simulations [Comtat et al., 1999] of a 3D phantom composed of 26 ellipsoids (phantom n° 1), acquired by a tomograph with a geometry similar to the High Resolution Research Tomograph (HRRT, Siemens). Scatter, randoms and attenuation were not simulated.

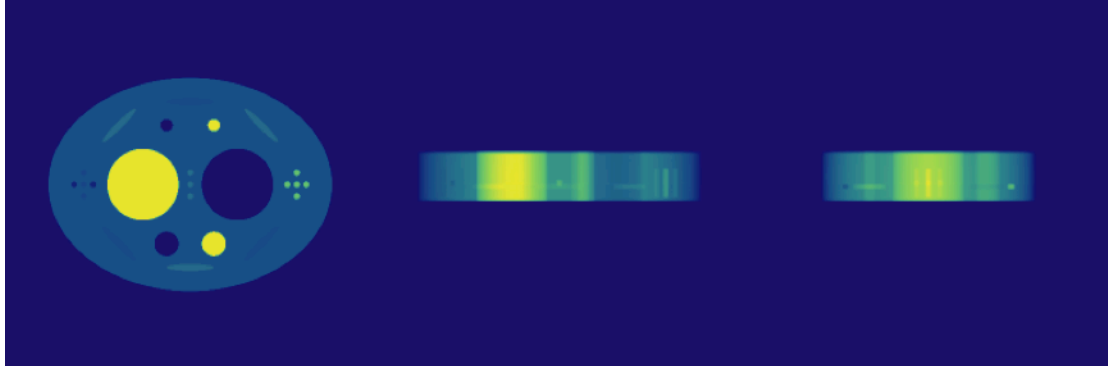


Figure 4.6- From the left to the right: sum of all the planes in the transaxial, coronal and sagittal directions of the phantom n° 1.

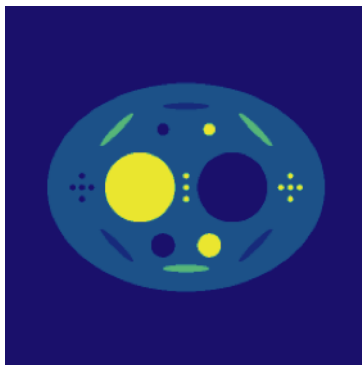


Figure 4.7- Transaxial slice n° 104 of the phantom n° 1.

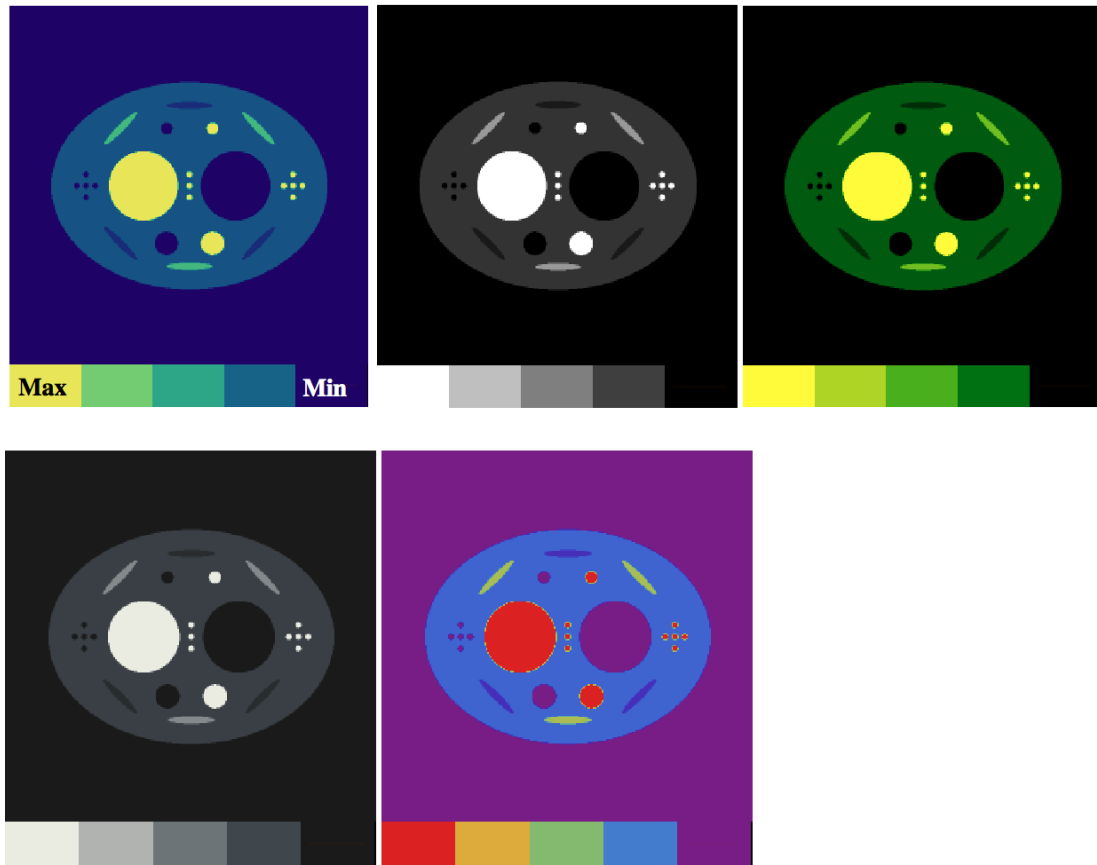


Figure 4.8- Transaxial slice n° 104 of the digital phantom n° 1 represented with the different color gradients used in this thesis.

Figure 4.8 shows the slice n° 104 of the digital phantom n° 1 using the different colour gradients utilized in this thesis. The diameter of the structures utilized in this thesis was 6 mm for the point source and 12, 20, 70 mm for the small, medium and large sources, respectively (see Figure 4.9).

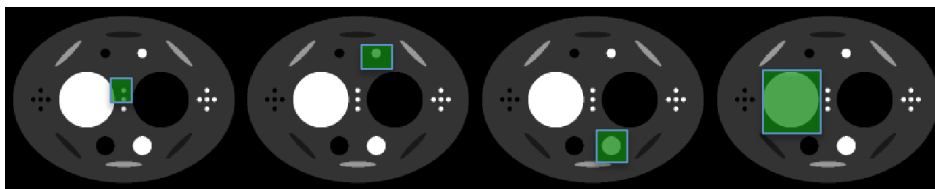


Figure 4.9- From the left to the right: Highlight of the point source and of the small , medium and large sources used in this thesis.

In this thesis, the contrast of the hot structures studied, as defined in (4.14), was 4. For the cold structures the contrast, as defined in (4.15), was 1.

The simulated dataset, with $\sim 1 \times 10^8$ counts, were binned as described in section 3.4.1. Three scales were used in the multiscale reconstruction. The fine scale corresponds to the simulated data binned with the usual dimensions. The medium and coarse scales were generated by adding the two adjacent LORs in the azimuthal direction and in the radial direction of the sinogram of the previous scale. Thus for scale s ($s=1,2,3$ for the fine, medium and coarse scales respectively), the sinograms used in this study had $256/2^{(s-1)}$ bins radially and $288/2^{(s-1)}$ bins along the azimuthal direction. The corresponding reconstructed images had $256/2^{(s-1)}$ pixels by $256/2^{(s-1)}$ pixels by 207 pixels (x, y and z directions respectively) (see Figure 4.10). In terms of physical dimensions these correspond to $1.21 \times 2^{(s-1)}$, $1.21 \times 2^{(s-1)}$ and 1.21 (mm) in the x, y and z directions, respectively. Figure 4.11 presents the sinogram of the slice $n^\circ 104$ of the segment zero and the corresponding histogram at the different scales. The maximum number of counts was of 172, 62 and 21 for the coarse, medium and fine scales, respectively.

The reconstructions of the data were done using all the data available (3D dataset) as well as using only the direct planes (2D dataset).

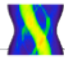


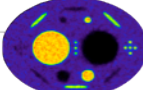
			
SinogramStackSize	(64x72x2209)	(128x144x2209)	(256x288x2209)
Scale	S3	S2	S1
Reconstructed ImageSize	(64x64x207)	(128x128x207)	(256x256x207)
			

Figure 4.10- 3D raw data dimensions and image dimensions used in the coarse ($s=3$), medium ($s=2$) and fine scale ($s=1$).

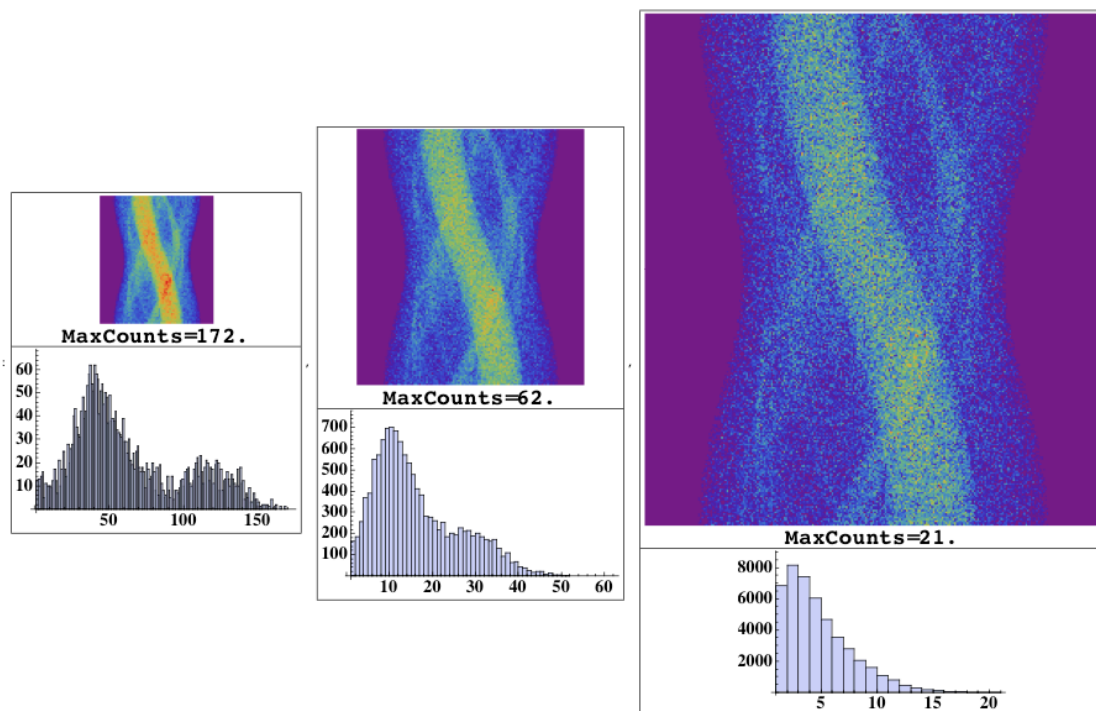


Figure 4.11- From left to right: sinogram of the slice n° 104 of 2D dataset (top) and the corresponding histogram (bottom) of the coarse, medium and fine scales, respectively.

4.2.3 Performance Criteria

Choice of the Interpolation Kernel

The effects of using different interpolators in the final image were studied having into account the variations of the reconstruction error in sinogram space, denoted by

$$\mathbf{SinoRecError}(k) = \sum_i (\mathbf{y}_1(i) - (\mathbf{H}_1 \boldsymbol{\lambda}_1^k)(i))^2, \quad (4.10)$$

and the number of iterations required by the stopping criterion. The criterion to choose the number of iterations to use in a particular scale was based on the image space reconstruction error, defined by:

$$\mathbf{imageRecError}(k) = \frac{\sqrt{\sum_j (\lambda_{true}(j) - \lambda_1^k(j))^2}}{\sum_j \lambda_{true}(j)}, \quad (4.11)$$

where the λ_{true} is the true activity image.

Visual inspection of the final reconstructed images, the analysis of profiles and the (logarithm) power spectrum of the 2D Fourier transform of the final image central slice [Burger et al., 2009],

$$|\mathbf{X}|(\lambda^K) = \text{Log}(\text{Abs}(\mathcal{F}_2\{\lambda^K\})), \quad (4.12)$$

were also used.

The texture of the reconstructed image slices were also studied by analysing the 2D co-occurrence matrix defined by :

$$\mathbf{C}_{\Delta x, \Delta y}(i, j) = \begin{cases} \sum_{p=1}^{128} \sum_{q=1}^{128} 1, & \text{if } \lambda^k(p, q) = i \text{ and } \lambda^k(p + \Delta x, q + \Delta y) = j \\ 0, & \text{otherwise} \end{cases} \quad (4.13)$$

with λ^k the estimated slice at iteration k organized in a 2 dimension space and mapped into 128 quantization levels. In this study we only report on the co-occurrence for $\Delta x = \Delta y = +1$.

Performance of the Multiscale Reconstruction Algorithm

The stopping criterion in the coarse scales was the minimum error in the image space. Based on the analysis of the reconstruction results using the different interpolators (see section 4.3.1), the Gaussian interpolator was chosen as interpolator kernel.

The performance of the MS and the ML-EM were evaluated taking into account the variation of the reconstruction error in the sinogram space (as in (4.10)). An analysis based on Regions of Interest (ROIs) in the reconstructed images (fine scale in the case of MS) was also made. For each ROI was analysed the hot and cold

contrast given by:

$$\text{contrast}_{\text{hot}} = \frac{R(k) - B(k)}{B(k)} \quad (4.14)$$

and

$$\text{contrast}_{\text{cold}} = 1 - \frac{R(k)}{B(k)} \quad (4.15)$$

, respectively, where R is the mean activity in the ROI and B the mean activity in the background (see Figure 4.12).

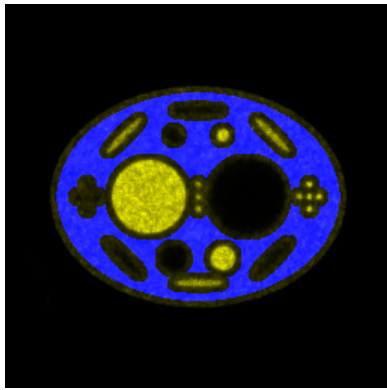


Figure 4.12- Representation of the background ROI (blue region).

Visual inspection of the final reconstructed images, as well as of the power spectrum (as expressed by (4.12)) of the reconstruction images and of the initial condition images were done in order to find reconstruction artefacts. The co-occurrence matrix was also analysed.

4.3 Results

4.3.1 Interpolator Operator

The performance of four different interpolators was tested: nearest neighbour interpolation (see (4.7)), cubic interpolation (see (4.8)), Gaussian interpolation(see (4.9)) and Lanczos interpolation (see (4.9)). The stopping criterion used in each scale was the minimum error in image space as expressed by (4.11).

Table 4.1 shows the iteration number where the minimum image space error was obtained for the different scales using the different interpolations.

Table 4.1 - Number of iterations needed to reach the minimum error in the image space using the 3D dataset and using the 2D dataset for the different interpolation methods (Gaussian, nearest neighbour, Lanczos and cubic) in the fine (S_1), medium (S_2) and coarse scales (S_3).

	3D dataset				2D dataset			
	Gaussian	Nearest	Lanczos	Cubic	Gaussian	Nearest	Lanczos	Cubic
S_3	14	14	14	14	13	13	13	13
S_2	21	23	20	21	7	6	6	8
S_1	17	17	15	18	3	3	3	3

Figure 4.13 presents the fine scale sinogram reconstruction error as a function of the number of iterations for the different interpolation algorithms using the 3D dataset (top row) and the 2D dataset (bottom row).

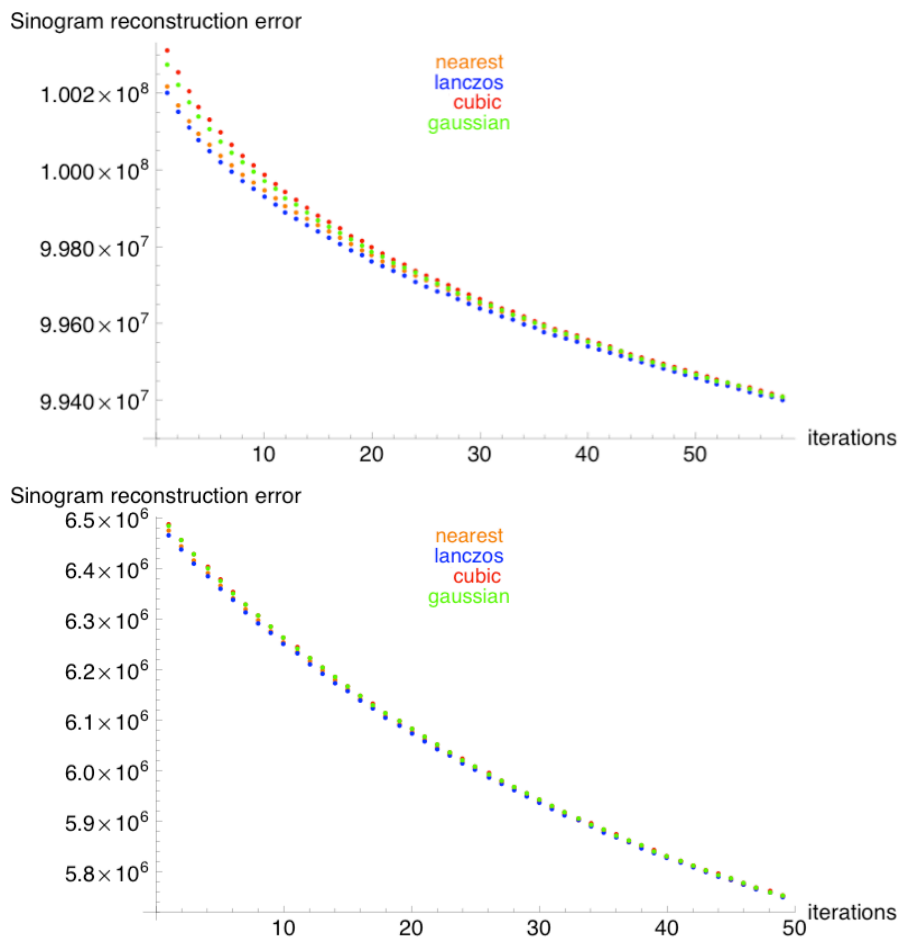


Figure 4.13- Sinogram reconstruction error in the fine scale as a function of the number of iterations for the different interpolation methods using all the available data (top) and using only the direct planes (bottom).

Figure 4.14 presents the sum of the transaxial planes of the reconstruction result using the Gaussian, nearest neighbour, cubic and Lanczos interpolation (from

left to right). The top (bottom) row corresponds to the reconstruction images obtained using the 3D dataset (2D dataset). Similarly, the sum of the coronal and sagittal planes are presented in Figure 4.15 and Figure 4.16, respectively.

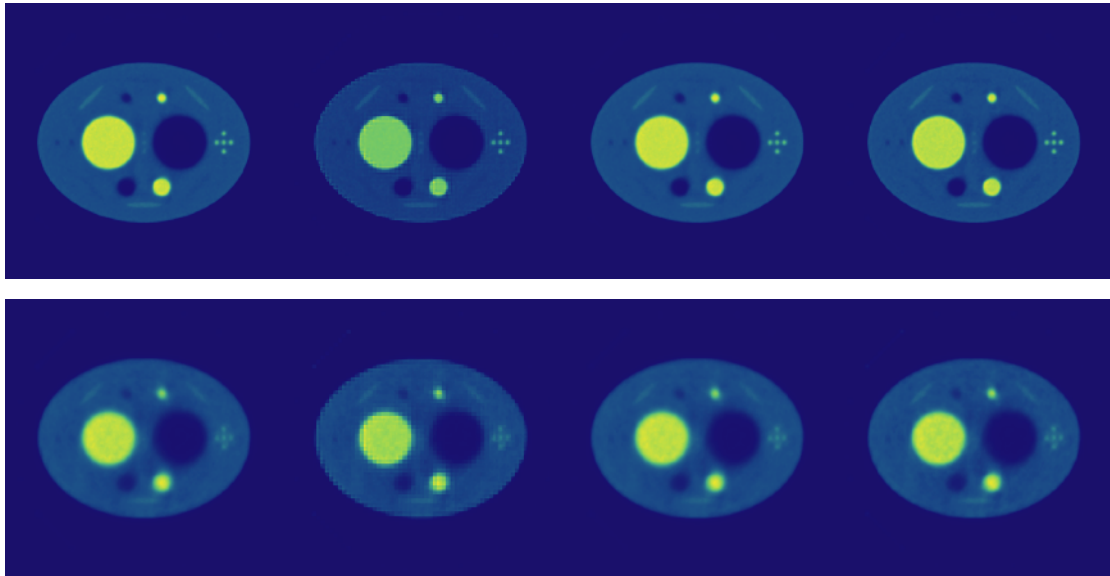


Figure 4.14- Sum of the transaxial planes of the reconstruction images obtained using the Gaussian, nearest neighbour, cubic and Lanczos interpolation (from left to right respectively) when the 3D dataset is used (top row) and when the 2D dataset is used in the reconstruction (bottom row).

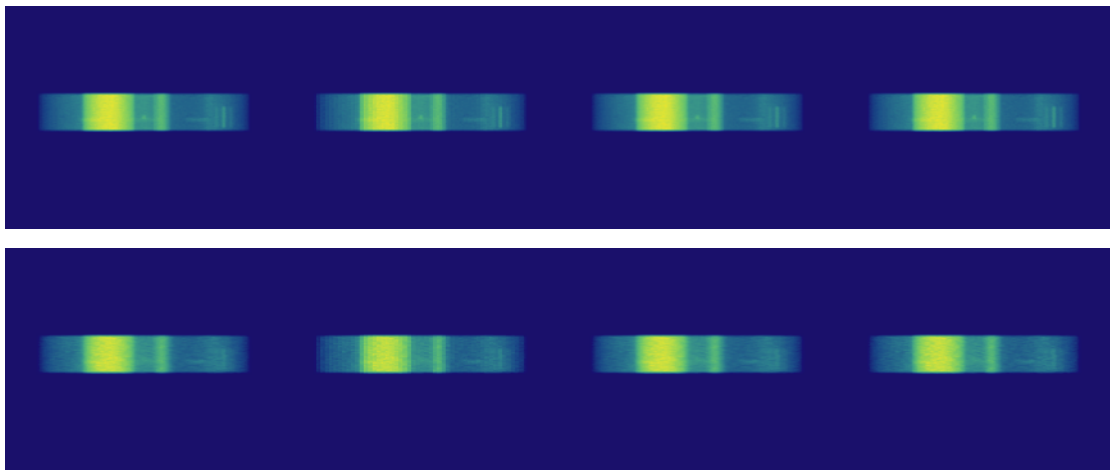


Figure 4.15- Sum of the coronal planes of the reconstruction results obtained with Gaussian, nearest neighbour, cubic and Lanczos interpolation (from left to right respectively) when the 3D dataset is used (top row) and when the 2D dataset is used in the reconstruction (bottom row).

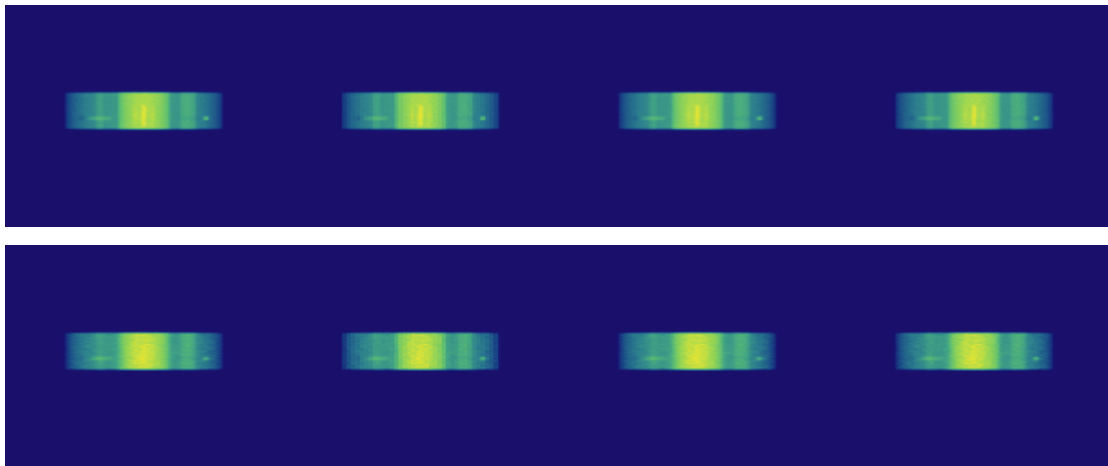


Figure 4.16- Sum of the sagittal planes of the reconstruction results obtained with Gaussian, nearest neighbour, cubic and Lanczos interpolation (from left to right respectively) when the 3D dataset is used (top row) and when the 2D dataset is used in the reconstruction (bottom row).

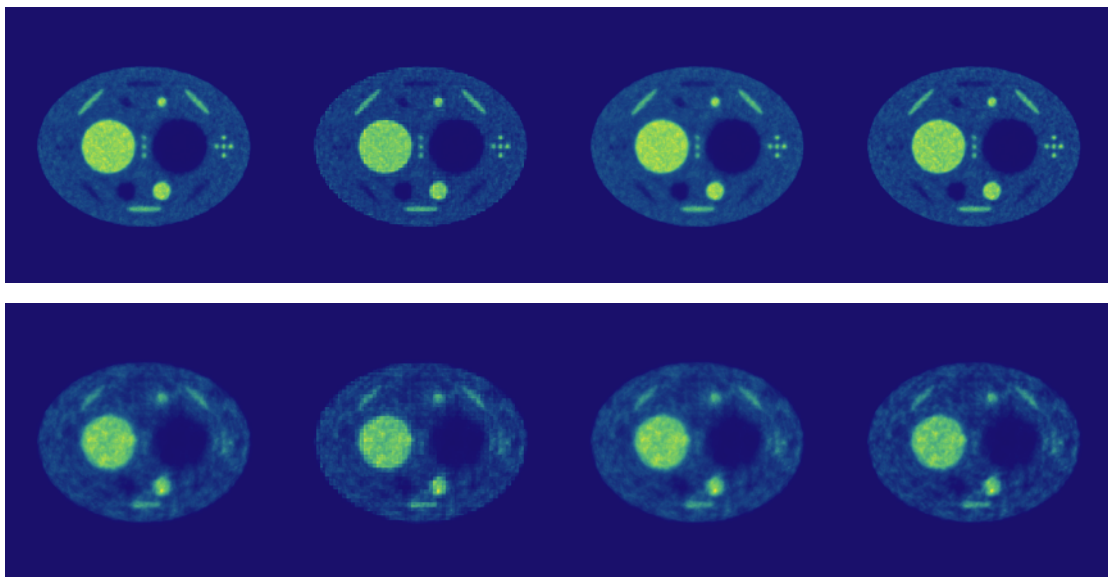


Figure 4.17- Transaxial slice n° 104 of the reconstruction results obtained with Gaussian, nearest neighbour, cubic and Lanczos interpolation (from left to right respectively) when the 3D dataset is used (top row) and when the 2D dataset is used in the reconstruction (bottom row).

Figure 4.17 shows the results obtained for transaxial slice n° 104 for the different resampling algorithms.

Figure 4.18 presents the profiles of the slice n° 104 of the reconstruction results as a function of the interpolation method when the 3D dataset (top row) and the 2D dataset (bottom row) are used in the reconstruction. The left column profiles cross a region with 3 small hot structures and the profiles in the right column cross a region with a big cold structure.

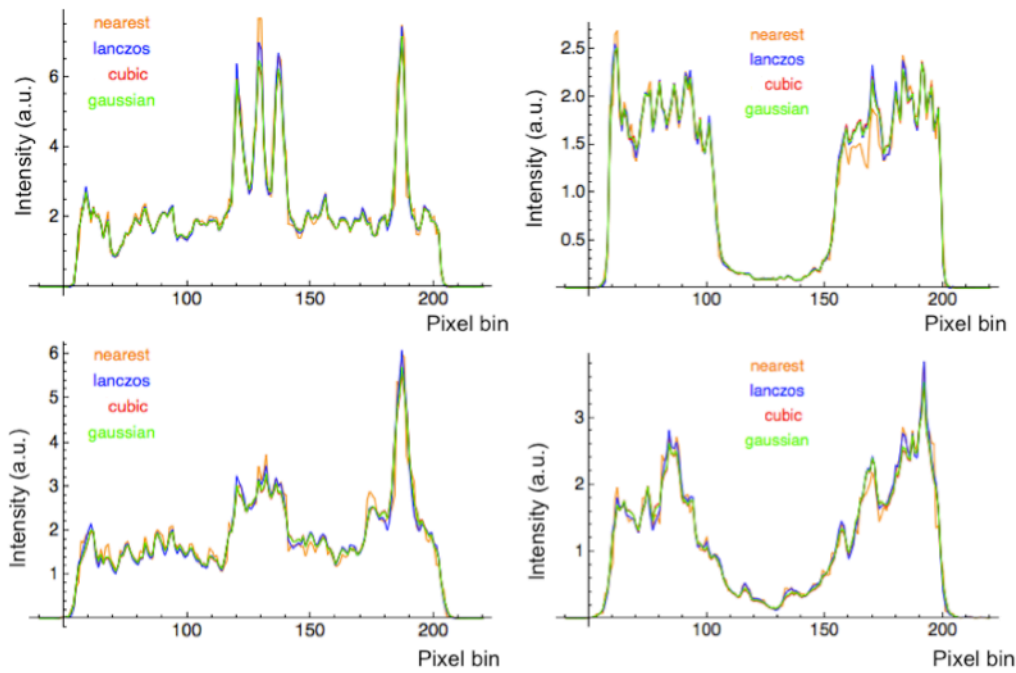


Figure 4.18- Profiles of transaxial slice n° 104 of the reconstruction results obtained with the Gaussian, nearest neighbour, cubic and Lanczos interpolation (from left to right) when the 3D dataset is used (top row) and when the 2D dataset is used in the reconstruction (bottom row). The profiles on the left cross a region with 3 small hot structures and the profiles on the right cross a region with a big cold structure.

The power spectra of the Fourier transform applied to the different initialization images used in the fine scale reconstructions are shown in Figure 4.19.

Figure 4.20 and Figure 4.21 show the co-occurrence matrix of the slice n° 104 in the transaxial plane of the initialization image in the fine scale using different interpolation methods when all available data were used and when only the direct planes were used in the reconstruction, respectively.

Figure 4.22 shows the power spectrum of the Fourier transform applied to the true phantom.

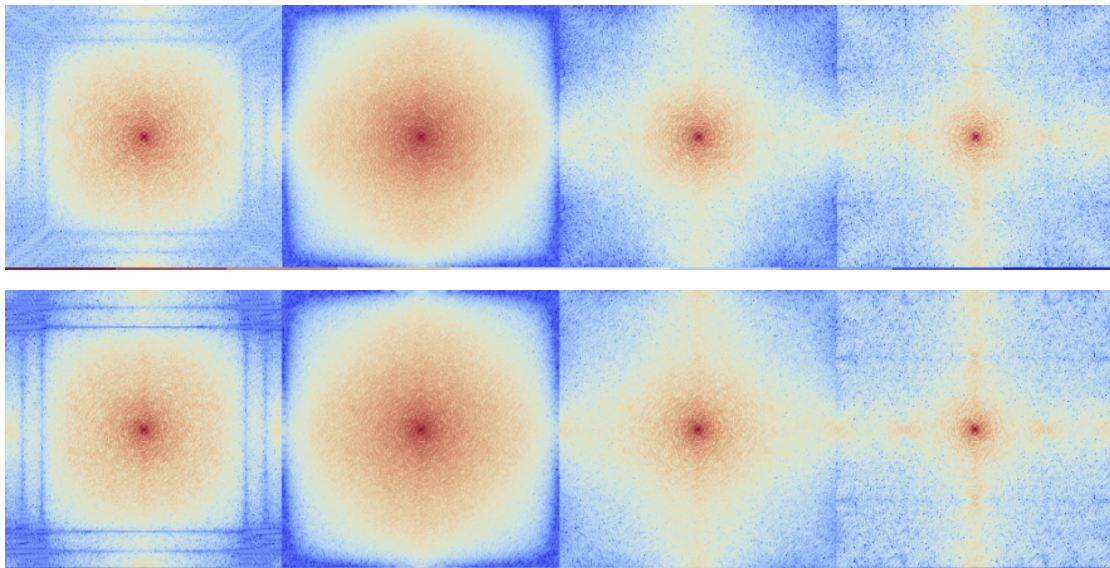


Figure 4.19- Power spectrum of the Fourier transform applied to the transaxial slice n° 104 of the fine scale initialization image using as interpolation method the Gaussian, the nearest neighbour, the cubic and the Lanczos kernel (from left to right respectively) when the 3D dataset is used (top row) and when the 2D dataset used in the reconstruction (bottom row).

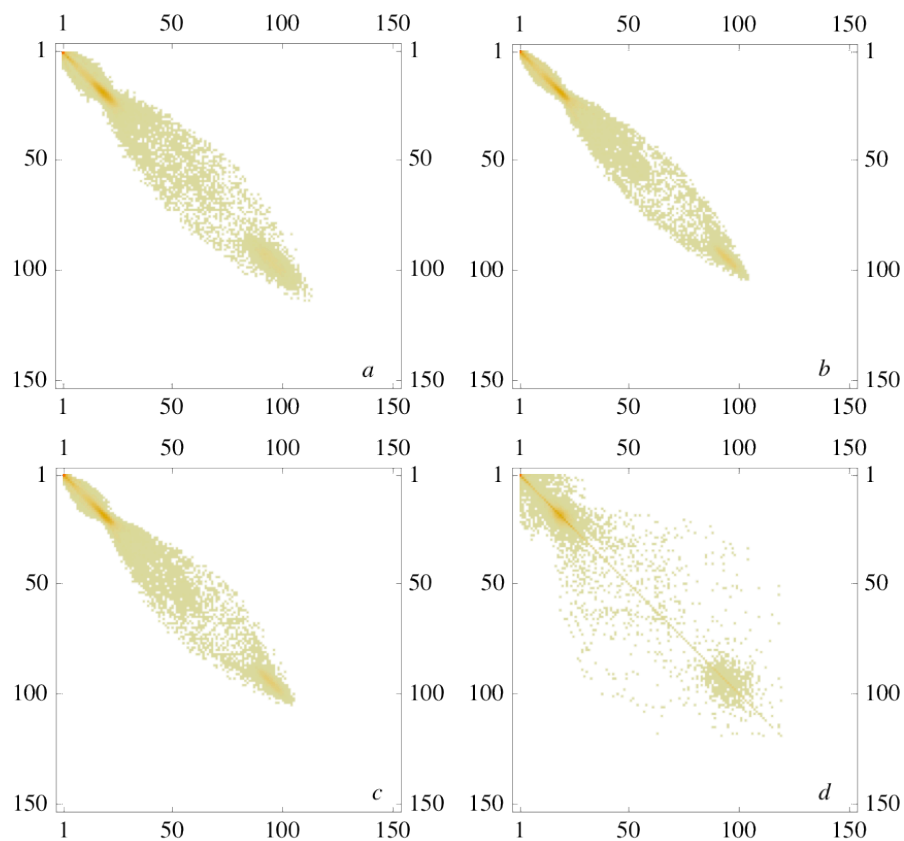


Figure 4.20- Co-occurrence matrix of the transaxial slice n° 104 of the initialization image in the fine scale ($s=1$) using different interpolation methods when the 3D dataset is used. The figures a, b, c, d correspond to the Lanczos, cubic, Gaussian and nearest neighbour kernel, respectively.

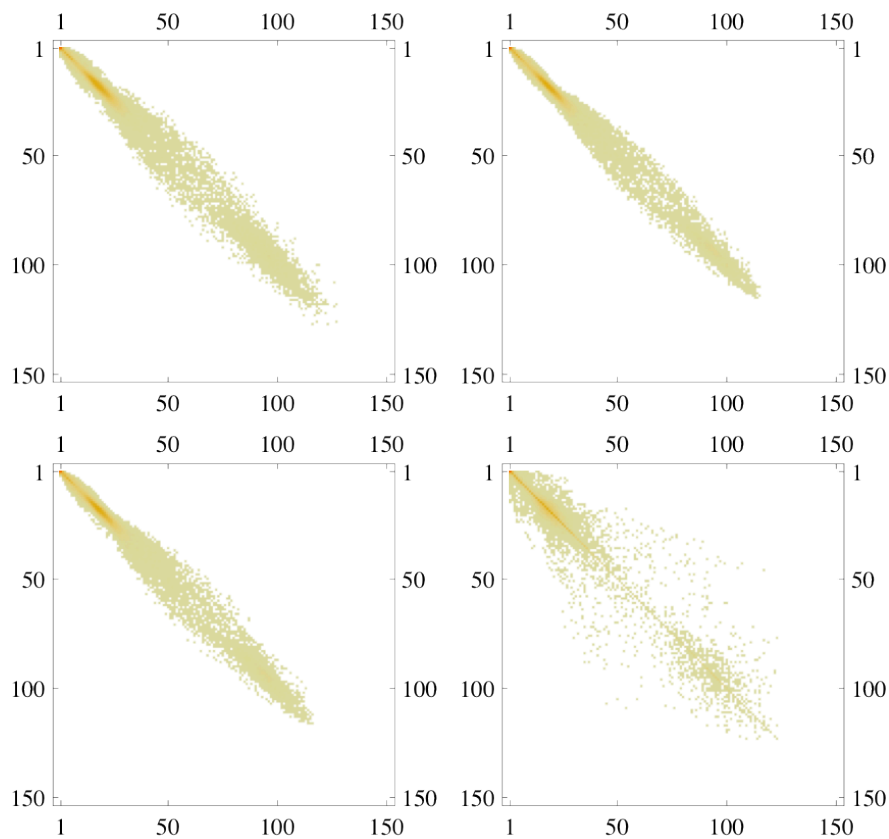


Figure 4.21- Co-occurrence matrix of the slice n° 104 in the transaxial plane of the initialization image in the fine scale ($s=1$) using different interpolation methods when the 2D dataset is used. The figures a, b, c, d correspond to the Lanczos, cubic, Gaussian and nearest neighbour kernel, respectively.

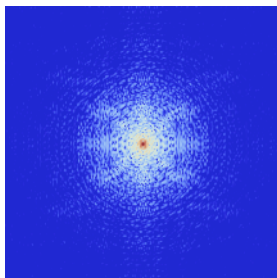


Figure 4.22- Power spectrum of the Fourier transform applied to the slice n° 104 of the phantom n° 1.

4.3.2 Performance of the Multiscale Reconstruction Algorithm

With the MS reconstruction, the minimum image space error was achieved at iterations 14, 21 and 17 in the coarse, medium and fine scales respectively. With ML-EM, the stopping criterion was achieved at iteration 26. In this study the time per

iteration in the coarse, medium and fine scales was about 15 seconds, 1.4 minutes and 7.2 minutes, respectively.

The central slice reconstruction results are presented in Figure 4.23.

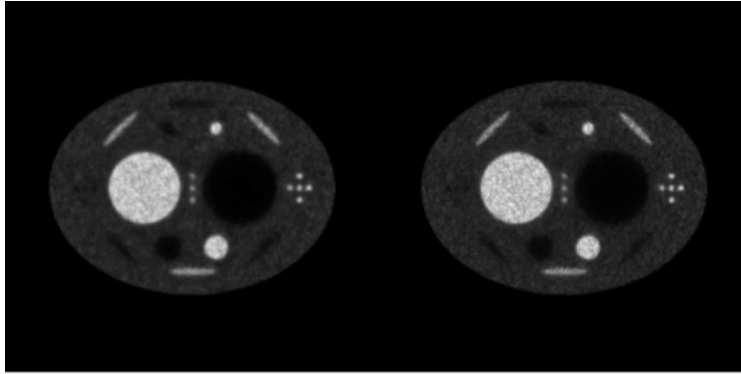


Figure 4.23- MS reconstruction result (left) and ML-EM reconstruction result (right) for slice n° 104.

Figure 4.24 presents the sinogram reconstruction error in the fine scale as a function of the iteration number using both methods.

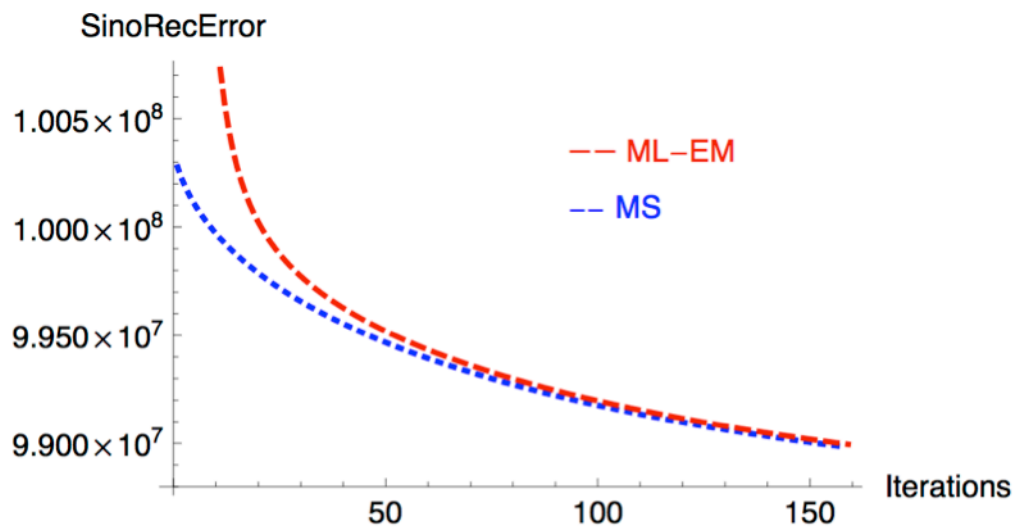


Figure 4.24- Sinogram reconstruction error in the fine scale as a function of the iteration number using the MS (blue) and ML-EM (red curve) reconstructions.

The contrast values in the fine scale as a function of the number of iterations for hot structures are presented in Figure 4.25.

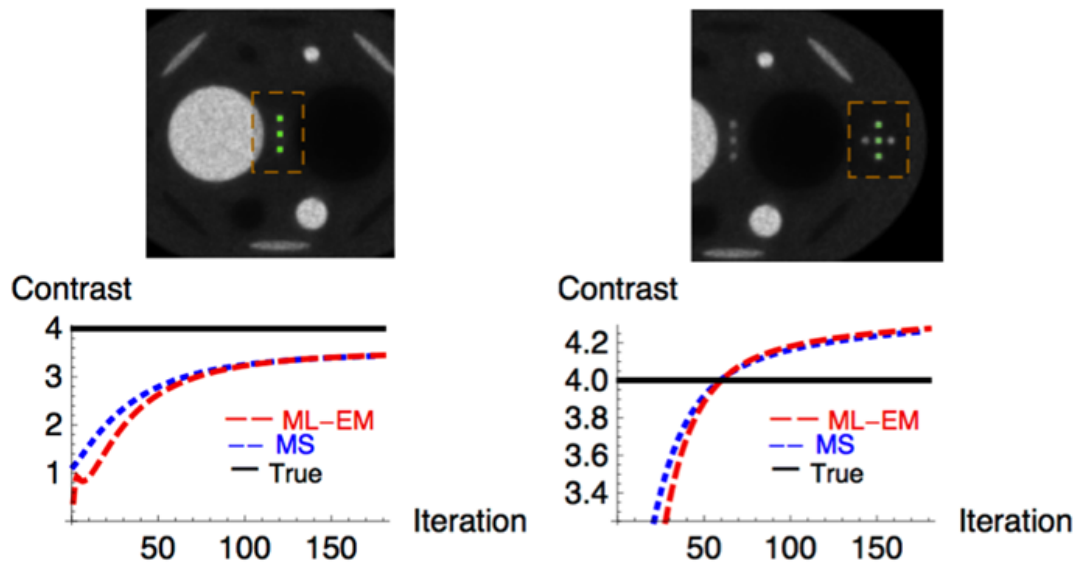


Figure 4.25- Contrast values in the fine scale as a function of the number of iterations for the central hot structures and the right hot structures (from left to the right, respectively). The black, blue and red curves correspond to the true phantom, MS and ML-EM reconstruction results for the 3D simulated data, respectively.

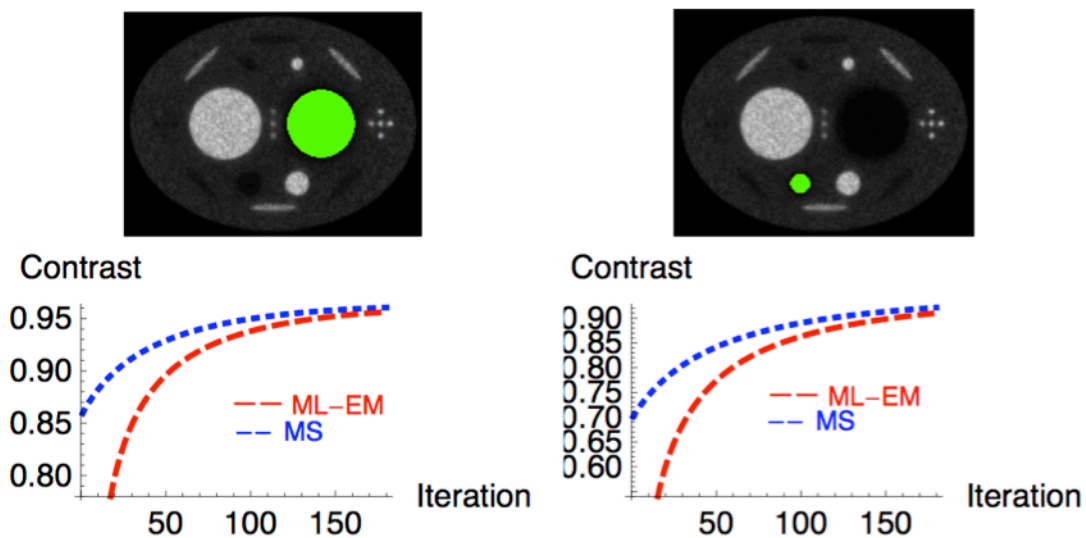


Figure 4.26- Contrast values in the fine scale as a function of the number of iterations for the large and medium cold structures (represented by the green region in the top left/right image). The blue and red curves correspond to the MS and ML-EM reconstruction results for the 3D simulated data, respectively.

Figure 4.26 shows the contrast in the fine scale as a function of the number of iterations for two cold structures.

Figure 4.27 presents the co-occurrence matrixes for slice n° 104 using both methods.

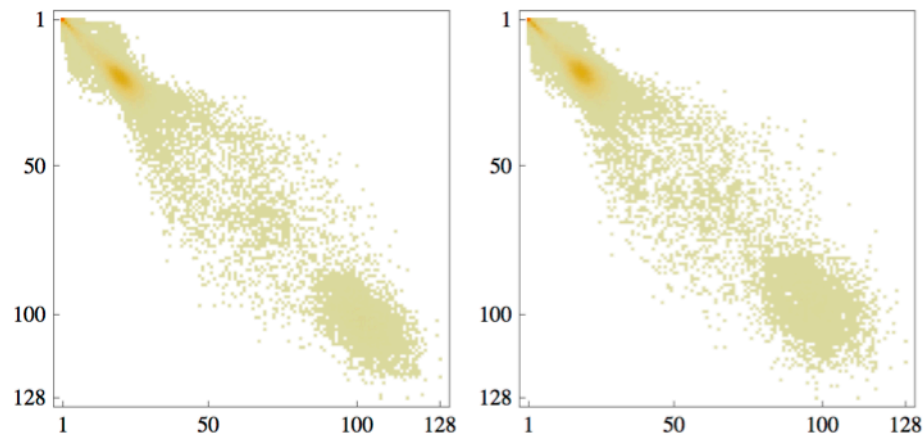


Figure 4.27- Co-occurrence matrix of the slice n° 104 of the reconstructed image using MS (left) and ML-EM (right).

4.4 Discussion

In MS the reconstruction result of the previous scale is mapped into the next scale and used as the initial estimate for the reconstruction at that scale. Four interpolator kernels were tested: the Gaussian, the nearest neighbour, the cubic and the Lanczos. The different interpolator operators resulted in a similar number of iterations to reach the stopping criterion (minimum error in the image space) at the different scales (see Table 4.1). The greatest variation was found for the Lanczos kernel. In the case of 2D reconstruction, the number of iterations was lower than with the 3D dataset due to the lower counting statistics of the data. This can also explain why the number of iterations for the 2D dataset decreases with the increase of the reconstruction scale. Among other factors, the maximum frequency that can be recovered in a given scale depends on the reconstruction scale as well as on the number of counts. The improvements in data statistics by the addition of more data segments (3D dataset) allowed to recover more details, and thus the number of iterations did not decrease in the finest scale.

The fine scale sinogram reconstruction error as a function of the iterations decreases with the increase of the number of iterations (see Figure 4.13). In the first iterations, the reconstruction using the Lanczos (cubic) interpolation had the lowest (highest) error. In the later iterations the errors of the different reconstructions

converged to the same value. Similar behaviour was found for the 2D MS reconstructions (see Figure 4.13).

The visual inspection of the reconstruction results shows that the use of the nearest neighbour interpolation introduces some block effects in the final image (see Figure 4.14 and Figure 4.15). The profile lines that cross three small and hot structures and a cold big structure (left and right row of the Figure 4.18, respectively) show similar behaviour for the different interpolation methods.

The analysis of the power spectra of the Fourier transform, applied to the different initialization images used into the fine scale reconstructions, shows that the Lanczos and the nearest interpolation introduce some high frequency artefacts, which can lead to the introduction of erroneous high frequencies in the initial image (see Figure 4.19). Based on these spectra, the Gaussian kernel is the most suitable to be used in the MS reconstruction. This kernel should allow a smoother initial image and so reducing the probability of having high frequency artefacts in the final image.

Due to the image block effects, the co-occurrence matrix of the initial image generated using the nearest neighbour interpolation has a completely different signature (see Figure 4.20 and Figure 4.21).

The use of MS allows reducing the reconstruction time. Although several iterations are needed in the coarse scales (14 iterations in the coarse scale and 21 in the medium scale), the number of iterations needed in the fine scale was smaller (17) than with ML-EM (26). Since the number of arithmetical operations per iteration is lower in the coarse scales, the overall time is reduced.

The analysis of the evolution of the sinogram error (see Figure 4.24) shows that in the first iterations the MS sinogram error is lower than with ML-EM and in the later iterations the errors converge to the same value. Similar sinogram errors were achieved at the iteration when the minimum image error was reached.

The multiscale reconstruction has a better contrast in the early fine scale iterations (see Figure 4.25 and Figure 4.26). In the case of the hot structures, in the later iterations, both methods converge to the same value (see Figure 4.26). The convergence speed of the different structures is not uniform: it was especially improved for the cold structures (see Figure 4.26).

Both reconstruction methods show similar co-occurrence signatures (see Figure 4.27).

4.5 Conclusion

Four different interpolation kernels were tested to map the reconstruction results between the different scales. The nearest neighbour interpolation introduces block effects in the reconstruction result. The analysis of the power spectrum of the Fourier transforms reveals that the Lanczos and the nearest neighbour interpolation introduce some artefacts, which can introduce erroneous high frequencies in the initial image. Based on the results of the comparative test, the Gaussian interpolation is the most suitable kernel to be used in the multiscale reconstruction.

The performance of the MS reconstruction was compared with the ML-EM. MS allows for the improvement of convergence speed. This conclusion is in agreement with the results reported by Raheja *et al.* [Raheja et al., 1999]. Our results show that the improvements in convergence speed are observed especially for cold regions.

Chapter 5

5 The Multiscale/Multiframe Reconstruction Approach

The multiscale/multiframe reconstruction (MS/MF) adds the concept of accumulated time frame to the multiscale reconstruction. This reconstruction scheme can be used to generate near real-time images in the scale that is the most suitable to the data statistics available at a given accumulated frame. If combined with high performance computing (HPC) techniques, the MS/MF may allow the optimization of the acquisition parameters on the fly.

The MS/MF reconstruction approach was developed, implemented, tested, optimized and characterised during this work. We start by presenting this novel reconstruction technique and by discussing possible applications where this reconstruction approach can be useful. We then study the effects of using the MS/MF in the final image. We compare the MS/MF reconstruction results with the reconstruction results obtained with the single scale/frame ML-EM. Finally, we discuss the potentialities of the MS/MF to generate near real-time images.

5.1 Multiscale/Multiframe Reconstruction

The multiscale/multiframe algorithm (MS/MF) introduces the concept of time frame to the MS reconstruction scheme proposed by Raheja *et al.* [Raheja et al., 1999]. Instead of starting the reconstruction using all the data, the reconstruction

begins using a temporal subset of the data in the coarsest scale, as can be seen in Figure 5.1.

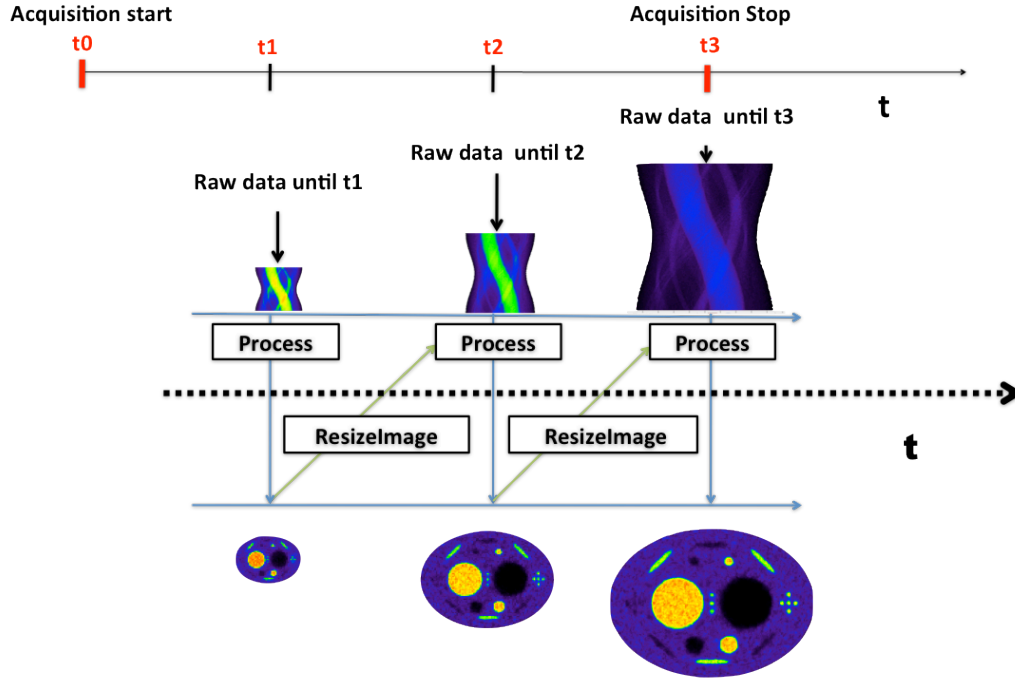


Figure 5.1- The Multiscale/Multiframe reconstruction scheme.

At the coarsest scale all the events acquired until the instant t_1 are processed. The resulting reconstructed image, after resizing, will be used as the initial condition to the medium scale, where all the events between the beginning of the acquisition (t_0) and the instant t_2 are reconstructed. As before, the medium scale image will then be used as the initial condition to the fine scale reconstruction, using all events between t_0 (acquisition start) and t_3 (acquisition stop). When applied to ML-EM, the general equation of the MS/MF reconstruction is given by,

$$\lambda_s^{k+1} = \frac{\lambda_s^k}{\mathbf{H}_s^T \mathbf{1}_{y_s}} \mathbf{H}_s^T \frac{\mathbf{y}_{s,t}}{\mathbf{H}_s \lambda_s^k} \quad (5.1)$$

where s represents a generic scale. \mathbf{H}_s is the system matrix at the scale s , $\mathbf{y}_{s,t}$ is the set of data accumulated from the beginning of the acquisition to time t , and binned onto the projection matrix at the scale s . $\mathbf{1}_{y_s}$ is a vector of ones with the same size as \mathbf{y}_s . The initial condition (λ_s^0) used in the scale s is given by (4.2):

$$\lambda_s^0 = \begin{cases} \mathbf{1}_{S_{max}}, & s = S_{max} \\ \mathbf{I}_s \lambda_s^{K_{s+1}}, & s \neq S_{max} \end{cases}$$

where K_{s+1} is the number of ML-EM iterations made in the previous scale ($s+1$), \mathbf{I} is the interpolation operator that maps the previous scale image to the next scale image and $\mathbf{1}_{S_{max}}$ is a constant image of ones with the same dimensions of the coarsest scale (S_{max}) image used. The main difference relative to the multiscale reconstruction is that the data used at a given scale depend on the accumulated time frame.

5.1.1 MS/MF Applications

The MS/MF could be useful to reconstruct images in systems with very high resolution and sensitivity, in adaptive systems for lesion detection, in in-beam PET systems and in systems with variable geometry and/or with a limited Field Of View.

During the acquisition the near real-time images can be used to detect regions with “anomalies”. Based on this information the acquisition parameters can be optimized taking into account not only the study but also the patient, i.e., MS/MF can be used to adaptively choose the acquisition parameters.

For scanners with high resolution and sensitivity, the near real-time images can be useful to optimize the acquisition time and/or to optimize the way in which the individual lines of response can be combined. Performing the reconstruction using different scales allows for the improvement of the convergence speed and reduces the reconstruction time (see section 5.3).

For systems with variable geometry, this reconstruction technique can be extremely useful. Based on the information extracted from the near real-time images, the geometry of the scanners can be optimized to account for the localization of the tumors. For example this reconstruction technique can be used in scanners like the ClearPem [Abreu et al., 2007] or Zoom-in PET System [Zhou et Qi, 2011].

Another area where this technique can be useful is on In-Beam PET [Yamaya et al, 2008], where the near real-time images can be used to optimize the irradiation of the target.

5.2 Material and Methods

5.2.1 Phantom n° 2 Dataset

We made analytic simulations [Comtat et al., 1999] of a 3D phantom composed of a truncated ellipsoid, phantom n° 2 (see Figure 5.2), acquired by a tomograph with a geometry similar to the High Resolution Research Tomograph (HRRT, Siemens). Scatter, randoms and attenuation were not simulated.

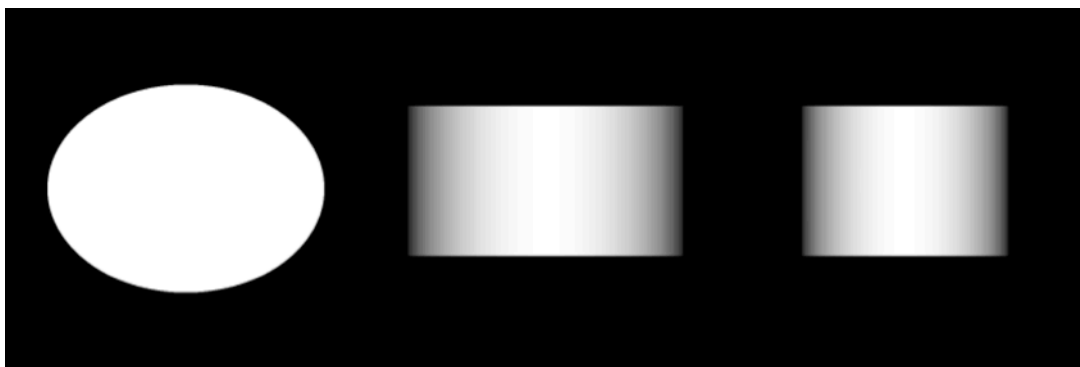


Figure 5.2- From the left to the right: sum of all planes of the digital phantom n° 2 in the transaxial, coronal and sagittal direction.

One MS/MF dataset with three scales/frames was generated with $3 \times 10^7 \times 4^{(3-s)}$ total counts per scale/frame ($s=1,2,3$ for the fine, medium and coarse scales, respectively). The number of counts per sinogram bin was chosen to be constant at the different scales/frames. The dimensions of the image and sinogram spaces for each scale/frame were the same as the data simulated in Chapter 4 (see section 4.2.2). Figure 5.3 presents the sinogram of the slice n° 104 of the segment zero and the corresponding histogram at the different scales.

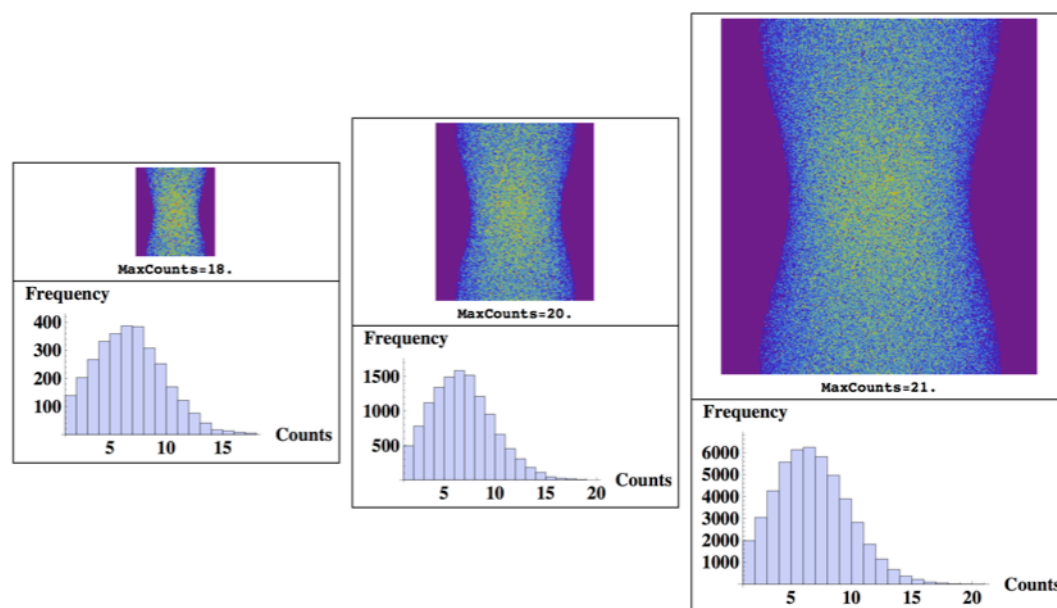


Figure 5.3- From left to right: sinograms of the central plane of segment zero for the digital phantom n° 2 at the coarse, medium and fine scales, respectively.

5.2.2 Phantom n° 1 Datasets

We made analytic simulations [Comtat et al., 1999] of the digital phantom n° 1 (see Figure 4.6) acquired by a tomograph with a geometry similar to the High Resolution Research Tomograph (HRRT, Siemens). Scatter, randoms and attenuation were not simulated.

Two multiscale/multiframe datasets were generated with different number of counts. The first dataset had $2 \times 10^7 \times 4^{(3-s)}$ total counts per scale/frame (high counts dataset) and the second has $2 \times 10^6 \times 4^{(3-s)}$ (low counts dataset). The number of counts per sinogram bin was chosen to be constant at the different scales/frames. The raw data used for the single scale/frame ML-EM is the fine scale/frame of each datasets. The dimensions of the image and sinogram spaces for each scale were the same as the data simulated in Chapter 4 (see section 4.2.2). Figure 5.4 and Figure 5.5 present the sinogram of the slice n° 104 of the segment zero and the corresponding histogram at the different scales for the high count and low count datasets, respectively.

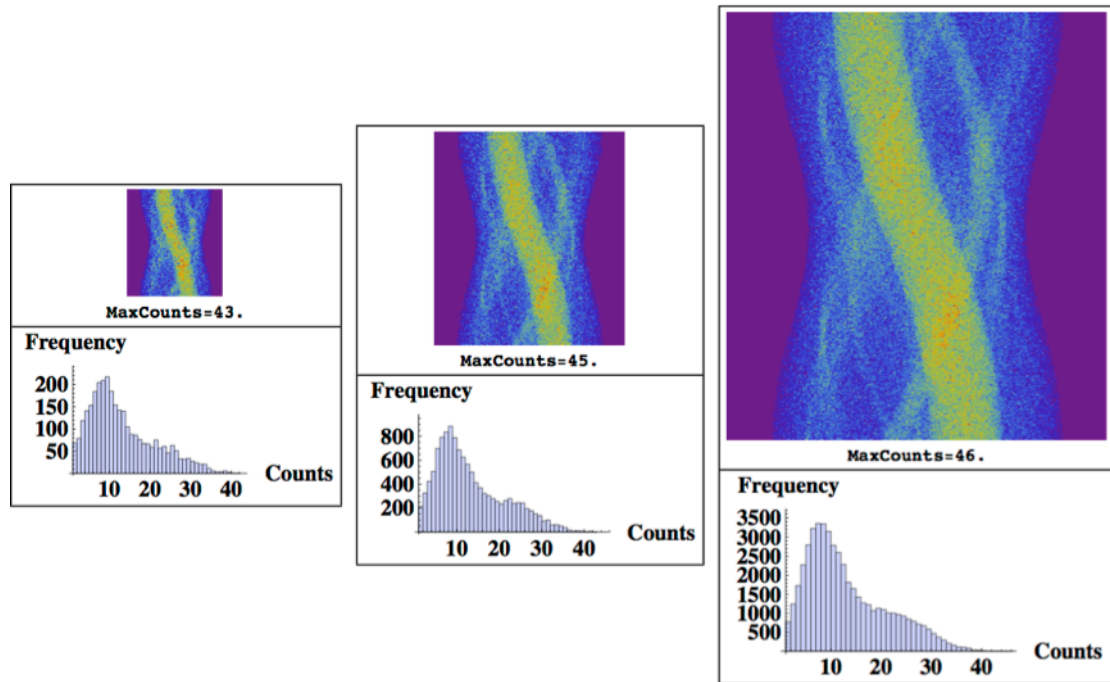


Figure 5.4- From left to right: sinograms of the central plane of segment zero for the phantom n° 1 high counts dataset at the coarse, medium and fine scales, respectively.

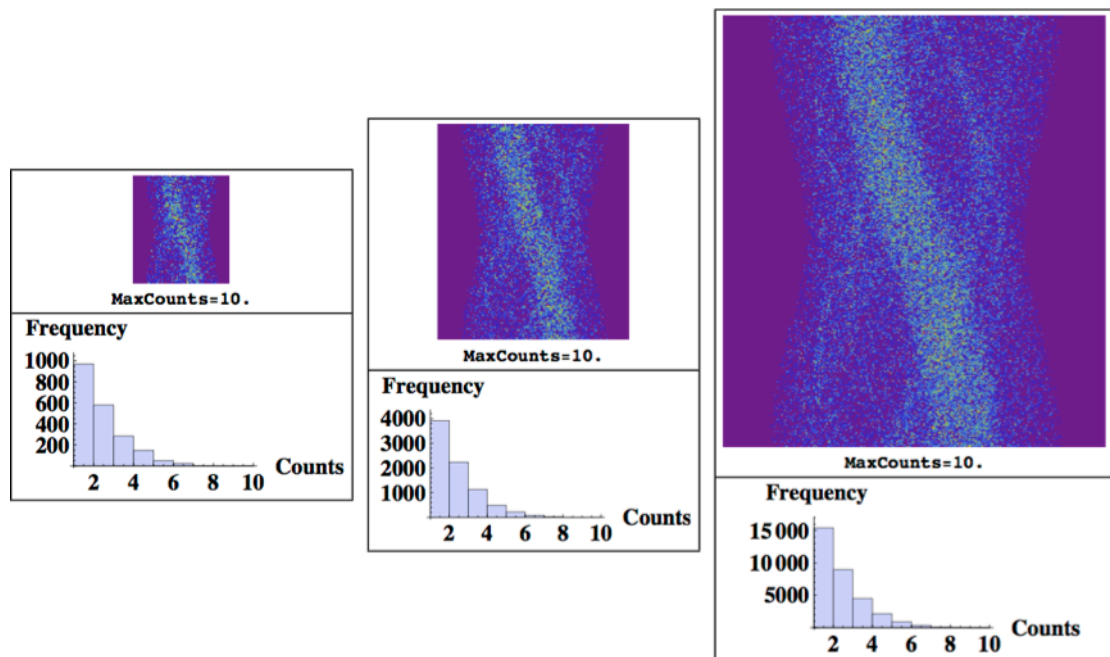


Figure 5.5- From left to right: sinograms of the central plane of segment zero for the phantom n° 1 low counts dataset at the coarse, medium and fine scales, respectively.

5.2.3 Micro-Deluxe Phantom Dataset

The MS/MF was also tested with a real 3D acquisition of a Micro-Deluxe phantom [MicroDeluxe, 2012] with the interior cylinder filled with a FDG solution (no activity in the rods). The diameters of the different phantom rods are 1.2, 1.6, 2.4, 3.2, 4.0 and 4.8 mm. After the acquisition the data were binned as described in section 3.4.1 (see Figure 5.6).

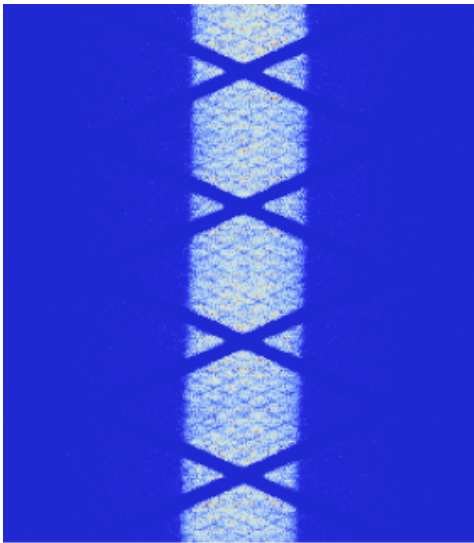


Figure 5.6- Central plane of the segment zero of the prompt Micro-Deluxe raw data acquired in the HRRT.

Since no list-mode data were available, a list of events was generated by a weighted random selection of the sinogram bins. The weight has into account the number of counts of the correspondent sinogram bin. Two accumulated prompt and delayed datasets where generated. The data correction was done during the iterative reconstruction (see (2.29)).

The number of counts per sinogram bin was chosen to be constant at the different scales/frames. The first was binned to the medium scale and the second to the fine scale (see section 4.2.2). The second accumulated frame had a total prompts counts equal to $\sim 5.7 \times 10^8$. The corresponding dimensions of the reconstructed images at each scale/frame were the same as the ones used in the section 4.2.2.

5.2.4 Performance Criteria

The performance of the two reconstruction methods was evaluated taking into account the variation of the reconstruction error in the sinogram (see (4.10)) and image (see (4.11)) spaces. In this study the time per iteration in the coarse, medium and fine scales was about 15 seconds, 1.4 minutes and 7.2 minutes, respectively. The texture analysis (see section 4.2.3) of the reconstructed images was also performed.

The contrast as a function of the number of iterations (see section 4.2.3) and the contrast as a function of the background standard deviation, *sdt*, (see Figure 4.12) were analysed for diferents ROIs of the phantom n°1.

For the Micro-Deluxe dataset the performance of the reconstrcutions was done by visual inspection and by taking into account the variation of the mean value of the central cold structure of the phantom (see Figure 5.7) as a function of the iterations.

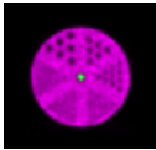


Figure 5.7- Representation of the central cold structure of the Micro-Deluxe phantom (green region).

5.3 Results

Several datasets were used to study the effects of using different scales/frames on the final reconstructed image and also to provide a proof of concept of the use of MS/MF to generate near real-time images. The performance of the MS/MF was compared with the (single grid) ML-EM.

We began by test the MS/MF using 3D datasets generated by an analytical simulation of phantoms n° 2 (see Figure 5.2) and n° 1 (see Figure 4.6). After that, we tested this reconstruction technique using pseudo real data acquired in the HRRT. The difference between the fine grid reconstruction results of the MS/MF and the (single grid) ML-EM is only due to the different initial conditions. In the case of the MS/MF the initial condition is the interpolated reconstruction result of the previous scale and in the case of the (single grid) ML-EM it is a volume with the constant value of one.

Although the reconstruction of the raw data is a volume, only the central slice was chosen in order to simplify the presentation of the reconstruction results. The criterion to select the number of iterations to perform in each scale was the minimum image space error.

5.3.1 Phantom nº 2 Dataset

Figure 5.8 and Figure 5.9 show the fine scale sinogram reconstruction error and the image space reconstruction error respectively, as a function of the iteration number for both reconstruction methods. The MS/MF achieved the minimum reconstruction image error at iterations 10, 9 and 10 in the coarse, medium and fine scales, respectively. ML-EM reached the minimum at the 17th iteration.

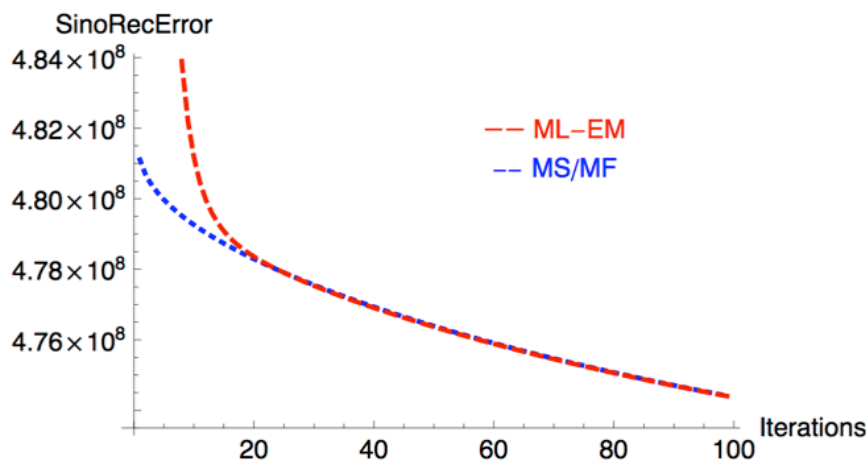


Figure 5.8- Phantom nº 2 dataset. Sinogram reconstruction error as a function of the iteration number done in the fine scale. For the MS/MF reconstruction 10 and 9 iterations were done in the coarse and medium scale, respectively.

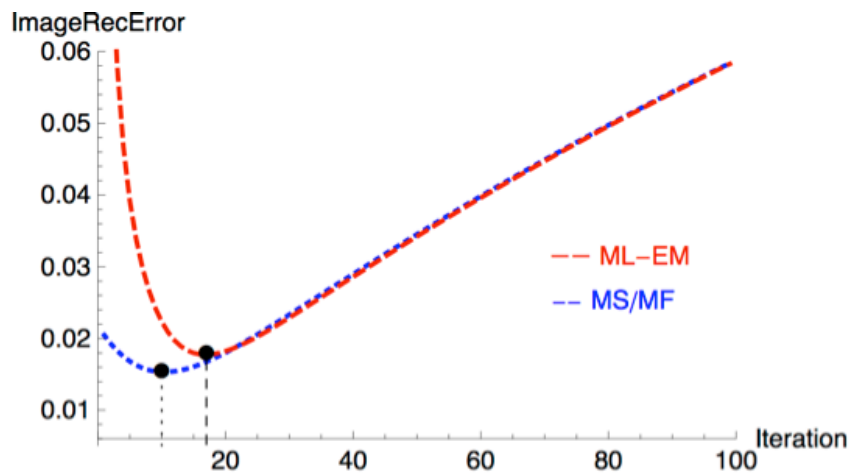


Figure 5.9- Phantom n° 2 dataset. Fine scale image space reconstruction error as a function of the iteration number. For the MS/MF reconstruction 10 and 9 iterations were done in the coarse and medium scale, respectively. The black point for each curve corresponds to the iteration where the minimum error was reached.

The sum of all planes of the reconstructed images in the transaxial, coronal and sagittal directions obtained with the MS/MF and ML-EM are presented in Figure 5.10 and Figure 5.11, respectively.

Figure 5.12 shows the reconstruction results for slice n° 104 obtained with MS/MF and ML-EM and Figure 5.13 presents the corresponding co-occurrence matrices.

Figure 5.14 shows the reconstruction results using MS/MF at different iterations.

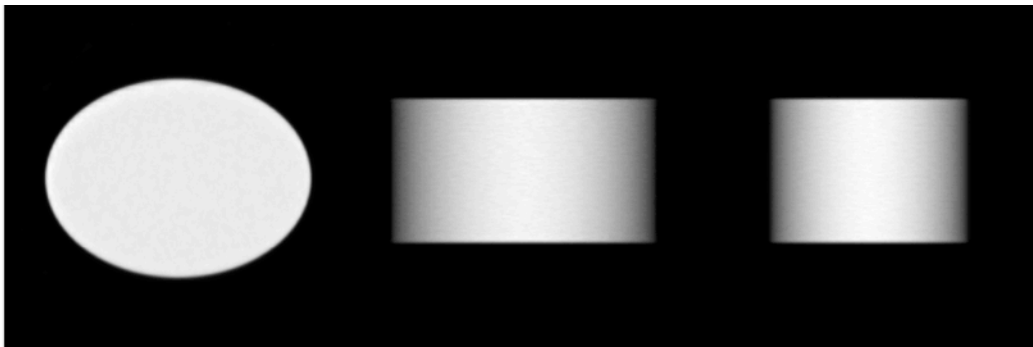


Figure 5.10- From the left to the right: sum of all the planes of the MS/MF reconstruction result in the transaxial, coronal and sagittal directions, respectively, using the phantom n° 2 dataset.

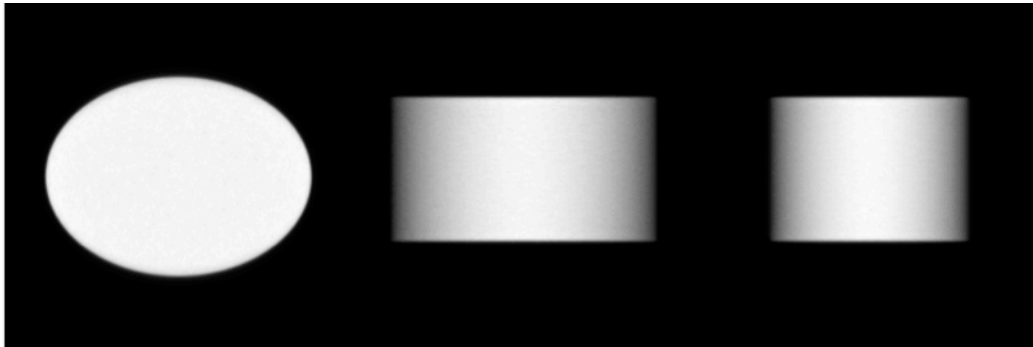


Figure 5.11- From the left to the right: sum of all planes of the ML-EM reconstruction result in the transaxial, coronal and sagittal directions, respectively, using the phantom n° 2 dataset.

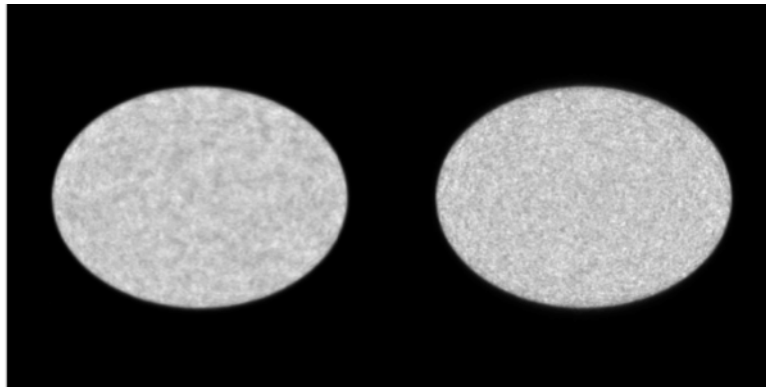


Figure 5.12- Phantom n° 2 dataset. MS/MF (left) and ML-EM (right) reconstruction results for the transaxial slice n° 104.

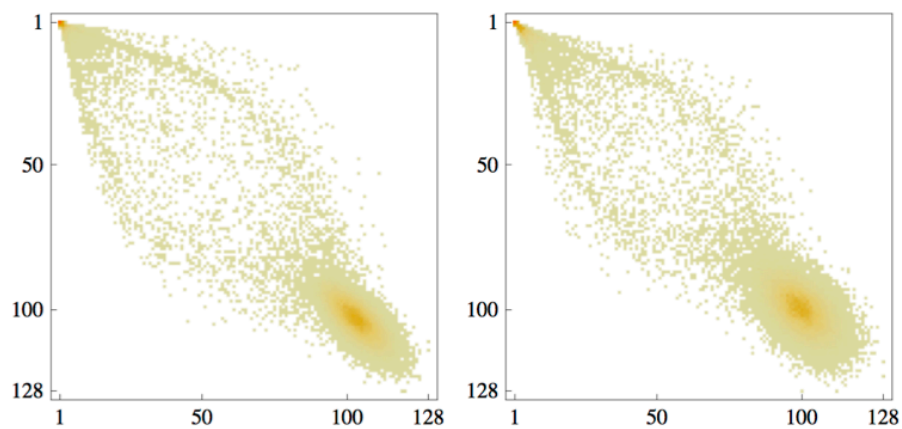


Figure 5.13- Phantom n° 2 dataset. Co-occurrence matrix of the reconstruction result for transaxial slice n° 104 with ML-EM (left) and MS/MF (right).

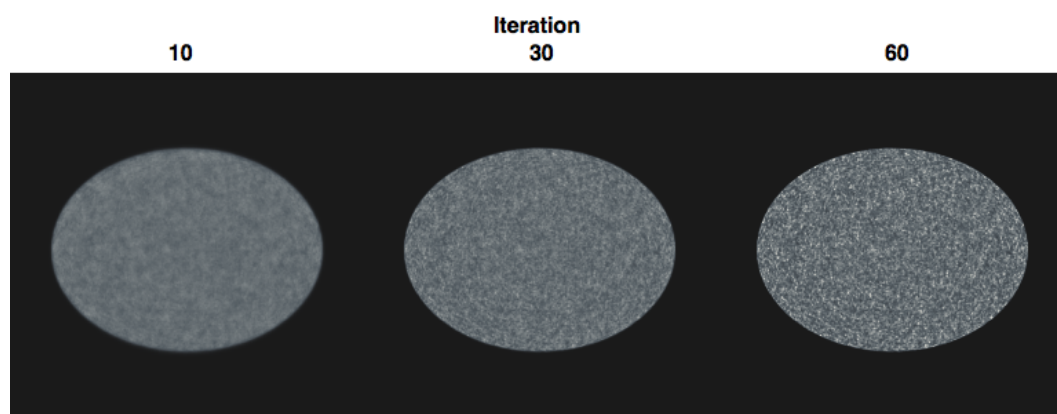


Figure 5.14- Phantom n° 2 dataset. Reconstruction results of the transaxial slice n° 104 using the MS/MF at iteration 10, 30 and 60.

5.3.2 Phantom n°1 Datasets

Figure 5.15 presents the slice n° 104 of the true image and of the resulting reconstructed images obtained with MS/MF and ML-EM using the high counts dataset. The MS/MF achieved the minimum reconstruction image error at iterations 24, 23 and 24 in the coarse, medium and fine scales, respectively. With ML-EM the minimum was reached at the 33th iteration.

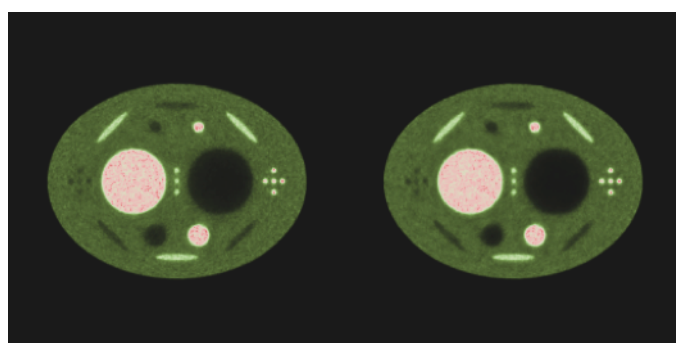


Figure 5.15- ML-EM reconstruction result (left) and MS/MF reconstruction result (right) for transaxial n° 104 using the high counts dataset.

With the low count dataset the MS/MF achieved the minimum reconstruction error at iterations 9, 9 and 10 in the coarse, medium and fine scales, respectively. With ML-

EM the stopping criterion was satisfied at iteration 16. Figure 5.16 presents the reconstruction results of the low counts dataset using both methods.

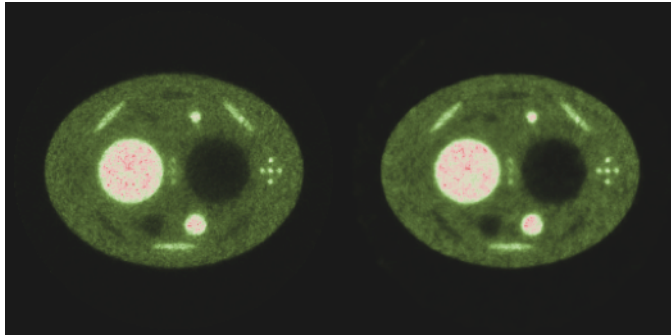


Figure 5.16- ML-EM reconstruction result (left) and MS/MF reconstruction result (right) for transaxial slice n° 104 using the low counts dataset.

The evolution of the sinogram reconstruction error as a function of the iterations for the high counts dataset and the low counts dataset are presented in Figure 5.17 and Figure 5.18, respectively.

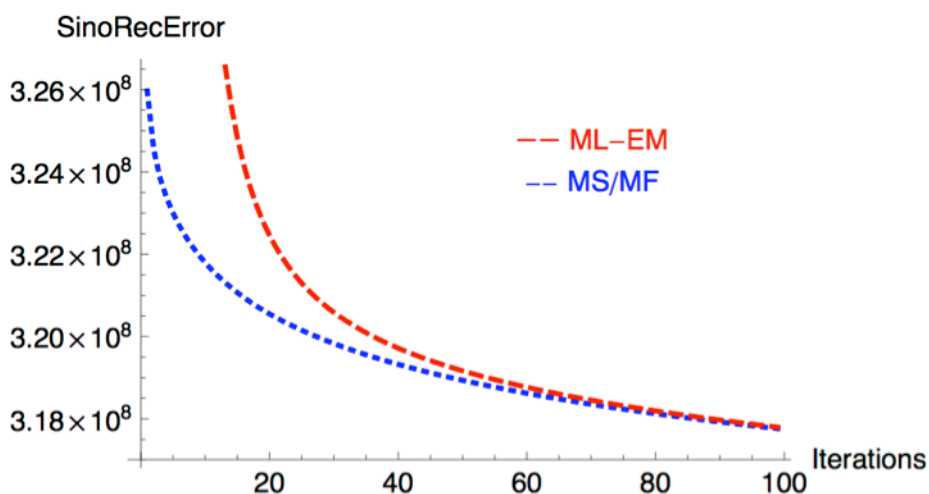


Figure 5.17 - High counts dataset. Sinogram reconstruction error as a function of the iteration number for the fine scale. The blue curve corresponds to the MS/MF error and the red to the ML-EM error. For the MS/MF reconstruction 24 and 23 iterations were done in the coarse and medium scale, respectively.

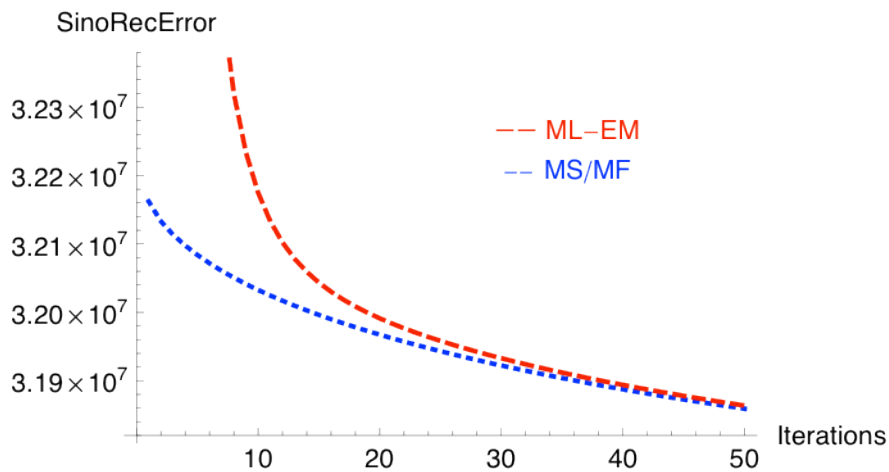


Figure 5.18- Low counts dataset. Sinogram reconstruction error as a function of the iteration number for the fine scale. The blue curve corresponds to the MS/MF error and the red to the ML-EM error. For the MS/MF reconstruction 9 iterations were done in the coarse and medium scale.

The contrast as a function of the iteration number was also studied for the different structures that compose the phantom using the reconstruction results of the high counts dataset. The top row of Figure 5.19 shows the results of the reconstruction of the high counts dataset for two hot structures. The bottom row shows the contrast as a function of the background standard deviation. Similar analysis is presented in Figure 5.20 for two cold structures.

We also investigated if the use of different scales introduces artefacts by visual inspection and by analysing the texture. Figure 5.21 and Figure 5.22 present the co-occurrence matrix of the reconstruction image with both methods using the high counts dataset and the low counts dataset, respectively.

The top row of Figure 5.23 presents the MS/MF results in the coarse (left) and medium (right) scales using the low counts dataset. The bottom of this figure presents the results of the first accumulated frame (left) and the second accumulated frame (right) using the ML-EM. Eight iterations were done in the first accumulated frame and 9 in the second.

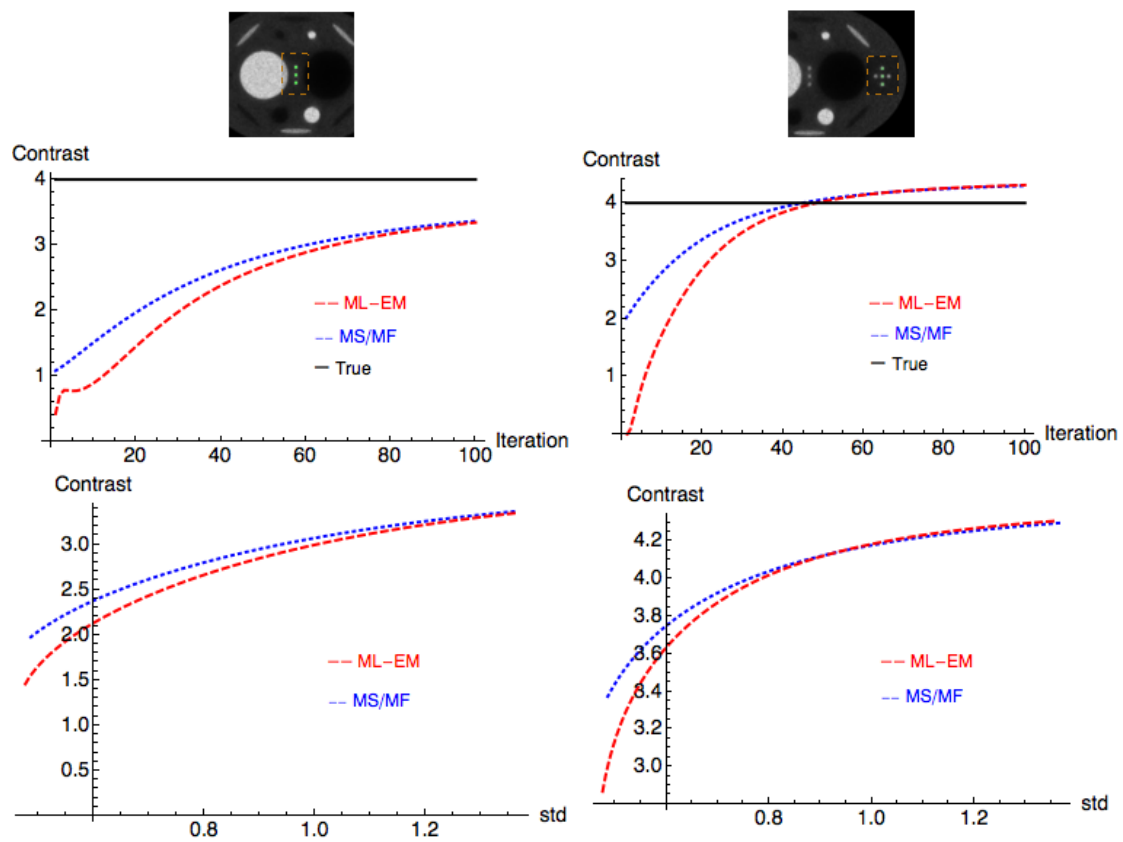


Figure 5.19- High counts dataset. Contrast values as a function of the number of iterations and contrast as a function of the background standard deviation (centre and bottom rows, respectively) for the hot structures with 6 mm of diameter shown in green inside the shaded rectangle of the images in the top row. The black, blue and red curves correspond to the true phantom, fine scale/frame MS/MF and ML-EM reconstruction results, respectively.

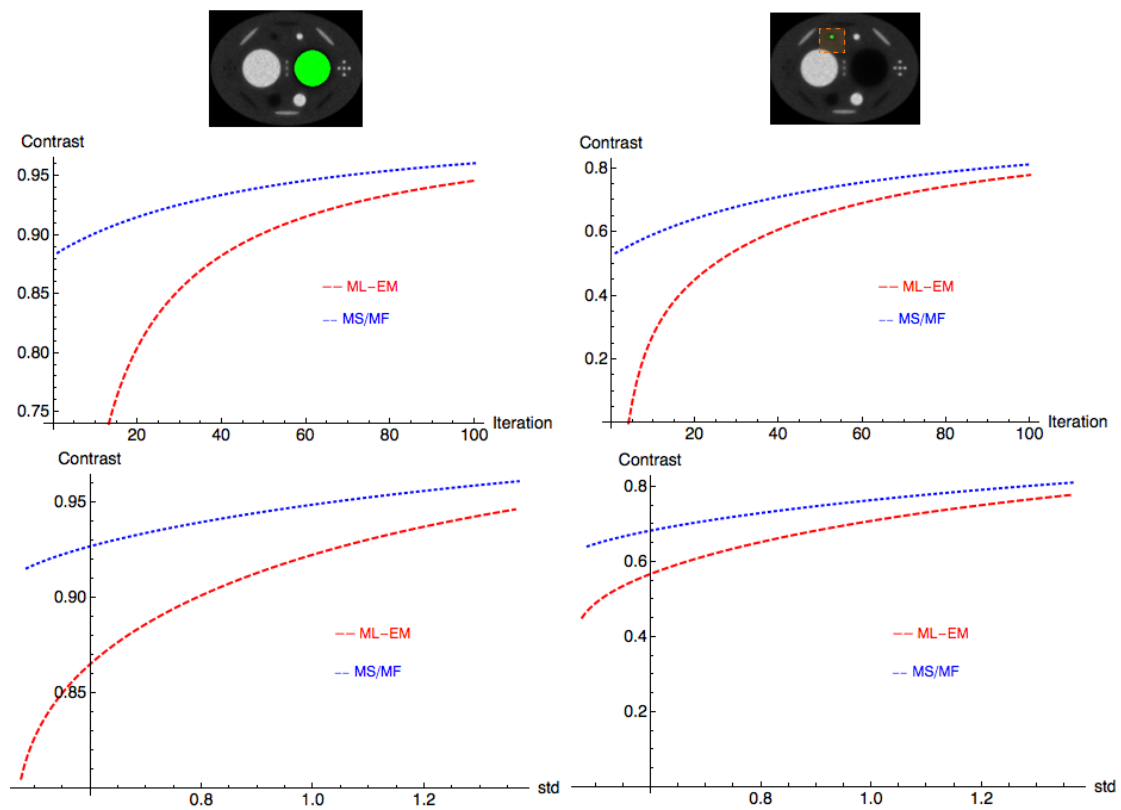


Figure 5.20- High counts dataset. Contrast values as a function of the number of iterations and contrast as a function of the background standard deviation (centre and bottom rows, respectively) for the big (with 70 mm of diameter) and small (with 12 mm of diameter) cold structures shown in green on the images in the top row. The blue and red curves correspond to the fine scale/frame MS/MF and ML-EM reconstruction results, respectively.

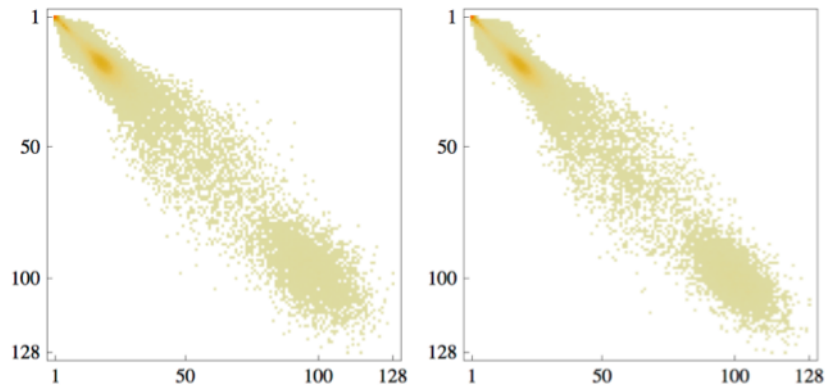


Figure 5.21- High counts dataset. Co-occurrence matrix of the reconstruction result for the slice n°104 with ML-EM (left) and with MS/MF (right).

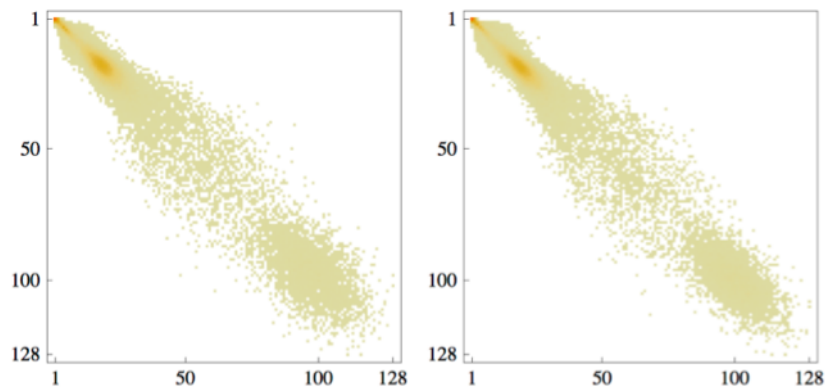


Figure 5.22- Low counts dataset. Co-occurrence matrix of the reconstruction result for the slice n°104 with ML-EM (left) and with MS/MF (right).

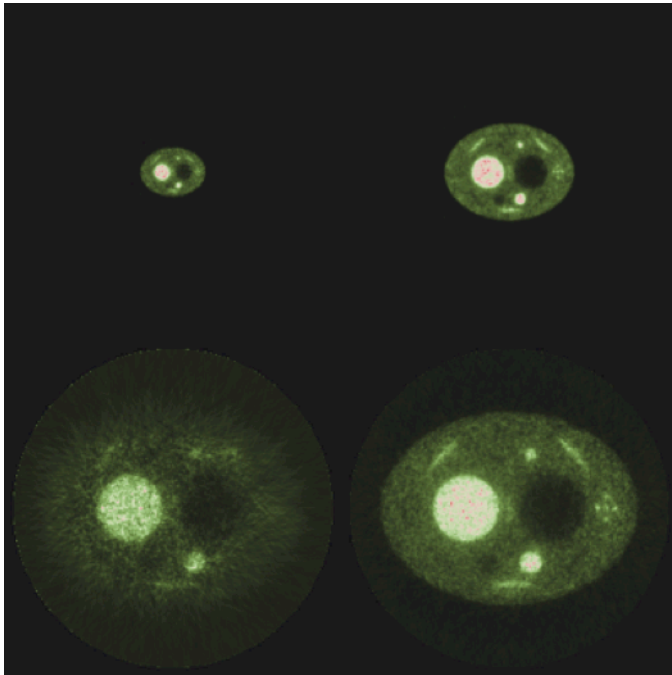


Figure 5.23- Low counts dataset. The top row corresponds to the reconstruction results (slice n° 104) using the MS/MF in the coarse scale (left) and medium scale (right). In the bottom the corresponding reconstruction results using the ML-EM are shown. The left (right) image corresponds to the first (second) accumulated frame.

5.3.3 Micro-Deluxe Phantom Dataset

The left image of Figure 5.24 shows the MS/MF reconstructed slice n° 104 in the medium scale with 30 iterations. The right image shows the fine scale MS/MF reconstruction with 75 iterations.

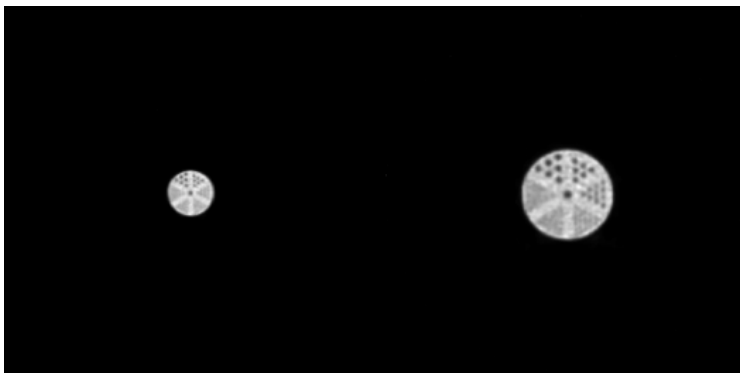


Figure 5.24- The left image corresponds to the Micro-Deluxe reconstruction result for the slice n° 104 of the first accumulated frame in the medium scale with 30 iterations. The right image shows the reconstruction of the second accumulated frame in the finest scale with 75 iterations.

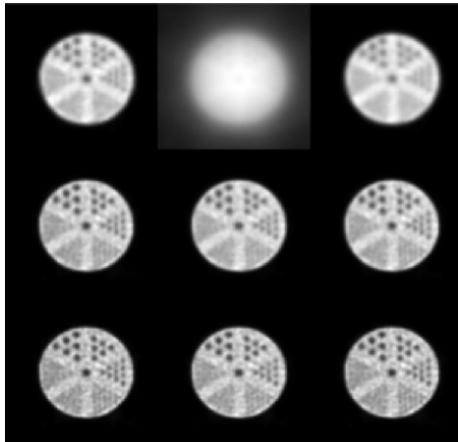


Figure 5.25- Left column corresponds to the MS/MF reconstruction results when were done 30 iterations in the medium scale, the central column correspond to the reconstruction results using the ML-EM algorithm and the right correspond to the MS/MF reconstruction results when were done 60 iterations in the medium scale. The top row corresponds to the reconstruction results with 1 iteration, the central row with 75 iterations and the bottom row with 150 iterations.

Figure 5.25 presents a qualitative reconstruction result of slice n° 104 for the Micro-Deluxe phantom using the MS/MF and the ML-EM. The left column corresponds to the MS/MF reconstruction results with 30 iterations in the previous scale, the central column shows the results with the ML-EM algorithm and the right column shows the MS/MF reconstruction results with 60 iterations in the previous scale. The top row corresponds to the reconstruction results with 1 iteration, the central row with 75 iterations and the bottom row with 150 iterations.

Figure 5.26 shows the mean value of the central cold structure (see Figure 5.7) as a function of the iteration number.

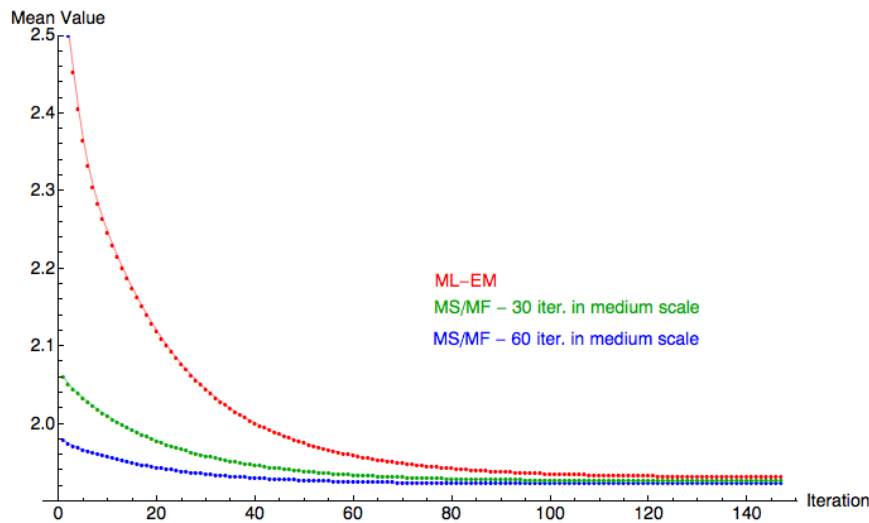


Figure 5.26- Mean value of the Micro-Deluxe central cold structure as a function of the iteration number for the fine scale. The green and blue curves correspond to the MS/MF reconstruction results with 30 and 60 iterations in the medium scale, respectively, and the red curve to the ML-EM reconstruction result. The mean values are expressed in arbitrary units (a.u.).

5.4 Discussion

The MS/MF reconstruction algorithm was characterized using different datasets. The performance of the proposed algorithm was compared with the reconstruction results obtained using the ML-EM algorithm.

We start by testing the MS/MF reconstruction algorithm using simulated 3D raw data of a uniform phantom (see Figure 5.2). At the early iterations the fine scale sinogram reconstruction error achieved by the MS/MF was lower when compared with the ML-EM (see Figure 5.8). For the later iterations both methods exhibit similar image (see Figure 5.9) and sinogram reconstruction errors. Based on visual analysis of the reconstruction results, the MS/MF did not introduce significant artefacts in the final image (see Figure 5.10 and Figure 5.11). However the MS/MF slice reconstruction result exhibits a different noise texture (see Figure 5.12). The analysis of the co-occurrence matrices (see Figure 5.13) confirms the visual difference in the texture of the images. In order to avoid the introduction of erroneous high frequencies into the initial image, several studies were made to select the most suitable interpolator operator (see section 4.3.1). Even so, the interpolation introduces correlations between neighboring pixels, which only slowly disappear during the fine

scale reconstruction (see Figure 5.14). Due to the redundancy of data in our study ($\sim 1.6 \times 10^8$ sinogram bins for only 1.3×10^7 images voxels) the nullspace of the fine scale matrix are highly likely to be trivial. Under this condition the ML solution is unique and therefore we expect both strategies to eventually converge to the same image.

The studies of the local effects of the use of different scales/frames in the final image and the potentialities of the MS/MF to perform reconstruction in near real-time were done using 2 simulated datasets of the phantom n° 1. As was found for the phantom n° 2, the analysis of the evolution of the sinogram error (Figure 5.17 and Figure 5.18) shows that, although both methods converge to the same value, the fine scale MS/MF sinogram error is lower in the early iterations. The global improvement of convergence speed by the use of scales/frames is in agreement with the results presented in Chapter 4 for multiscale reconstruction. As was found for the MS (see section 4.3.2), for the hot regions the advantage of using different scales/frames disappears for the later iterations (Figure 5.19). However, when this happens, the reconstruction should already have been stopped (the minimum error in the image space has been already achieved). Based on the co-occurrence matrices (see Figure 5.21 and Figure 5.22) and visual analysis (Figure 5.15 and Figure 5.16) of the final reconstructed images, we conclude that the low count reconstruction results exhibits a different noise texture, as the one found in the reconstruction results of the phantom n° 2. As we can see in Figure 5.19, both strategies allow the same contrast level for the hot structures if we iterate enough. However, the same contrast can be achieved faster with MS/MF, with approximately the same noise. When we observe the contrast as a function of the background standard deviation (Figure 5.19), no significant differences between the two strategies were found. For the cold ROIs (see Figure 5.20), there is a lack of convergence. Since in ML-EM the convergence of regions with low tracer uptake is slower, the maximum number of iterations used may not have been enough.

In applications that require near real-time reconstruction, performing the accumulated frames reconstruction using the usual acquisition protocol is not feasible. Since the number of operations per iteration is reduced in the coarse scales, the MS/MF method can be used to perform near real-time reconstructions at different

scales/frames. The time spent in one coarse scale (medium scale) iteration corresponds to $\sim 5\%$ (20%) of the time spent in one iteration in the fine scale.

As we can see in Figure 5.23, the choice of the reconstruction scale should take into account the counting statistics available at a given frame, since the maximum frequencies that can be recovered depend on this parameter. Although the voxel size of the ML-EM reconstruction (bottom left of Figure 5.23) is smaller compared with the coarse scale (top left of Figure 5.23) the low statistics in this early frame does not allow for the recovery of the high resolution details. This is confirmed by the lower number of iterations (8 iterations) required by the stopping criterion when compared with the 16 iterations required for the reconstruction of the complete dataset.

The effects on the final reconstruction image were also tested using pseudo real data. Based on visual inspection, the use of scales/frames in the reconstruction of the Micro-Deluxe data did not introduce significant artefacts on the reconstructed images (Figure 5.24 and Figure 5.25). Despite the lack of resolution of the medium scale image, it is possible to identify the phantom type. As happened with the simulated data, the MS/MF approach improves the convergence speed in the fine scale (see Figure 5.26).

5.5 Conclusions

A MS/MF reconstruction technique has been presented and its performance evaluated.

The use of a better initial condition for the finest scale improves the convergence speed allowing a reduction of the overall reconstruction time.

The near real-time images generated by the MS/MF reconstruction algorithm may allow the optimization of the acquisition parameters on the fly. The choice of the reconstruction scale should take into account the data statistics available at a given accumulated frame.

A different noise structure was found in the MS/MF reconstructed images. Improvements in the interpolation operator should reduce the correlation between the voxels.

MS/MF could be useful to perform image reconstruction in systems with very high resolution and sensitivity, in adaptive systems for lesion detection, for in-beam PET systems and in systems with variable geometry.

Chapter 6

6 A Generalized Morozov Discrepancy Criterion for the MS/MF

The MS/MF reconstruction introduces new variables that must be optimized. In this chapter we present a generalized Morozov discrepancy criterion for Poisson data to adaptively select the number of iterations needed in each scale. Based on this generalization a weighted discrete Fourier Morozov criterion (WDF-Morozov) as well as the Morozov criterion can be derived. In the WDF-Morozov, the weights can be chosen to improve the performance of the stopping criterion. This is particularly useful when the modelling of the system matrix is not perfect.

We begin by doing an overview of the stopping criteria proposed for PET data iterative reconstruction. We then present the generalized Morozov discrepancy criterion. The performance of the Morozov criterion was tested using different simulated datasets. A proof of concept of the use of the WDF-Morozov criterion is also presented.

6.1 Stopping Criteria

Due to the data noise and the ill-posedness nature of the problem, the maximum likelihood solution is too noisy and in certain cases can lead to “night sky” solutions [Barrett et al., 2003].

Although the value of the objective function continues to increase, the solution starts to be very noisy (as can be seen in Figure 6.1). This happens because the algorithm tries to fit the noise of the raw data (as can be seen in Figure 6.2). The increase of the image noise with the number of iterations can also be noticed by the analysis of the co-occurrence matrix (see Figure 6.3). Several strategies can be used to avoid this problem, such as introducing a regularization term, stopping the reconstruction earlier or filter the image after the final reconstruction.

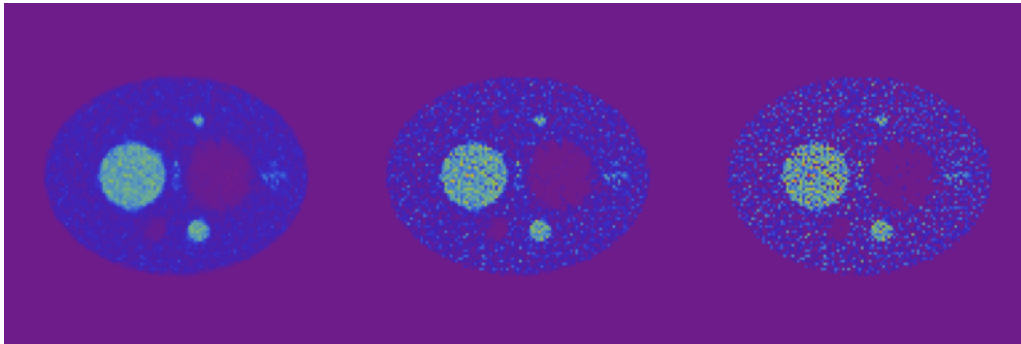


Figure 6.1 - From left to right: Reconstructed image using the ML-EM algorithm at iterations 30, 100 and 400.

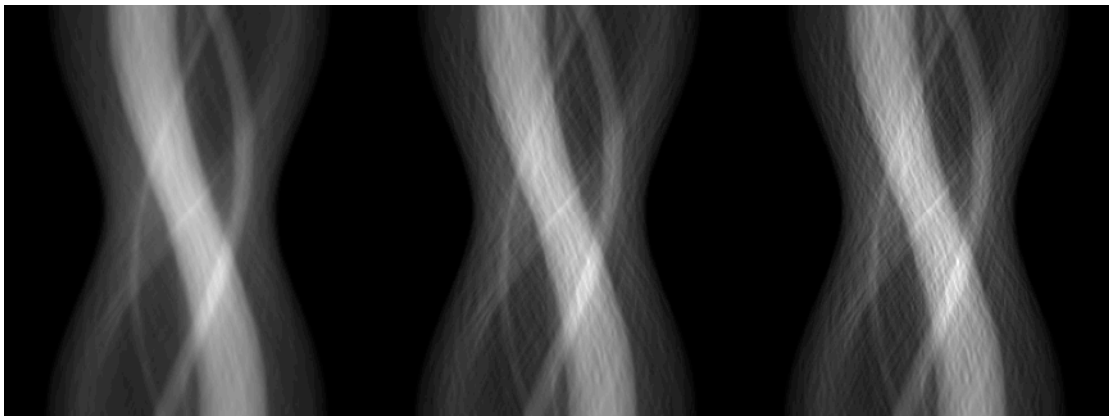


Figure 6.2 - From left to right: estimated sinogram at iterations 30, 100 and 400.

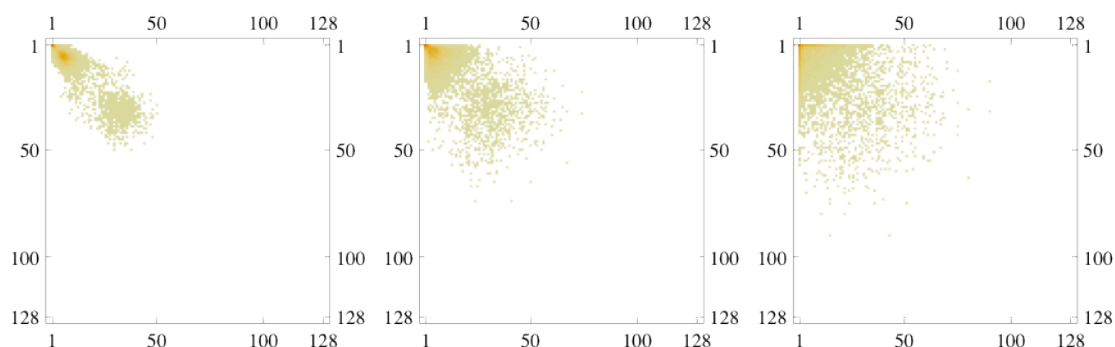


Figure 6.3 - From left to right: co-occurrence matrix (128 levels) for the reconstruction image at iterations 30, 100 and 400.

Veklerov *et al.* [Veklerov and Llacer, 1987] used a stopping criterion based on the Pearson χ^2 goodness-of-fit to stop the ML-EM reconstruction when the image solution is feasible, i.e., consistent with the data. A feasible reconstructed image corresponds to the one that could have caused or produced the observed data by the statistical process that governs the measurement [Veklerov and Llacer, 1987]. When compared with the Filtered Backprojection reconstruction, the solution given by this criterion shows low noise specially in the cold regions [Veklerov and Llacer, 1987]. The main problem of this method is its high sensitivity to small inaccuracies in the system matrix. To overpass this problem, Llacer *et al.* [Llacer et Veklerov, 1989] introduced a factor that expresses the inaccuracies in the system matrix modelling. Its value is chosen based on experience. The authors tested this criterion with real data (Hoffman brain phantom) acquired with the UCLA ECAT-111. They reported that the images obtained were sharp and did not presented noise deterioration.

In 1993 Llacer *et al.* [Llacer et al., 1993] tested a stopping criterion based on the cross-validation (CV) technique. This technique begins by split the data into n independent datasets and then each dataset is reconstructed using the ML-EM algorithm. At each iteration, the cross-validation likelihood between the different estimated solutions is computed. The reconstruction of a particular dataset stops when its cross-validation likelihood starts to decrease. The final reconstructed image corresponds to the sum of the n reconstructed images. Llacer *et al.* [Llacer et al., 1993] claim that this technique works well with simulated images and with a wide range of real data sets. For acquisitions with a very high number of counts they report that the maximum was never reached (due to the lack of accuracy in the system

matrix model used). They also reported, if the data corrections did not preserve the Poisson characteristics of the data the stopping point would occur later. Selivanov *et al.* [Selivanov et al., 2001] tested this stopping rule with 2D dynamic reconstruction using data acquired in the Sherbrooke high-resolution animal tomograph [Lecomte et al., 1996]. When the number of counts of the dynamic series was sufficiently high, they reported that the CV stopping rule ensures a good balance between noise and quantitative accuracy of the estimated images. However, for low-count dynamic series the reconstruction stopped too early, i.e., the estimated image exhibited low noise and the quantitative accuracy was lower. Johnson [Johnson, 1994] studied the dependence between the total photon number of counts and iteration number at which the cross-validation likelihood function is maximized. As expected, he found that the CV optimal iteration depends on the total counts. To avoid problems related to the data split he proposed a Jackknife processing scheme [Reeds, 1978]. Under this approach the events are split into n subsets. The union of the $n-1$ subsets is used to perform the reconstruction and only one is used in the cross validation.

For the MGEM (see section 4.1), Ranganath *et al.* used a criterion based on the variation of the log-likelihood [Rangana et al., 1988]. The reconstruction algorithm MREM (see section 4.1) used a stopping criterion based on wavelets. Tests performed by Rahej *et al.* [Raheja et al., 1999] led to the establishment of a relationship between the energy of the high-high wavelet band [Daubechies, 1992] of the reconstructed image and the minimum image space error. The change of scale is done when the energy in the high-high band reaches a maximum.

A similar problem is to select the regularization parameter of the regularized deblurring and denoising algorithms for Poisson data. The maximization of the likelihood function for Poisson data is equivalent to the minimization of the generalized Kullback-Leibler divergence. Bertero et al. [Bertero et al., 1998] [Zanella et al, 2009] propose a criterion based on the discrepancy principle for Poisson data. The selection criterion is justified by the statistical properties of the Poisson noise [Zanella et al, 2009]. They also tested this criterion as a stopping rule for the iterative deconvolution of astronomical images.

6.2 A Generalized Morozov Discrepancy Principle

In this study a generalized Morozov discrepancy criterion for Poisson data [Defrise et DeMol., 1987], [Bertero et al., 1998] was used to select the number of iterations needed in each scale.

The residual error due to Poisson noise can be defined as

$$\mathbf{r} = \mathbf{y} - \mathbf{H}\boldsymbol{\lambda}, \quad (6.1)$$

where \mathbf{H} is the system matrix, \mathbf{y} the measured data and $\boldsymbol{\lambda}$ the activity image.

Assuming that the raw data is consistent with the Poisson hypothesis, the second moment of the raw data is given by:

$$E(\mathbf{r}\mathbf{r}^T) = \mathbf{D}_{\mathbf{H}\boldsymbol{\lambda}} \approx \mathbf{D}_{\mathbf{y}}, \quad (6.2)$$

where $\mathbf{D}_{\mathbf{y}}$ is a diagonal matrix with the projection data, and $\mathbf{D}_{\mathbf{H}\boldsymbol{\lambda}}$ is a diagonal matrix corresponding to the activity image projected to the projection space. This relation can be used to establish a stopping criterion. Consider a $M \times L$ matrix \mathbf{Q} , with M the dimensions of the raw data and L an arbitrary integer number. Then,

$$\mathbf{Q}E(\mathbf{r}_k\mathbf{r}_k^T)\mathbf{Q}^T \approx \mathbf{Q}\mathbf{D}_{\mathbf{y}}\mathbf{Q}^T. \quad (6.3)$$

By taking the trace of both sides of equation (6.3) the relation continues to hold,

$$Tr\{\mathbf{Q}E(\mathbf{r}_k\mathbf{r}_k^T)\mathbf{Q}^T\} \approx Tr\{\mathbf{Q}\mathbf{D}_{\mathbf{y}}\mathbf{Q}^T\} \quad \text{with} \quad Y(i,j) = \delta_{i,j}\mathbf{y}_i. \quad (6.4)$$

In the case of an iterative reconstruction we can calculate the estimated residual error at the iteration k as,

$$\mathbf{r}_k = \mathbf{y} - \mathbf{H}\boldsymbol{\lambda}_k. \quad (6.5)$$

The reconstruction can be stopped when an approximated equivalent of (6.4) is satisfied:

$$\text{Tr}\{\mathbf{Q}E(\mathbf{r}_k\mathbf{r}_k^T)\mathbf{Q}^T\} = \text{Tr}\{\mathbf{Q}\mathbf{Y}\mathbf{Q}^T\} \quad \text{with} \quad \mathbf{Y}(i,j) = \delta_{i,j}\mathbf{y}_i. \quad (6.6)$$

Equation (6.6) is a generalization of the Morozov discrepancy principle for Poisson data. A proper choice of the \mathbf{Q} matrix could allow for the improvement of the performance of the stopping criterion. For example, this generalization allows us to formulate the Morozov stopping criterion as a weighted discrete Fourier Morozov criterio. The (usual) Morozov stopping criterion is found by taking the \mathbf{Q} equal to the identity matrix.

6.2.1 Morozov Criterion

The Morozov stopping criterion can be found by choose the \mathbf{Q} matrix as the identity matrix. In this case equation can be simplified to:

$$\text{Tr}\{\mathbf{r}_k\mathbf{r}_k^T\} \approx \sum_i \mathbf{y}_i. \quad (6.7)$$

The Morozov stopping criterion is satisfied when the sum of the squares of the estimated residuals at a given iteration is roughly equal to the sum of the number of counts in the raw data. Although the ML-EM algorithm only ensures the increase of the likelihood function, in general, with the increase of the number of iterations the left-hand side (LHS) of (6.7) decreases.

Initially ($k=0$) the LHS of (6.7) is larger because the initial image estimated does not fit the data. In our experiments with simulated data, we observe that with the increasing number of iterations the LHS decreases and after a given number of iterations it is roughly equal to the total number of counts (right-hand side (RHS) of (6.7).

6.2.2 Weighted Discrete Fourier Morozov Criterion

A weighted discrete Fourier Morozov Criterion (WDF Morozov) can be found by choose the matrix \mathbf{Q} equal to the weighted discrete Fourier transform as expressed by:

$$\mathbf{Q} = \mathbf{W}\mathbf{F}, \quad (6.8)$$

where \mathbf{W} is the diagonal matrix with the weights and \mathbf{F} the Fourier matrix. For the sake of simplicity, we consider the case where the 1D discrete Fourier transform is applied in the radial direction to the sinogram elements with a given azimuthal angle denoted by $\mathbf{r}_{\phi,k} = \mathbf{r}_{\phi,k}(x_r)$. The correspondent measured elements are defined by $\mathbf{y}_{\phi} = \mathbf{y}_{\phi}(x_r)$. Under these assumption the LHS of (6.6) can be expressed by,

$$\|\mathbf{W}\mathbf{F}_1\mathbf{r}_{\phi,k}\|^2 = \sum_l \mathbf{W}(l,l)^2 \left| \sum_j e^{-\frac{2\pi ijl}{M}} \mathbf{r}_{\phi,k}(j) \right|^2. \quad (6.9)$$

The RHS of (6.6) can be written as:

$$\text{Tr}\{\mathbf{Q}\mathbf{Y}_{\phi}\mathbf{Q}^T\} = \text{Tr}\{\mathbf{W}\mathbf{F}_1\mathbf{Y}_{\phi}\mathbf{F}_1^T\mathbf{W}^T\} = \text{Tr}\{\mathbf{F}_1^T\mathbf{W}^T\mathbf{W}\mathbf{F}_1\mathbf{Y}_{\phi}\}. \quad (6.10)$$

In order to simplify the equation (6.10) please note that $\mathbf{W}^T\mathbf{W}\mathbf{F}_1\mathbf{Y}_{\phi}$ can be given by:

$$(\mathbf{W}^T\mathbf{W}\mathbf{F}_1\mathbf{Y}_{\phi})_{(lj)} = \mathbf{W}(l,l)^2 e^{-\frac{2\pi ijl}{M}} \mathbf{y}_{\phi}(j). \quad (6.11)$$

and then $\mathbf{F}_1^T\mathbf{W}^T\mathbf{W}\mathbf{F}_1\mathbf{Y}_{\phi}$ can be calculated by,

$$(\mathbf{F}_1^T\mathbf{W}^T\mathbf{W}\mathbf{F}_1\mathbf{Y}_{\phi})_{kj} = \sum_l e^{\frac{+2\pi ikl}{M}} \mathbf{W}(l,l)^2 e^{-\frac{2\pi ijl}{M}} \mathbf{y}_{\phi}(j). \quad (6.12)$$

Taking into account (6.12), the RHS of (6.6) can be expressed as:

$$\text{Tr}\{\mathbf{Q}\mathbf{Y}_{\phi}\mathbf{Q}^T\} = \sum_j (\mathbf{F}_1^T\mathbf{W}^T\mathbf{W}\mathbf{F}_1\mathbf{Y}_{\phi})_{jj} = (\sum_j \mathbf{y}_{\phi}(j)) (\sum_l \mathbf{W}(l,l)^2). \quad (6.13)$$

Finally, from (6.9) and (6.13), the weighted discrete Fourier Morozov Criterion is given by:

$$\sum_l \mathbf{W}(l, l)^2 \left| \sum_j e^{-\frac{2\pi i j l}{M}} \mathbf{r}_{\phi, k}(j) \right|^2 \approx \sum_j \mathbf{y}_{\phi}(j) \sum_l \mathbf{W}(l, l)^2. \quad (6.14)$$

The corresponding stopping criterion take into account the different azimuthal angles is given by:

$$\sum_{\phi} \left(\sum_l \mathbf{W}(l, l)^2 \left| \sum_j e^{-\frac{2\pi i j l}{M}} \mathbf{r}_{\phi, k}(j) \right|^2 \right) \approx \sum_{\phi} \left(\sum_j \mathbf{y}_{\phi}(j) \sum_l \mathbf{W}(l, l)^2 \right). \quad (6.15)$$

The performance of the traditional Morozov criterion can be improved by giving different weights to the different frequencies.

6.3 Material and Methods

6.3.1 Reconstruction Using the ML-EM

2D Reconstruction

Simulated 2D data of a phantom composed of a hot and a cold source (see Figure 6.4), phantom n° 3, with 3×10^7 counts were used to test the performance of the Morozov stopping criterion. Figure 6.5 shows the sinogram of the direct plane n°104 and the corresponding histogram.

The number of iterations required by the Morozov criterion and by the minimum image space reconstruction error (MISRE) criterion was compared.

3D Reconstruction

The impact of the number of segments in the performance of the Morozov stopping criterion was tested using simulated data of the phantom n° 1 (see section 4.2.2) with 1×10^8 total counts.

The high counts dataset (see 5.2.2) and the medium counts dataset (generated using the same phantom but now with $1.5 \times 10^7 \times 4^{(3-s)}$ total counts at the scale s) were also used to test the performance of the Morozov criterion applied to 3D data reconstruction.

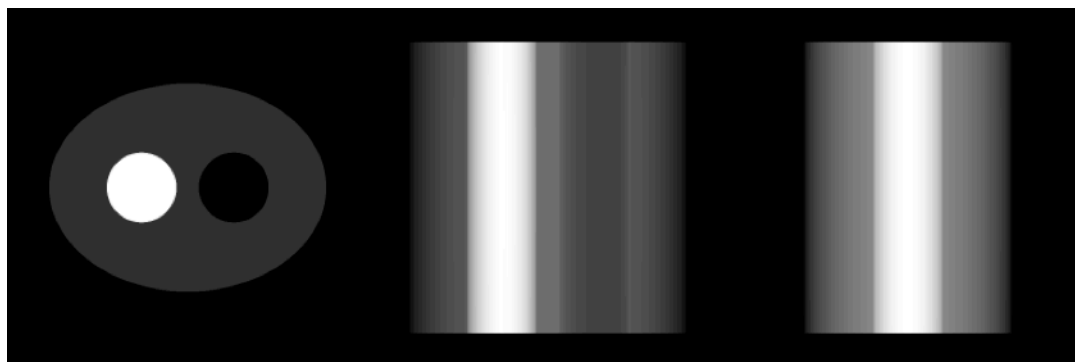


Figure 6.4- Representation of phantom n° 3. From left to right: sum of all planes in the transaxial, coronal and sagittal directions.

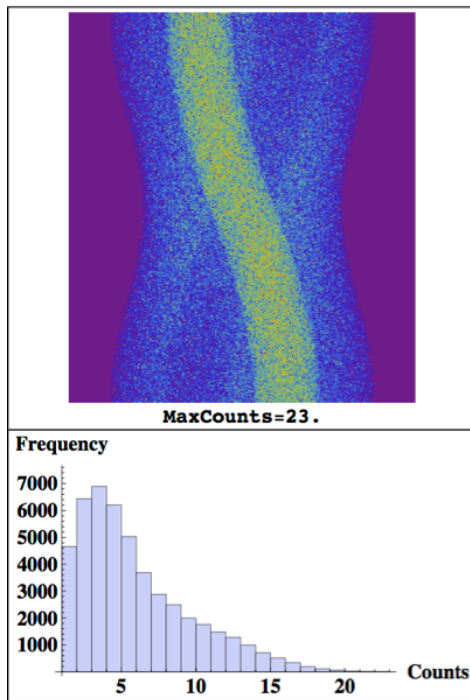


Figure 6.5- Phantom n° 3 dataset. Sinogram of slice n° 104 of segment zero(top) and corresponding histogram (bottom).

6.3.2 Reconstruction Using the MS/MF

3D Reconstruction using the MS/MF

The Morozov stopping criterion, after been applied to the ML-EM reconstruction was tested if was suitable to the MS/MF reconstruction approach. Two MS/MF datasets of the phantom n° 1 (see Figure 4.7) were tested: the high counts dataset (see section 5.2.2) and the medium counts dataset (see section 6.3.1). Three scales (coarse, medium and fine) were used, as shown in Figure 4.1. The performance of the MS/MF reconstruction using the Morozov stopping criterion was compared with the MS/MF using the minimum image space reconstruction error (MISRE) as a stooping criterion and the ML-EM using the Morozov stopping criterion. The ML-EM raw data corresponds to the fine scale/frame of each dataset. As in the previous chapter, the Gaussian interpolator was used to project the coarse scale reconstruction result to the next.

Effects of the Use of Different Scales/Frames in the Final Image

Three datasets were used in this study: the high and low counts datasets of the phantom n° 1 (see section 5.2.2) and the phantom n° 2 dataset (see section 5.2.1). For each dataset 20 noise realizations were generated.

The performance of the MS/MF was compared with the (single scale/frame) ML-EM using two initial conditions: a volume with constant value of one (Ones-ML-EM) and the image reconstructed result with the 2D Filtered Backprojection algorithm using a Hanning filter with cutoff equal to 0.8 times the Nyquist frequency (FBP-ML-EM). Prior to the Filtered Backprojection reconstruction, the 3D data were rebinned using the Single-Slice Rebinning algorithm [Defrise et al., 2005] to obtain a 2D sinogram for each slice. The raw data used for the single scale/frame ML-EM reconstructions correspond to the fine scale/frame of each noise realization.

The performance of the three reconstruction methods was evaluated taking into account the mean image across all noise realizations (for the slice crossing the central plane $z=104$) denoted by

$$\bar{\lambda}(j, m) = \langle \tilde{\lambda}(j, nr, m) \rangle_{nr}, \quad (6.16)$$

where $\tilde{\lambda}(j, nr, m)$ corresponds to the estimated value of the pixel j for the nr^{th} noise realization (with $nr = \{1, \dots, NR\}$) of a given dataset reconstructed with the method m . The operator $\langle x \rangle_d$ stands for the mean value of matrix $\langle x \rangle$ in the direction of d .

The bias and the standard deviation were also calculated using

$$\mathbf{bias}(j, m) = \bar{\lambda}(j, m) - \lambda(j) \quad (6.17)$$

and

$$\mathbf{std}(j, m) = \sqrt{\frac{1}{NR - 1} \sum_{nr=1}^{NR} (\tilde{\lambda}(j, nr, m) - \bar{\lambda}(j, m))^2}, \quad (6.18)$$

respectively.

Another performance metric used was the reconstruction error in the sinogram space (see (4.10)). Using the notation introduced in this section, (4.10) can be expressed by,

$$\mathbf{RecSinoError}(k, nr, m) = \text{Tr}\{\mathbf{r}_k(k, nr, m)\mathbf{r}_k^T(k, nr, m)\}, \quad (6.19)$$

where k is the iteration number.

Additionally, different post-reconstruction smoothing Gaussian filters were applied to the different reconstructed images to generate the contrast versus noise trade-off curves for three different ROIs (denoted as ROI_l with $l = \{1,2,3\}$). The full width at half maximum (FWHM) of the filters used were equal to $1.44 * \Delta$ mm, $\Delta = \{1,2,3,4,5,6,7,8,9\}$. For each ROI different parameters were calculated, such as the mean contrast,

$$\langle \mathbf{Contrast} \rangle = \langle \mathbf{Contrast}(l, nr, m, filter) \rangle_{nr}, \quad (6.20)$$

where the contrast is calculated using

$$\mathbf{Contrast}(l, nr, m, filter) = \frac{\langle \mathbf{ROI}_l(j_l, nr, m, filter) \rangle_{j_l} - \langle \mathbf{ROI}_b(j_b, nr, m, filter) \rangle_{j_b}}{\langle \mathbf{ROI}_b(j_b, nr, m, filter) \rangle_{j_b}} \quad (6.21)$$

with the background ROI (Figure 4.12) represented by ROI_b and the pixel $j_l \in ROI_l$ and the pixel $j_b \in ROI_b$.

The standard deviation of the contrast and the mean of the standard deviation of the background, denoted by

$$\mathbf{std}(\mathbf{Contrast}) = \mathbf{std}_{nr}(\mathbf{Contrast}(l, nr, m, filter)) \quad (6.22)$$

and

$$\langle \mathbf{std}(\mathbf{BackGround}) \rangle = \langle \mathbf{std}_{j_b}(\mathbf{ROI}_b(j_b, nr, m, filter)) \rangle_{nr}, \quad (6.23)$$

respectively, were also evaluated.

6.3.3 WDF-Morozov Criterion

The effect of the use of different weights in the WDF-Morozov was studied using a 2D simulated dataset of the phantom n° 1 (see section 5.2.2) with 1×10^8 counts (WDF-Morozov dataset). Figure 6.6 presents the sinogram of the slice n° 104 of the segment zero and the corresponding histogram at the different scales. A 2D discrete Fourier transform was applied in the radial and azimuthal direction. In Figure 6.25 and Figure 6.26 are presented the binary masks used as weights. For visualization purposes, the zero-frequency component was shifted to the centre of the spectrum.

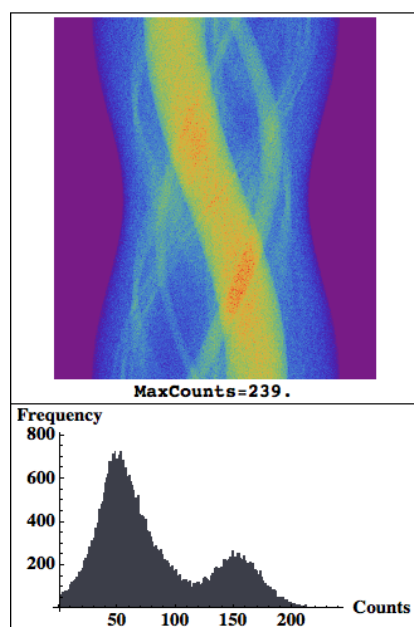


Figure 6.6- WDF-Morozov dataset. Sinogram of slice n° 104 of segment zero (top) and corresponding histogram (bottom).

6.4 Results

Several tests were done to study the performance of the Morozov stopping criteria to adaptively select the number of iterations needed in each scale.

We began by studying the performance of the Morozov stopping criterion when applied to the ML-EM. After that, it was tested if this criterion was suitable to be used

in the MS/MF. Finally, is presented a proof of concept of the use of the WDF-Morozov criterion.

6.4.1 Reconstruction Using the ML-EM

2D Reconstruction Using ML-EM

Figure 6.7 present the reconstruction error in the sinogram and image spaces as a function of the number of iteration. The number of iteration required by the Morozov criterion was 8 and by the MISRE was 9.

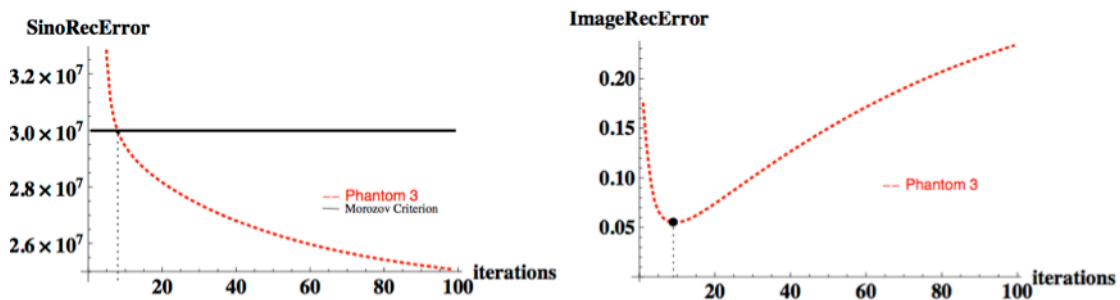


Figure 6.7- Left image: sinogram space error as a function of the number of iterations and corresponding Morozov stopping criterion using the phantom n° 3 dataset. Right image: image space reconstruction error as a function of the number of iterations.

3D Reconstruction Using ML-EM

Two studies were done based on 3D reconstruction using the ML-EM algorithm. We start by testing if the number of polar segments used in the reconstruction has influence in the performance of the Morozov stopping criterion. Depending to its ring difference, a given LOR is associated to a segment. The raw data were binned into 15 polar segments ($[-7, +7]$). The segment zero corresponds to the direct planes. The sign of the segment depend on the polar angle associated.

Table 6.1 presents the number of iterations required by the Morozov stopping criterion and by the MISRE criterion as a function of the range of polar segments used in the reconstruction.

Table 6.1 - Comparison of the number of iterations required by the Morozov stopping criterion and by the MISRE criterion when the range of polar segments used in the reconstruction changes.

Range of segments	Morozov (iterations)	MISRE (iterations)
{0}	8	10
[-1,1]	18	19
[-5,5]	20	21
[-7,7]	22	23

We also studied the influence of the number of counts on the Morozov criterion, using two datasets with different noise levels.

Figure 6.8 presents the reconstruction error in the sinogram and image spaces, as a function of the number of iterations for the high counts (top of the figure) and the medium counts (bottom of the figure) datasets. The Morozov criterion required 36 (30) iterations for the high (medium) counts dataset. The minimum error was achieved at the iteration 33 and 30 for the high and medium counts dataset, respectively.

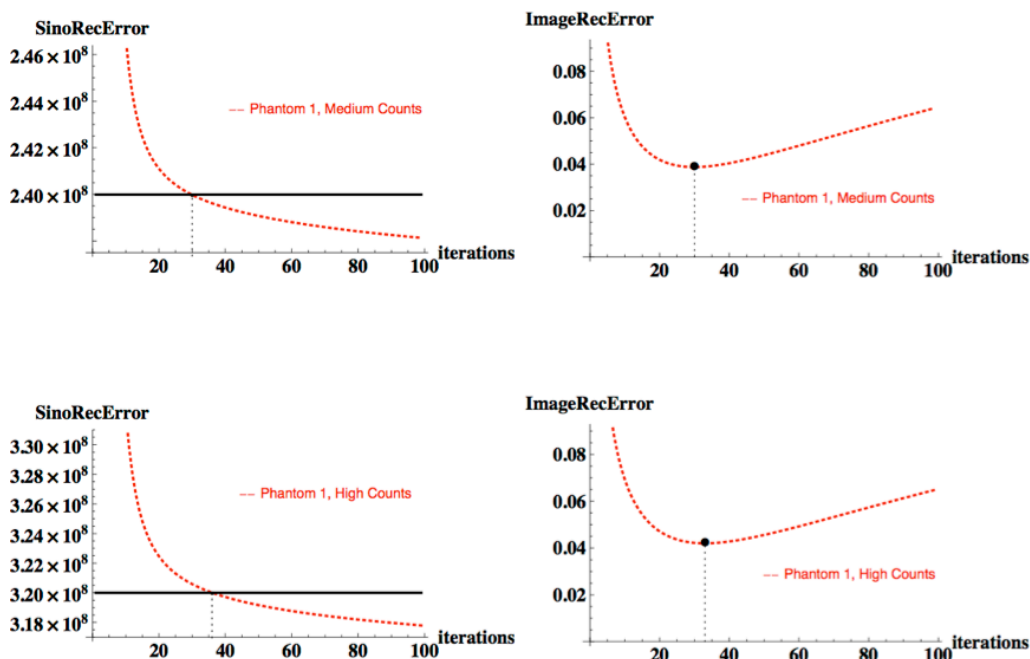


Figure 6.8- 3D reconstruction using ML-EM. Left column: sinogram space error as a function of the number of iterations and the corresponding Morozov stopping criterion. Right column: image space error as a function of the number of iterations. The top row shows results for the medium counts dataset and the bottom row for the high counts dataset.

6.4.2 Reconstruction Using the MS/MF

3D Reconstruction Using the MS/MF

In this study it was assessed if the Morozov is suitable to be used in the MS/MF. Two MS/MF datasets with different noise levels were used: the high counts and the medium counts datasets of phantom n° 1.

Table 6.3 shows, for the different scales, the number of iterations required by the Morozov and MISRE criteria using the high counts dataset.

Table 6.4 presents similar information but for the medium counts dataset. The stopping criterion used in the MS/MF reconstruction was the Morozov, i.e., the number of iterations done in the previous scales was chosen based on that criterion.

Table 6.2 - Comparison of the number of iterations required by the Morozov and MISRE criteria using the high counts dataset.

	Morozov (iterations)	MISRE (iterations)
S=3	24	24
S=2	21	23
S=1	27	26

Table 6.3 - Comparison of the number of iterations required by the Morozov and MISRE criteria using the medium counts dataset.

	Morozov (iterations)	MISRE (iterations)
S=3	20	21
S=2	19	21
S=1	22	23

Figure 6.9 and Figure 6.10 present the reconstruction errors in the sinogram and image spaces as a function of the number of iterations for the two datasets at the medium scale and fine scales, respectively.

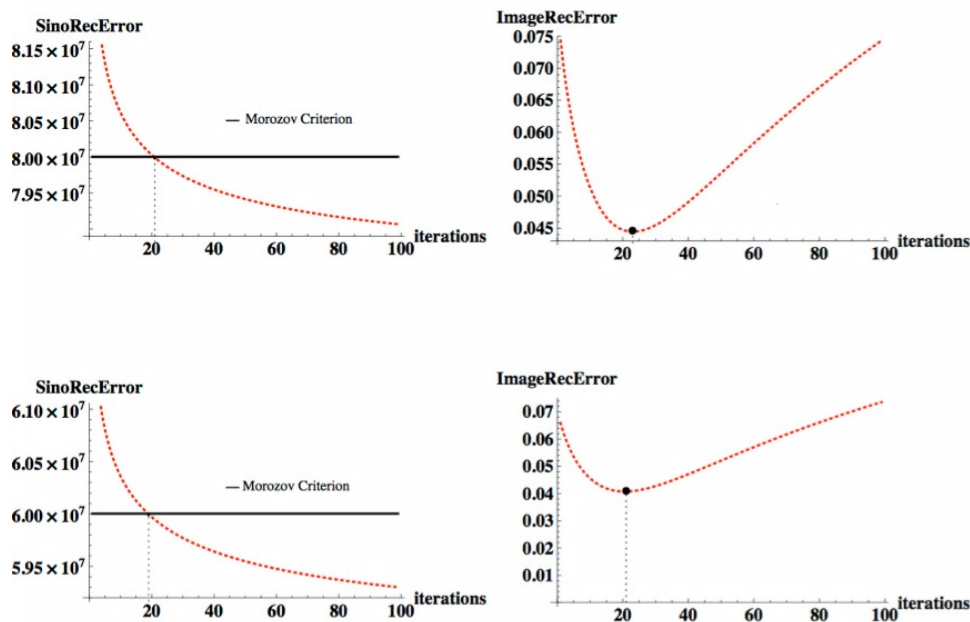


Figure 6.9 - Medium scale 3D reconstruction using MS/MF: The left column shows the sinogram space error as a function of the iterations and the corresponding Morozov stopping criterion. The right column presents the image space error as a function of iterations. The top line shows the results using the high counts dataset and in the bottom line the medium counts dataset.

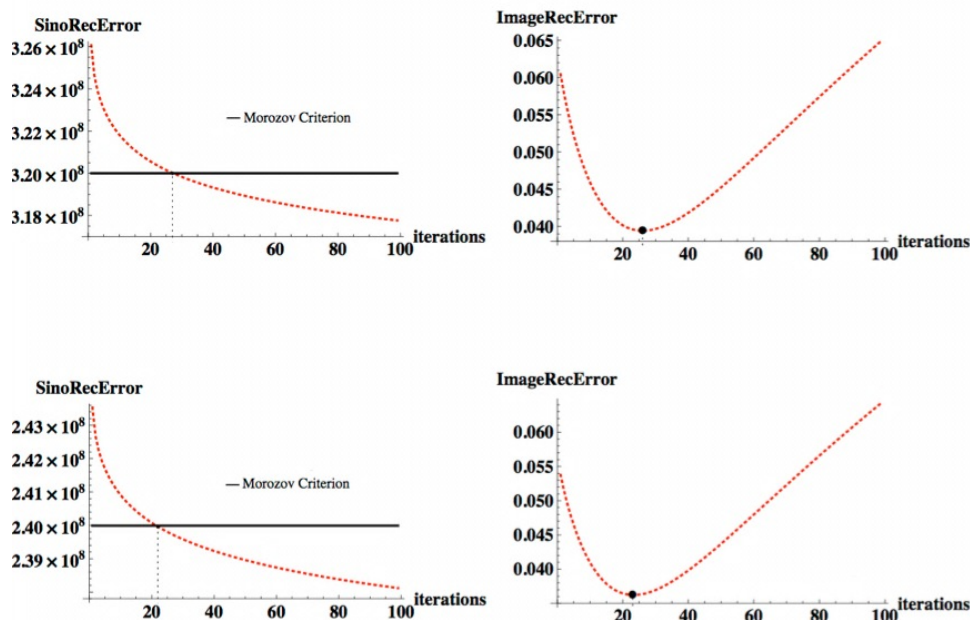


Figure 6.10 - Fine scale 3D reconstruction using MS/MF: The left column shows the sinogram space error as a function of the iterations and the corresponding Morozov stopping criterion. The right column presents the image space error as a function of iterations. In the top line are presented the results using the high counts dataset and in the bottom line the medium counts dataset.

Effects of the Use of Different Scales/Frames in the Final Image

In this study we extended the characterization of the performance of the MS/MF algorithm (see section 5.3). We compared the MS/MF reconstruction results with the reconstruction results obtained with the single scale/frame ML-EM, using as initial estimate either a uniform image or the reconstruction obtained by the Filtered Backprojection (FBP) algorithm. The number of iterations to perform in each scale/frame was chosen based on the Morozov criterion (using all projection space data and all image space data available at a given scale/frame).

Although the reconstruction result is a volume, the central slice n° 104 was selected to simplify the presentation of the results.

Figure 6.11 and Figure 6.12 show the fine scale sinogram reconstruction error for the high counts data and low counts data, respectively, as a function of the iteration number for the three reconstruction methods. For each reconstructed method the error curves obtained for the different realizations are overlapped.

Figure 6.13 presents the distribution of the number of fine scale iterations required by the Morozov criterion for the different noise realizations and reconstruction methods.

Figure 6.14 shows the distribution of the number of iterations required by the Morozov criterion, using the MS/MF, for the different noise realizations in the coarse and medium scale.

Figure 6.15 presents a representative reconstruction of a noise realization obtained with the different reconstruction methods and data.

Figure 6.16, Figure 6.17 and Figure 6.18, show the mean ((6.16)), bias ((6.17)) and standard deviation ((6.18)), respectively, for the different reconstruction methods and data.

Figure 6.19 and Figure 6.20 present vertical profiles of the standard deviation images that contain a region with a hot and cold structure, respectively, for the high counts data. Figure 6.21 shows vertical profiles of the standard deviation images for the phantom n° 2 data.

The contrast versus noise trade-off curves was also studied for different hot structures that compose the phantom n° 1. Figure 6.22 and Figure 6.24 show these curves for groups of hot structures positioned at the center and right side of the

phantom, respectively. Figure 6.23 shows the contrast versus noise trade-off curves for a medium size hot source.

For the MS/MF, the mean time to perform the reconstruction of the first accumulated frame in the coarse scale was 6.5 minutes. The overall mean reconstruction time was 235 minute for the MS/MF, 266 minutes for the Ones-ML-EM and 259 minutes for the FBP-ML-EM.

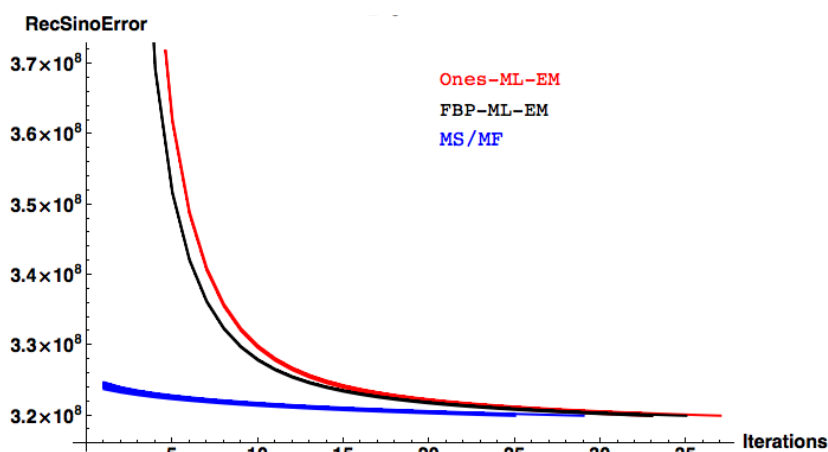


Figure 6.11- High counts data. Sinogram reconstruction error as a function of the iteration number for all realizations using the different reconstruction methods. For each reconstructed method the error curves obtained for the different realizations are overlapped. The stopping criterion was the Morozov criterion. The horizontal scale only represents the iterations done at the fine scale. The initial MS/MF iterations at the coarse scales are not taken into account.

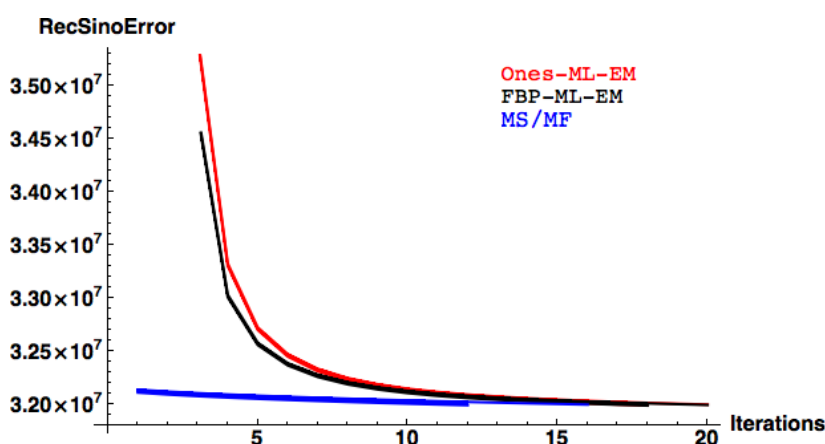


Figure 6.12- Low counts data. Sinogram reconstruction error as a function of the iteration number for all realizations using the different reconstruction methods. For each reconstructed method the error curves obtained for the different realizations are overlapped. The stopping criterion was the Morozov criterion. The horizontal scale only represents the iterations done at the fine scale. The initial MS/MF iterations at the coarse scales are not taken into account.

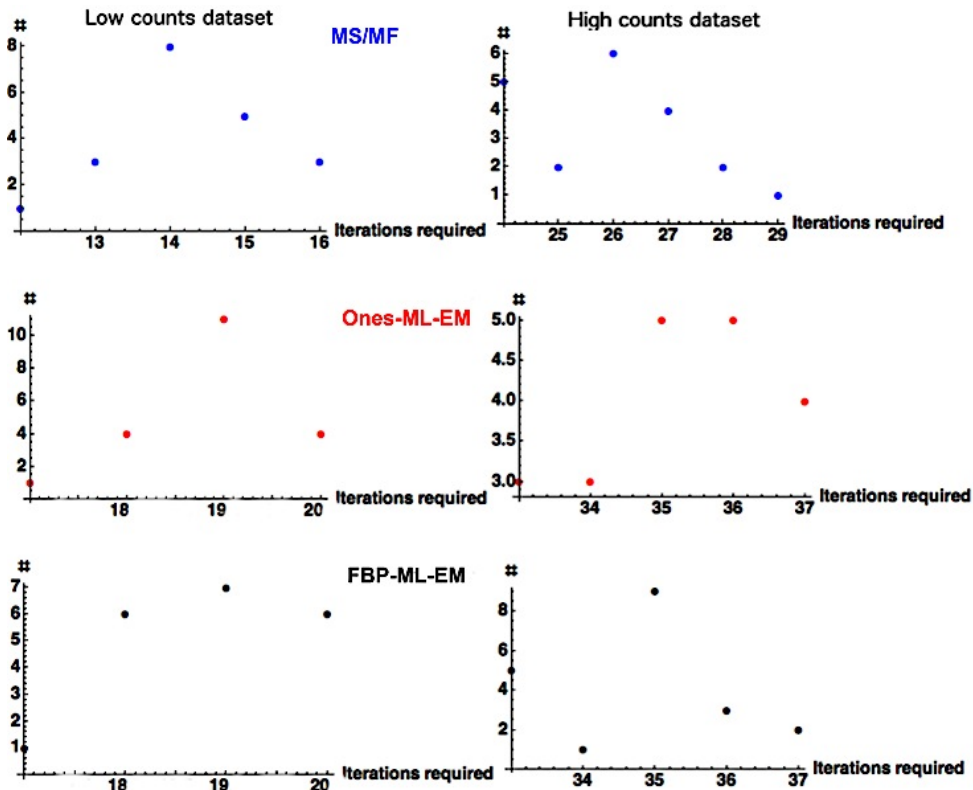


Figure 6.13- Fine scale distribution of the number of iterations required by the Morozov criterion for the different noise realizations using the MS/MF (top), the Ones-ML-EM (medium) and the FBP-ML-EM (bottom). The left column corresponds to the low counts data and the right column to the high counts data. Several iterations in the coarse scales were done in the MS/MF reconstruction.

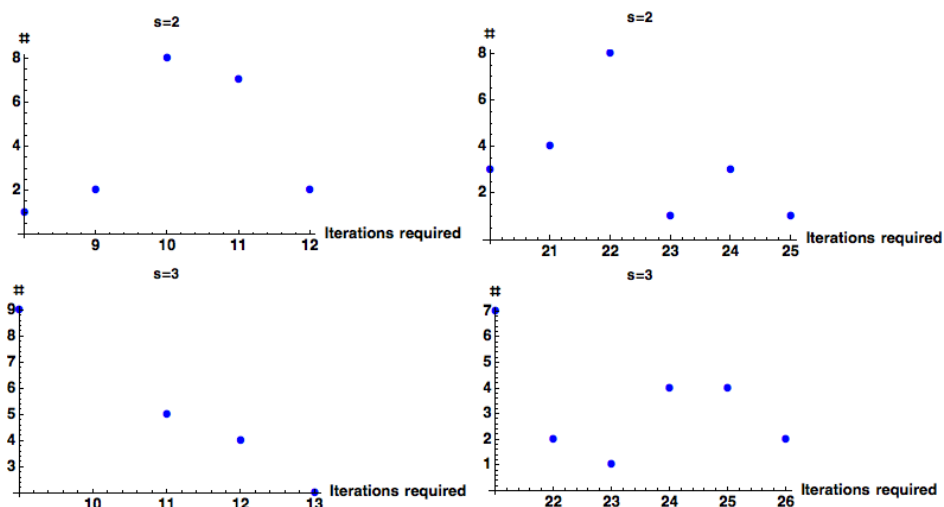


Figure 6.14- Distribution of the number of iterations required by the Morozov criterion for the different noise realizations reconstructed using the MS/MF in the medium scale (top row) and in the coarse scale (top row). The left plots correspond to the low counts data and the right to the high counts data.

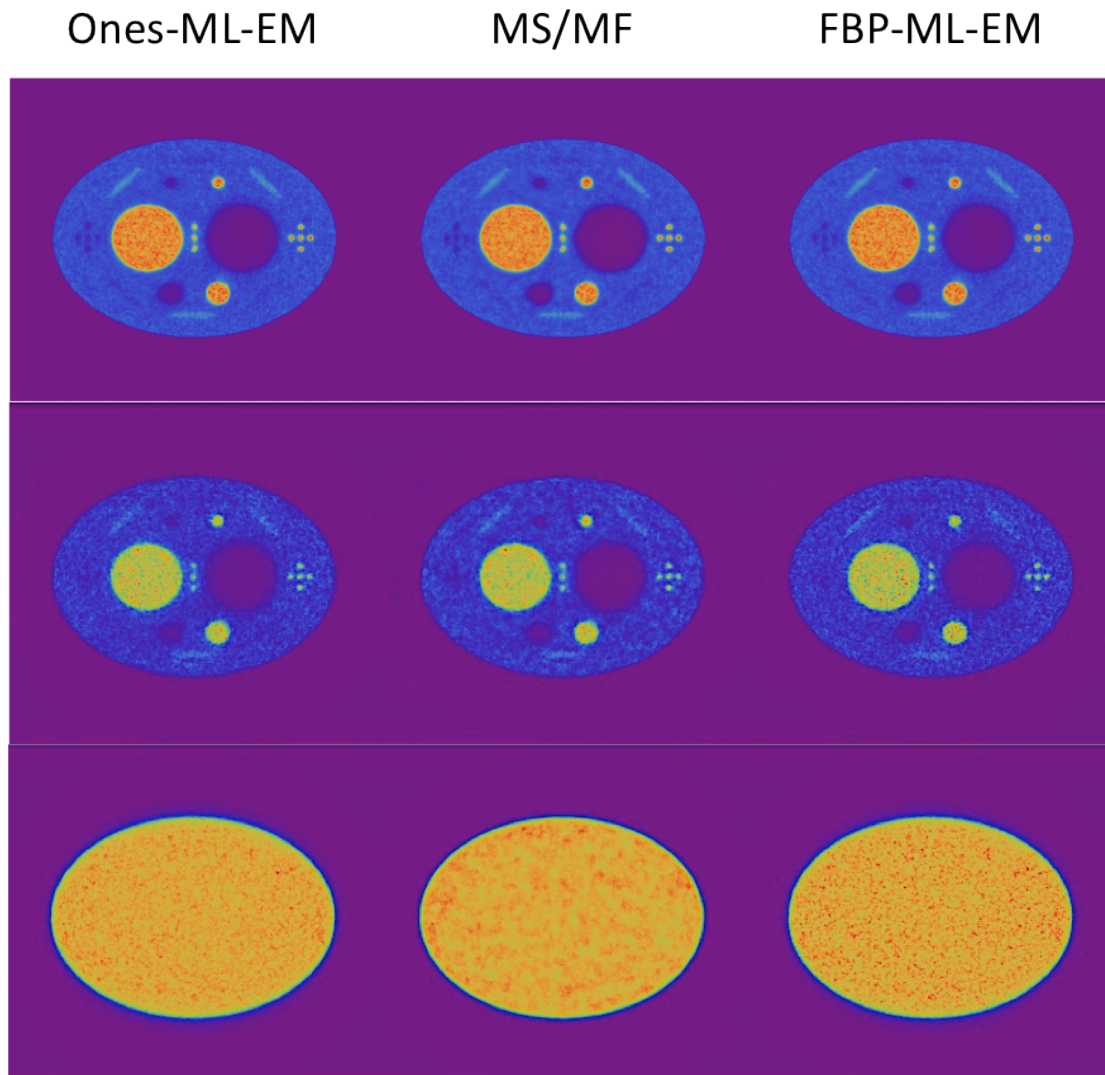


Figure 6.15- Reconstruction results of a representative noise realization using the Ones-ML-EM (left), the MS/MF (center) and the FBP-ML-EM(right). The top row corresponds to the reconstruction results with the high counts dataset, the middle with the low counts dataset and the bottom with the phantom n° 2 dataset.

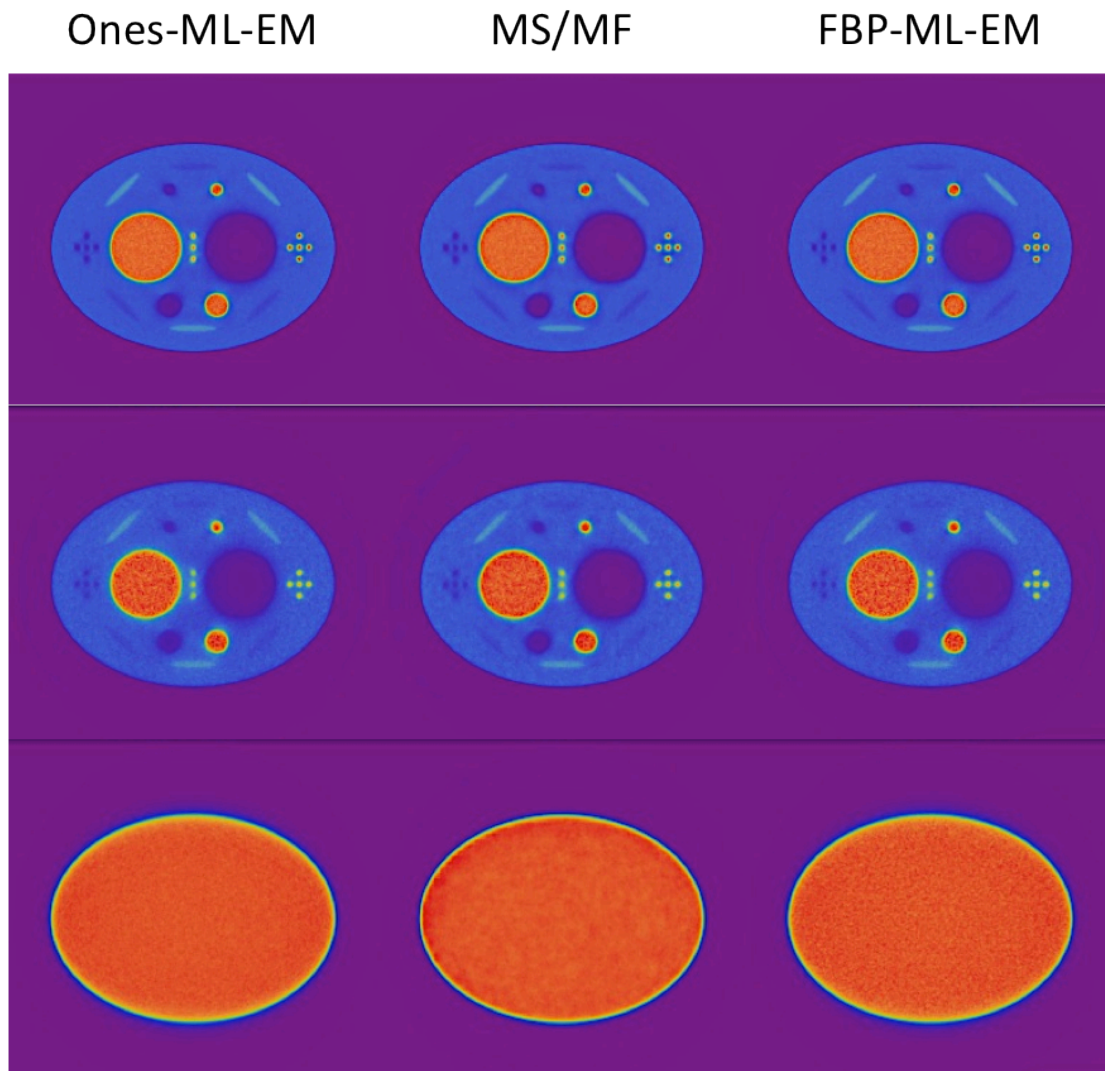


Figure 6.16- Average of the reconstruction results using the Ones-ML-EM (left), the MS/MF (center) and the FBP-ML-EM(right). The top row corresponds to the reconstruction results with the high counts data, the middle with the low counts data and the bottom with the phantom n° 2 data.

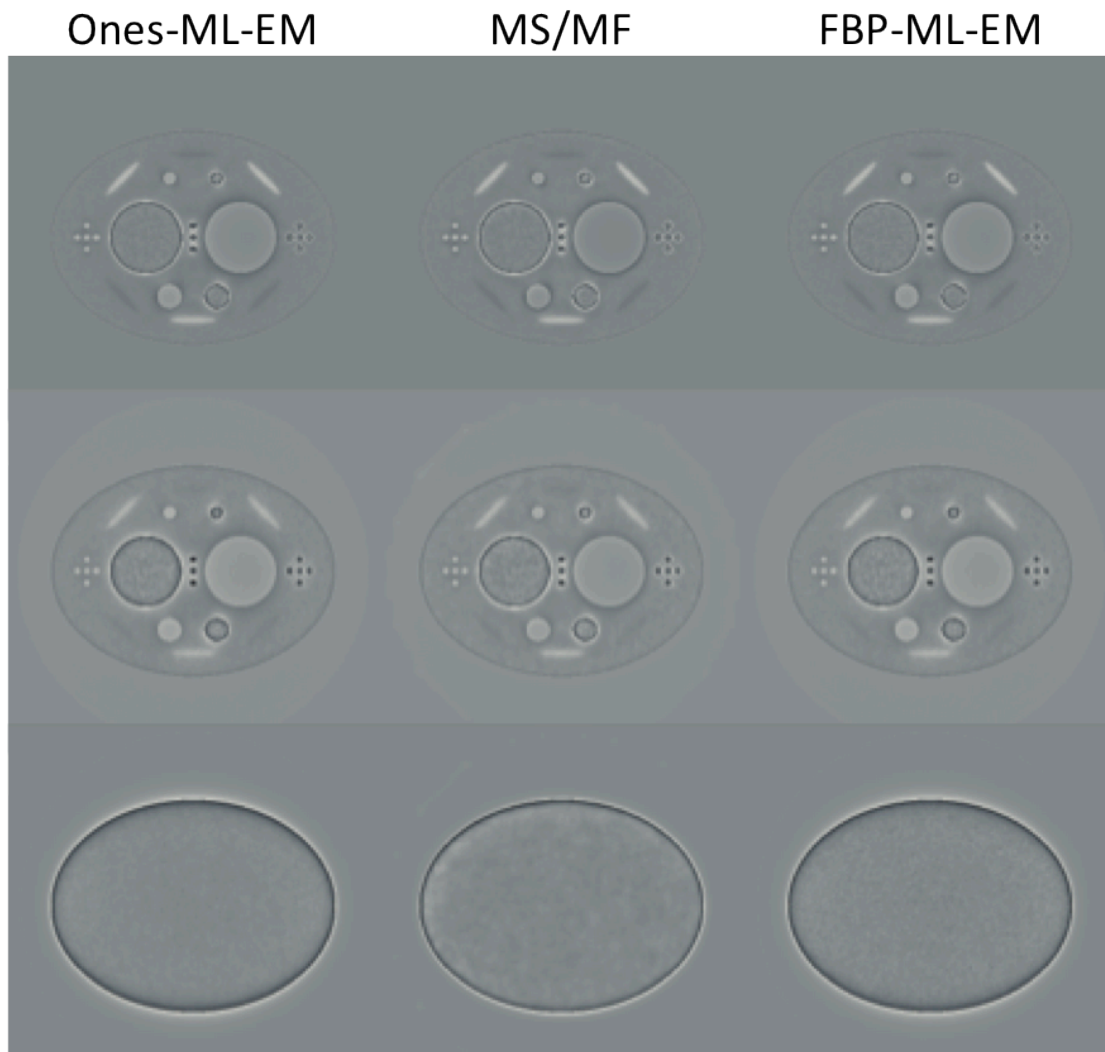


Figure 6.17- Bias images achieved using the Ones-ML-EM (left), the MS/MF (center) and the FBP-ML-EM(right). The top row corresponds to the reconstruction results with the high counts data, the middle with the low counts data and the bottom with the phantom n° 2 data. The stopping reconstruction criterion was the Morozov criterion.

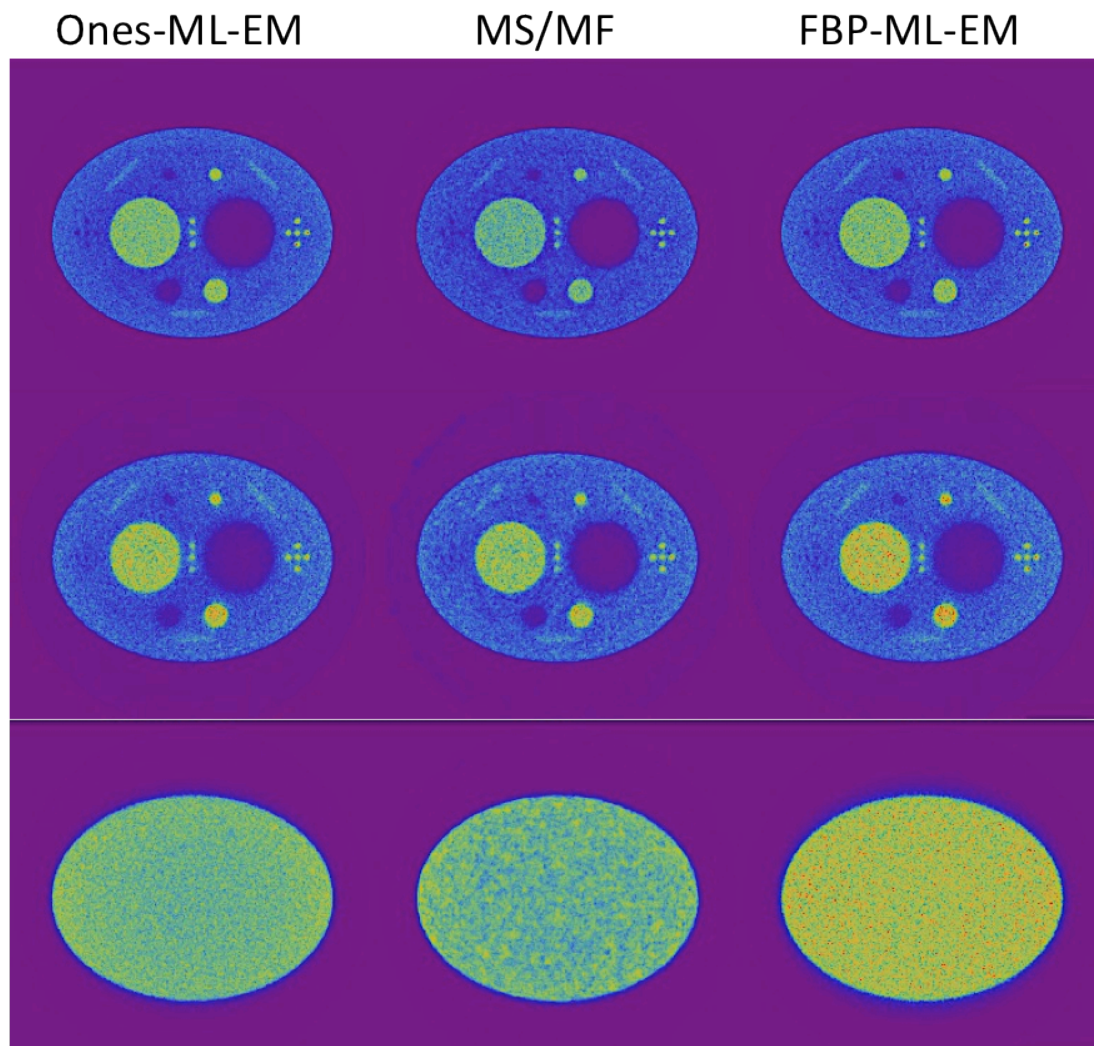


Figure 6.18- Standard deviation images achieved using the Ones-ML-EM (left), the MS/MF (center) and the FBP-ML-EM(right). The top row corresponds to the reconstruction results with the high counts data, the middle with the low counts data and the bottom with the phantom n° 2 data. The stopping reconstruction criterion was the Morozov criterion.

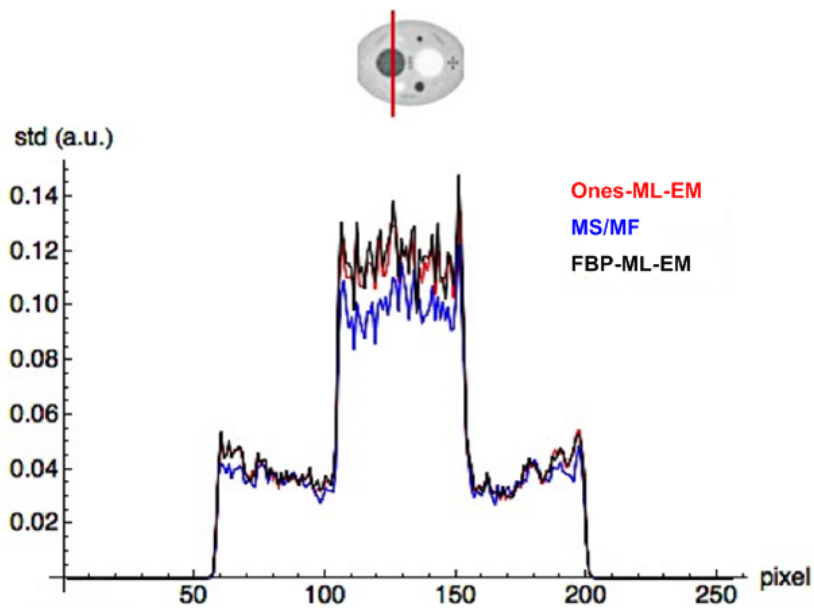


Figure 6.19- Vertical profiles of the standard deviation images for the high counts data. The profile contains a region with a hot structure as shown in the top image. The red, blue and black curves correspond to the reconstruction results using the Ones-ML-EM, the MS/MF and the FBP-ML-EM, respectively. The stopping reconstruction criterion was the Morozov criterion.

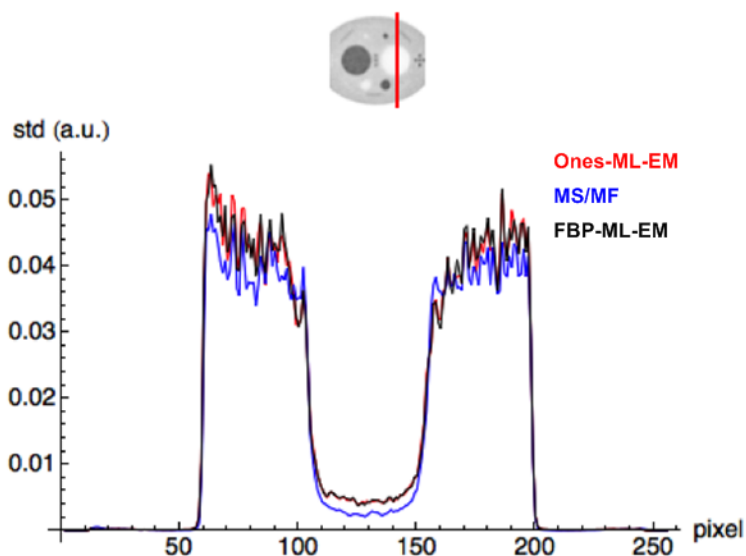


Figure 6.20- Vertical profiles of the standard deviation images for the high counts data. The profile contains a region with a cold structure as shown in the top image. The red, blue and black curves correspond to the reconstruction results using the Ones-ML-EM, the MS/MF and the FBP-ML-EM, respectively. The stopping reconstruction criterion was the Morozov criterion.

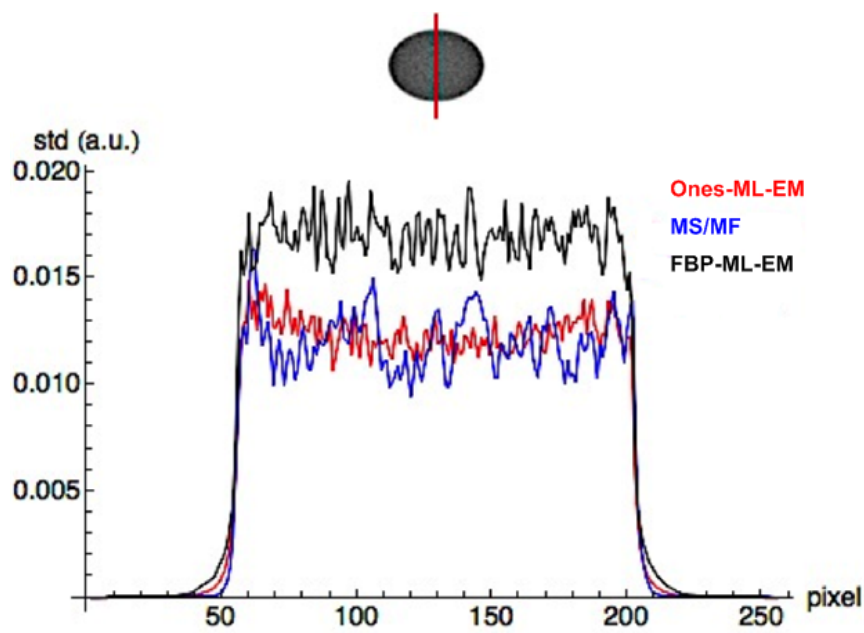


Figure 6.21- Vertical profiles of the standard deviation images for the phantom n° 2 data. The red, blue and black curves correspond to the reconstruction results using the Ones-ML-EM, the MS/MF and the FBP-ML-EM, respectively. The stopping reconstruction criterion was the Morozov criterion.

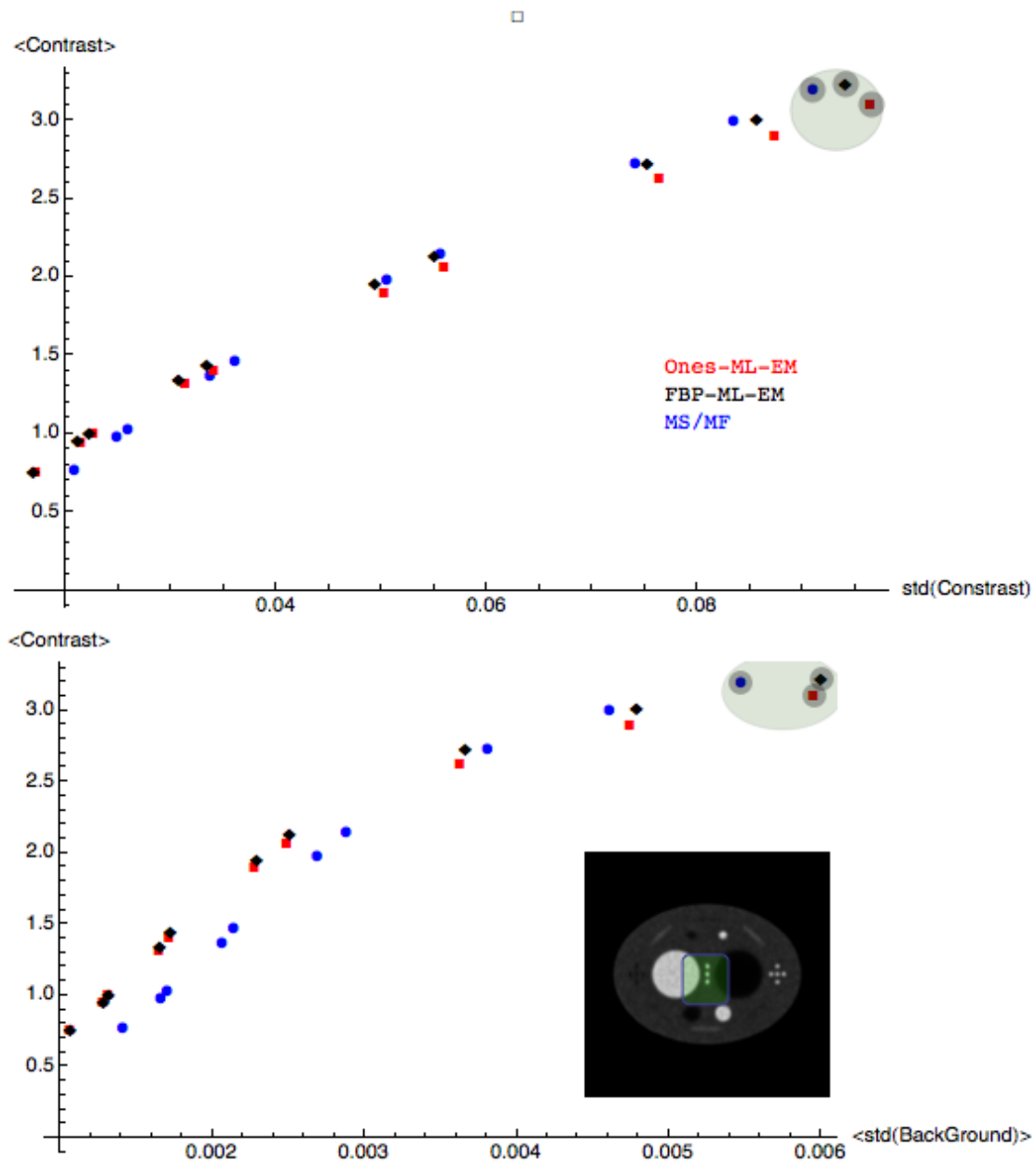


Figure 6.22- Contrast versus noise trade-off curves for the central point sources with 6 mm of diameter (green point sources in the figure of the bottom row) for the high counts data. The top row presents the mean contrast for the different noise realizations versus the standard deviation of the contrast as a function of the different post-reconstruction smoothing filter's FWHM and reconstruction method. In the bottom row is presented the mean ROI Contrast for the different noise realization versus the mean of the standard deviation of the background reconstructed values as a function of the different post- reconstruction smoothing filter's FWHM and reconstruction method. The highlight points correspond to the unfiltered reconstructed data.

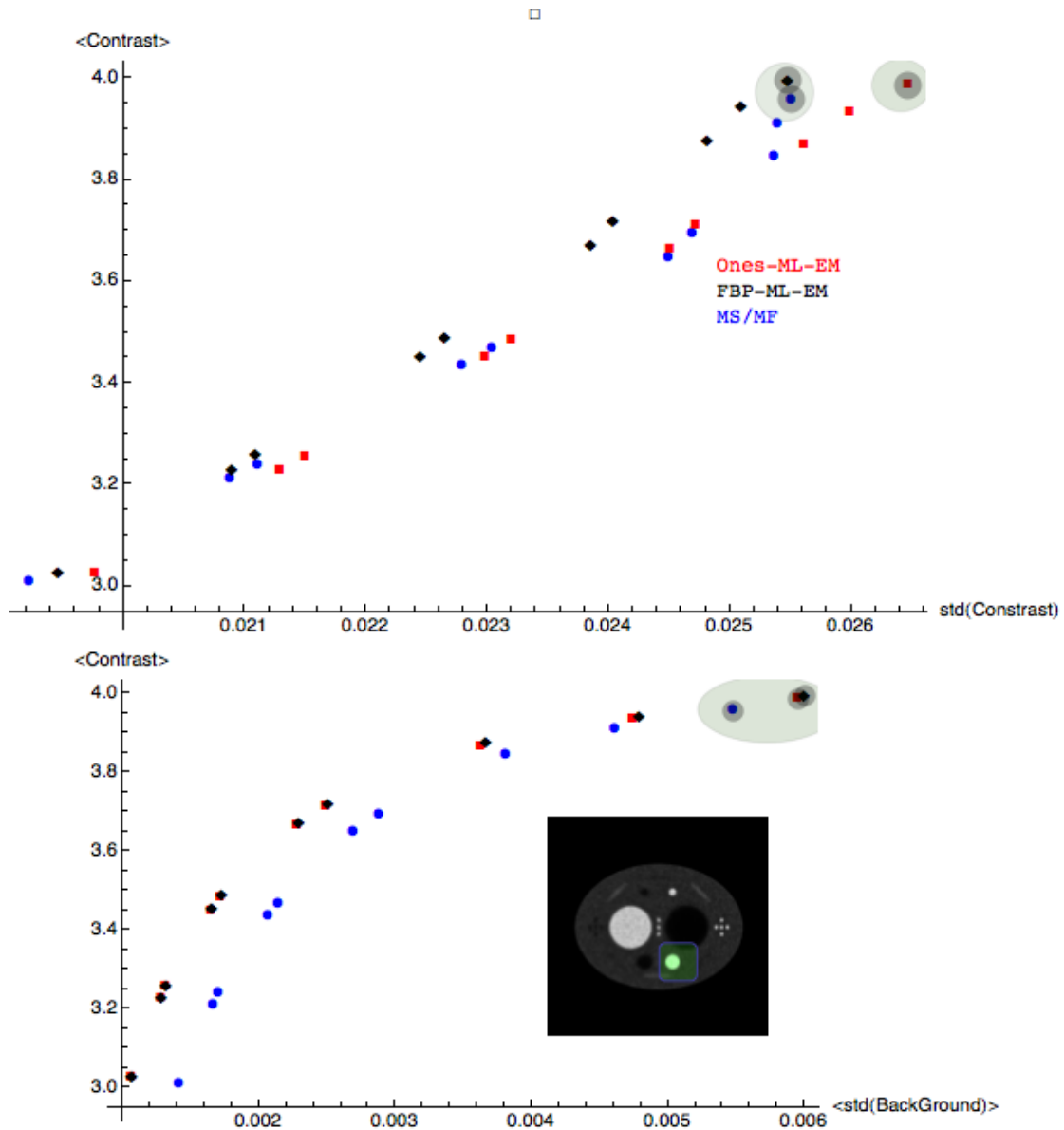


Figure 6.23- Contrast versus noise trade-off curves for a source with 20 mm of diameter (green point sources in the image of the bottom row) for the high counts data. The top row presents the mean contrast for the different noise realizations versus the standard deviation of the contrast as a function of the different post-reconstruction smoothing filter's FWHM and reconstruction method. In the bottom row is presented the mean ROI Contrast for the different noise realizations versus the mean of the standard deviation of the background reconstructed values as a function of the different post- reconstruction smoothing filter's FWHM and reconstruction method. The highlight points correspond to the unfiltered reconstructed data.

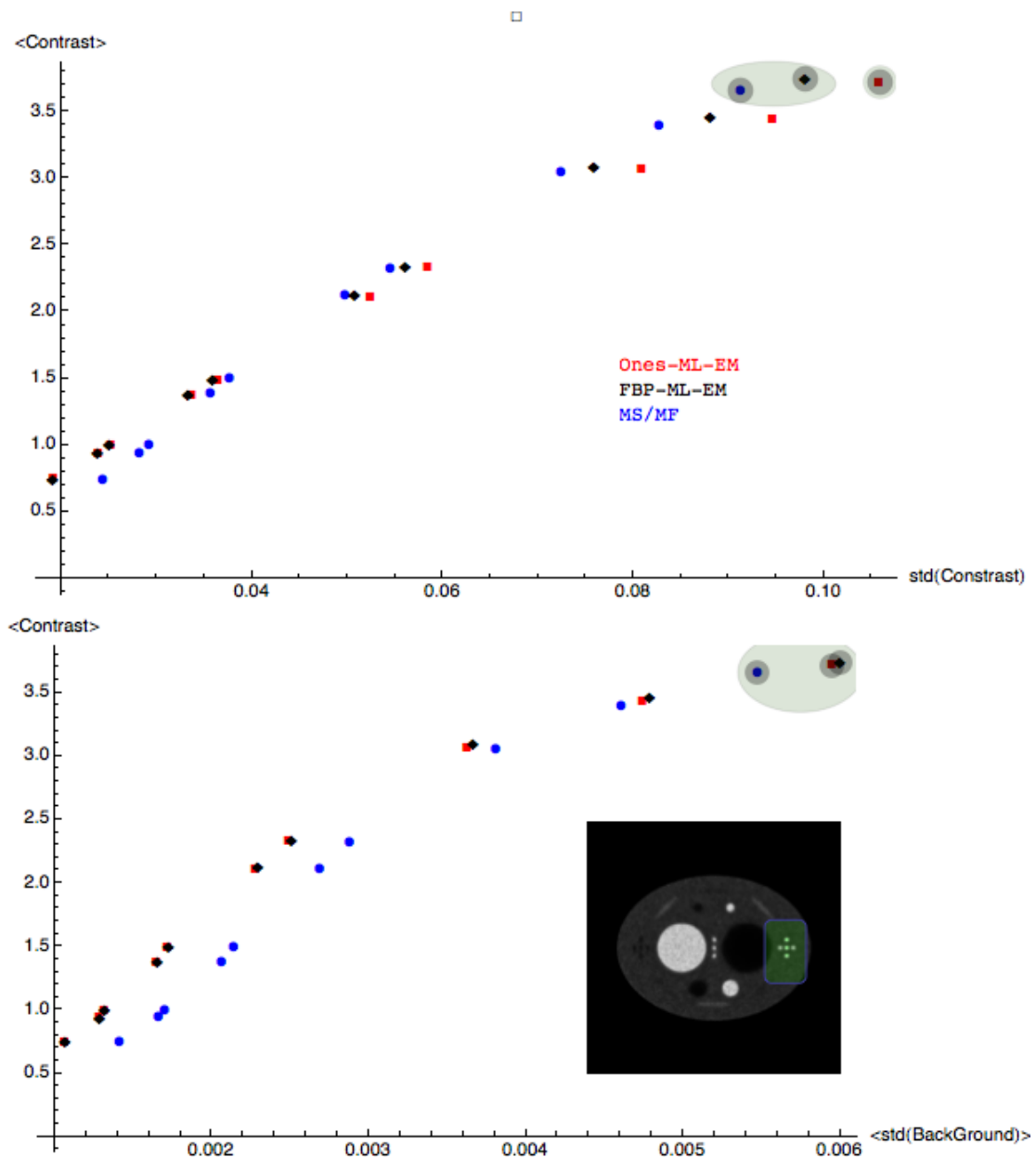


Figure 6.24- Contrast versus noise trade-off curves for the lateral point sources with 6 mm of diameter (green point sources in the figure of the bottom row) for the high counts data. The top row presents the mean contrast for the different noise realizations versus the standard deviation of the contrast as a function of the different post-reconstruction smoothing filter's FWHM and reconstruction method. In the bottom row is presented the mean ROI Contrast for the different noise realization versus the mean of the standard deviation of the background reconstructed values as a function of the different post- reconstruction smoothing filter's FWHM and reconstruction method. The highlight points correspond to the unfiltered reconstructed data.

6.4.3 WDF-Morozov Criterion

Figure 6.25 and Figure 6.26 present the effect of using different low-pass and high-pass filters on the number of iterations required by the WDF-Morozov criterion. The minimum image space error was achieved at iteration 31.

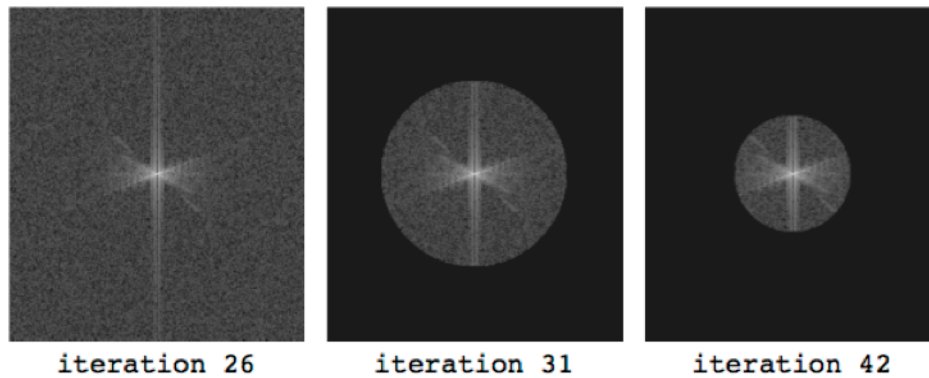


Figure 6.25- Stop iteration requested by the WDF-Morozov criterion when no filter is used (all the weights are equal) and when two different low pass filters are applied. In the top row is showed the power spectrum of the slice n° 104 of the raw data multiply by the correspondent filter mask. The minimum image space error was achieved at iteration 31.

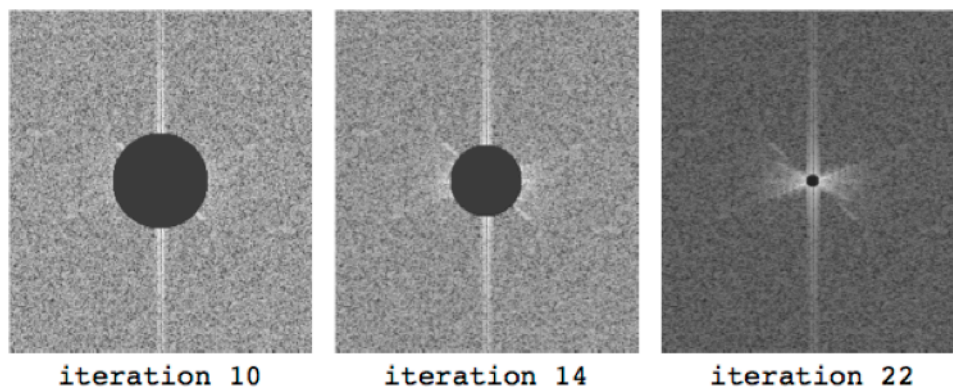


Figure 6.26- Stop iteration using the WDF-Morozov criterion with different high pass filters, In the top row is showed the power spectrum of the slice n° 104 of the raw data multiply by the correspondent filter mask. The minimum image space error was achieved at iteration 31.

6.5 Discussion

Two stopping criteria derived from the generalized Morozov criterion were tested using different simulated datasets. These criteria allow to adaptively select the number of iterations to perform into a given scale. The performance of these criteria was compared with the minimum image space error, the optimal criterion. In practice this criterion cannot be used in real applications because the true image is unknown.

The Morozov stopping criterion was applied to ML-EM reconstruction as well as to the MS/MF reconstruction. The datasets used were generated using analytic simulations.

When applied to the reconstruction of 2D data using the ML-EM, the Morozov criterion chose the stopping iteration near the minimum image space error.

The stop iteration selected by the Morozov criterion as a function of the range of segments used in the reconstruction is also similar to the optimal iteration (see Table 6.1). As expected, with the addition of segments, the number of iterations required by the proposed criterion increases. Good performance was also achieved with the 3D datasets (see Figure 6.8).

Based on simulated data, the Morozov criterion seems appropriate to be used in the MS/MF reconstruction. The number of iterations required by this criterion is near the optimal (see Table 6.2 and Table 6.3). This criterion allows to adaptively choose the number of iterations having into account the counting statistics of the data. (see Figure 6.9).

The effects on the final image of the use of the Morozov criterion as a stopping criterion to the MS/MF were also studied. The study results are in agreement with the ones reported in the section 5.3. The analysis of the evolution of the sinogram error for the fine scale shows that the MS/MF allows improving the convergence (see Figure 6.11 and Figure 6.12). As we can see in Figure 6.13 the number of iterations required by the stopping criterion for the MS/MF was lower when compared with the single scale/frame reconstructions and as expected the number of iterations required by the stopping criterion was lower for the low counts data than for the high counts data.

Initializing the ML-EM iteration with the FBP reconstruction instead of a uniform image only led to a modest gain in convergence.

As expected, the different noise structure introduced by the use of scales/frames (section 5.4) was also found in the reconstruction results using the low counts data and phantom n° 2 data (see Figure 6.15).

The mean (see Figure 6.16), bias (see Figure 6.17) and standard deviation images (see Figure 6.18) also present the different noise structure for MS/MF. Further work will be needed to verify whether a better interpolation method may reduce this effect.

Comparable bias values (see Figure 6.17) were obtained for the different reconstructed methods. The values of the standard deviation (see Figure 6.18) for the high and low counts data were also similar. The vertical profiles (see Figure 6.19 and Figure 6.20) suggest that the standard deviation obtained by the MS/MF is lower. However for the phantom n° 2 the profile obtained with the Ones-ML-EM is comparable (see Figure 6.21). For this phantom the FBP-ML-EM standard deviation values are higher.

Similar contrast with approximately the same noise can be achieved with the three reconstructed methods for the different ROIs (see Figure 6.22, Figure 6.23 and Figure 6.24). Nevertheless, the MS/MF allows achieving the final contrast with less fine scale iterations.

Related to the WDF-Morozov criterion, the results shows that when low frequencies are selected the number of iterations required by this criterion increases (see Figure 6.25). On the contrary, the selection of the high frequencies decreases the number of iterations (see Figure 6.26). With real data, due to the simplification done in the modelling of the system matrix, is expected that the number of iterations required by the Morozov criterion would be too high. The proper choice of a filter could allow solving this problem.

6.6 Conclusions

In this chapter a generalized Morozov stopping criterion for Emission Tomography was presented. Based on this generalization two criterion were derived: the (usual) Morozov and the WDF-Morozov. The main motivation was to develop a stopping criterion suitable for the MS/MF reconstruction. These criteria allow to

adaptively choose the number of iterations to perform in a given scale based on the statistics of the data.

Based on simulated data, the Morozov criterion seems appropriate to be used in the MS/MF reconstruction. The reconstruction results obtained are in agreement with the ones reported in chapter 5.

A proof of concept of the use of the WDF-Morozov criterion was done. This criterion can be very useful when the modelling of the system matrix is inaccurate. The right choice of the weights could allow to overcome this problem.

Chapter 7

7 Main Conclusions and Possible Developments

Positron Emission Tomography (PET) is a quantitative nuclear medicine imaging technique that allows to measure the radiotracer's concentration and the estimation of physiological parameters. When compared with Computer Tomography (CT) or Magnetic Resonance Imaging (MRI), PET has poor resolution and high sensitivity. In this thesis, reconstruction techniques were developed to improve the resolution of the final image, as well as to improve the convergence rate and reducing the reconstruction computation time.

Resolution modelling techniques allow for the improvement of spatial resolution and contrast of the reconstructed images. These improvements are achieved by better modelling the system matrix used during the reconstruction process. A method for the estimation of the sinogram blurring kernel adapted to the High Resolution Research Tomograph is presented in **Chapter 3**. The High Resolution Research Tomograph is a specialized scanner that provides high resolution PET images of the human brain. Due to its high resolution and sensitivity this scanner can also be used in pre-clinical studies.

The proposed method permits the incorporation of the effects of the inter-crystal penetration into the reconstruction process. The blurring kernel model has into account the angle of incidence (α angles) formed by the intersection of the LOR with the detector head. Due to the polygonal geometry of the HRRT, the degradation in

resolution is spread fairly uniform across the FOV. The annihilation photons penetrate with non-normal α angles independently of the radial position. The α angles were organized in a sinogram format (α sinogram). Due to the geometry of the HRRT, the α sinogram was decomposed into 3 distinct regions. The widths of the measured radial profiles depend on the α angles. For ranges of α angles more close to the normal (90°) the corresponding profile width was smaller than the width of profiles with more oblique ranges of α angles. This behaviour was expected because the inter-crystal penetration only occurs for oblique angles of incidence.

The blurring kernel was modelled as a spatial varying asymmetric Gaussian function. The estimation of the radial model parameters was done using only one measurement.

The performance of the reconstruction using the estimated sinogram blurring kernel was compared with the case where no resolution modelling was used and where resolution modelling was applied in the image space. Point source data acquired at different radial distances were reconstructed using the different methods. The proposed method leads to an improvement of spatial resolution as well as allows for the reduction of the variation of the radial and tangential FWHM.

In **Chapter 4** the performance of a multiscale reconstruction algorithm is evaluated and the most suitable interpolator operator is chosen. The Multiscale reconstruction algorithms try to improve the convergence rate and reduce the reconstruction computation time by processing the data at different scales. In this approach, the reconstructed image on the previous scale is interpolated into the next scale and used as initial image for the reconstruction at that scale. At coarse scales the low frequency components of the image can be reconstructed with low computational effort. For dyadic scales, the maximum frequency that can be recovered on the coarse scale corresponds to approximately one-half of the maximum frequency that can be recovered on the next scale. A digital 3D phantom composed of hot and cold structures was especially designed to study the variations of the resolution and of the contrast. The use of analytic simulations allowed having full control over the data generated.

The reconstruction results using different interpolator methods (nearest neighbour, cubic, Gaussian and Lanczos) were compared. The tests results showed

that the Gaussian interpolator is the most suitable kernel to be used in MS reconstruction.

The performance of the MS reconstruction was compared with the ML-EM algorithm. This study confirmed that MS reconstruction allows to reduce the overall reconstruction time. Although we had to perform several iterations in the coarse scales, the number of iterations required in the finest scale was smaller than with the ML-EM reconstruction approach. Similar co-occurrence matrices were found for the reconstruction results obtained with both methods. The improvements in convergence speed obtained by processing the data in different scales were especially high for lower tracer uptake regions.

In **Chapter 5** a novel reconstruction algorithm was presented, the Multiscale/Multiframe algorithm, that introduces the concept of accumulated time frame to the multiscale reconstruction. This approach can be used to generate near real-time images in the scale that is the most suitable to the data statistics available at a given accumulated frame. Usually the dimensions of the reconstructed volume or the projection space binning do not change during the image reconstruction process. In MS/MF the reconstruction begins during the acquisition, using all the events acquired until a given instant, in a coarse scale. Then the reconstruction result of the previous scale is used as initial condition for the reconstruction at a finer scale using a larger temporal data subset. In the finest scale, all the events acquired until the end of the acquisition are processed using the usual dimensions for the image and projection space. If combined with high performance computing (HPC) techniques, this reconstruction approach may allow the optimization of the acquisition parameters on the fly. MS/MF could be useful to reconstruct images in systems with very high resolution, in systems with variable/adaptable geometry for lesion detection or in in-beam PET systems. MS/MF can be easily adapted to list-mode reconstruction algorithms.

The proposed algorithm was characterized using different datasets. The use of the reconstruction result of the previous scale as initial condition for the reconstruction at the finest scale improved the convergence speed and reduced the overall computation time. As was found for the MS, the gain in the convergence speed in the fine scale reconstruction was higher for cold structures.

A different noise structure was found in the MS/MF reconstructed images. In

MS/MF the interpolation introduces correlations between neighbouring pixels that disappear slowly during the fine scale reconstruction. The analysis of the co-occurrence matrices confirms the visual differences in the texture of the reconstructed images.

Reconstructing in near real-time in the fine scale is usually not feasible. MS/MF can be used to perform near real-time reconstruction. In our reconstruction setup, one coarse (medium) scale iteration corresponds to $\sim 5\%$ ($\sim 20\%$) of the time spent in one iteration in the fine scale. Furthermore, since the maximum frequencies that can be recovered depend on the data statistics available at a given accumulated frame, the choice of the reconstruction scale should take into account this parameter.

The proposed reconstruction algorithm was also used to reconstruct a Micro-Deluxe phantom. The use of scales/frames did not introduce significant artifacts in the reconstruction image and allowed for the improvement of the convergence speed.

Most PET reconstruction algorithms try to maximize the likelihood function for Poisson noise. Due to the ill-posed nature of the problem and to the data noise, the maximum likelihood solution is noisy. Several strategies can be used to solve this problem. In clinical environment is common to stop the reconstruction before the maximum of the objective function is reached. **Chapter 6** presents a generalized Morozov discrepancy criterion for Poisson data to adaptively select the number of iterations needed in each scale. Based on this generalization, two stopping rules were derived: the WDF-Morozov and the (usual) Morozov criterion.

Based on simulation data, the Morozov criterion seems suitable for the MS/MF reconstruction. Similar reconstruction results were found using this criterion when compared with the minimum image space error criterion. The WDF-Morozov weights can be chosen to improve the performance of the stopping criterion. This is particularly useful when the modelling of the system matrix is not perfect.

In the future it would be interesting to test and to optimize the reconstruction techniques presented in this thesis, resolution modelling and MS/MF reconstruction approach, with the protocols used in Institute of Nuclear Sciences Applied To Health (ICNAS). A study should be done to assess the feasibility of combining these techniques for the tracer kinetic analysis. Since one of the main objectives of the MS/MF reconstruction is to generate near real-time images, the performance of the reconstruction code should be optimized taking into account the last advances in high

performance computing.

List of Figures

Figure 1.1- Schematic representation of the different stages of a PET exam.....	6
Figure 1.2- Schematic representation of the positron emission and the annihilation process. The positron range and non-collinearity effect are highly exaggerated. .	7
Figure 1.3- Schematic representation of a typical PET block detector.....	10
Figure 1.4- Different type of events: trues (a),singles(b),multiple (c), scatter (d) and random(e).....	12
Figure 1.5- Schematic representation of the 2D (left) and the 3D (right) acquisition mode.....	13
Figure 1.6- Parameterization of a line of response.	14
Figure 1.7- The attenuation path of two annihilation photons emitted from a point source inside the object.....	16
Figure 1.8- Representation of the inter-crystal penetration. The dash line represents the LOR assigned and the continuous line to the real LOR.....	21
Figure 2.1- One dimensional projection of a 2D object as the collection of all parallel line-integrals for an angle ϕ relative to the scanner. The x and y are the coordinate axes related to the scanner. The y_r and x_r are the coordinate axes related to the lines of response (LOR). Adapted from [Defrise et Kinahan, 1998].	24
Figure 2.2- Illustration of the 2D central-section theorem. Adapted from [Defrise et Kinahan, 1998].....	26
Figure 2.3- 2D image reconstruction based on the central slice theorem.....	27
Figure 2.4- A simplified flowchart of an iterative reconstruction. Adapted from [Cherry et al., 2006].	29
Figure 2.5- Siddon algorithm concept. The reduction of the complexity of the computation is done having into consideration that the voxels consist of the intersection of orthogonal sets of equally spaced parallel planes.....	31

- Figure 2.6- ART algorithm. Estimated solution sequence (y^i) for a toy problem with two LORs (λ_1, λ_2) and two pixels (y_1, y_2). The initial pixels values were equal to y^0 36
- Figure 3.1- Schematic representation of the angles of incidence (α_a and α_b angles) formed by the intersection of a LOR with the detector heads.53
- Figure 3.2- Sinograms of the α angles calculated for the intersection of the LORs with the A head (left) and B head (right) represented in Figure 3.1 by α_a and α_b , respectively.54
- Figure 3.3- Representation of the sum of two α sinograms ($\alpha_a + \alpha_b$).55
- Figure 3.4- Relation between the α sinogram regions with the angles between the detector heads in coincidence. In Region 1 the events are detected by the pairs of heads that are face to face. For the events detected in Region 2 the angle between the A head and the B head is 135° and in Region 3 this angle is 90°55
- Figure 3.5- Relations between the coincidences detected in the different pairs of detector heads and the corresponding localizations in the sinogram. The numbers in the figure on the right correspond to the head number defined in the figure on the left. Only the sinogram part between the two dashed lines will be used. Adapted from [Knoß, 2004].56
- Figure 3.6- Representation of the sinogram n° 104 of segment zero (direct planes) of the raw data used to estimate the blurring model parameters.57
- Figure 3.7- Representation of a sinogram decomposition having into account the α Regions 1 (left), the α Regions 2 (centre) and the α Regions 3 (right). The line source was positioned with a radial offset of ~ 13 cm from the centre of the scanner.58
- Figure 3.8- Sinogram n° 104 of the direct planes for the point sources acquired at different radial positions. Left: source position approximately at 1 cm from the centre (dataset 1). Centre: point source at 5 cm from the centre (dataset 2). Right: point source at 10 cm from the centre (dataset 3).59
- Figure 3.9- Measured radial profiles (orange points) used in the estimation of the sinogram resolution kernel parameters for the different α Regions. The blue line corresponds to the fitted curve [Levenberg, 1944]. The central slices of the segment zero of a line source acquisition were used to generate these profiles. .60

- Figure 3.10- From the left to the right column: reconstruction results of a pseudo point source positioned with a radial offset of $\sim 1\text{cm}$, $\sim 5\text{cm}$ and $\sim 10\text{cm}$ from the scanner centre, respectively. A block iterative reconstruction approach with 16 disjoint balanced subsets was used. For each dataset a ROI of the transaxial slice with the maximum counts is presented. Only data from the segment zero was processed. From the top to the bottom row: reconstruction results achieved by the SRM-EM (10 iterations), IRM-EM [Comtat et al., 2008] (10 iterations) and noRM-EM (5 iterations), respectively. The voxel size was equal to $0.24 \times 0.24 \times 1.22 \text{ mm}^3$62
- Figure 3.11- Radial $\text{FWMH}_{\text{nema}}$ as a function of the radial offset. The blue, red and yellow points correspond to the results obtained using the noRM-EM, the IRM-EM and the SRM-EM, respectively. The FWHW was calculated following the NEMA NU 2- 2001 guidelines for spatial resolution measurements.62
- Figure 3.12 Tangential $\text{FWMH}_{\text{nema}}$ as a function of the radial offset. The blue, red and yellow points correspond to the results obtained using the noRM-EM, the IRM-EM and the SRM-EM, respectively. The FWHW was calculated following the NEMA NU 2- 2001 guidelines for spatial resolution measurements.63
- Figure 3.13- Radial asymmetric $\text{FWHM}_{\text{left}}$ as a function of the radial offset. The blue, red and yellow points correspond to the results obtained using the noRM-EM, the IRM-EM and the SRM-EM, respectively.63
- Figure 3.14- Radial asymmetric $\text{FWHM}_{\text{right}}$ as a function of the radial offset. The blue, red and yellow points correspond to the results obtained using the noRM-EM, the IRM-EM and the SRM-EM, respectively.63
- Figure 3.15- Tangential asymmetric $\text{FWHM}_{\text{left}}$ as a function of the radial offset. The blue, red and yellow points correspond to the results obtained using the noRM-EM, the IRM-EM and the SRM-EM, respectively.64
- Figure 3.16- Tangential asymmetric $\text{FWHM}_{\text{right}}$ as a function of the radial offset. The blue, red and yellow points correspond to the results obtained using the noRM-EM, the IRM-EM and the SRM-EM, respectively.64
- Figure 4.1- Schematic representation of the multiscale reconstruction.68
- Figure 4.2- Example of the representation of an image using a non-uniform grid. Left: image using a non-uniform grid with the border pixels highlighted. Right: the same image without highlighting the borders of the pixels. The top line represents a case where the non-uniform grid allows to obtain an image with

better quality than the image at the bottom, where the non-uniform representation adds artefacts.	71
Figure 4.3- Representation of the one-dimensional cubic kernel.	73
Figure 4.4- Representation of the one-dimensional Gaussian kernel.	74
Figure 4.5- Representation of the one-dimensional Lanczos kernel.....	74
Figure 4.6- From the left to the right: sum of all the planes in the transaxial, coronal and sagittal directions of the phantom n° 1.	75
Figure 4.7- Transaxial slice n° 104 of the phantom n° 1.	75
Figure 4.8- Transaxial slice n° 104 of the digital phantom n° 1 represented with the different color gradients used in this thesis.....	76
Figure 4.9- From the left to the right: Highlight of the point source and of the small , medium and large sources used in this thesis.	76
Figure 4.10- 3D raw data dimensions and image dimensions used in the coarse (s=3), medium (s=2) and fine scale (s=1).	77
Figure 4.11- From left to right: sinogram of the slice n° 104 of 2D dataset (top) and the corresponding histogram (bottom) of the coarse, medium and fine scales, respectively.	78
Figure 4.12- Representation of the background ROI (blue region).	80
Figure 4.13- Sinogram reconstruction error in the fine scale as a function of the number of iterations for the different interpolation methods using all the available data (top) and using only the direct planes (bottom).....	81
Figure 4.14- Sum of the transaxial planes of the reconstruction images obtained using the Gaussian, nearest neighbour, cubic and Lanczos interpolation (from left to right respectively) when the 3D dataset is used (top row) and when the 2D dataset is used in the reconstruction (bottom row).	82
Figure 4.15- Sum of the coronal planes of the reconstruction results obtained with Gaussian, nearest neighbour, cubic and Lanczos interpolation (from left to right respectively) when the 3D dataset is used (top row) and when the 2D dataset is used in the reconstruction (bottom row).	82
Figure 4.16- Sum of the sagittal planes of the reconstruction results obtained with Gaussian, nearest neighbour, cubic and Lanczos interpolation (from left to right	

- respectively) when the 3D dataset is used (top row) and when the 2D dataset is used in the reconstruction (bottom row).83
- Figure 4.17- Transaxial slice n° 104 of the reconstruction results obtained with Gaussian, nearest neighbour, cubic and Lanczos interpolation (from left to right respectively) when the 3D dataset is used (top row) and when the 2D dataset is used in the reconstruction (bottom row).83
- Figure 4.18- Profiles of transaxial slice n° 104 of the reconstruction results obtained with the Gaussian, nearest neighbour, cubic and Lanczos interpolation (from left to right) when the 3D dataset is used (top row) and when the 2D dataset is used in the reconstruction (bottom row). The profiles on the left cross a region with 3 small hot structures and the profiles on the right cross a region with a big cold structure.....84
- Figure 4.19- Power spectrum of the Fourier transform applied to the transaxial slice n° 104 of the fine scale initialization image using as interpolation method the Gaussian, the nearest neighbour, the cubic and the Lanczos kernel (from left to right respectively) when the 3D dataset is used (top row) and when the 2D dataset used in the reconstruction (bottom row).85
- Figure 4.20- Co-occurrence matrix of the transaxial slice n° 104 of the initialization image in the fine scale ($s=1$) using different interpolation methods when the 3D dataset is used. The figures a, b, c, d correspond to the Lanczos, cubic, Gaussian and nearest neighbour kernel, respectively.85
- Figure 4.21- Co-occurrence matrix of the slice n° 104 in the transaxial plane of the initialization image in the fine scale ($s=1$) using different interpolation methods when the 2D dataset is used. The figures a, b, c, d correspond to the Lanczos, cubic, Gaussian and nearest neighbour kernel, respectively.....86
- Figure 4.22- Power spectrum of the Fourier transform applied to the slice n° 104 of the phantom n° 1.86
- Figure 4.23- MS reconstruction result (left) and ML-EM reconstruction result (right) for slice n° 104.87
- Figure 4.24- Sinogram reconstruction error in the fine scale as a function of the iteration number using the MS (blue) and ML-EM (red curve) reconstructions. 87
- Figure 4.25- Contrast values in the fine scale as a function of the number of iterations for the central hot structures and the right hot structures (from left to the right,

respectively). The black, blue and red curves correspond to the true phantom, MS and ML-EM reconstruction results for the 3D simulated data, respectively.	88
Figure 4.26- Contrast values in the fine scale as a function of the number of iterations for the large and medium cold structures (represented by the green region in the top left/right image). The blue and red curves correspond to the MS and ML-EM reconstruction results for the 3D simulated data, respectively.	88
Figure 4.27- Co-occurrence matrix of the slice n° 104 of the reconstructed image using MS (left) and ML-EM (right).	89
Figure 5.1- The Multiscale/Multiframe reconstruction scheme.	94
Figure 5.2- From the left to the right: sum of all planes of the digital phantom n° 2 in the transaxial, coronal and sagittal direction.	96
Figure 5.3- From left to right: sinograms of the central plane of segment zero for the digital phantom n° 2 at the coarse, medium and fine scales, respectively.	97
Figure 5.4- From left to right: sinograms of the central plane of segment zero for the phantom n° 1 high counts dataset at the coarse, medium and fine scales, respectively.	98
Figure 5.5- From left to right: sinograms of the central plane of segment zero for the phantom n° 1 low counts dataset at the coarse, medium and fine scales, respectively.	98
Figure 5.6- Central plane of the segment zero of the prompt Micro-Deluxe raw data acquired in the HRRT.	99
Figure 5.7- Representation of the central cold structure of the Micro-Deluxe phantom (green region).	100
Figure 5.8- Phantom n° 2 dataset. Sinogram reconstruction error as a function of the iteration number done in the fine scale. For the MS/MF reconstruction 10 and 9 iterations were done in the coarse and medium scale, respectively.	101
Figure 5.9- Phantom n° 2 dataset. Fine scale image space reconstruction error as a function of the iteration number. For the MS/MF reconstruction 10 and 9 iterations were done in the coarse and medium scale, respectively. The black point for each curve corresponds to the iteration where the minimum error was reached.	102

- Figure 5.10- From the left to the right: sum of all the planes of the MS/MF reconstruction result in the transaxial, coronal and sagittal directions, respectively, using the phantom n° 2 dataset.....102
- Figure 5.11- From the left to the right: sum of all planes of the ML-EM reconstruction result in the transaxial, coronal and sagittal directions, respectively, using the phantom n° 2 dataset.....103
- Figure 5.12- Phantom n° 2 dataset. MS/MF (left) and ML-EM (right) reconstruction results for the transaxial slice n° 104.103
- Figure 5.13- Phantom n° 2 dataset. Co-occurrence matrix of the reconstruction result for transaxial slice n°104 with ML-EM (left) and MS/MF (right).....103
- Figure 5.14- Phantom n° 2 dataset. Reconstruction results of the transaxial slice n° 104 using the MS/MF at iteration 10, 30 and 60.104
- Figure 5.15- ML-EM reconstruction result (left) and MS/MF reconstruction result (right) for transaxial n° 104 using the high counts dataset.....104
- Figure 5.16- ML-EM reconstruction result (left) and MS/MF reconstruction result (right) for transaxial slice n° 104 using the low counts dataset.105
- Figure 5.17 - High counts dataset. Sinogram reconstruction error as a function of the iteration number for the fine scale. The blue curve corresponds to the MS/MF error and the red to the ML-EM error. For the MS/MF reconstruction 24 and 23 iterations were done in the coarse and medium scale, respectively.....105
- Figure 5.18- Low counts dataset. Sinogram reconstruction error as a function of the iteration number for the fine scale. The blue curve corresponds to the MS/MF error and the red to the ML-EM error. For the MS/MF reconstruction 9 iterations were done in the coarse and medium scale.106
- Figure 5.19- High counts dataset. Contrast values as a function of the number of iterations and contrast as a function of the background standard deviation (centre and bottom rows, respectively) for the hot structures with 6 mm of diameter shown in green inside the shaded rectangle of the images in the top row. The black, blue and red curves correspond to the true phantom, fine scale/frame MS/MF and ML-EM reconstruction results, respectively.107
- Figure 5.20- High counts dataset. Contrast values as a function of the number of iterations and contrast as a function of the background standard deviation (centre and bottom rows, respectively) for the big (with 70 mm of diameter) and small (with 12 mm of diameter) cold structures shown in green on the images in the

- top row. The blue and red curves correspond to the fine scale/frame MS/MF and ML-EM reconstruction results, respectively..... 108
- Figure 5.21- High counts dataset. Co-occurrence matrix of the reconstruction result for the slice n°104 with ML-EM (left) and with MS/MF (right). 109
- Figure 5.22- Low counts dataset. Co-occurrence matrix of the reconstruction result for the slice n°104 with ML-EM (left) and with MS/MF (right). 109
- Figure 5.23- Low counts dataset. The top row corresponds to the reconstruction results (slice n° 104) using the MS/MF in the coarse scale (left) and medium scale (right). In the bottom the corresponding reconstruction results using the ML-EM are shown. The left (right) image corresponds to the first (second) accumulated frame. 110
- Figure 5.24- The left image corresponds to the Micro-Deluxe reconstruction result for the slice n° 104 of the first accumulated frame in the medium scale with 30 iterations. The right image shows the reconstruction of the second accumulated frame in the finest scale with 75 iterations. 110
- Figure 5.25- Left column corresponds to the MS/MF reconstruction results when were done 30 iterations in the medium scale, the central column correspond to the reconstruction results using the ML-EM algorithm and the right correspond to the MS/MF reconstruction results when were done 60 iterations in the medium scale. The top row corresponds to the reconstruction results with 1 iteration, the central row with 75 iterations and the bottom row with 150 iterations. 111
- Figure 5.26- Mean value of the Micro-Deluxe central cold structure as a function of the iteration number for the fine scale. The green and blue curves correspond to the MS/MF reconstruction results with 30 and 60 iterations in the medium scale, respectively, and the red curve to the ML-EM reconstruction result. The mean values are expressed in arbitrary units (a.u.)..... 112
- Figure 6.1 - From left to right: Reconstructed image using the ML-EM algorithm at iterations 30, 100 and 400. 118
- Figure 6.2 - From left to right: estimated sinogram at iterations 30, 100 and 400. ... 118
- Figure 6.3 - From left to right: co-occurrence matrix (128 levels) for the reconstruction image at iterations 30, 100 and 400. 119

- Figure 6.4- Representation of phantom n° 3. From left to right: sum of all planes in the transaxial, coronal and sagittal directions.125
- Figure 6.5- Phantom n° 3 dataset. Sinogram of slice n° 104 of segment zero(top) and corresponding histogram (bottom).126
- Figure 6.6- WDF-Morozov dataset. Sinogram of slice n° 104 of segment zero (top) and corresponding histogram (bottom).129
- Figure 6.7- Left image: sinogram space error as a function of the number of iterations and corresponding Morozov stopping criterion using the phantom n° 3 dataset. Right image: image space reconstruction error as a function of the number of iterations.130
- Figure 6.8- 3D reconstruction using ML-EM. Left column: sinogram space error as a function of the number of iterations and the corresponding Morozov stopping criterion. Right column: image space error as a function of the number of iterations. The top row shows results for the medium counts dataset and the bottom row for the high counts dataset.131
- Figure 6.9 - Medium scale 3D reconstruction using MS/MF: The left column shows the sinogram space error as a function of the iterations and the corresponding Morozov stopping criterion. The right column presents the image space error as a function of iterations. The top line shows the results using the high counts dataset and in the bottom line the medium counts dataset.133
- Figure 6.10 - Fine scale 3D reconstruction using MS/MF: The left column shows the sinogram space error as a function of the iterations and the corresponding Morozov stopping criterion. The right column presents the image space error as a function of iterations. In the top line are presented the results using the high counts dataset and in the bottom line the medium counts dataset.133
- Figure 6.11- High counts data. Sinogram reconstruction error as a function of the iteration number for all realizations using the different reconstruction methods. For each reconstructed method the error curves obtained for the different realizations are overlapped. The stopping criterion was the Morozov criterion. The horizontal scale only represents the iterations done at the fine scale. The initial MS/MF iterations at the coarse scales are not taken into account.135
- Figure 6.12- Low counts data. Sinogram reconstruction error as a function of the iteration number for all realizations using the different reconstruction methods. For each reconstructed method the error curves obtained for the different

- realizations are overlapped. The stopping criterion was the Morozov criterion. The horizontal scale only represents the iterations done at the fine scale. The initial MS/MF iterations at the coarse scales are not taken into account.....135
- Figure 6.13- Fine scale distribution of the number of iterations required by the Morozov criterion for the different noise realizations using the MS/MF (top), the Ones-ML-EM (medium) and the FBP-ML-EM (bottom). The left column corresponds to the low counts data and the right column to the high counts data. Several iterations in the coarse scales were done in the MSMF reconstruction.136
- Figure 6.14- Distribution of the number of iterations required by the Morozov criterion for the different noise realizations reconstructed using the MS/MF in the medium scale (top row) and in the coarse scale (top row). The left plots correspond to the low counts data and the right to the high counts data.136
- Figure 6.15- Reconstruction results of a representative noise realization using the Ones-ML-EM (left), the MS/MF (center) and the FBP-ML-EM(right). The top row corresponds to the reconstruction results with the high counts dataset, the middle with the low counts dataset and the bottom with the phantom n° 2 dataset.137
- Figure 6.16- Average of the reconstruction results using the Ones-ML-EM (left), the MS/MF (center) and the FBP-ML-EM(right). The top row corresponds to the reconstruction results with the high counts data, the middle with the low counts data and the bottom with the phantom n° 2 data.138
- Figure 6.17- Bias images achieved using the Ones-ML-EM (left), the MS/MF (center) and the FBP-ML-EM(right). The top row corresponds to the reconstruction results with the high counts data, the middle with the low counts data and the bottom with the phantom n° 2 data. The stopping reconstruction criterion was the Morozov criterion.....139
- Figure 6.18- Standard deviation images achieved using the Ones-ML-EM (left), the MS/MF (center) and the FBP-ML-EM(right). The top row corresponds to the reconstruction results with the high counts data, the middle with the low counts data and the bottom with the phantom n° 2 data. The stopping reconstruction criterion was the Morozov criterion.....140

- Figure 6.19- Vertical profiles of the standard deviation images for the high counts data. The profile contains a region with a hot structure as shown in the top image. The red, blue and black curves correspond to the reconstruction results using the Ones-ML-EM, the MS/MF and the FBP-ML-EM, respectively. The stopping reconstruction criterion was the Morozov criterion.141
- Figure 6.20- Vertical profiles of the standard deviation images for the high counts data. The profile contains a region with a cold structure as shown in the top image. The red, blue and black curves correspond to the reconstruction results using the Ones-ML-EM, the MS/MF and the FBP-ML-EM, respectively. The stopping reconstruction criterion was the Morozov criterion.141
- Figure 6.21- Vertical profiles of the standard deviation images for the phantom n° 2 data. The red, blue and black curves correspond to the reconstruction results using the Ones-ML-EM, the MS/MF and the FBP-ML-EM, respectively. The stopping reconstruction criterion was the Morozov criterion.142
- Figure 6.22- Contrast versus noise trade-off curves for the central point sources with 6 mm of diameter (green point sources in the figure of the bottom row) for the high counts data. The top row presents the mean contrast for the different noise realizations versus the standard deviation of the contrast as a function of the different post-reconstruction smoothing filter's FWHM and reconstruction method. In the bottom row is presented the mean ROI Contrast for the different noise realization versus the mean of the standard deviation of the background reconstructed values as a function of the different post- reconstruction smoothing filter's FWHM and reconstruction method. The highlight points correspond to the unfiltered reconstructed data.143
- Figure 6.23- Contrast versus noise trade-off curves for a source with 20 mm of diameter (green point sources in the image of the bottom row) for the high counts data. The top row presents the mean contrast for the different noise realizations versus the standard deviation of the contrast as a function of the different post-reconstruction smoothing filter's FWHM and reconstruction method. In the bottom row is presented the mean ROI Contrast for the different noise realizations versus the mean of the standard deviation of the background reconstructed values as a function of the different post- reconstruction smoothing filter's FWHM and reconstruction method. The highlight points correspond to the unfiltered reconstructed data.144

- Figure 6.24- Contrast versus noise trade-off curves for the lateral point sources with 6 mm of diameter (green point sources in the figure of the bottom row) for the high counts data. The top row presents the mean contrast for the different noise realizations versus the standard deviation of the contrast as a function of the different post-reconstruction smoothing filter's FWHM and reconstruction method. In the bottom row is presented the mean ROI Contrast for the different noise realization versus the mean of the standard deviation of the background reconstructed values as a function of the different post- reconstruction smoothing filter's FWHM and reconstruction method. The highlight points correspond to the unfiltered reconstructed data. 145
- Figure 6.25- Stop iteration requested by the WDF-Morozov criterion when no filter is used (all the weights are equal) and when two different low pass filters are applied. In the top row is showed the power spectrum of the slice n° 104 of the raw data multiply by the correspondent filter mask. The minimum image space error was achieved at iteration 31. 146
- Figure 6.26- Stop iteration using the WDF-Morozov criterion with different high pass filters, In the top row is showed the power spectrum of the slice n° 104 of the raw data multiply by the correspondent filter mask. The minimum image space error was achieved at iteration 31. 146

List of tables

Table 1.1- List of radionuclides used in PET imaging. The E_{\max} corresponds to the maximum kinetic energy of the emitted positrons. Adapted from [Cherry et al., 2006].	6
Table 1.2- Properties of common scintillator materials used in PET. Adapted from [Cherry et al., 2006].	11
Table 3.1- Estimated position of the point sources for each acquisition, relatively to the centre of the scanner.	59
Table 3.2- Estimated values for the radial component parameters σ_{left} and σ_{right} when the decomposition of the acquired sinogram data have into account the α Regions. The corresponding range of α angles is also presented.	61
Table 4.1 - Number of iterations needed to reach the minimum error in the image space using the 3D dataset and using the 2D dataset for the different interpolation methods (Gaussian, nearest neighbour, Lanczos and cubic) in the fine (S_1), medium (S_2) and coarse scales (S_3).	81
Table 6.1 - Comparison of the number of iterations required by the Morozov stopping criterion and by the MISRE criterion when the range of polar segments used in the reconstruction changes.	131
Table 6.2 - Comparison of the number of iterations required by the Morozov and MISRE criteria using the high counts dataset.	132
Table 6.3 - Comparison of the number of iterations required by the Morozov and MISRE criteria using the medium counts dataset.	132

Bibliography

- [Abreu et al., 2007] M. C. Abreu, "Clear-PEM: A PET imaging system dedicated to breast cancer diagnostics," *Nuclear Instruments and Methods A*, Vol. 571, pp. 81–84, 2007.
- [Abreu et. al, 2007] M. C. Abreu, et al., "Clear-PEM: A PET imaging system dedicated to breast cancer diagnostics," *Nuclear Instruments & Methods in Physics Research Section a-Accelerators Spectrometers Detectors and Associated Equipment*, vol. 571, pp. 81–84, 2007.
- [Adam et al., 2000] L. E. Adam, J. S. Karp, and R. Freifelder, "Energy-based scatter correction for 3-D PET scanners using NaI(Tl) detectors," *IEEE Transactions on Medical Imaging*, Vol. 19, No. 5, pp. 513–521, 2000.
- [Alessio et al., 2006] A. Alessio, P. Kinahan, and T. Lewellen, "Modeling and incorporation of system response functions in 3-D whole body PET," *IEEE Transactions on Medical Imaging*, Vol. 25, Issue 7, 2006.
- [Alpert et al., 2006] N. M. Alpert, A. Reilhac, T. C. Chio, and I. Selesnick, "Optimization of dynamic measurement of receptor kinetics by wavelet denoising," *Neuroimage*, Vol. 30, No. 2, pp. 444–451, 2006.
- [Bailey, 2005] D. L Bailey, "Data Acquisition and Performance Characterization in PET", in *Positron Emission Tomography- Basic Sciences*, Springer-Verlag, London, 2005.
- [Barrett et al., 2003] H. H. Barrett and K. Myers, *Foundations of Image Science*, Wiley-Interscience, 2003.
- [Bertero et al., 1998] M. Bertero and P. Boccacci, *Introduction to Inverse Problems in Imaging*, Institute of Physics Publishing, London, 1998.
- [Bhatia et al., 1996] M. Bhatia, W. C. Karl, and A. S. Willsky, "A wavelet-based method for multiscale tomographic reconstruction," *IEEE Transactions on Medical Imaging*, Vol. 15, No. 1, pp. 92–101, 1996.
- [Bouman et al., 1996] C. A. Bouman and K. Sauer, "A unified approach to statistical tomography using coordinate descent optimization," *IEEE Transactions on Medical Imaging*, Vol. 5, No. 3, pp. 480–492, 1996.

- [Bowen et al., 1994] C. Bowen, C. Michel, and C. Nahmias, “Analytic 3D scatter correction in PET using the Klein-Nishina equation,” in *IEEE Nuclear Science Symposium and Medical Imaging Conference Record*, vol. 3, pp. 1339–1342, 1994.
- [Brankov et al., 2004] J. G. Brankov, Y. Yang, and M. N. Wernick, “Tomographic Image Reconstruction Based on a Content-Adaptive Mesh Model,” *IEEE Transactions on Medical Imaging*, Vol. 23, No. 2, pp. 202–212, 2004.
- [Brasse et al., 2005] D. Brasse, P. Kinahan, and C. Lartizien, “Correction Methods for Random Coincidences in Fully 3D Whole-Body PET: Impact on Data and Image Quality,” *Journal of Nuclear Medicine*, Vol. 46, No.5, 2005.
- [Briggs, 2000] W. Briggs, A multigrid tutorial. Society for Industrial and Applied Mathematics, Philadelphia, 2000.
- [Browne et DePierro, 1996] J. Browne and A. de Pierro, “A row-action alternative to the EM algorithm for maximizing likelihood in emission tomography,” *IEEE Transactions on Medical Imaging*, Vol. 15, No. 5, pp. 687-699, 1996.
- [Burger et al., 2009] W. Burger and M. Burge, Principles of digital image processing. Springer-Verlag New York Inc, p. 260, 2009.
- [Byars et al., 2005] L. G. Byars, M. Sibomana, Z. Burbar, J. Jones, V. Panin, W. C. Barker, J.-S. Liow, R. E. Carson, and C. Michel, “Variance reduction on randoms from coincidence histograms for the HRRT,” in *IEEE Nuclear Science Symposium Conference Record*, Vol. 5, pp. 2622–2626, 2005.
- [Byrne, 1998] C. L. Byrne, “Accelerating the EML algorithm and related iterative algorithms by rescaled block-iterative methods,” *IEEE Transactions on Medical Imaging*, Vol. 7, No. 1, pp. 100–109, 1998.
- [Casey et al., 1996] M. E. Casey, H. Gadagkar, and D. Newport, “A component based method for normalization in volume PET”, in *International Meeting on Fully Three-Dimensional Image Reconstruction in Radiology and Nuclear Medicine Conference Records*, pp. 66–71, 1996.
- [Catana et al., 2008] C. Catana, D. Procissi, Y. Wu, M. S. Judenhofer, J. Qi, B. J. Pichler, R. E. Jacobs, and S. R. Cherry, “Simultaneous in vivo positron emission tomography and magnetic resonance imaging,” in *Proceedings of the National Academy of Sciences U.S.A.*, Vol. 105, No. 10, pp. 3705–3710, 2008.

- [Censor et al., 1983] Y. Censor, P. Eggermont, and D. Gordon, "Strong underrelaxation in Kaczmarz's method for inconsistent systems," *Numerische Mathematik*, Vol. 41, Issue 1, 1983.
- [Cherry et al., 1997] S. Cherry, Y. Shao, and S. Siegel, "MicroPET: a high resolution PET scanner for imaging small animals," *IEEE Transactions on Nuclear Science*, Vol. 44, No. 3, 1997.
- [Cherry et al., 2006] S. Cherry, M. Dahlbom, and M. Phelps, "PET physics, instrumentation, and scanners," in *PET: Physics, Instrumentation, And Scanners*, Springer, London, 2006.
- [Cherry et Huan, 1995] S. R. Cherry and Sung-Cheng Huang, "Effects of scatter on model parameter estimates in 3D PET studies of the human brain," *IEEE Transactions on Nuclear Science*, Vol. 42, No. 4, pp. 1174–1179, 1995.
- [Cherry, 2006] S. Cherry, "The 2006 Henry N. Wagner Lecture: Of mice and men (and positrons)-advances in PET imaging technology", *Journal of Nuclear Medicine*, Vol. 47, No. 11, 2006.
- [Cho et al., 1990] Z. H. Cho, C. M. Chen, and S. Lee, "Incremental algorithm- a new fast backprojection scheme for parallel beam geometries," *IEEE Transactions on Medical Imaging*, Vol. 9, No. 2, pp. 207–217, 1990.
- [Choi, 1998] H. Choi, "Direct-Fourier reconstruction in tomography and synthetic aperture radar", *Intl. J. Imaging Sys. and Tech*, Vol. 9, 1998.
- [Cloquet et al., 2010] C. Cloquet, F. C. Sureau, M. Defrise, G. van Simaey, N. Trotta, and S. Goldman, "Non-Gaussian space-variant resolution modelling for list-mode reconstruction," *Physics in Medicine and Biology*, Vol. 55, No. 17, pp. 5045–5066, 2010.
- [Comtat et al., 1999] C. Comtat, P. Kinahan, M. Defrise, and C. Michel, "Simulating whole-body PET scanning with rapid analytical methods," in *IEEE Nuclear Science Symposium Conference Record*, vol. 3, pp. 1260–1264, 1999.
- [Comtat et al., 2004] C. Comtat, F. Bataille, C. Michel, and J. Jones, "OSEM-3D reconstruction strategies for the ECAT HRRT," in *IEEE Nuclear Science Symposium Conference Record*, Vol. 6, pp. 3492 - 3496, 2004.
- [Comtat et al., 2008] C. Comtat, F. Sureau, M. Sibomana, and I. Hong, "Image based resolution modeling for the HRRT OSEM reconstructions software," in *IEEE Nuclear Science Symposium Conference Record*, pp.4120-4123, 2008.

- [Conti, 2009] M. Conti, "State of the art and challenges of time-of-flight PET," *Physica Medica*, Vol. 25, Issue 1, 2009.
- [Couceiro et al., 2012] M. Couceiro, P. Crespo, L. Mendes, N. Ferreira, R. F. Marques, and P. Fonte, "Spatial resolution of human RPC-PET system," *Nuclear Instruments and Methods A*, Vol. 661, Sup. 1, 2012.
- [Couceiro et. al, 2007] M. Couceiro, A. Blanco, N. C. Ferreira, R. F. Marques, P. Fonte, and L. Lopes, "RPC-PET: Status and perspectives," *Nuclear Instruments and Methods A*, Vol. 580, pp. 915–918, 2007.
- [Daube-Witherspoon et al., 2002] M. Daube-Witherspoon, J. Karp, and M. Casey, "PET performance measurements using the NEMA NU 2-2001 standard," *Journal of Nuclear Medicine*, Vol. 43, No. 10, pp. 1398-1409, 2002.
- [Daubechies, 1992] I. Daubechies, Ten lectures on wavelets. Society for Industrial and Applied Mathematics, Philadelphia, 1992.
- [Deans, 1983] S. R. Deans, The Radon transform and some of its applications. Krieger Pub Co, Florida ,1983.
- [Defrise et al., 1991] M. Defrise, D. Townsend, D. Bailey, and A. Geissbuhler, "A normalization technique for 3D PET data," *Physics in Medicine and Biology*, Vol.36, No.7, 1991.
- [Defrise et al., 1997] M. Defrise, P. Kinahan, D. Townsend, and C. Michel, "Exact and approximate rebinning algorithms for 3-D PET data," *IEEE Transactions on Medical Imaging*, Vol. 16, No.2, pp. 145-58, 1997.
- [Defrise et al., 2005] M. Defrise, P. E. Kinahan, and C. Michel, "Image Reconstruction Algorithms in PET", in Positron emission tomography: basic sciences, Springer-Verlag, London, 2005.
- [Defrise et DeMol, 1987] M. Defrise and C. De Mol, "A note on stopping rules for iterative regularization methods and filtered svd", in Inverse Problems: An interdisciplinary Study, Academic Press, 1987.
- [Defrise et Kinahan, 1998] M. Defrise and P. Kinahan, "Data acquisition and image reconstruction", in The theory and practice of 3D PET, Springer, London, 1998.
- [Delaney et Bresler, 1994] A. Delaney and Y. Bresler, "Multiresolution tomographic reconstruction using wavelets," in *International Conference Image Processing Proceedings*, Vol. 2, pp. 830 - 834, 1994.
- [DeMan et Basu, 2004] B. de Man and S. Basu, "Distance-driven projection and backprojection in three dimensions," *Physics in Medicine and Biology*, Vol. 49, No. 11, 2004.

- [Dempster et al., 1977] A. Dempster, N. Laird, and D. Rubin, "Maximum likelihood from incomplete data via the EM algorithm," *Journal of the Royal Statistical Society*, Vol. 39, No. 1, pp. 1-38, 1977.
- [DePierro et Yamagishi, 2001] A. de Pierro and M. Yamagishi, "Fast EM-like methods for maximum 'a posteriori' estimates in emission tomography," *IEEE Transactions on Medical Imaging*, Vol. 20, No. 4, 2001.
- [DePierro, 1993] A. de Pierro, "On the relation between the ISRA and the EM algorithm for positron emission tomography," *IEEE Transactions on Medical Imaging*, Vol. 12, Issue 2, 1993.
- [DePierro, 2003] A. Pierro, "Fast scaled gradient decomposition methods for maximum likelihood transmission tomography," in *IEEE 25th Annual International Conference of the Engineering in Medicine and Biology Society Proceedings*, Vol. 1, pp. 829 - 832, 2003.
- [Drzezga et al., 2011] A. Drzezga, A.J. Beer; S. Fürst; S. Ziegler; S.G. Nekolla; M. Schwaiger, "Integrated Whole Body MR/PET Imaging. First Examples of Clinical Application," *MAGNETOM Flash*, Issue 1, pp.102-110, 2011.
- [Egger et al., 1996] M. L. Egger, A. Herrmann Scheurer, C. Joseph, and C. Morel, "Fast volume reconstruction in positron emission tomography: implementation of four algorithms on a high-performance scalable parallel platform," in *IEEE Nuclear Science Symposium Conference Record*, vol. 3, pp. 1574–1578, 1996.
- [Eggermont et al., 1981] P. Eggermont, G. Herman, and A. Lent, "Iterative Algorithms for Large Partitioned Linear-Systems, with Applications to Image-Reconstruction," *Linear Algebra and its Applications*, Vol. 40, pp. 37–67, 1981.
- [Eriksson et al., 2002] L. Eriksson, K. Wienhard, M. Eriksson, and M. Casey, "The ECAT HRRT: NEMA NEC evaluation of the HRRT system, the new high-resolution research tomograph," *IEEE Transactions on Nuclear Science*, Vol. 49, No. 5, 2002.
- [Fakhri et al., 2011] G. el Fakhri, S. Surti, C. M. Trott, J. Scheuermann, and J. S. Karp, "Improvement in Lesion Detection with Whole-Body Oncologic Time-of-Flight PET," *Journal of Nuclear Medicine*, Vol. 52, No. 3, pp. 347–353, 2011.
- [Ferreira et al., 2000] N. C. Ferreira, R. Trebossen, C. Lartizien, V. Brulon, P. Merceron, and B. Bendriem, "A hybrid scatter correction for 3D PET based on an estimation of the distribution of unscattered coincidences: implementation on the ECAT EXACT HR+," in *IEEE Nuclear Science Symposium Conference Record*, Vol. 2, pp. 136-143, 2000.

- [Ferreira et al., 2009] N. Ferreira, R. Bugalho, and A. Trindade, "Development of component-based normalization correction for the Clear-PEM system," in *IEEE Nuclear Science Symposium Conference Record*, pp. 2846-2848, 2009.
- [Fessler et al., 1997] J. A. Fessler, E. P. Ficaro, N. H. Clinthorne, and K. Lange, "Grouped-coordinate ascent algorithms for penalized-likelihood transmission image reconstruction," *IEEE Transactions on Medical Imaging*, Vol. 16, No. 2, pp. 166–175, 1997.
- [Fessler, 1994] J. Fessler, "Penalized weighted least-squares image reconstruction for positronemission tomography," *IEEE Transactions on Medical Imaging*, Vol.13, No.2, 1994.
- [Fessler, 2004] J. Fessler, NSS/MIC statistical image reconstruction short course notes, Rome, 2004.
- [Gimenez et al., 2006] M. Gimenez, J. Benlloch, and M. Rafecas, "Comparison of different approaches based on Monte Carlo methods to calculate the system matrix for small animal PET," *Nuclear Instruments and Methods A*, Vol. 569, Issue 2, pp. 346–349, 2006.
- [Gonzalez et al., 2005] R. C. Gonzalez, E. R. Woods, S. L. Eddins, *Digital Image Processing Using Matlab*, Pearson Prentice Hall, May 2005.
- [Gordon, 1974] R. Gordon, "A tutorial on ART", *IEEE Transactions on Nuclear Science*, Vol. NS-21, pp. 78–93, 1974.
- [Herman, 1980] G. T. Herman, *Image reconstruction from projections*. Academic Press, 1980.
- [Holdsworth et al., 2001] C. H. Holdsworth, C. S. Levin, T. H. Farquhar, M. Dahlbom, and E. J. Hoffman, "Investigation of accelerated Monte Carlo techniques for PET simulation and 3D PET scatter correction," *IEEE Transactions on Medical Imaging Nuclear Science*, Vol. 48, No. 1, pp. 74–81, 2001.
- [Hudson et Larkin, 1994] H. Hudson and R. Larkin, "Accelerated image reconstruction using ordered subsets of projection data," *IEEE Transactions on Medical Imaging*, Vol.13, No. 4, 1994.
- [Hunter et Lange, 2004] D. Hunter and K. Lange, "A Tutorial on MM Algorithms," *The American Statistician*, Vol. 58, 2004.
- [Jan et al., 2004] S. Jan, C. Comtat, R. Boisgard, and R. Trebossen, "Comparative study of microPET® FOCUS and ECAT HRRT PET systems for small rodents imaging," in *IEEE Nuclear Science Symposium*

Conference Record, Vol. 6, pp. 3430 - 3432, 2004.

- [Johnson, 1994] V. E. Johnson, "A note on stopping rules in EM-ML reconstructions of ECT images," *IEEE Transactions on Medical Imaging*, Vol. 13, No. 3, pp. 569–571, 1994.
- [Jong et al., 2007] H. de Jong, F. van Velden, R. Kloet, and F. Buijs, "Performance evaluation of the ECAT HRRT: an LSO-LYSO double layer high resolution, high sensitivity scanner," *Physics in Medicine and Biology* Vol. 52, No. 5, pp. 1505-1526, 2007.
- [Joseph, 1982] P. Joseph, "An Improved Algorithm for Reprojecting Rays through Pixel Images," *IEEE Transactions on Medical Imaging*, Vol. 3, pp.-192-196, 1982.
- [Kemerink et al., 2011] G. J. Kemerink, M. G. W. Visser, R. Franssen, E. Beijer, M. Zamburlini, S. G. E. A. Halders, B. Brans, F. M. Mottaghy, and G. J. J. Teule, "Effect of the positron range of ^{18}F , ^{68}Ga and ^{124}I on PET/CT in lung-equivalent materials," *European Journal of Nuclear Medicine and Molecular Imaging*, Vol. 38, No. 5, pp. 940–948, 2011.
- [Kinahan et al., 1998] P. E. Kinahan, D. W. Townsend, T. Beyer, and D. Sashin, "Attenuation correction for a combined 3D PET/CT scanner," *Medical Physics*, Vol. 25, No. 10, pp. 2046–2053, 1998.
- [Knoß, 2004] C. Knoß, Evaluation and Optimization of the High Resolution Research Tomograph (HRRT), Shaker Verlag, Aachen, 2004.
- [Lange et Carson, 1984] K. Lange and R. Carson, "EM reconstruction algorithms for emission and transmission tomography", *Journal of Computer Assisted Tomography*, Vol. 8, No. 2, pp. 306–316, 1984.
- [Lecomte et al., 1984] R. Lecomte, D. Schmitt, and G. Lamoureux, "Geometry Study of a High Resolution PET Detection System Using Small Detectors," *IEEE Transactions on Nuclear Science*, Vol. 31, No. 1, pp. 556–561, 1984.
- [Lecomte et al., 1996] R. Lecomte, J. Cadorette, S. Rodrigue, D. Lapointe, D. Rouleau, M. Bentourkia, R. Yao, and P. Msaki, "Initial results from the Sherbrooke avalanche photodiode positron tomograph," *IEEE Transactions on Nuclear Science*, Vol. 43, No. 3, pp. 1952–1957, 1996.
- [Levenberg, 1944] K. Levenberg, "A Method for the Solution of Certain Non-Linear Problems in Least Squares". *Quarterly of Applied Mathematics*, No. 2, pp. 164–168, 1944.

- [Levin et al., 1995] C. S. Levin, M. Dahlbom, and E. J. Hoffman, "A Monte Carlo correction for the effect of Compton scattering in 3-D PET brain imaging," *IEEE Transactions on Medical Imaging Nuclear Science*, Vol. 42, No. 4, pp. 1181–1185, 1995.
- [Levin et Zaidi, 2007] C. Levin and H. Zaidi, "Current trends in preclinical PET system design," *PET Clinics*, Vol. 2, Issue 2, pp. 125–160, 2007.
- [Lewellen, 2008] T. Lewellen, "Recent developments in PET detector technology," *Physics in Medicine and Biology*, Vol. 53, No. 17, 2008.
- [Lewitt et Matej, 2003] R. Lewitt and S. Matej, "Overview of methods for image reconstruction from projections in emission computed tomography," in *Proceedings of the IEEE*, Vol. 91, No. 10, pp. 1588–1611, 2003.
- [Llacer et al., 1993] J. Llacer, E. Veklerov, K. J. Coakley, E. J. Hoffman, "Statistical analysis of maximum likelihood estimator images of human brain FDG PET studies," *IEEE Transactions on Medical Imaging*, Vol. 12, No. 2, pp. 215–231, 1993.
- [Llacer et Veklerov, 1989] J. Llacer, E. Veklerov, "Feasible images and practical stopping rules for iterative algorithms in emission tomography," *IEEE Transactions on Medical Imaging*, Vol. 8, No. 2, pp. 186–193, 1989.
- [Lucy, 1974] L. Lucy, "An iterative technique for the rectification of observed distributions," *Astronomical Journal*, Vol. 79, No. 6, pp. 745–754, 1974.
- [Matej et Bajla, 1990] S. Matej and I. Bajla, "A high-speed reconstruction from projections using direct Fourier method with optimized parameters-an experimental analysis," *IEEE Transactions on Medical Imaging*, Vol. 9, No. 4, pp. 421–429, 1990.
- [Meikle et Badawi, 2005] S. R. Meikle and R. D. Badawi, "Quantitative Techniques in PET", in *Positron Emission Tomography- Basic Sciences*, Springer-Verlag, London, 2005.
- [MicroDeluxe, 2012] *Micro Deluxe Datasheet*. [on-line] Available on: http://www.spect.com/pub/Mini_and_Micro_Deluxe_Phantom_and_Hot_Spot_Insert.pdf. [January de 2012].
- [Mumcuoglu et al., 1996] E. U. Mumcuoglu, R. M. Leahy, S. R. Cherry, and E. Hoffman, "Accurate geometric and physical response modelling for statistical image," in *IEEE Nuclear Science Symposium Conference Records*, Vol. 3, pp. 1569–1573, 1996.

- [NEMA, 1994] NEMA Standards Publication NU 2-1994. Performance Measurements of Positron Emission Tomographs. Rosslyn, VA: National Electrical Manufacturers Association, 1994.
- [NEMA, 2001] NEMA Standards Publication NU 2-2001. Performance Measurements of Positron Emission Tomographs. Rosslyn, VA: National Electrical Manufacturers Association, 2001.
- [Nowak et Kolaczyk, 2000] R. D. Nowak and E. D. Kolaczyk, "A statistical multiscale framework for Poisson inverse problems," *IEEE Transactions on Information Theory*, Vol. 46, No. 5, pp. 1811–1825, 2000.
- [Nuyts et al., 2001] J. Nuyts, C. Michel, and P. Dupont, "Maximum-likelihood expectation-maximization reconstruction of sinograms with arbitrary noise distribution using NEC-transformations," *IEEE Transactions on Medical Imaging*, Vol. 20, No. 5, pp. 365–375, 2001.
- [Nuyts, 2012] J. Nuyts. (September, 2011). *Nuclear Medicine Technology and Techniques*. [On-line]. Available: ftp://134.58.179.7/pub/nuyts/cursus/cursus_nucleo.pdf. [January 10, 2012].
- [Oh et al., 2003a] S. Oh, A. B. Milstein, C. Bouman and K.J.Webb, "Multigrid algorithms for optimization and inverse problems," in *Proceedings the SPIE SPIE/IS&T Conference on Computational Imaging*, Vol. 5016, pp.59-70, 2003.
- [Oh et al., 2003b] S. Oh, A. B. Milstein, C. A. Pouman, and K. J. Webb, "Adaptive nonlinear multigrid inversion with applications to Bayesian optical diffusion tomography," in *Proc. IEEE Workshop on Statistical Signal Processing*, St. Louis, USA, Sep. 2003.
- [Oh et al., 2005] E. A. Philippe, N. Mullani, W. Wong, and R. Hartz, "Real-Time Image Reconstruction for Time-of-Flight Positron Emission Tomography (TOFPET)," *IEEE Transactions on Nuclear Science*, Vol. 29, No. 1, pp. 524–528, 1982
- [Oh et al., 2005] S. Oh, A. B. Milstein, C. A. Bouman, and K. J. Webb, "A general framework for nonlinear multigrid inversion," *IEEE Transactions on Medical Imaging*, Vol. 14, No. 1, pp. 125–140, 2005.
- [Oh et al., 2006] S. Oh, C. A. Bouman, and K. J. Webb, "Multigrid tomographic inversion with variable resolution data and image spaces," *IEEE Transactions on Image Processing*, Vol. 15, No. 9, pp. 2805–2819, 2006.
- [Ollinger, 1995] J. M. Ollinger, "Detector efficiency and Compton scatter in fully 3D PET," Nuclear Science, in *Nuclear Science Symposium and Medical Imaging Conference*, Vol. 3, No. 4, pp. 1280–1284, 1995.

- [Ollinger, 1996] J. M. Ollinger, "Model-based scatter correction for fully 3D PET," *Physics in Medicine and Biology*, Vol. 41, No. 1, pp. 153–176, 1996.
- [Ortuno et al., 2010] J. E. Ortuno, G. Kontaxakis, J. L. Rubio, P. Guerra, and A. Santos, "Efficient methodologies for system matrix modelling in iterative image reconstruction for rotating high-resolution PET," *Physics in Medicine and Biology*, Vol. 55, No. 7, pp. 1833–1861, 2010.
- [Pan et Yagle, 1991] T. Pan and A. Yagle, "Numerical Study of Multigrid Implementations of Some Iterative Image-Reconstruction Algorithms," *IEEE Transactions on Medical Imaging*, Vol. 10, No. 4, pp. 572–588, 1991.
- [Panin et al., 2006a] V. Panin, F. Kehren, C. Michel, and M. Casey, "Fully 3-D PET reconstruction with system matrix derived from point source measurements," *IEEE Transactions on Medical Imaging*, Vol. 25, Issue 7, pp. 907–921, 2006.
- [Panin et al., 2006b] V. Panin, F. Kehren, H. Rothfuss, D. Hu, C. Michel, and M. Casey, "PET reconstruction with system matrix derived from point source measurements," *IEEE Transactions on Nuclear Science*, Vol. 53, pp. 152–159, 2006.
- [Panin et al., 2007] V. Panin, M. Chen, and C. Michel, "Simultaneous update iterative algorithm for variance reduction on random coincidences in PET," in *IEEE Nuclear Science Symposium Conference Record*, Vol. 4, 2007.
- [Peyrin et al., 1993] F. Peyrin, M. Zaim, and R. Goutte, "Construction of wavelet decompositions for tomographic images," *Journal of Mathematical Imaging and Vision*, Vol. 3, No. 1, pp. 105–122, 1993.
- [Philippe et al., 1982] E. A. Philippe, N. Mullani, W. Wong, and R. Hartz, "Real-Time Image Reconstruction for Time-of-Flight Positron Emission Tomography (TOFPET)," *IEEE Transactions on Nuclear Science*, Vol. 29, No. 1, pp. 524–528, 1982.
- [Politte et Snyder, 1988] D. G. Politte and D. L. Snyder, "The use of constraints to eliminate artifacts in maximum-likelihood image estimation for emission tomography," *IEEE Transactions on Nuclear Science*, Vol. 35, No. 1, pp. 608–610, 1988.
- [Qi et Leahy, 2006] J. Qi and R. Leahy, "Iterative reconstruction techniques in emission computed tomography," *Physics in Medicine and Biology*, Vol. 51, No. 15, 2006.

- [Qi et al., 1998] J. Qi, R. Leahy, S. Cherry, and A. Chatziioannou, "High-resolution 3D Bayesian image reconstruction using the microPET small-animal scanner," *Physics in Medicine and Biology*, Vol.43, No. 2, 1998.
- [Qi et Huesman, 2002] J. Qi and R. H. Huesman, "Scatter correction for positron emission mammography," *Physics in Medicine and Biology*, Vol. 47, No. 15, pp. 2759–2771, 2002.
- [Qi, 2006] J. Qi, "Maximum-likelihood estimation of detector response for PET image reconstruction," in *IEEE 28th Annual International Conference of the Engineering in Medicine and Biology Society Proceedings*, Vol.1, pp. 2530-2533, 2006.
- [Rafecas et al., 2002] M. Rafecas, G. Boning, and B. Pichler, "Effect of noise in the probability matrix used for statistical reconstruction of PET data," in *IEEE Nuclear Science Symposium Conference Record*, Vol. 3, pp. 1787 - 1791, 2002.
- [Raheja et al., 1999] A. Raheja, T. F. Doniere, and A. P. Dhawan, "Multiresolution expectation maximization reconstruction algorithm for positron emission tomography using wavelet processing," *IEEE Transactions on Nuclear Science*, Vol. 46, No. 3, pp. 594–602, 1999.
- [Raheja et Dhawan, 2000] A. Raheja and A. P. Dhawan, "Wavelet based multiresolution expectation maximization image reconstruction algorithm for positron emission tomography," *Computerized Medical Imaging Graphics*, Vol. 24, No. 6, pp. 359–376, 2000.
- [Rahmim et al., 2008] A. Rahmim, J. Tang, M. A. Lodge, S. Lashkari, M. R. Ay, R. Lautamaeki, B. M. W. Tsui, and F. M. Bengel, "Analytic system matrix resolution modeling in PET: an application to Rb-82 cardiac imaging," *Physics in Medicine and Biology*, Vol. 53, No. 21, pp. 5947–5965, 2008.
- [Rangana et al., 1988] M. V. Rangana, T.H. Dhawan and N. Mullani, "A multigrid expectation maximization reconstruction algorithm for positron emission tomography," *IEEE Transactions on Medical Imaging*, Vol. 7, No. 4, pp. 273–278, 1988.
- [Rapisarda et Bettinardi, 2010] E. Rapisarda and V. Bettinardi, "Image-based point spread function implementation in a fully 3D OSEM reconstruction algorithm for PET," *Physics in Medicine and Biology*, Vol. 55, No. 14, pp. 4131-4151, 2010.

- [Reader et al., 2006] A. J. Reader, F. C. Sureau, C. Comtat, R. Trébossen, and I. Buvat, "Joint estimation of dynamic PET images and temporal basis functions using fully 4D ML-EM," *Physics in Medicine and Biology*, Vol. 51, No. 21, pp. 5455–5474, 2006.
- [Reader et al., 2002] A. Reader, S. Ally, F. Bakatselos, and R. Manavaki, "One-Pass List-Mode EM Algorithm for High-Resolution 3-D PET Image Reconstruction Into Large Arrays," *IEEE Transactions on Nuclear Science*, Vol. 49, No. 3, pp. 693-699, 2002.
- [Reader et al., 2003] A. Reader, P. Julyan, H. Williams, D. Hastings, and J. Zweit, "EM algorithm system modeling by image-space techniques for PET reconstruction," *IEEE Transactions on Nuclear Science*, Vol. 50, pp. 1392–1397, 2003.
- [Reeds, 1978] J. Reeds, "Jackknifing maximum likelihood estimates," *The Annals of Statistics*, Vol. 6, No. 4, 1978.
- [Richardson, 1972] W. Richardson, "Bayesian-based iterative method of image restoration," *Journal of the Optical Society of America*, Vol. 62, Issue 1, pp. 55-59, 1972.
- [Sánchez-Crespo et al., 2004] A. Sánchez-Crespo, P. Andreo, and S. Larsson, "Positron flight in human tissues and its influence on PET image spatial resolution," *European Journal of Nuclear Medicine and Molecular Imaging*, Vol. 31, No.1, pp. 44-51, 2004.
- [Sathiakumar et al., 2010] C. Sathiakumar, S. Som, S. Eberl, and P. Lin, "NEMA NU 2-2001 performance testing of a Philips Gemini GXL PET/CT scanner," *Australas Physical Engineering Science in Medicine*, Vol. 33, No. 2, pp. 199–209, 2010.
- [Schmitt et al., 1988] D. Schmitt, B. Karuta, C. Carrier, and R. Lecomte, "Fast point spread function computation from aperture functions in high-resolution positron emission tomography," *IEEE Transactions on Medical Imaging*, Vol. 7, No. 1, pp. 2–12, 1988.
- [Schmitz et al., 2005] R. Schmitz, A. Alessio, P. Kinahan, "The Physics of PET/CT scanners," in *PET and PET/CT: A Clinical Guide*, Thieme, New York, 2005.
- [Schumacher et al., 2008] H. Schumacher, S. Heldmann, and E. Haber, "Iterative reconstruction of spect images using adaptive multi-level refinement," *Bildverarbeitung Für Die Medizin 2008*, 2008.
- [Selivanov et al., 2001] V. V. Selivanov, D. Lapointe, M. Bentourkia, and R. Lecomte, "Cross-validation stopping rule for ML-EM reconstruction of dynamic PET series: effect on image quality and quantitative

- accuracy,” *IEEE Transactions on Nuclear Science*, Vol. 48, No. 3, pp. 883–889, 2001.
- [Shao et al., 1994] Lingxiong Shao, R. Freifelder, and J. S. Karp, “Triple energy window scatter correction technique in PET,” *IEEE Transactions on Medical Imaging*, Vol. 13, No. 4, pp. 641–648, 1994.
- [Shepp et Vardi, 1982] L. Shepp and Y. Vardi, “Maximum Likelihood Reconstruction for Emission Tomography,” *IEEE Transactions on Medical Imaging*, Vol. 1, No. 2, pp. 113–122, 1982.
- [Siddon, 1985] R. L. Siddon, “Fast calculation of the exact radiological path for a three-dimensional CT array,” *Medical Physics*, Vol. 12, No. 2, pp. 252–255, 1985.
- [Sitek et al., 2006] A. Sitek, R. H. Huesman, and G. T. Gullberg, “Tomographic reconstruction using an adaptive tetrahedral mesh defined by a point cloud,” *IEEE Transactions on Medical Imaging*, Vol. 25, No. 9, pp. 1172–1179, 2006.
- [Snyder et al., 1987] D. L. Snyder, M. I. Miller, L. J. Thomas, and D. G. Politte, “Noise and edge artifacts in maximum-likelihood reconstructions for emission tomography,” *IEEE Transactions on Medical Imaging*, Vol. 6, No. 3, pp. 228–238, 1987.
- [Soret et al., 2007] M. Soret, S. Bacharach, and I. Buvat, “Partial-Volume Effect in PET Tumor Imaging,” *Journal of Nuclear Medicine*, Vol. 48, No. 6, 2007.
- [Stazyk et al., 1992] M. W. Stazyk, J. G. Rogers, and R. Harrop, “Full data utilization in PVI using the 3D radon transform,” *Physics in Medicine and Biology*, Vol. 37, No. 3, pp. 689–704, 1992.
- [Stute et al., 2011] S. Stute, D. Benoit, A. Martineau, N. S. Rehfeld, and I. Buvat, “A method for accurate modelling of the crystal response function at a crystal sub-level applied to PET reconstruction,” *Physics in Medicine and Biology*, Vol. 56, No. 3, pp. 793–809, 2011.
- [Sureau et al., 2008] F. C. Sureau, A. J. Reader, C. Comtat, C. Leroy, M.-J. Ribeiro, I. Buvat, and R. Trébossen, “Impact of image-space resolution modeling for studies with the high-resolution research tomograph,” *Journal of Nuclear Medicine*, Vol. 49, No. 6, pp. 1000–1008, 2008.
- [Surti et Karp, 2004] S. Surti and J. Karp, “Imaging characteristics of a 3-dimensional GSO whole-body PET camera,” *Journal of Nuclear Medicine*, Vol. 45, No. 4, pp. 1040–1049, 2004.
- [Tai et al., 2003] Y. Tai, A. Chatziioannou, Y. Yang, and R. Silverman, “MicroPET II: design, development and initial performance of an improved microPET scanner for small-animal imaging,” *Physics in Medicine and Biology*, Vol. 48, No.11, 2003.

- [Tohme et Qi, 2009] M. Tohme and J. Qi, "Iterative image reconstruction for positron emission tomography based on a detector response function estimated from point source measurements," *Physics in Medicine and Biology*, Vol. 54, No. 12, pp. 3709–3725, 2009.
- [Tong et Alessio, 2010] S. Tong and A. Alessio, "Noise and signal properties in PSF-based fully 3D PET image reconstruction: an experimental evaluation," *Physics in Medicine and Biology*, Vol. 55 No. 5, pp 1453-1473, 2010.
- [Townsend et Beyer, 2005] D. W. Townsend and T. Beyer, "Anato-molecular imaging: combining structure and function", in *Positron Emission Tomography- Basic Sciences*, Springer-Verlag, London, 2005.
- [Turkheimer et al., 1999] F. E. Turkheimer, M. Brett, D. Visvikis, and V. J. Cunningham, "Multiresolution analysis of emission tomography images in the wavelet domain," *Journal of Cerebral Blood Flow & Metabolis*, Vol. 19, No. 11, pp. 1189–1208, 1999.
- [Van Slambrouck et Nuyts, 2010] K. Van Slambrouck and J. Nuyts, "A patchwork (back)projector to accelerate artifact reduction in CT reconstruction," in *Nuclear Science Symposium and Medical Imaging Conference*, pp. 2625–2629, 2010.
- [Van Slambrouck et Nuyts, 2011] K. Van Slambrouck and J. Nuyts, "Accelerated convergence with image-block iterative reconstruction," *Nuclear Science Symposium and Medical Imaging Conference*, pp. 2576 - 2580, 2011.
- [Veklerov and Llacer, 1987] E. Veklerov and J. Llacer, "Stopping rule for the MLE algorithm based on statistical hypothesis testing", *IEEE Transactions on Medical Imaging*, Vol 6 , No. 4, pp. 313–319, 1987.
- [Verhaeghe et al., 2008] J. Verhaeghe, D. van de Ville, and I. Khalidov, "Dynamic PET Reconstruction Using Wavelet Regularization With Adapted Basis Functions," *IEEE Transactions on Medical Imaging*, Vol. 27, No.7, pp. 943-959, 2008.
- [Watson, 2000] C. Watson, "New, faster, image-based scatter correction for 3D PET," *IEEE Transactions on Medical Imaging Nuclear Science*, Vol. 47, No. 4, pp. 1587 - 1594, 2000.
- [Wirrwar et al., 1997] A. Wirrwar, H. Vosberg, H. Herzog, H. Halling, S. Weber, and H.-W. Muller-Gartner, "4.5 tesla magnetic field reduces range of high-energy positrons-potential implications for positron emission tomography," *IEEE Transactions on Nuclear Science*, Vol. 44, No. 2, pp. 184–189, 1997.

- [Yamaya et al, 2008] T. Yamaya, T. Inaniwa, S. Minohara, E. Yoshida, N. Inadama, F. Nishikido, K. Shibuya, C. F. Lam, and H. Murayama, "A proposal of an open PET geometry," *Physics in Medicine and Biology*, Vol. 53, No. 3, pp. 757–773, 2008.
- [Ye et al., 1999] J. C. Ye, C. A. Bouman, R. P. Millane, and K. J. Webb, "Non linear multigrid optimization for Bayesian diffusion tomography," in *Proceedings IEEE 6th International Conference Image Processing*, Kobe, Japan, 1999.
- [Zanella et al, 2009] R. Zanella, P. Boccacci, L. Zanni, and M. Bertero, "Efficient gradient projection methods for edge-preserving removal of Poisson noise," *Inverse Problems*, Vol. 25, 2009.
- [Zeng, 2010] G. Zeng, "Medical Image Reconstruction: A Conceptual Tutorial," Springer, London, 2010.
- [Zhou et Qi, 2011] J. Zhou and J. Qi, "Adaptive imaging for lesion detection using a zoom-in PET system," *IEEE Transactions on Medical Imaging*, Vol. 30, No. 1, pp. 119–130, 2011.